UNIVERSIDAD POLITÉCNICA DE CATALUÑA

Programa de Doctorado:

AUTOMATITZACIÓN AVANZADA I ROBÓTICA

Tesis doctoral

EXPERIMENTAL CHARACTERIZATION AND DIAGONOSIS TOOLS FOR PROTON EXCHANGE MEMBRANE FUEL CELLS

Mauricio Primucci

Directores:

Dr. J. Riera Colomer and Dra. M. Serra Prat

Institut d'Organització i Control de Sistemes Industrials

Junio de 2012

Universitat Politècnica de Catalunya

Institut d'Organització i Control de Sistemes Industrials

PhD program: Automatització Avançada i Robòtica

This thesis was completed at:

Institut de Robòtica i Informàtica Industrial, CSIC-UPC

Thesis advisors:

Jordi Riera Colomer

Maria Serra Prat

A Cecilia, a Ivo y a toda mi familia

Agradecimientos

En primer lugar quisiera agradecer a mis directores de tesis, Maria Serra y Jordi Riera, por el apoyo, la infinita paciencia y la dedicación brindada todos estos años. Esta etapa de mi vida quedará gratamente en el recuerdo por la aportación al desarrollo personal y profesional realizada por ellos. También, agradecer profundamente a Marta Basualdo, profesora de la carrera de Ingeniería Electrónica en la *Universidad Nacional de Rosario*, quien me dirigió en mi proyecto final de carrera y me ayudó y alentó a realizar este doctorado.

Al *Institut de Robòtica i Informàtica Industrial (IRII)*, donde he realizado la tesis doctoral, por el gran soporte tanto personal como ecónomico. También agradecer a la *Agència de Gestió d'Ajuts Universitaris i Recerca (AGAUR)* por la beca pre-doctoral que me han concedido para poder llevar a cabo esta tesis. También al *Consejo Superior de Investigaciones Científicas (CSIC)* y a la *Universitat Politècnica de Catalunya (UPC)* por los contratos que me permitieron seguir vinculado al *IRII*.

A mis compañeros de trabajos en el laboratorio: Miguel Allue y Attila Husar, por su continuo apoyo y sin los cuales la parte experimental de esta tesis no habría sido posible, muchas gracias por el soporte. A los compañeros del *IRII* con los que he compartido muy buenos momentos y que formaran parte de los buenos recuerdos de esta etapa, entre ellos: Jorge, Carlos, Stephan, Cristián, Michael y tantos otros. Especialmente, quiero reproducir una frase que me ha dado un toque de humor cuando lo necesitaba: "*las tesis no se acaban, se abandonan*", gracias Carlos por compartirla conmigo.

Por último y más importante, quisiera agradecer profundamente el soporte, paciencia y apoyo de mi familia, especialmente a Cecilia y a Ivo, que iluminan el camino de mi vida. A mis padres, Susana y Elso, a mis hermanos, Daniel y Laura, y también a Irma, Armando y Sebastián, por el incondicional afecto y el amor brindado todos estos años.

Abstract

A fuel cell is a device that gives electric power directly from electrochemical reduction and oxidation reactions. PEM fuel cells present some properties that make them appropriate for portable and transport applications: high efficiency, no emissions, solid electrolyte, low operating temperatures and high power density. However, some technical problems can be improved, durability of the materials and the appropriate control of the operating conditions. One important aspect of the operating conditions is the water management. The right water content is needed in the electrolyte and catalyst layers to maximize the efficiency of the PEMFC by minimizing the voltage losses. Water content in the fuel cell is given basically by the generation of the water in the cathode due to the reaction, the humidity of the inlet gases and the transport trough the membrane.

This thesis studies, proposes and compares different experimental characterisation methods aimed to provide performance indicators of the PEMFC water state.

A systematic use of Electrochemical Impedance Spectroscopy technique is presented and its results are studied in order to analyse the influence of different operating conditions over the PEMFC response. The variables under analysis include: load current, pressure temperature and gas relative humidity. All these variables are considered with inlet gases feeding: H_2/O_2 and H_2/Air.

A set of relevant characteristics from the EIS response has been considered. Several equivalent circuits has been analysed and those that have the best fitting with the experimental EIS data are selected. When air is used as oxidant, a simple equivalent circuit with a resistance and a Warburg element is proposed. When Oxygen is used as oxidant, a more complex equivalent circuit is needed. A detailed sensitive analysis is performed indicating those parameters that best capture the influence of the operating conditions.

A new experimental characterisation technique, based on the inlet gases humidification interruption is proposed. This dynamic technique combines the information extracted from EIS and the temporal response in order to study the water transport and storage effects in the PEMFC. Two advantages of this proposed technique is the simple hardware configuration used and the relative low impact on the fuel cell response, making attractive the humidification interruption as an in-situ technique.

Three different sets of performance indicators are proposed as diagnosis tool.

Relevant Characteristics from the EIS response, if properly monitored, can give a diagnostic of the fuel cell internal state. After an analysis, the chosen ones are: low and high frequency resistances (R_{LF} and R_{HF}) and the frequency of the maximum phase ($f_{\phi max,LF}$). These Relevant Characteristics are helpful to determine if the PEMFC with the current operating conditions is well humidified. If the zone defined by RLF decrease, RHF slight increase and the $f_{\phi max,LF}$ increase, is minimal, the cathode is optimally humidified.

Equivalent Circuit are used in order to give a physical interpretation. The selected parameters as performance indicators are: membrane resistance, R_m, time constant and resistance of diffusion process (using Warburg elements: T_W and R_W). In this case, the humidification of the fuel cell is optimum if the zone where R_W and T_W decrease and R_m has slow increase, is minimal.

Model Based performance indicators are proposed: membrane resistance R_m, effective diffusion coefficient, D_{eff} and effective active area, A_{eff}. The optimal humidification occurs when the zone where D_{eff} is stationary and R_m has not changed significantly, is minimal. The parameter A_{eff} involved in this last diagnosis procedure can be detached from the humidification interruption test and be used to estimate the effective active area and then is also helpful to compare the PEMFC performance in different operating conditions.

Resmen

Una pila de combustible es un dispositivo que da energía eléctrica a partir de reacciones electroquímicas de reducción y oxidación. Las pilas del tipo PEM presentan propiedades que las hacen adecuadas para aplicaciones de transporte: alta eficiencia, cero emisiones, electrolito sólido, bajas temperaturas de operación y alta densidad de potencia. Sin embargo, algunos problemas técnicos deben ser estudiados: la durabilidad de los materiales y la correcta selección de las condiciones de funcionamiento. Una de las más importantes es la gestión del agua. Un balance adecuado de agua es necesario para maximizar la eficiencia de la PEMFC reduciendo al mínimo las pérdidas de tensión. El contenido de agua en la PEMFC viene dado por la generación de agua en el cátodo debido a la reacción, la humedad de los gases de entrada y el transporte de agua a través de la membrana.

La tesis estudia, propone y compara los diferentes métodos de caracterización experimental con el objetivo de obtener indicadores del estado de agua en la PEMFC.

Se realiza un uso sistemático de la técnica "espectroscopía de impedancia electroquímica (EIS)" y el análisis de la influencia de las diferentes condiciones de operación sobre la respuesta de la PEMFC. Las variables estudiadas son: corriente de carga, presión de los gases, temperatura, humedad relativa y también la alimentación de los gases de entrada: H_2/O_2 y H_2/aire.

Se presenta un conjunto de características relevantes de la respuesta del EIS y se usan para dar valores iniciales a los circuitos equivalentes. Se estudian diferentes configuraciones de circuitos equivalentes y se seleccionan aquellos que tienen la mejor conexión con los datos experimentales.

Se realiza un análisis de sensibilidad de los parámetros de los circuitos equivalentes con respecto a las diferentes condiciones de operación, para encontrar aquellos que sean útiles para representar estas variaciones.

Una nueva técnica experimental de caracterización, basada en la interrupción de la humidificación de los gases de entrada es propuesta. Esta técnica combina la información de la respuesta temporal con la frecuencial (EIS) y es útil para analizar la influencia del agua en la respuesta de la PEMFC. Algunas ventajas de esta técnica son: la fácil implementación física y el bajo impacto sobre la respuesta de la PEMFC, lo cual convierte en esta técnica en candidata para ser utilizada "In-situ".

Se proponen tres conjuntos de indicadores de performance de la pila como herramientas de diagnosis.

En primer lugar, se presentan las "Características Relevantes" de la respuesta de la EIS que dan un diagnóstico del estado interno de la PEMFC. Después de un análisis, las características seleccionadas son: las resistencias de baja y alta frecuencia (R_{LF} y R_{HF}) y la frecuencia del máximo de fase ($f_{\phi max,LF}$). Estas características sirven para determinar la correcta humidificación de la pila en las condiciones actuales de operación. El cátodo está correctamente humidificado si la respuesta de las características, muestran que la zona definida por: R_{LF} bajando, R_{HF} subiendo ligeramente y $f_{\phi max,LF}$ está subiendo, es mínima.

En segundo lugar, se usan los "Circuitos Equivalentes" para dar una interpretación física a los indicadores. Los parámetros seleccionados son: la resistencia de la membrana, R_m, la resistencia y la constante de tiempo de la difusión (R_W y T_W). En este caso, la humidificación correcta del cátodo ocurre cuando la zona donde: R_W y T_W bajan, R_m sube ligeramente, es mínima.

Por ultimo, se proponen indicadores de performance utilizando un modelo: R_m, coeficiente de difusión efectivo, D_{eff} y el área activa efectiva, A_{eff}. La humidificación óptima del cátodo ocurre cuando la zona donde: D_{eff} es estable y R_m no cambia significativamente, es mínima. El parámetro A_{eff} es útil para estimar el área activa efectiva aun cuando no se realice una interrupción de humidificación y comparar la respuesta de la PEMFC bajo diferentes condiciones de operación.

Nomenclature

- FC: Fuel Cell
- PEMFC: Polymer Electrolyte Membrane Fuel Cell, alternately: Proton Exchange Membrane Fuel Cell
- GDL: gas diffusion layer
- MEA: Membrane Electrode Assembly
- SSE: sum of squared error
- H_2: Hydrogen molecule
- H^+: Hydrogen proton
- e^-: electron
- O_2: Oxygen molecule
- H_2O: Water molecule
- W_{el}: electrical work, [J]
- n: number of interchanged electrons on reaction
- F: Faraday's constant, 96487 [C/(g.mol)]
- E: potential or voltage, [V]
- G: Free Gibbs Energy, [J]
- T: temperature, [^{o}C] or [^{o}K]
- H: enthalpy, [J]
- S: entropy, [J/^{o}K]
- R: universal gas constant, 8.32 [J/(mol.^{o}K)]
- P: pressure, [bar] or [PSI]
- i: current density, [A/cm^2]
- E^0: standard state condition potential, [V] (at 25 [^{o}C] or 298.15 [^{o}K] and 1 [atm])
- i_0: exchange current density, [A/cm^2]

- $E_{T,P}$: Potential at determinate temperature and pressure, [V]
- $i_0 (i_{0,a}, i_{0,c})$: exchange current density (anode, cathode), [A/cm^2].
- $i_a (i_c)$: anode (cathode) current density, [A/cm^2].
- $k_{0,f}, k_{0,b}$: forward and backward reaction rate reference coefficients, [cm/seg].
- C_{Ox}, C_{Rd}: Oxidation and Reduction surface concentration, [mol/cm^3].
- α: electron transfer coefficient.
- α_{Ox}, α_{Rd}: Oxidation and Reduction transfer coefficient.
- $E_a (E_c)$: anode (cathode) potential, [V].
- $E_r (E_{r,a}, E_{r,c})$: reversible or equilibrium potential (anode, cathode),[V].
- Δ: difference
- $\Delta V_{act} (\Delta V_{act,c})$: Activation losses, [V].
- $\Delta V_{act,a} (\Delta V_{act,c})$:Anode (Cathode) Activation losses, [V].
- ΔV_{ohm}: Ohmic losses, [V].
- R_{int}: internal resistance, [Ωcm^2].
- R_m: ionic (also called ´’membrane”) resistance, [Ωcm^2].
- $R_{int,elec}$: electronic internal resistance, [Ωcm^2].
- $R_{int,cont}$: contact internal resistance, [Ωcm^2].
- D: diffusion coefficient, [cm^2/seg].
- C: concentration, [mol/cm^2]
- i_L: limiting current, [A/cm^2].
- ΔV_{conc}: concentration losses, [V].
- PCI: Peripheral Component Interconnect.
- VI: Virtual Instrument.
- FPGA: Field Programmable Gate Array.

- VHDL: Programming language, combination of VHSIC (Very High Speed Integrated Circuit) and HDL (Hardware Description Language).
- Rtos: Real Time Operating System.
- ORR: Oxygen Reduction Rate.
- MEA: Membrane Electrode Assembly.
- AC: Alternating Current.
- DC: Direct Current.

Subscripts and superscripts

- FC: fuel cell
- H_2: Hydrogen
- O_2: Oxygen
- H_2O: Water
- N_2: Nitrogen
- v: vapour
- l: liquid
- eff: effective
- B: bulk
- S: surface
- $'$:real part of complex value
- $''$: imaginary part of complex value

List of Figures

List of Tables

Contents

Chapter 1

Introduction

1.1 Motivation

The fuel cell systems is a field of study in constant development and there is great expectancy on the technological an scientific achievements in the industrial and automotive sectors and in the society in general.

The fuel cell is a device that provides directly electric power from electrochemical reduction and oxidation reactions. The process is developed in a continuous way while the cell is fed with the enough quantity of reactants (fuel and oxidant). The fuel is fundamentally hydrogen and the oxidant is pure oxygen or air, both generally in form of gas.

The principle of operation of the fuel cell arises from an experiment registered by Sir William Grove in the year 1839 (see Larminie & Dicks [2003]), when studying the electrolysis of the water diluted in an acid electrolyte, hydrogen and oxygen were obtained applying an electrical current.

From that date, many investigations have been carried out. But the strongest interest began when the NASA (from the decade of the 1960) used fuel cells to provide the cabin of a space ship with electricity. From this application, the industry recognized the commercial potential that has a fuel cell and from this moment it is a technology in constant development trying to be a complete commercial product (see Thomas & Zalbowritz [2000]).

Typically, the process of electricity generation from fuels involves several energy conversion steps (Barbir [2005]), namely:

1. Combustion of fuel, that converts chemical energy of fuel into heat
2. Steam generation, using the heat obtained from the combustion to boil water
3. Mechanical energy generation, using the obtained steam to run a turbine
4. Electricity generation, using the mechanical energy to run a generator

A fuel cell circumvents all these processes and generates electricity in a single step without involving any moving parts (see figure 1.1). It is this simplicity that attracts lots of attention: fuel cells can be less expensive and far more efficient than the four steps process depicted.

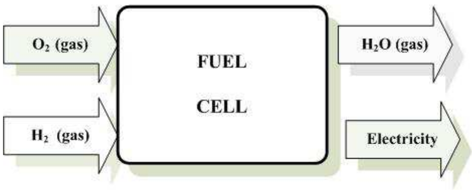

Figure 1.1: General concept of fuel cell system

In a fuel cell, the hydrogen combustion reaction is splited into two electrochemical half reactions:

$$\begin{array}{c} H_2 \rightleftharpoons 2H^+ + 2e^- \\ \frac{1}{2}O_2 + 2H^+ + 2e^- \rightleftharpoons H_2O \end{array} \quad (1.1)$$

By spatially separating these reactions, the electrons obtained from the oxidation reaction are forced to flow through an external circuit (constituting an electrical current), doing a useful work before they complete the reaction. This spatially separation in a fuel cell is accomplished by an electrolyte. An electrolyte is a material that allows ions (charged atoms) to flow and impedes the flow of electrons. The oxidation and reduction reactions take place in the catalyst layers which are the fundamental parts of the anode and cathode electrodes. Therefore, a fuel cell consists basically in two electrodes (one for each half reaction), an electrolyte and an external circuit connection.

A fuel cell is, in some aspects, very similar to a battery. It has an electrolyte, negative and positive electrodes and it generates DC electricity through electrochemical reactions. However, unlike a battery, a fuel cell requires constant supply of fuel and oxidant in order to work. Batteries generate electricity by the electrochemical reactions that involve material that is inside the battery. When the material is consumed, the batteries reduce the performance until they are finished. Unlike batteries, fuel cells allow easy independent scaling between power (determined by the fuel cell size) and capacity (determined by the fuel reservoir size). Fuel cell can be scaled from the 1-Watt range (mobile phone) to Mega-Watt range (power plant). Fuel cells offer potentially higher energy densities than batteries and can be quickly recharged by re-fueling, whereas the batteries must be thrown away or plugged in for time-consuming recharge.

Compared with combustion engines the main advantage of fuel cells is that they produce electricity directly from chemical energy and they can be far more efficient. Fuel cells have no moving parts, what makes them potentially highly reliable and silent. Also, undesirable products such as NO_x or SO_x and other particle emissions are zero if pure hydrogen is used as fuel.

However, there are some serious drawbacks for the fuel cells production and mass commercialization. Cost represents a major barrier to fuel cell market presence. Because of high costs, fuel cell technology is currently only economically competitive in a few specialized applications. Power density is another significant limitation. Power density expresses how much power a fuel cell can produce per unit volume or per unit mass. Although fuel cell power densities have improved quickly over the past decades, further improvements are required if fuel cells are to compete with fossil fuels in portable and automotive applications. Fuel availability and storage pose further problems. Some of the fuel cell types are operated with pure hydrogen gas, a fuel that is not widely available, has a low volumetric energy density and is difficult to store. In low temperature fuel cell types, alternative fuels (gasoline, methanol, etc.) are difficult to use directly and reforming stages are needed, increasing the requirement of auxiliary equipment.

Many different types of fuel cell exist, and they differ mainly by their electrolyte and the operation temperature range. A summary of the different types of fuel cells is showed in table 1.1 (from Gomez Romero [2002]).

Type	**Electrolyte**	**Work Temp.**	**Fuel**	**Advantages**	**Problems**
Polymeric (PEM)	Polymeric Membrane	30-100 ^{o}C	H_2	Fast Start-Up Solid Electrolyte	Pure H_2needed Expensive catalysts
Direct Methanol (DMFC)	Nafion®	30-100 ^{o}C	CH_3OH	Liquid fuel	Slow reaction Fuel crossover from anode to cathode
Alkaline (AFC)	KOH (liquid)	65-220 ^{o}C	H_2	Better current behaviour due to fast cathodic reaction	Reactants elimination needed
Phosphoric Acid (PAFC)	H_3PO_4	175-200 ^{o}C	H_2	Efficiency until 85 % with heat co-generation	Low power & current Expensive catalysts
Molten Carbonate (MCFC)	Carbonates Li,Na,K	600-1000 ^{o}C	H_2	Better conductivity High current	Problems with control elements
Solid Oxide (SOFC)	$(Zr,Y)O_2$	800-1000 ^{o}C	H_2	Better conductivity High current	Problems with control elements

Table 1.1: Fuel cells types

The Polymer Electrolyte Membrane (alternative name: Proton Exchange Membrane) Fuel Cells are being pursued for a wide variety of applications, especially for fuel cell vehicles prime power (FCVs) (see reference EG&G Services [2002]). As a consequence of the high interest in FCVs and hydrogen, the investment in PEMFC over the past decade easily surpasses that of all other types of fuel cells. Although significant development of PEMFC for stationary applications has taken place, many developers now focus on automotive and portable applications.

The PEM fuel cell presents some properties that make it attractive in front of other types of cells. The fact of having a solid electrolyte allows a compact construction and a simpler sealing. This makes that it does not require a fixed position, which makes it appropriate for portable and transport applications. Also, working at low temperatures, allows a quick start up, giving energy from the same instant that it is fed with reactants. They also present a high power density (W/Kg) in comparison with other fuel cells types.

Diverse issues of the PEM fuel cell technology appear as the main issues to be resolved:

- To know which are the main degradation mechanisms
- To know which are the proper operating conditions for high performance and low degradation
- Specifically, to know how to optimally manage the water inside the cell
- To obtain tools for the in-situ and online estimation of the internal fuel cell state
- To obtain controllers that operate the systems efficiently

One of the most important problem to tackle in the fuel cell operation is to maintain the appropriated inlet flow rates of oxygen and hydrogen, minimizing the compressor consumption

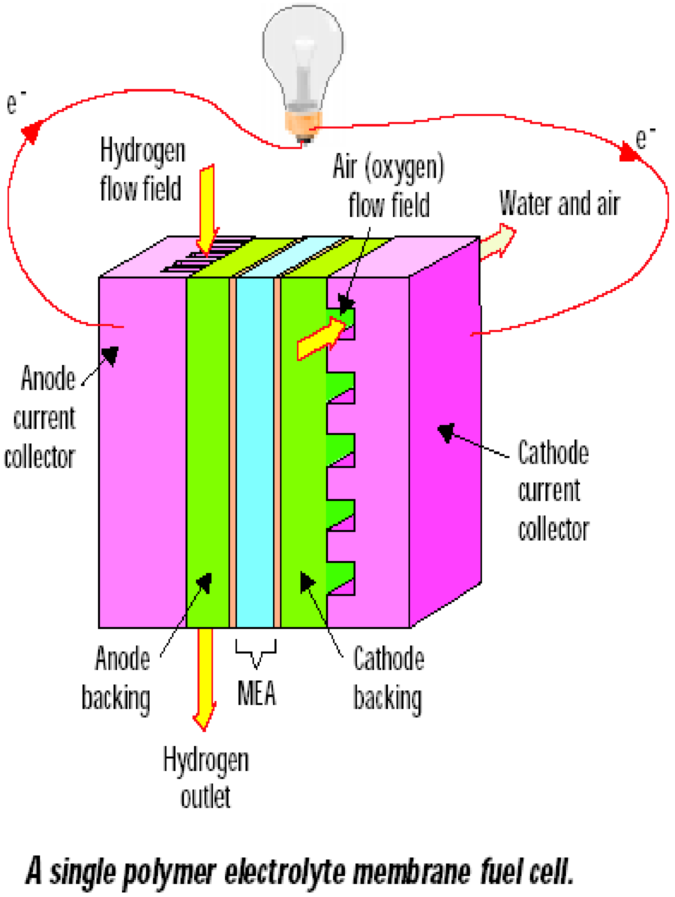

Figure 1.2: Fuel cell description

which is the cause of the greatest inefficiency of the fuel cells (Methekar *et al.* [20007], Wang *et al.* [2008], Kunusch *et al.* [2012]). The air flow control systems must also protect the fuel cell stack from oxygen starvation during the step changes of current demand. Several controllers of the air and hydrogen flows have already been proposed with this aim (Vega-Leal *et al.* [2007], Pukrushpan *et al.* [2004b]). A set of validated control proposals is now available.

Nevertheless, another important problem which has not been so well studied and solved. This problem is how to maintain inside the PEM fuel cell an appropriate water balance (present in vapour and liquid form) in the different cell parts (channels, gas diffusion layer and membrane). The importance of a good water management comes given by the characteristics of the polymeric electrolyte material. A balanced water content is necessary in the electrolyte to obtain high proton conductivity (EG&G Services [2002]). The water content in the different parts of cell is given basically by: generation of water in the cathode reaction, humidification of the inlet gases and the transport of water through membrane.

Without an appropriate management of the water, the fuel cell durability can be drastically shortened. If a dehydration of the membrane occurs, the contact between the membrane and the electrode degrades and the proton resistance increases. On the other hand, if an excess of water occurs the diffusion of the oxygen gas from the channels to the catalyst layer is more difficult.

There is a strong motivation to evaluate and analyse the experimental response of the *Polymer Electrolyte Fuel Cell* under different operating conditions, particularly the *water management* ones. In the state of the art of the water modelling and the water influence on the performance, there is a need of water management experimentally-based results.

1.2 Thesis objectives

As it has been explained in Larminie & Dicks [2003], the PEMFC can be a key element in the future energy scenario, because it permits the introduction of the hydrogen vector to the actual energy system. However in order to make the PEMFC competitive, further development of the technology is required.

This thesis is focused on the experimental results of the water management of PEMFC, which has an important impact in their performance and durability. The main objectives of this thesis are:

- To improve and propose new techniques for the in-situ characterisation of PEMFC aimed to reflect the water distribution inside the PEMFC. These techniques should be easy to implement, low in cost and include the information extracted from standard techniques, based on both time and frequency responses.

- To obtain models that include the effects of water on the performance of the PEMFC. Specially, experimental models that describe the effective behaviour of the PEMFC system response

- To propose performance indicators and diagnosis tools based on the studied characterisation techniques that permit to describe qualitatively and quantitatively the internal state of the PEMFC with respect to the water.

1.3 Outline of the thesis

This thesis is about the *experimental characterization* of *Polymer Electrolyte Membrane Fuel Cell (PEMFC)* response.

In this chapter, the motivation and objectives of this thesis is presented.

The rest of the thesis is organized according to the following chapters:

Chapter 2, "*Fuel cell system description*", provides a review of theoretical description of Polymer Electrolyte Membrane Fuel Cell operating principles. Also, the description of the fuel cell laboratories where the experimental results were obtained is done.

Chapter 3, "*PEMFC experimental characterisation techniques*", gives a detailed description about standard characterisation techniques applied to fuel cell. In this chapter, the response under different operating conditions (current, temperature, pressure and relative humidity) is showed. From the experimental Electrochemical Impedance Spectroscopy response a set of *relevant characteristics* is defined. The fuel cell response is modelled and parametrised trough a set of *equivalent circuits*, using the relevant characteristics information.

Chapter 4, "*Design of experimental techniques for PEMFC characterisation*", presents new characterisation tests. A description of the physical implementation of *humidification interruption* and the obtained experimental responses are detailed. A physical interpretation of the evolution of the different variables and the relevant characteristics is presented.

Chapter 5, "*Diagnosis tools for PEMFC from humidification interruption tests*". In this chapter, the information obtained from the characterisation techniques described in chapter 4, is combined in order to present new *performance indicators.* Three different diagnosis strategies are detailed based on these performance indicators: one of them uses some frequency response *relevant characteristics*, the second one uses some parameters of *equivalent circuit models*, and the third one is based on *fundamental physical models.*

Chapter 6, named as "*Conclusions and future work*", provides the conclusions of this thesis and a proposal of future work to continue the research of this investigation.

Chapter 2

Fuel cell system description

In this chapter, a Polymer Electrolyte Membrane Fuel Cell (PEMFC) system is presented. The operating principles, the internal structure, the internal reactions and the current-voltage response are described and studied.

As in this thesis the experimental work is very important, the fuel cell laboratories involved in this thesis are described: the CEA (French Atomic Energy Commission, Grenoble) fuel cell laboratory and the IRII (Institut de Robòtica i Informàtica Industrial) fuel cell laboratory.

2.1 Operating principles

In order to understand the behaviour of a PEMFC, in the next sections, details about its internal structure, current-voltage characteristics and losses are presented.

2.1.1 PEMFC Internal Structure

The PEM Fuel cell is composed by two collector plates that contain gas distribution channels, two gas diffusion layers(GDL), two electrodes and a polymeric membrane, distributed as can be seen in figure 2.1, extracted from Yao *et al.* [2004]. A brief description of each one of these elements is given in the following sections.

Collector plates (see figure 2.2, and references: Nikam [2002],FICT [2003],CFCE [2003]) have to comply some characteristics (see Barbir [2005]):

- Electrically conductive, because they are the electrical contact between the fuel cell and an external electric circuit.
- Impermeable to gas, to avoid losses of reactants.
- Thermally conductive, to conduct heat from/to cell to achieve effective cooling/heating process.
- Provide structural support, must have adequate strength but also must be lightweight.
- Conformable for a gas circulation path designing.

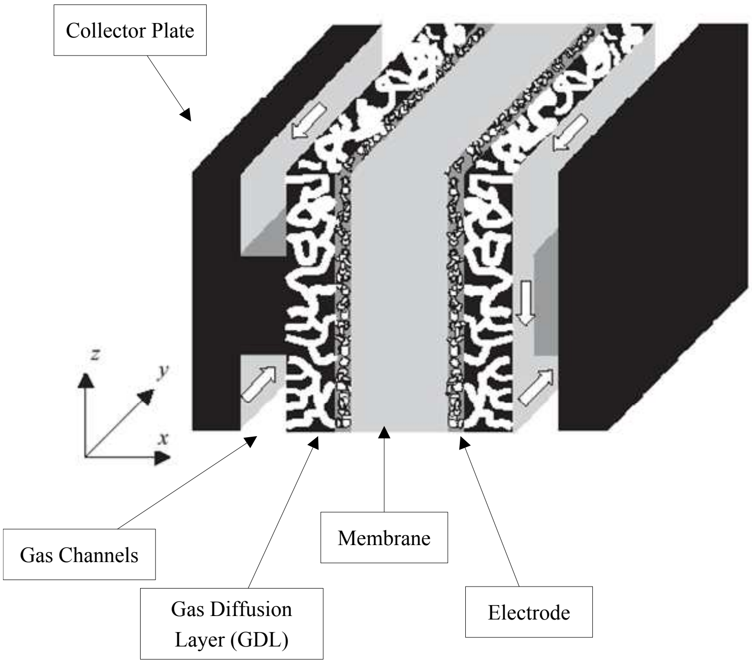

Figure 2.1: Fuel cell internal structure

In addition, the collector plates must be corrosion resistant in the fuel cell environment (for example, with the humidity of the inlet gases) and the also building materials must be inexpensive. To keep the costs down also the manufacturing process must be suitable for a mass production. Most used materials are: Graphite-based (thermoplastics: polypropylene, polyethylene or thermoset resins: with fillers like carbon derivates combinations) or Metallic-based (Aluminium,Steel, Titanium or Nickel).

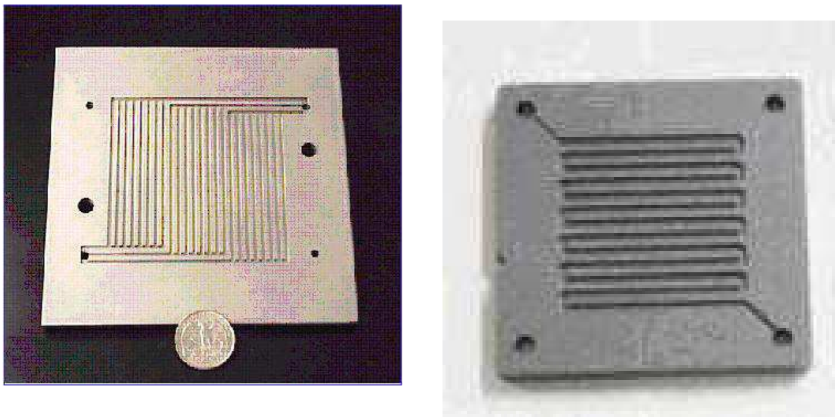
(a) (b)

Figure 2.2: Collector plates designs

Gas diffusion layer (named GDL) is a layer between the catalyst layer/membrane and collector plates (gas channels). This layer has several important functions (see Barbir [2005]):

- Provides a pathway for reactant gases from the flow field channels to the catalyst layer, allowing them access to the entire active area
- Electrically connects the electrode with the collector plates, completing the electrical circuit
- Conducts heat generated by the electrochemical reaction in the catalyst layer to flow filed channels (heat removal)
- Provides a pathway for produced water from reaction sites to flow field channels
- Acts as mechanical support to the Membrane Electrode Assembly (MEA)

These requirements make that the GDL material must be sufficiently porous, electrically and thermally conductive, sufficiently rigid to support the MEA, but must have some flexibility to maintain a good electrical contact. The most used material are carbon fibber-based, such as carbon fibber paper or carbon cloth (see figure 2.3, extracted from Toray Industries [2003]).

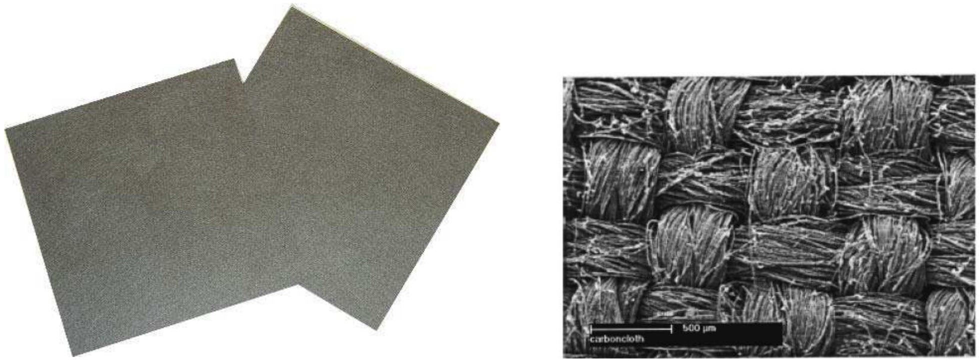

(a) Gas Diffusion layer (GDL) (b) Details of GDL of carbon cloth

Figure 2.3: Gas diffusion layer designs

Electrodes consist on thin catalyst layers pressed between polymeric membrane and a porous substrate (GDL). In this thin layer the electrochemical reactions occurs when species (Oxygen/Air from cathode channels and Hydrogen from the membrane) combines. Electrons travel trough the electrically conductive solids, so the catalyst particles should be in contact with the solid phase. Protons travel trough the polymeric membrane, then the catalyst particles should be in contact with the membrane. Finally, gases arriving from channels trough porous phase (GDL) must arrive to the reaction sites. Hence, electrode phase must also be porous to allow gases and water generated by the reaction circulate to channels. The most common used catalyst for both reactions (reduction of oxygen and hydrogen oxidation) is Platinum (Pt). In the first days of fuel cells, a high platinum load was used (about 28 [mg/cm^2]), but since different studies on 1990's, the load is reduced with the use of supported catalyst structure (0.3 to 0.4 mg[mg/cm^2]). These studies show that the catalyst surface area is more important than the weight. In consequence, it is important to have small platinum particles with a large surface area and finely dispersed on the surface of the porous area (see Barbir [2005]).

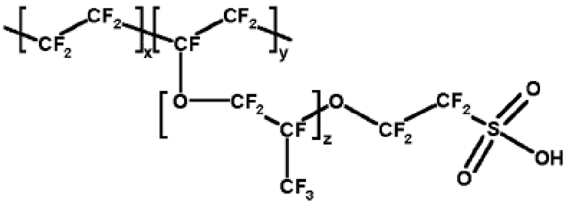

Figure 2.4: Nafion Structure

Polymeric Membrane is one of the principal components of PEM fuel cell. The membrane must have a high proton conductivity, present a good reacting gas separation, and must be mechanically and chemically stable under the working conditions. Typically, a membranes are made by a perfluorocarbon-sulfonic acid ionomer (named PSA). The best-know commercial membrane material is Nafion®, made by Dupont, which uses perfluoro-sulfonylfluoride ethyl-propyl-vinyl ether (PSEPVE) (see figure 2.4). These type of polymers have a strong proton conduction dependency on membrane structure and on water content. For this reason, the working limit is 100 [°C].

Because the catalyst layer must be in contact with membrane, developers make an assembly. This electrode and membrane assembly is named “MEA” (Membrane-Electrode Assembly) and contains the polymeric membrane and the electrodes on both sides, with a determined platinum load (see figure 2.5 and see Barbir [2005]).

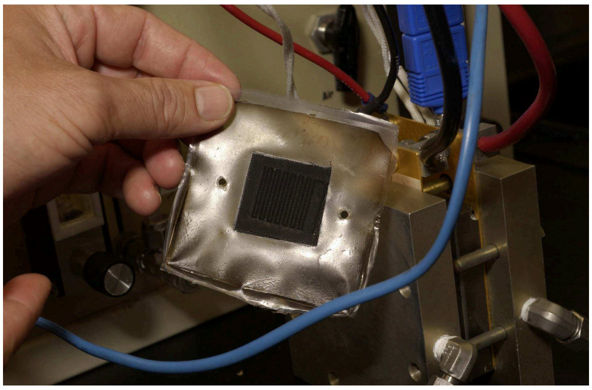

Figure 2.5: Membrane-Electrode Assembly

2.1.2 Reactions inside the PEM fuel cell

At the *anode* side, (frequently called “fuel” side), the hydrogen arrives in gas form to the catalyst layer trough the gas diffusion layer and then, hydrogen splits into electrons and protons (see Larminie & Dicks [2003]). The protons travel trough the membrane and, on the other hand, the electrons travel through to an external circuit. At the *cathode* side (frequently called “oxidant” side), the oxygen molecules (from pure oxygen or air) react at the catalyst layer with the protons arriving from anode side and the electrons coming from the external circuit, producing water and releasing heat energy.

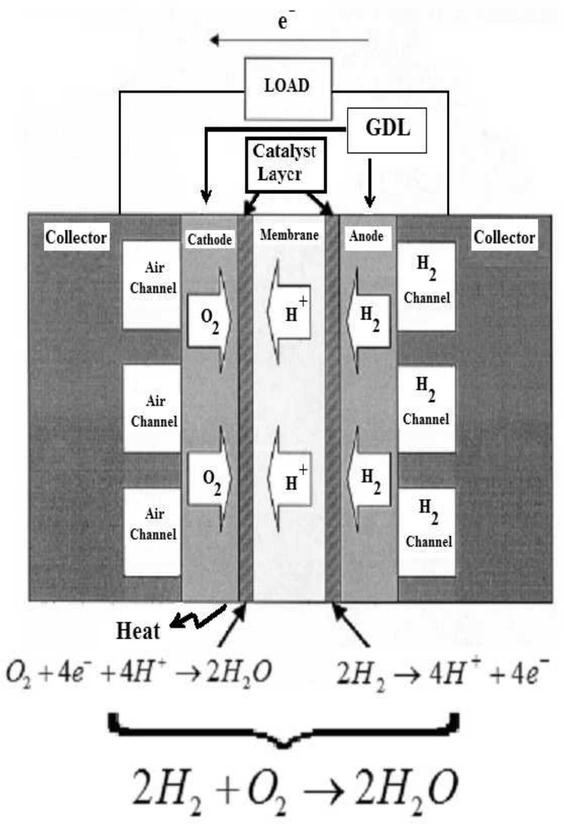

Figure 2.6: Fuel cell reactions on PEM fuel cell

A simple way to define and present the internal reactions at both sides can be described as (see figure 2.6):

- At the anode side (negative electrode) *Oxidation* occurs, the hydrogen releases electrons and creates protons:
$$2H_2 \longrightarrow 4H^+ + 4e^- \tag{2.1}$$
- At the cathode side (positive electrode) *Reduction* occurs, the oxygen reacts with electrons and protons:
$$O_2 + 4e^- + 4H^+ \longrightarrow 2H_2O \tag{2.2}$$
- The *total reaction* is summarised as:
$$2H_2 + O_2 \longrightarrow 2H_2O \tag{2.3}$$

2.1.3 Current-Voltage response

The typical response of a fuel cell is the current-voltage response, called the *polarisation curve*. In figure 2.7 a typical polarisation curve is presented (extracted from EG&G Services [2002]).

The maximum electrical work obtainable from a fuel cell is given by the change in the Gibbs free energy of the electrochemical reaction (see section "Open circuit voltage") and the actual performance is lower than its ideal potential because several types of irreversible losses are present, as is shown in figure 2.7. These losses are often referred as *polarization losses* and a description of them is done in the section 2.1.5.

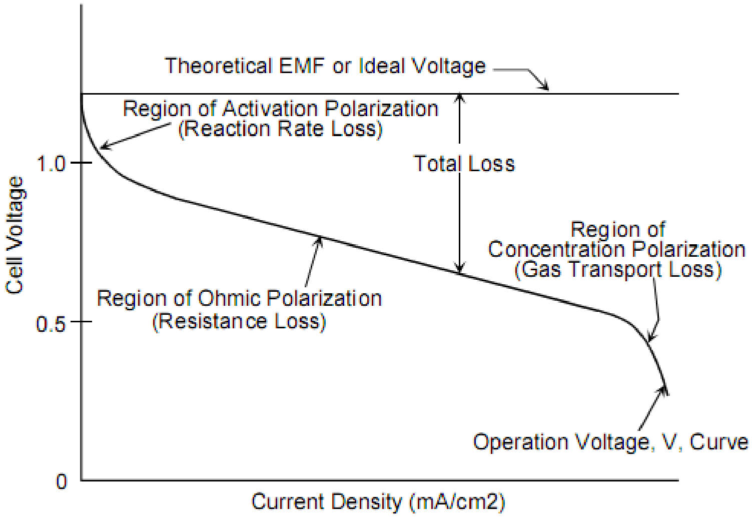

Figure 2.7: Typical polarisation curve

2.1.4 Open circuit voltage

The Nernst potential is the "ideal" open circuit cell potential. This potential sets the upper limit or maximum performance achievable by a fuel cell. To obtain this voltage, the change in the Gibbs free energy (ΔG) due to the electrochemical reactions (equation 2.3) is used.

The maximum electrical work (W_{el}) available for the fuel cell is:

$$W_{el} = \Delta G = -nFE \tag{2.4}$$

where, n is the number of electrons participating on reaction, F is Faraday's constant and E is the ideal potential of the cell.

For the reactants and the products at their standard state conditions (25 [°C] or 298.15 [°K] and 1 [atm]), Gibbs energy is:

$$\Delta G_0 = -nFE_0 \tag{2.5}$$

The ideal standard potential E_0 for a fuel cell in which H_2 and O_2 react, is 1.229 [V] with liquid water product, or 1.18 [V] with gaseous water product. The difference between these values represents the Gibbs free energy change of vaporization of water at standard conditions.

The Gibbs free energy change is given by the following equation:

$$\Delta G = \Delta H - T\Delta S \tag{2.6}$$

where ΔH is the enthalpy change and ΔS is the entropy change. The total thermal energy available is ΔH. The available free energy is equal to the enthalpy change less the quantity $T\Delta S$, which represents the unavailable energy resulting from the entropy change within the system.

Developing equation 2.6 (see EG&G Services [2002]), the ***Nernst*** potential is calculated:

$$E_{T,P} = E_0 + \frac{RT}{nF} \ln \left(\frac{P_{H_2} P_{O_2}^{0.5}}{P_{H_2O}} \right) \tag{2.7}$$

where E_0 is ideal cell potential at standard state, R is universal gas constant, T is actual temperature, P_{H_2}, P_{O_2} and P_{H_2O} are hydrogen, oxygen and water partial pressures and $E_{T,P}$ is the theoretical open circuit cell potential for given conditions of temperature and pressure.

2.1.5 Voltage losses

The actual cell voltage is lower than the ideal potential because several types of irreversible losses are present, as is shown in figure 2.7. Multiple phenomena contribute to the irreversible losses in the fuel cell:

- *Activation losses*: These losses come from the activation energy need to overcome the electrochemical reactions at the electrodes. These losses depend on the reactions, the catalyst material and distribution, and the current density.
- *Ohmic losses*: Ohmic losses are caused by the ionic resistance in the electrolyte and electrodes, the electronic resistance in the electrodes, the current collectors, and the contact resistances. Ohmic losses are proportional to the current density, depending also of material used and on working temperature.
- *Concentration (Mass transport) losses*: resulting of finite mass transport limitations rates of reactants and depend strongly of the current density, the reactant activity and the electrode structure.

2.1.5.1 Activation losses

The transfer of electrical charge is the activation energy barrier that the charge must overcome in moving from the electrolyte to the electrode or vice versa (see Barbir [2005]). So, the *activation polarisation loss* is the energy loss caused by the transfer of the electrical charge. At equilibrium there is not charge through the membrane. However, in the anode and in the cathode there exists an exchange current. The exchange current density is the inverse of the barrier that charge has to overcome moving from electrolyte to the catalyst surface.

The exchange current density i_0 is a measure of an electrode readiness to proceed with the electrochemical reaction. It depends of the concentration of the reactants and generally in the anode it is much larger than in the cathode.

From the Butler-Volmer Equation, the current-potential relationship is obtained:

$$i_0 = nFk_{0,f}C_{ox}\exp\left(\frac{-\alpha_{Rd}FE_r}{RT}\right) = \tag{2.8}$$

$$= nFk_{0,b}C_{Rd}\exp\left(\frac{\alpha_{Ox}FE_r}{RT}\right) \tag{2.9}$$

$$i_a = -i_{0,a}\exp\left(\frac{\alpha_{Ox,a}F\left(E_a - E_{r,a}\right)}{RT}\right) \tag{2.10}$$

$$i_c = -i_{0,c}\exp\left(\frac{\alpha_{Rd,c}F\left(E_c - E_{r,c}\right)}{RT}\right) \tag{2.11}$$

where:

- $i_0(i_{0,a}, i_{0,c})$ is the exchange current density (anode, cathode), [A/cm^2].
- $i_a(i_c)$ is the anode (cathode) current density [A/cm^2].
- $k_{0,f}, k_{0,b}$ are the forward and backward reaction rate reference coefficients [cm/seg].
- C_{Ox}, C_{Rd} are the Oxidation and Reduction surface concentration, [mol/cm^3].
- α_{Ox}, α_{Rd} are the Oxidation and Reduction transfer coefficient.
- $E_a(E_c)$ is the anode (cathode) potential [V].
- $E_r(E_{r,a}, E_{r,c})$ is the reversible or equilibrium potential (anode, cathode),[V].

The higher the exchange current density, the lower the activation polarisation losses. $\Delta V_{act,a} : anode, \Delta V_{act,c} : cathode$ can be expressed in the following way:

$$\Delta V_{act,a} = E_a - E_{r,a} = \frac{RT}{\alpha_a F}\ln\left(\frac{i}{i_{0,a}}\right) \tag{2.12}$$

$$\Delta V_{act,c} = E_{r,c} - E_c = \frac{RT}{\alpha_c F}\ln\left(\frac{i}{i_{0,c}}\right) \tag{2.13}$$

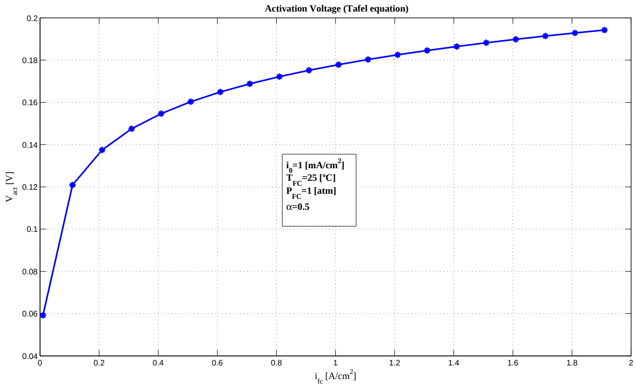

Figure 2.8: Activation losses (simulation)

where:

- $\alpha_a(\alpha_c)$: Anode (Cathode) transfer coefficient.
- $\Delta V_{act,a}(\Delta V_{act,c})$: Anode (Cathode) Activation losses, [V].

By definition, the reversible potential of the hydrogen oxidation is zero at all temperatures, therefore $E_{r,a}$=0. Activation polarisation of the hydrogen oxidation reaction is much smaller than activation polarisation of the oxygen reduction reaction.

A simplified way to present the activation losses is the *Tafel equation*:

$$\Delta V_{act} = -\frac{RT}{\alpha nF}\ln(i_0) + \frac{RT}{\alpha nF}\ln(i) \tag{2.14}$$

where the term $\frac{RT}{\alpha nF}$ is called the *Tafel slope* and is obtained from the slope of a plot of V_{act} as a function of $log(i)$, see figure 2.9. There is a strong incentive to develop electrocatalysts that yield a lower Tafel slope for electrochemical reactions so that the increases of the current density result only in a minimal increment in the activation polarization.

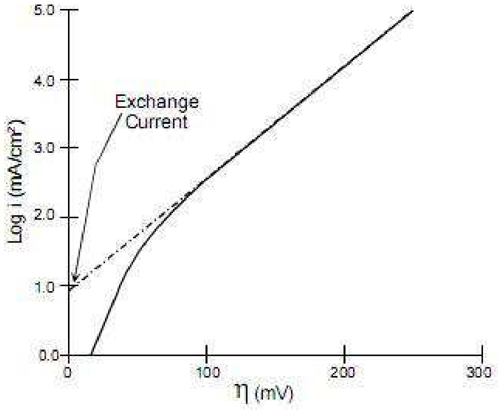

Figure 2.9: Tafel slope

The processes involving absorption of reactant species, the transfer of electrons across the double layer, a desorption of product species and the nature of the electrode surface, also contribute to the activation polarization.

2.1.5.2 Ohmic losses

There is one important factor in the electrochemical generation of electricity: the charge transport. Charge transport consists of the movement of charges from the electrode where they are produced to the electrode where they are consumed (see reference O'Hayre *et al.* [2009]). Two major types of charged species inside a PEMFC: *electrons* and *ions*. Since both electrons and ions are involved in the electrochemical reactions, both types of charge must be transported. The transport of electrons versus the ions is fundamentally different, primarily due to the large difference in mass between the two charges. In most fuel cells, ion charge transport is far more difficult than electron charge transport; therefore it dominates the losses.

Then, from the case where charge transport is dominated by electrical driving forces, the molar flux can be written as:

$$j = \sigma \frac{dV}{dx} \tag{2.15}$$

where j represents the charge flux, σ is conductivity (propensity of a material to permit charge flow) and dV/dx is the electric field providing the driving force for change transport. Then, consider the transport of the charge of uniform conductor, with a cross-sectional area A and length L, the charge transport gives:

$$j = \sigma \frac{V}{L} \Rightarrow V = j \left(\frac{L}{\sigma} \right) \tag{2.16}$$

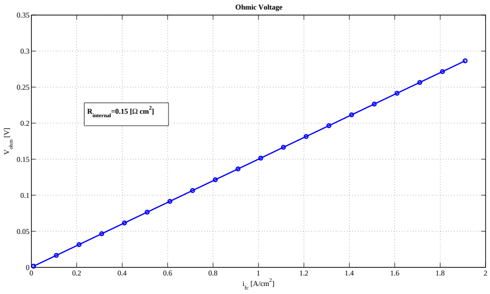

Figure 2.10: Ohmic losses (simulated)

The voltage losses due a charge transport can be presented in a form similar of the *Ohm Law*, using the relation between current density (charge flux) and current, $i = j.A$, the equation 2.16 can be rewritten as:

$$V = i \left(\frac{L}{A\sigma} \right) = i.R_{ohmic} \tag{2.17}$$

And the ohmic losses can be described as:

- i: current $[A]$.
- R_{ohmic}: total cell internal resistance, including ionic (R_m), electronic($R_{int,elec}$), and contact resistances ($R_{int,cont}$), $[\Omega]$: $R_{ohmic} = R_m + R_{int,elec} + R_{int,cont}$.

2.1.5.3 Concentration losses

As a reactant is consumed at the electrode by electrochemical reaction, there is a loss of potential due to inability of the surrounding material to maintain the concentration of reactants. That is, a concentration gradient is formed (EG&G Services [2002]). Several processes may contribute to concentration polarisation: the slow diffusion on gas phase in electrode pores, the solution/dissolution of reactants and products into the electrolyte, or the diffusion of reactants and products trough the electrolyte from reaction site.

At almost all current densities, the slow transport of reactants and products to the electrochemical reaction sites is the major contributor to concentration polarisation loss.

The rate of mass transport to an electrode surface in many cases can be described by Fick's law of diffusion:

$$i = \frac{nFD(C_B - C_S)}{\delta} \tag{2.18}$$

where, D is the diffusion coefficient of the reacting species, C_B and C_S are bulk and surface concentration, and δ is the gas diffusion layer thickness. The limiting current i_L is a measure of the maximum rate at which the reactant can be supplied to an electrode:

$$i_L = \frac{nFDC_B}{\delta} \tag{2.19}$$

From *Nernst* equation (eq. 2.7), the concentration losses is expressed as:

$$\Delta V_{conc} = \frac{RT}{nF} \ln\left(\frac{C_B}{C_S}\right) \tag{2.20}$$

And combining equations 2.20 and 2.18, is obtained the following expression:

$$\Delta V_{conc} = \frac{RT}{nF} \ln\left(\frac{i_L}{i_L - i}\right) \tag{2.21}$$

Concentration losses evolution is showed in figure 2.11.

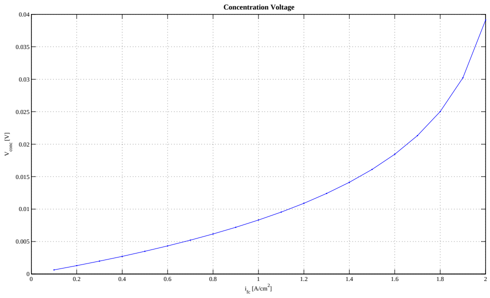

Figure 2.11: Concentration losses

2.1.6 Current-voltage response: polarization curve

The *Polarization curve* is one of the most important characteristic of a the fuel cell: is the *current-voltage* response (see figure 2.12). It may be used for diagnostic purposes, as well as for sizing and control of a fuel cell.

The cell voltage includes the contribution from the open circuit voltage ($E_{T,P}$) and taking in account described losses (activation, ohmic and concentration), the relationship between current and voltage is described by the equation:

$$V_{cell} = E_{T,P} - \Delta V_{act} - \Delta V_{ohm} - \Delta V_{conc} \tag{2.22}$$

$$= E_0 + \frac{RT}{nF} \ln\left(\frac{P_{H_2} P_{O_2}^{0.5}}{P_{H_2O}}\right) - \frac{RT}{\alpha nF} \ln(\frac{i}{i_0}) - i.R_{ohmic} - \frac{RT}{nF} \ln\left(\frac{i_L}{i_L - i}\right) \tag{2.23}$$

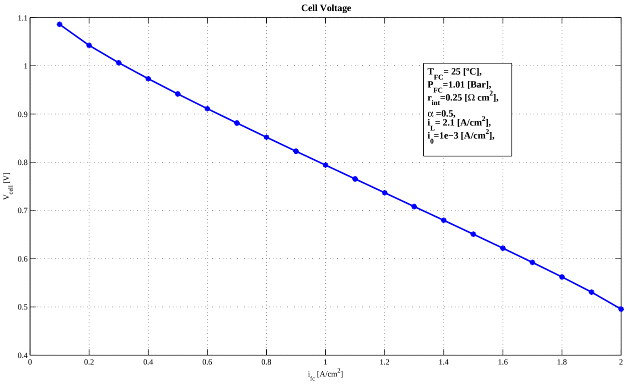

Figure 2.12: Polarization curve

The goal of the fuel cell developers is to minimize the polarization losses, so that V_{cell} approaches to $E_{T,P}$. This goal is achieved by modifications to the fuel cell cell design (improvement in electrodes structures, better electrocatalysts, more conductive electrolyte, thinner cell components, etc.). For a given cell design, it is possible to improve the cell performance by modifying the operating conditions (e.g., increase the pressure of the system, work at higher temperature, adding water vapour to the inlet gases, etc.). However, for any fuel cell, compromises exist between achieving the higher performance by operating increasing the temperature or the pressure and the problems associated with the stability/durability of cell components encountered at the more conditions.

2.2 Fuel cell laboratory description

One of the objectives of this thesis is the experimental validation of the fuel cell behaviour. At the time of this thesis starts, there is not a fuel cell laboratory in the “Institut de Robòtica i Informàtica Industrial”. So, using the experience acquired working in other projects and the inestimable help and direction of Dr. Attila Husar, specially for the mechanical connections and all system requeriments, the gas handling issues and its experience into fuel cell systems, the first station was created.

The equipment for the experimental test station and the single fuel cell were purchased from the company “ElectroChem Inc”, but unfortunately the team did not have enough experience to operate it and the failures in the equipment together with the reduced support from the company, derived in the need of adquiring experience from other laboratories.

That was the objective of the stage at the CEA (“Commissariat à l’énergie atomique et aux énergies alternatives”, Grenoble, France) and LAGEP/UCB1 (“Laboratoire d’Automatique et de Génie dEs Procédés”, Lyon, France). The visit gave good results as experimental technology knowledge acquired and the theoretic concepts interchanged. Special thanks are given to Dr. Alejandro Franco (from CEA) and to Dr. Bernard Maschke (UCB Lyon 1/LAGEP) and all the persons involved in this visit.

In the next section a brief description of the CEA laboratory and results is presented. After this section, a description of the “Test Station 1” of the “Institut de Robòtica i Informàtica Industrial” is done, with some of the obtained results.

2.2.1 CEA Fuel cell laboratory description

The test bench named “PAC-Maille” is single-cell experimental setup (see figure 2.13 and table 2.1, information extracted from the reference Franco [2005]), that allows to reproduce the operational conditions of a fuel cell, with the focus in the hydration and the composition of the gas. This experimental setup is very useful to model validation tasks. It is composed of two main flow circuits:

- One circuit named *oxygen circuit*, with oxygen/nitrogen/water vapour feeding.
- Another circuit named *hydrogen circuit*, with hydrogen/nitrogen/water vapour feeding.

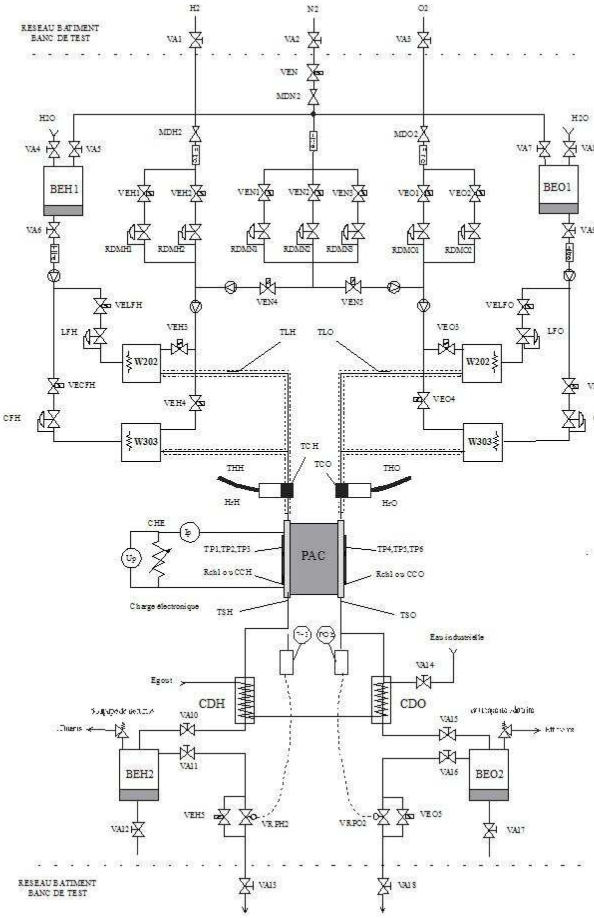

Figure 2.13: CEA “PAC-Maille” test bench

A gas feeding conditioning is performed in both circuits. This conditioning includes the measuring and the regulation of the mass flows, the gas compositions, pressures, temperatures as well as dew point temperatures of all gases inside the test bench (see table 2.1).

Name	Item
BEH1	Demineralized water tank (H_2 side, 1^o)
BEO1	Demineralized water tank (O_2 side, 1^o)
BEH2	Demineralized water tank (H_2 side, 2^o)
BEO2	Demineralized water tank (O_2 side, 2^o)
W2O2H	Small Evaporator (H_2 side)
W2O2O	Small Evaporator (O_2 side)
W3O3H	Big Evaporator (H_2 side)
W3O3O	Big Evaporator (O_2 side)
RDMxx	Mass flow regulator
VExx	Electrovalve
VA	Anti-return valve
MDxx	Pressure regulator (manual)
CDH	Condenser (H_2 side)
CDO	Condenser (O_2 side)
VRPO2	Pressure regulator (O_2 side)
VRPH2	Pressure regulator (H_2 side)
TPxx	Cell temperature

Table 2.1: References of "PAC-Maille" test bench

In this test station, the inlet gases are humidified by adding a saturated water vapour in the temperature range from 20 to 95 [°C]. The degree of humidification of the inlet gases is controlled by the dew point temperature of the feeding gas and the effective control of the output gas temperature of the mixer. Temperatures are regulated with ± 5 [°C] of resolution. The system allows the gas feeding either be humidified or not. The pressure range from 1 to 4 absolute [bar], pressure is regulated about ±50 [mbar] of resolution.

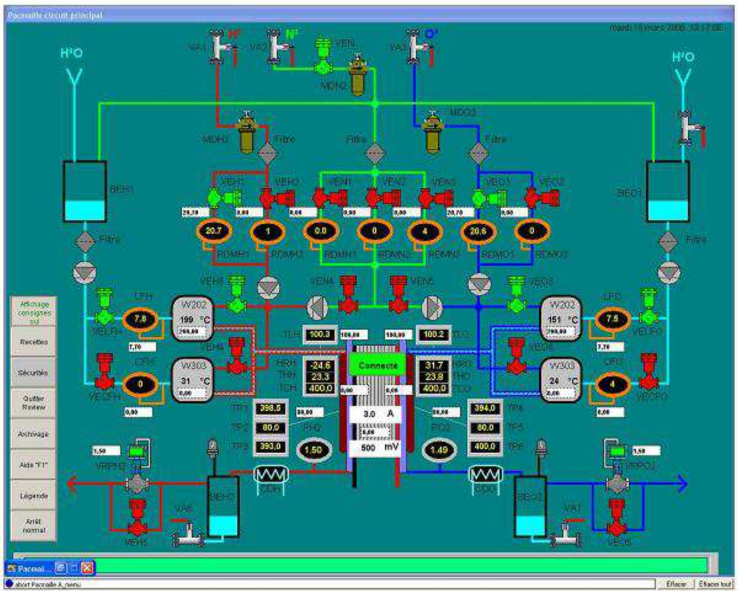

Figure 2.14: Interface control of test station PAC-Maille

An electronic load is connected to impose the desired stationary current over the fuel cell. This electronic load and the test bench are controlled by personal computer and data acquisition cards ensuring the data storage and the human interface (see figure 2.14). The gas mass flow, the pressure of gases, the cell temperature and desired stationary current are controlled with the help of an automatic system designed with RSView ®, the signal conditioning as well as the emergency system management which causes an emergency stop if there is risk of a damage (too high temperature, current, differential pressure between anode and cathode, etc.).

There is also a specialized analysis system composed of an electrochemical interface Solartron ®1287, and the transfer function analyser Solartron ®1260, connected to PC.

The programs Zview/Zplot ®help to plot the response of electrochemical impedance spectroscopy (EIS) and its treatment after measurement. Data obtained are converted in order to be exported to the Excel ®and Matlab ®.

As a conclusion, the result of this is the great knowledge extracted from working with an experimental system and the general recommendations for understanding the limitations and safety issues in a laboratory.

2.2.1.1 Polarisation curves

In figure 2.15, the polarisation curves obtained at the CEA laboratory are presented (using Air and Oxygen as oxidant). Both curves are obtained for the conditions presented in table 2.2.

Oxidant	T_{FC} **[°C]**	P_{FC} **[Bar]**	Φ_{FU} **[NL/h]**	Φ_{OX} **[NL/h]**	**RH** [%]
Oxygen	80	1.5	20.9	10.4	100
Air	60	1.0	20.9	49.4	100

Table 2.2: Operating conditions of CEA polarisation response

The principal difference between Oxygen and Air is that the diffusion losses are important at high currents when working with air.

During the visit, a large set of EIS at different operating conditions (pressure, temperature, current and oxidant) were obtained and there are presented in chapter 3.

2.2.2 IRII Fuel cell laboratory description

The Fuel cell Control Laboratory at IRII is used for the validation and testing of control strategies of fuel cell based energy conversion systems. The facilities are equipped with a supervisor system which monitors necessary safety conditions regarding gas leaks and power failure alarms management through automatic air extraction and safe shut-down routines for the test stations in case of emergency.

The laboratory has five test stations, four of them are provided with Oxygen, Hydrogen, Nitrogen and Air inlets in order to work with fuel cells. The fifth one is used for basic fuel cell demonstration applications. Each of the four test stations is equipped with the necessary

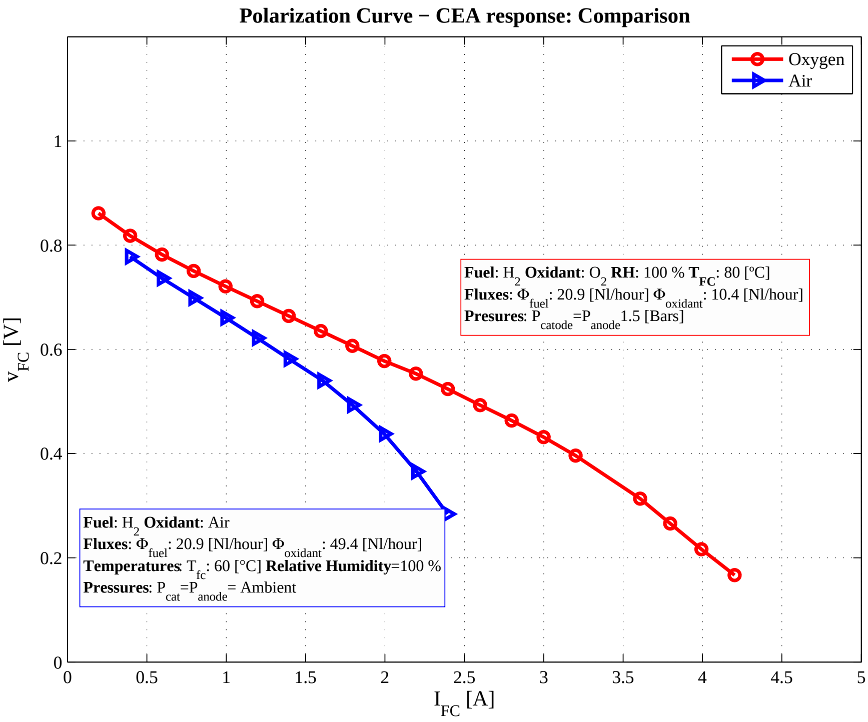

Figure 2.15: CEA polarisation curves (Air and O_2)

sensors and actuators to handle a fuel cell in a safe and automated way, as well as to modify the working conditions that affect a fuel cell (humidity, temperature, flow, etc.).

Each station is designed with certain functionality depending on the type of experiment and fuel cell employed. The simplest single fuel cell up to low and medium-power fuel cell stacks are characterized in test station 1.

Test station 2 is based on a 1200 [W] fuel cell and its connection to different electrical converters and energy-storage systems in order to validate energy control strategies and different levels of hybridization. The test station 3, utilizes an environmental chamber as its main element, which controls the relative humidity, temperature and oxygen concentration to evaluate the fuel cell systems (a new-wide range of possibilities on the field of fuel cells tests).

Built on a vertical panel, test station 4 has all the components of a standard electrical operation automotive system based on fuel cells. This test station is used primarily to validate supervisor fault-tolerant control systems.

In this thesis, the *test station 1* is used to obtain the experimental data of the single fuel cell under analysis. In the following sections, a brief description of the different aspects of this station is done.

2.2.3 Hardware description of Test station 1

In this section, a brief description of installed hardware of the *Test Station 1* is given.

2.2.3.1 Single fuel cell

The fuel cell response is studied using a single fuel cell (see figure 2.16, with the following characteristics:

- **Builder:** Electrochem, Inc.
- **Name:** EFC05-01SP®.
- **Type:** Single fuel cell.
- **Serial Number:** E3408
- **Active Area:** 5 [cm^2].
- **Membrane Assembly:** Nafion$^{\text{TM}}$ 115 and 1 [$mgPt/cm^2$] (platinum load at both sides) and Toray® carbon fiber paper "TGP-H-060" with 0.19 [mm] thickness as GDL.
- **Flow path:** 3 pass serpentine flow pattern 0.1524 x 0.1524 x 0.0764(depth) [cm].

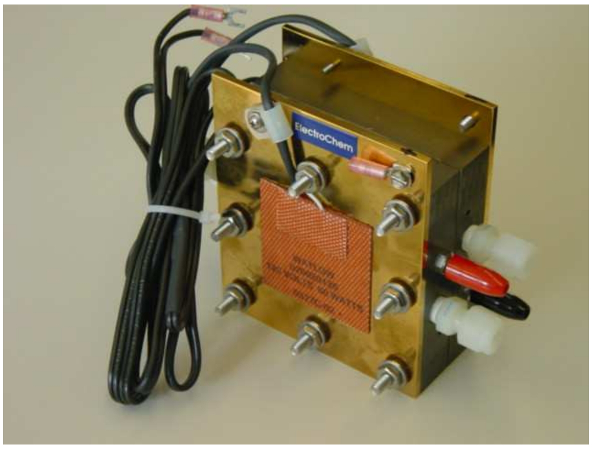

Figure 2.16: Electrochem®single fuel cell used in this thesis

2.2.3.2 Flow system distribution

The distribution of the inlet gases flow in the *experimental test station 1* is reflected in figure 2.17. The **gas flow distribution** of the station consists in three main parts: *Valve control*, *Flow control* and *Humidifier Control*.

The *Valve control* is the stage where the selection of the inlet gases is done. The gases are coming from the gas bottles installed outside the building and after internal pressure regulators, all gases are available to be connected to the system. Using a set of manual selection valves, the *Valve control* is appropriate to select the inlet gas configuration.

The *Flow control* is the mass flow control and the back pressure regulator stage. It consists of the **MTS-A-150** system (from Quintech/Electrochem®) and the system includes the following components that allow the independent gas flow control of the reactant mixtures, the cell temperature measurement and its control:

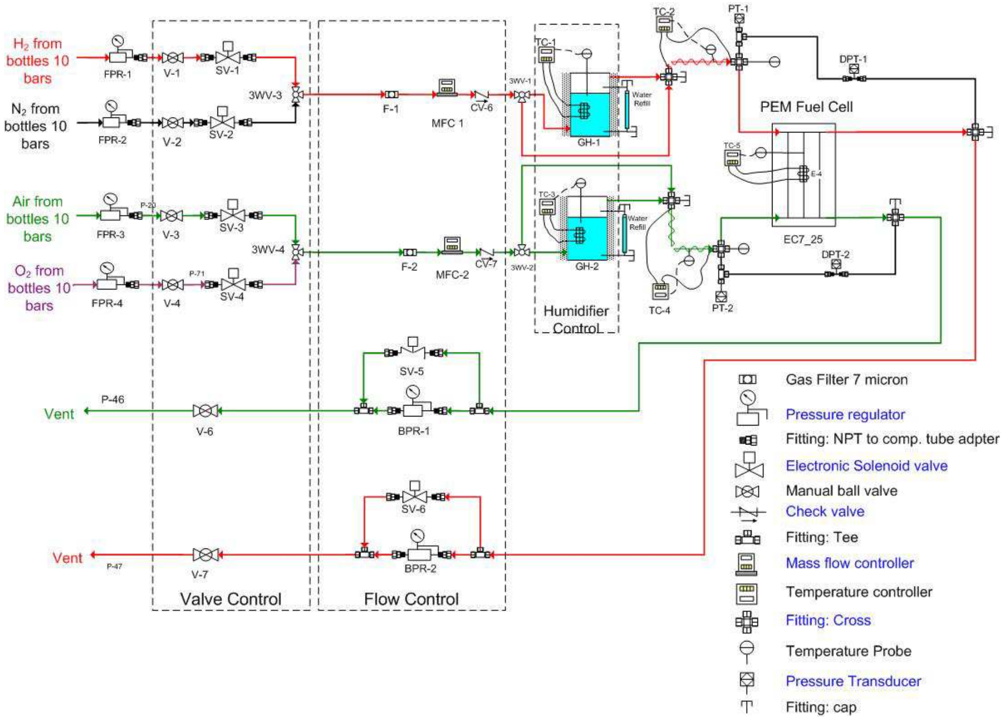

(a) Diagram of flow distribution

Figure 2.17: Fuel cell laboratory flow system distribution

- Two mass flow controllers.
- Two manual back pressure regulators.
- Cell temperature controller (a K-type thermocouple is included).

Figure 2.18: Flow control

Humidifier control is the one of the most important stages of the flow system. As the PEMFC needs water in order to present a correct operation, an humidified mass flow must be provided to the inlet gases.

Initially, the humidifier system **HSA-TC-GTL** is installed. According to the Electrochem ®(see figure 2.19(a)): “the HSA unit is a self-contained module providing safe and convenient humidification of reactant gases for fuel cell testing. It operates by bubbling each gas through a heated reservoir of high purity water. ElectroChem ®proprietary design provides for high quality humidification without the generation of water slugs or intermittent flow”.

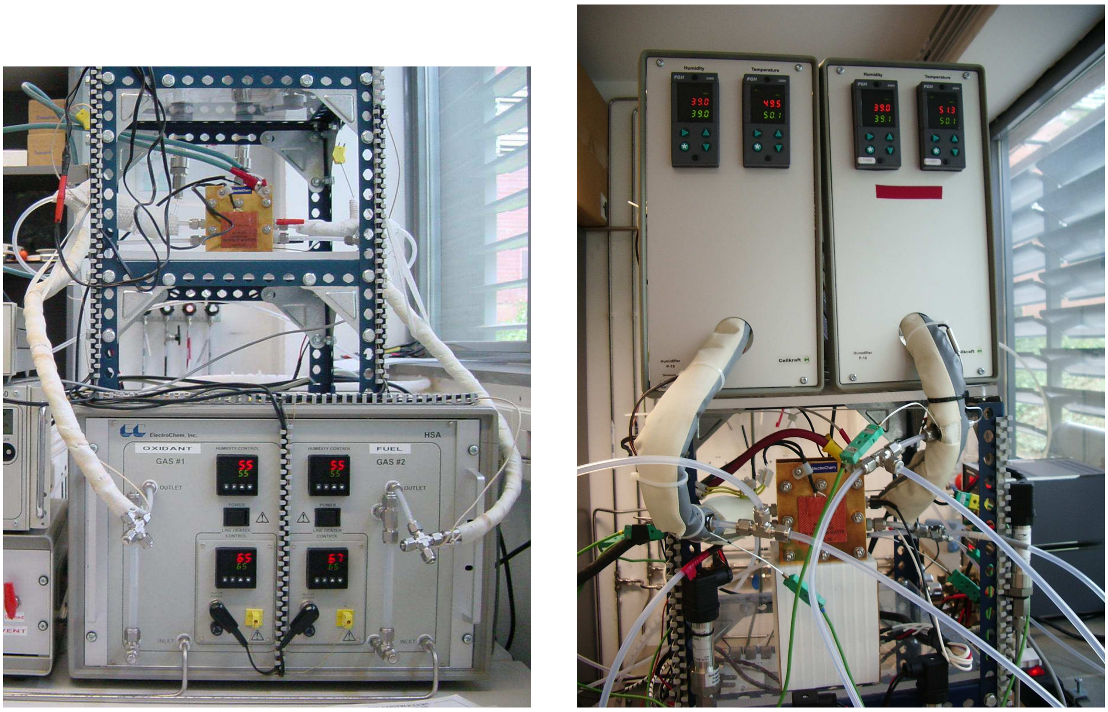

(a) Electrochem (b) Cellkraft

Figure 2.19: Humidifier control

But, after a large number of tests, the group takes the decision to **replace** this humidifier. There is one main reason for the *humidifier case* replacement: the **liquid water presence** at the fuel cell. As can be seen in figures 2.20(a) and 2.20(b). Once the system is working under stable conditions, during EIS tests number 4 and 5, the evolution shows a step variation in the voltage (without any change of the operating conditions) and at the same time a liquid water droplet is observed to go out of the system. It is very difficult to understand this fact, considering that the humidifier temperature is lower than line heater and than the cell temperature. In fact, from temperature measurement, the inlet gas is entering at 80 % of relative humidity. As a consequence of this malfunction in was not possible to perform the comparison between the results obtained in the CEA laboratory and those obtained in the IRII laboratory.

After different test days and repeating the same situation (causing cell performance degradation), an important decision was taken: **to replace the humidifier**.

The humidifiers were replaced by **Cellkraft P-10 humidifiers** (see figure 2.19(b)), with a standard configuration, one for each side (anode and cathode side). The P-Series humidifier generates an humidified air flow by the transfer of the water molecules through a membrane to the gas flow. The humidity is controlled by setting the temperature of the water surrounding the membrane tubes. An humidity sensor monitors the humidity of the outlet gas and gives feedback to the membrane heaters. The Cellkraft ®membrane concept gives a stable performance in the full flow range, without droplets in the low or in high flow rate. The units can be operated in the range from zero to full flow without problems.

Important note: All the experimental results presented in next chapters, are done with

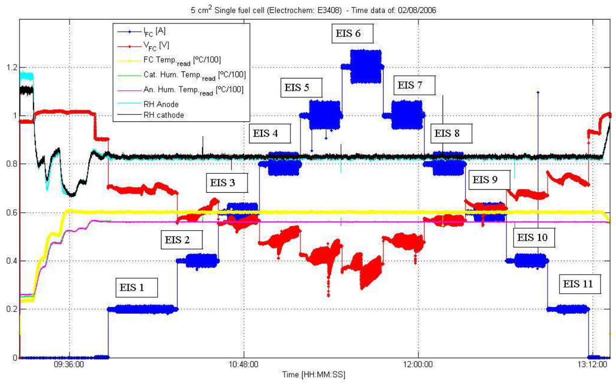

(a) Day response of test

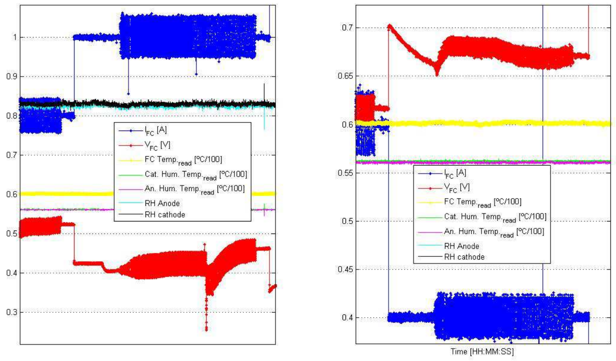

(b) Detailed voltage evolution

Figure 2.20: Electrochem humidifier response

the *Cellkraft*®humidifiers. In case of using any of the Electrochem ®humidifier results, a comment after presenting the results is inserted.

2.2.3.3 Test Station 1: Electronic equipment

A description about the main electronic devices used in the test station is presented in this subsection. In special, among the other measurement devices (temperature sensors, current clamp, etc.) the most important ones are the *Electronic Load* and the *Spectrum Analyser*

The *programmable electronic load* used is the **TDI RBL 488-800** (Transistor Device Inc.) is selected in order to obtain a good precision at lower voltages. The RBL488-800 model is ready to address all low-to-mid power load and test requirements and provides different modes of operation.

The 800W RBL model has the following characteristics:

- High speed adjustable Slew Rate
- Front panel or Remote Control
- Operation to less than 200mv (this is an important feature for fuel cell tests).

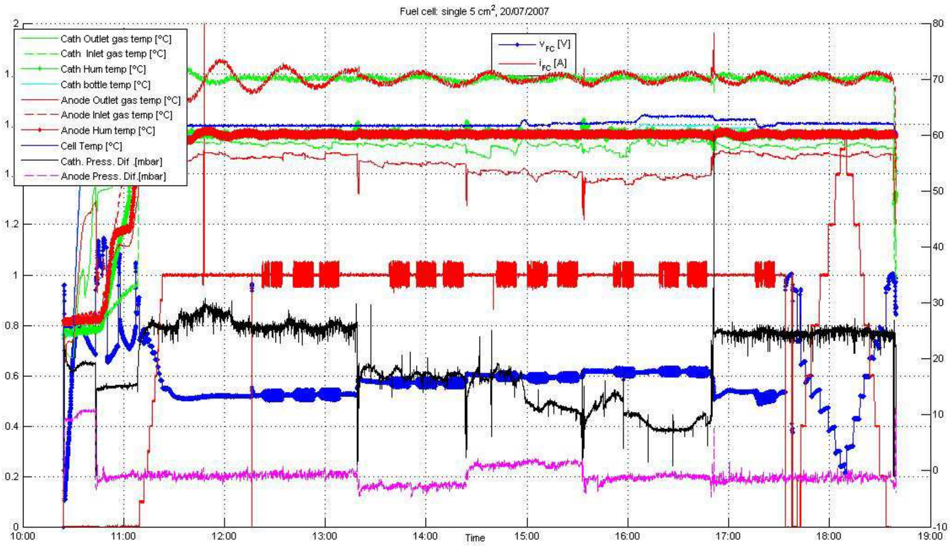

Figure 2.21: Cellkraft humidifier response

- Pulse load shaping
- Full range switching

In the laboratory, the selected model is the **RBL488 100-120-800** with the working ranges: *Voltages*: 10 [V], 50 [V] and 100 [V]; *Current*: 2 [A], 20 [A] and 120 [V]; *Power*: 800 [W]; and *Short Circuit*: 0.007 [Ω].

Figure 2.22: Agilent 35670 Spectrum analyzer

The other important equipment is the *Spectrum Analyser*, because it is needed in order to get the frequency response of the fuel cell system. The **Agilent 35670A** (see figure 2.22)is a versatile FFT analyser with built in source for general spectrum and network analysis, and for system and correlation analysis. Some of the features of this analyser can be summarized as:

- 102.4 [kHz] at 1 channel, 51.2 kHz at 2 channel

- 100, 200, 400, 800 and 1600 lines of resolution
- 90 dB dynamic range, 130 dB in swept-sine mode
- Source: Random, Burst random, Periodic chirp, Burst chirp, Pink noise, Sine, Arbitrary waveform
- Measurements: Linear, Cross, and Power Spectrum, Power Spectral Density, Frequency Response, Coherence
- Octave analysis with triggered waterfall display

This spectrum analyser it is used to force a sine wave current to the system. After the voltage measure response, it calculates the impedance spectra of the fuel cell, suitable for the Electrochemical Impedance Spectroscopy, described in the next chapter.

2.2.4 Software description

Fortunately, in fuel cell laboratory there are persons with valuable experience and knowledge help me to develop new systems and tests. Special thanks to Miguel Allue and Dr. Attila Husar for all their help in the experimental part.

The LabVIEW®(short form of Laboratory Virtual Instrumentation Engineering Workbench) is the software platform used for developing and performing the experimental tests in the test bench.

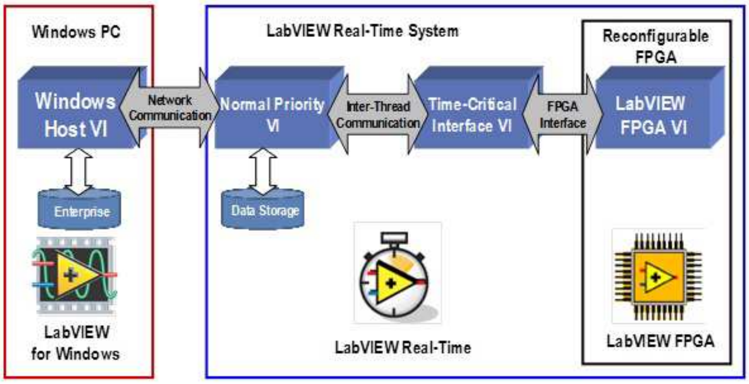

Figure 2.23: Labview system architecture

From reference Cañada Gracia & Allue Fantova [2009], the selected architecture for *Test station 1* is the presented in figure 2.23. It consists of two computers, one with the *LabVIEW Real-Time System*, named **PC Rtos** and the other with Windows XP operating system and *LabVIEW for Windows* installed, named **PC Host**.

With this configuration, it is allowed the programming environment integration in one computer: *PC Host*. Using the LabVIEW®in the *PC Host*, the real time application can be prepared and programmed in this computer and downloaded to *PC Rtos*. This architecture has also another advantage: can be used with the series “CompactRIO” (where RIO= Reconfigurable Input Output), a wide range of hardware and software from National Instruments by a simple way.

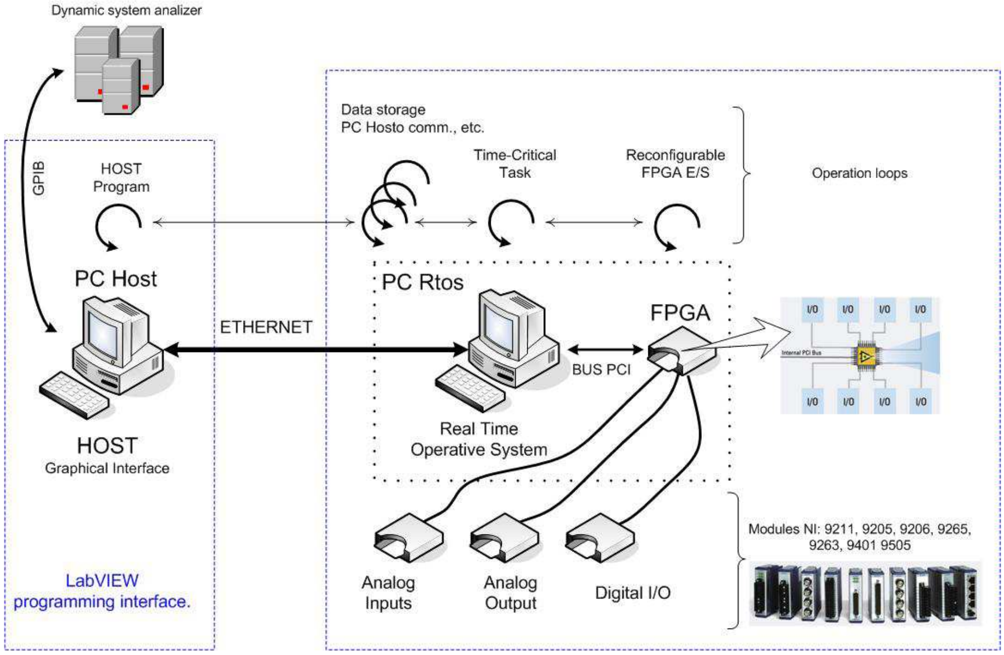

Figure 2.24: Labview system configuration

PC host serve as a LabVIEW development environment, executing human-machine task and communication with real-time system. This computer offers the possibility of the change in the operating conditions, allows make graphical and numerical representation of all variables, test configuration, configure other equipment via GPIB and data treatment once the test is finished.

In the **PC Rtos**, two systems are integrated: *LabVIEW Real-Time* and *LabVIEW FPGA* system, making this tool working as dedicated real-time system. *LabVIEW FPGA* gives more real time, reconfigurable hardware and high rates of speed. Also, the programming of this modules can be done in this computer, using the graphical interface and other tools in order to give the task priority, configuration and project type (PC Host, PC Rtos or FPGA).

The *LabVIEW FPGA* is the responsible of management of the data acquisition and extraction system loops, act as security manager and programming the critical task inside the system as very high rate. Programming this module, gives the feature of hardware execution code, allowing priority definition and deterministic task to be executed by this module.

The *LabVIEW Real-Time application* has two parts: the time-critical loop and the normal priority loop. These loops are contained within separate VI's and can be configured depending on the task. Any code that must execute deterministically is placed in the time-critical loop, with all other code in the normal priority loop. In figure 2.24 a simplified diagram of the system is showed.

The human machine interface used is programmed in LabVIEW taking in account the amount of variables available to graph and the set points allowed to modify.

The *Rtos human machine interface* is depicted in figure 2.25(a), where the important services for data acquisition are defined. The control loops can be stopped and also the sampling time of the data flow can be setted.

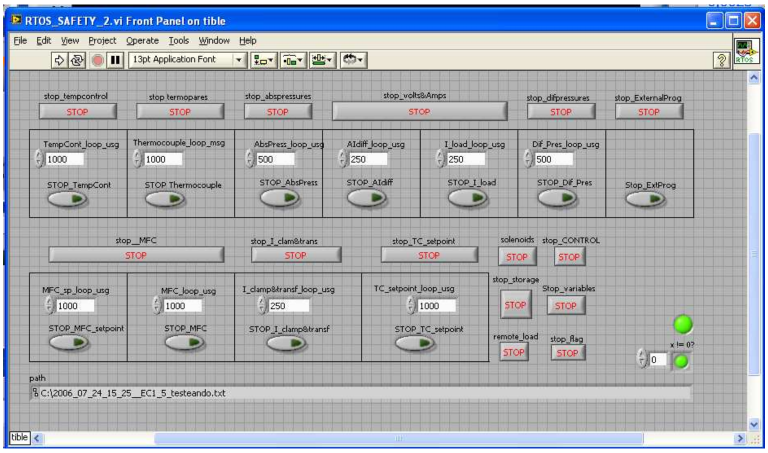

TempCont_loop_usg 1000

Thermocouple_loop_msg 1000

AbsPress_loop_usg 500

AIdiff_loop_usg 250

I_load_loop_usg 250

Dif_Pres_loop_usg 500

MFC_sp_loop_usg 1000

MFC_loop_usg 1000

I_clamp&transf_loop_usg 250

TC_setpoint_loop_usg 1000

path C:\2006_07_24_15_25__EC1_5_testeando.txt

(a) RTOS

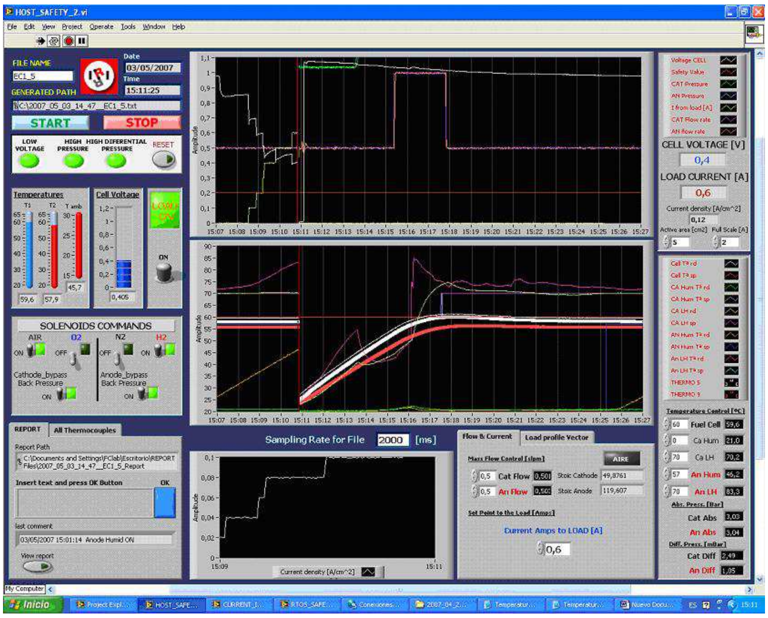

FILE NAME EC1_5

Date 03/05/2007

Time 15:11:25

GENERATED PATH C:\2007_05_03_14_47__EC1_5.txt

Report Path C:\Documents and Settings\FClab\Escritorio\REPORT Files\2007_05_03_14_47__EC1_5_Report

last comment 03/05/2007 15:01:14 Anode Humid ON

Sampling Rate for File 2000 [ms]

CELL VOLTAGE [V] 0,4

LOAD CURRENT [A] 0,6

Current density [A/cm^2] 0,12

Active area [cm2] 5

Full Scale [A] 2

Current Amps to LOAD [A] 0,6

(b) HOST

Figure 2.25: Human Machine Interface

The *Host Human Machine Interface* is presented in figure 2.25(b) and consists in the following parts:

- Test Information and commands.

In the left side of screen the information about the current test data acquisition is presented (Date, Time, generated path and filename selection, temperature and voltage indications). There is also the possibility of comments insertion in a web page style report generated in parallel with the acquisition data. There are also a set of soleinod commands (controlling the electrovalves in flow case) and the command for electronic load connection.

- Values and graphs of measured variables.

In this part, an online graphic of selected variables is presented. There are two zones, one zone is for variables like current, voltage and total pressure of the system, all in similar range of variation. The other zone is for temperatures (measured and set points), including fuel cell, humidifiers and line heaters ones. Also, an evolution of measured current density is graphed in a special plot.

- Set point of different controlled variables.

In this part, desired values of different temperatures (fuel cell, humidifiers and line heaters), mass flow (anode and cathode side) and load current are available to change during test. Those values are sent to dedicated control loops in order to get the system to desired conditions.

2.2.5 Final distribution used in Test Station 1

Even that the fuel cell stations are under constant evolution, the current hardware configuration of the *Test Station 1* is presented in figures 2.26 and 2.27.

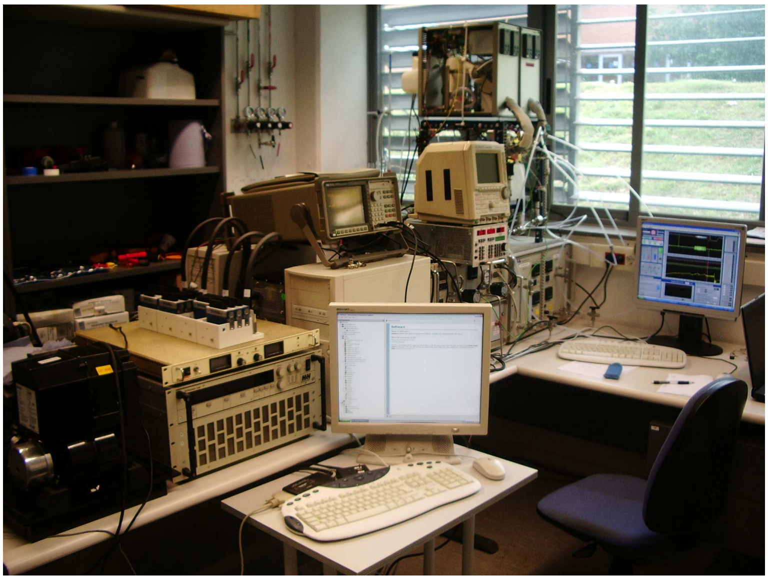

Figure 2.26: Test Station 1

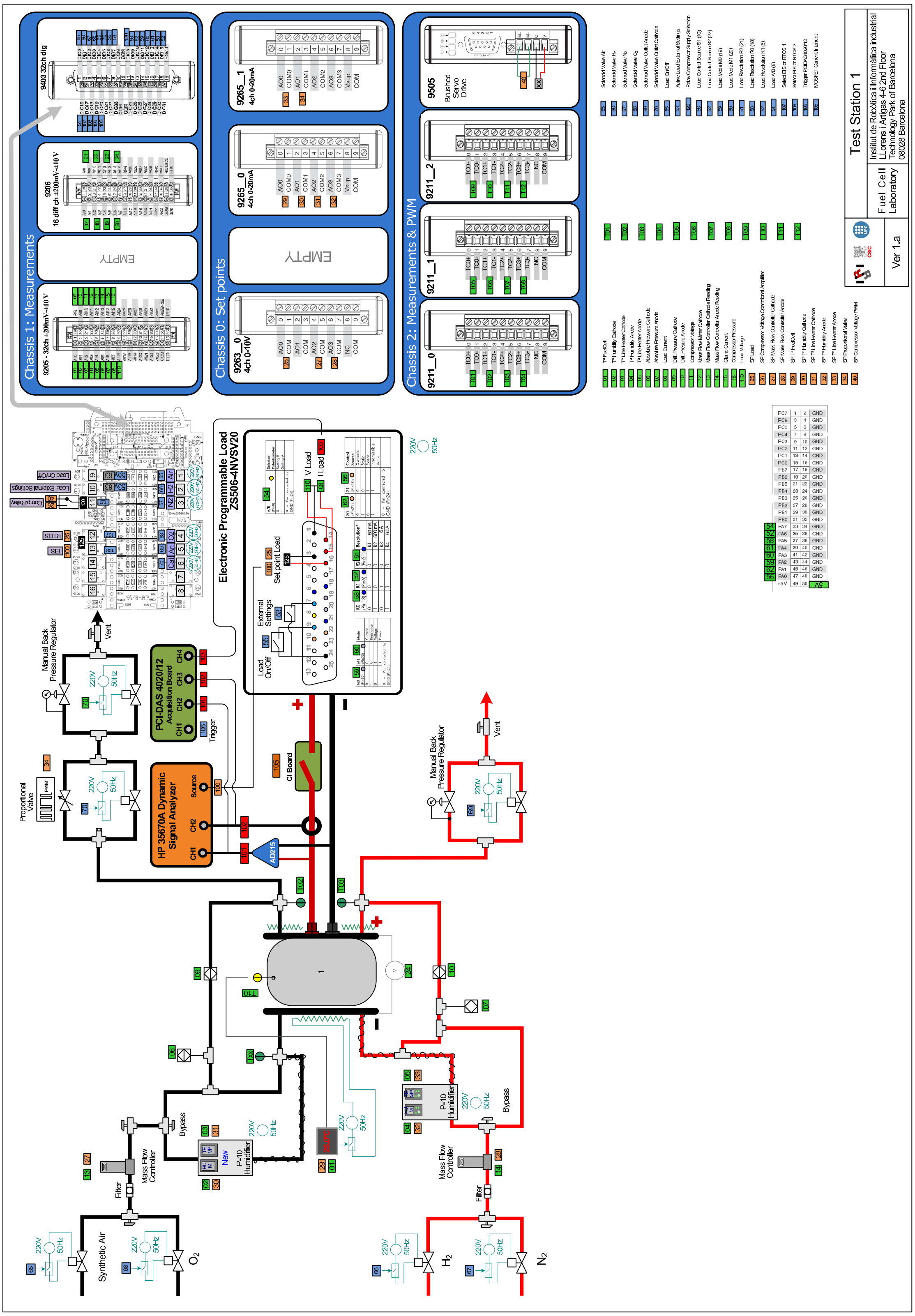

Figure 2.27: Test Station 1 scheme

2.2.6 Polarisation curves at IRII laboratory

In the figure 2.28 the polarisation curves obtained in the IRII experimental laboratory are presented. The polarisation curves are obtained using *Air* as oxidant with the operating conditions presented on table 2.3.

Oxidant	P_{FC} **[Bar]**	Φ_{H_2} **[SLPM]**	Φ_{Air} **[SLPM]**	RH_{FC} [%]
Air	P_{amb}	0.324	0.823	100

Table 2.3: Operating conditions at IRII laboratory

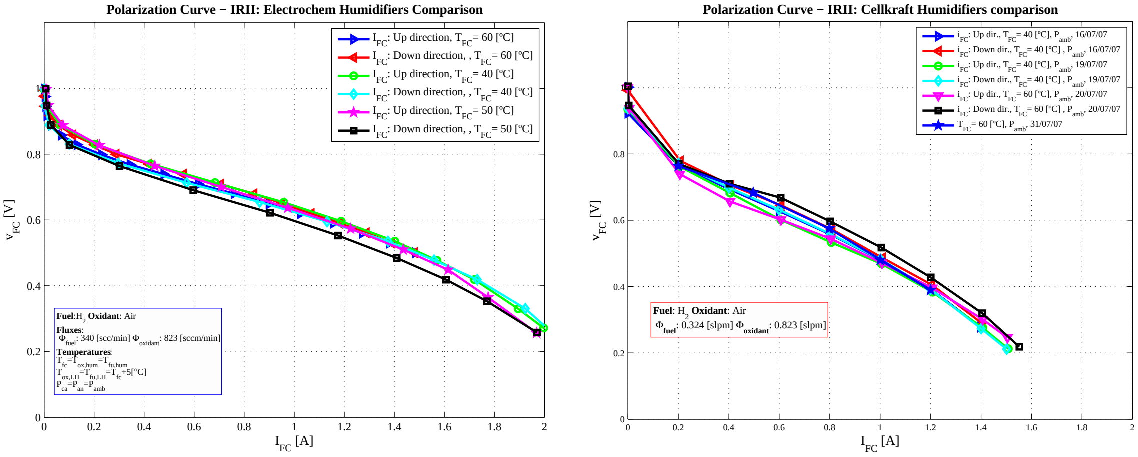

(a) Electrochem humidifiers (b) Cellkraft humidifiers

Figure 2.28: IRII polarisation curves

Comparing the results of the obtained polarisation curves, the response of the fuel cell system are very similar, but when the "Cellkraft humidifiers" are used, the response seems to be degraded compared with the "Electrochem humidifiers" one.

This is due to a the liquid water presence in the GDL and the catalyst layer, when the *Electrochem humidifier* is used, see the humidification problems described in the section 2.2.3.2.

2.3 Conclusions

In this chapter, a description of a PEMFC principles and physical properties are presented. The common used hardware that composes the PEMFC, is described and its functionality is presented. The influence in the cell response is commented.

The current-voltage response is defined and all the internal losses, are analysed and the relation with physical components is studied.

The experimental distribution and first results in form of polarisation curve are presented. A brief description of the CEA laboratory is presented. This test bench was used, during a research stage, for the first experimental tests of the single fuel cell. The most important result of this stage is the experience acquired to start working on experimental standard characterisation tests (Electrochemical Impedance Spectroscopy), its implementation and results interpretation trough specialized software.

The IRII fuel cell laboratory is presented and detailed with a description of the relevant aspects of the hardware and software employed. Some experimental polarisation curves are also shown, comparing the results of the two *humidifiers case* used in this thesis.

Chapter 3

PEMFC experimental characterisation techniques

3.1 Introduction

The main objective of this chapter is to introduce and to analyse the experimental response variations for different operating conditions. Special attention is given to the water presence that affects the fuel cell responses, for example, changing relative humidity of the input gases. Another important objective of this chapter is to propose procedures to obtain characteristics and parameters from experimental responses in order to use them in future diagnosis studies.

In this chapter, a brief description and results of standard experimental characterisation techniques applied to PEMFC are presented. In section 3.2, the standard dynamic characterisation techniques are described. In section 3.3 , these techniques are applied to a PEMFC and the experimental results at different nominal operating points are presented. In section 3.4, the relevant characteristics of the frequency response are identified. In section 3.5 equivalent circuit models are analysed.

Finally, in section 3.6 a possible fuel cell performance indicator is proposed.

3.2 Dynamic Characterisation techniques

In this section, the main standard dynamic characterisation techniques applied to fuel cell systems are explained.

3.2.1 Current Interrupt

The "Current Interrupt" technique consists in the observation of the fuel cell voltage evolution when the electrical circuit connection is opened and the current falls to zero (see figure 3.1 and the reference Larminie & Dicks [2003]). After the current is interrupted the voltage goes to "Open Circuit Voltage (OCV)" with a time constant (named "τ" in figure 3.1) which depends on the non ohmic losses of the fuel cell (activation and concentration).

There are different manners to implement this technique. Wruck et al. (Wruck *et al.*

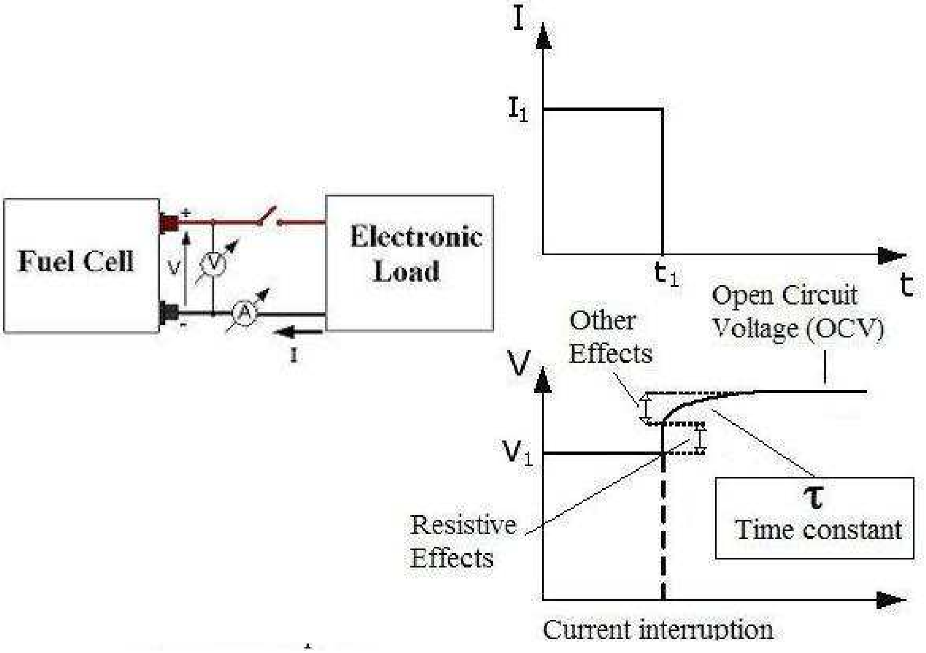

Figure 3.1: Current Interrupt: scheme and typical response

[1987]) propose electronic circuits suitable to make periodic current interruptions with measurements of the voltage at closed and open circuit situation. The voltage measurement when circuit is opened gives an estimation of the ohmic resistance of the system and also allows to investigate other effects, like the double layer capacitance (local and global effects) or the gas concentration gradient variation. Application of the designed circuit in order to observe the relaxation of the polarization at different operational currents, is done on commercial fuel cell.

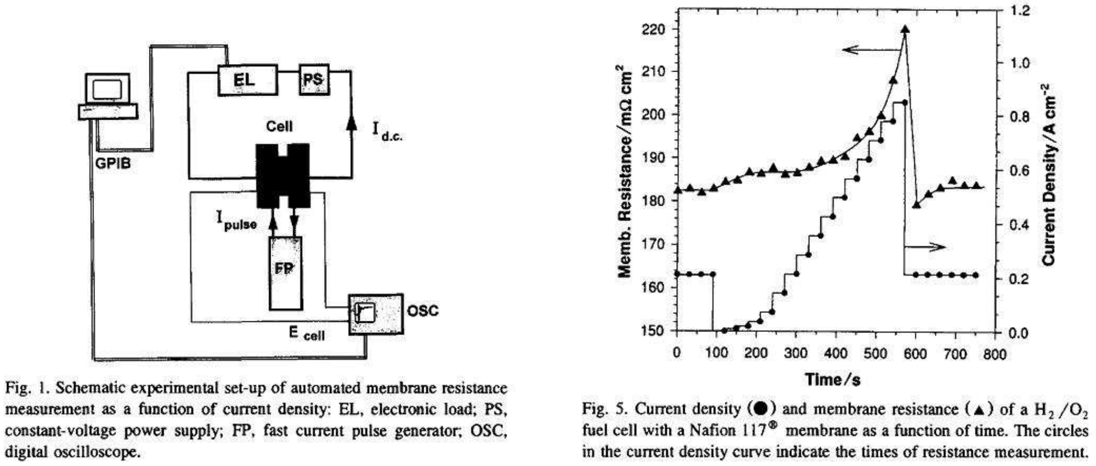

Fig. 1. Schematic experimental set-up of automated membrane resistance measurement as a function of current density: EL, electronic load; PS, constant-voltage power supply; FP, fast current pulse generator; OSC, digital oscilloscope.

Fig. 5. Current density (●) and membrane resistance (▲) of a H_2/O_2 fuel cell with a Nafion 117® membrane as a function of time. The circles in the current density curve indicate the times of resistance measurement.

(a) Connection diagram

(b) Results

Figure 3.2: Implementation of current Interruption

Following a similar approach, Büchi et al. (Büchi *et al.* [1995] and Büchi & Scherer [1996]), presented an electronic circuit and a methodology in order to obtain a measure of the membrane resistance by fast current pulses. The fuel cell is connected to an electronic load and a DC voltage source, which imposes the operating current. They propose a parallel connection between the current pulse generation circuit and the cell (see figure 3.2(a)), where the electronic circuit adds a lower current to the operating current. Then, this circuit interrupts this lower current and the voltage evolution is studied, specially the first part attributed to ohmic losses (see figure 3.2(b)). This is an important improvement, because the system is always working and the current interruption is applicable even when the fuel cell system is normally working.

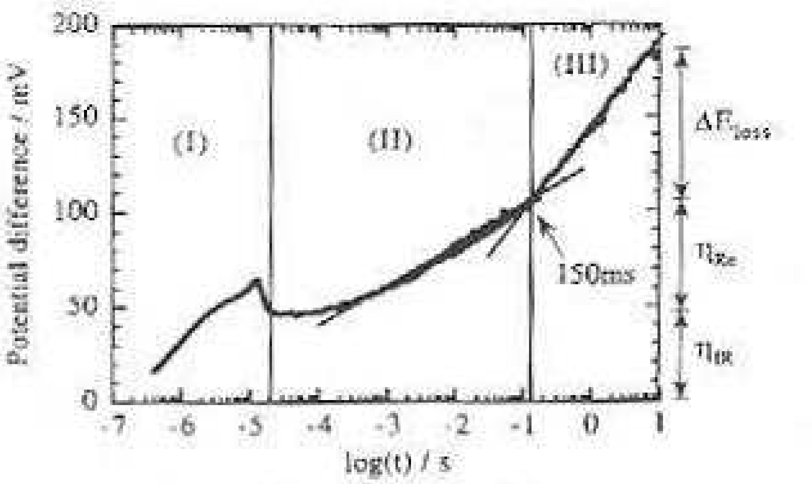

Fig. 3. A full view of the time response for current interruption with a logarithmic time scale at 923 K, U_f/U_{ox} = 60/40%.

Figure 3.3: Regions of voltage evolution of MCFC

Also, Lee et al. (Lee *et al.* [1998]), apply the current interrupt technique for voltage relaxation investigation. This method is employed on Molten Carbonate Fuel Cell (MCFC), where the evolution of the voltage from stationary operating point to open circuit voltage is studied. The responses of current interruption of the MCFC were measured as functions of temperature, gas utilization and oxidant gas composition O_2/CO_2. After the study presented in this article, the conclusion was: the single cell shows three different relaxation patterns or time regions, during the potential decay to OCV: the shortest time region is due to *ohmic losses* (region I, less than 20 μs); region II is an intermediate region related to the *reaction overpotential* (from 20 μs to 150 ms); and region III is the remaining time, due to Nernst losses (see the regions of the voltage evolution in figure 3.3).

3.2.2 Electrochemical Impedance Spectroscopy

Electrochemical Impedance Spectroscopy (EIS) is a well known characterization technique widely used in studies of electrochemical systems, such as batteries and electrolytic cells. It has been utilized by an increasing number of researchers for PEM fuel cell studies in recent years. This technique is a powerful tool for investigating the mechanisms of electrochemical reactions, for measuring the dielectric and gas transport properties of materials and to evaluate the electrode kinetics (see reference Macdonald [2006] and Larminie & Dicks [2003]).

Common uses of EIS analysis in PEM fuel cells are to find out the Oxygen Reduction Rate (ORR), to characterize transport (diffusion) losses and to evaluate and optimize the membrane electrode assembly (MEA) (see reference Wu *et al.* [2008a]).

The power of this technique arises from: (i) it is a linear technique and the results are readily interpreted in terms of Linear System Theory, (ii) if measured over an infinite frequency range, the impedance contains all the information that can be extracted from the system by linear electrical perturbation/response techniques, (iii) the experimental efficiency, defined as the amount of information transferred to the observer compared to the information produced by the experiment, is really high, and (iv) the obtained data can be analysed using frequency analysis tools. The EIS characterisation technique is often used in different fields, including the fuel cells (see references: Wagner *et al.* [1998], Paganin *et al.* [1998] and Diard *et al.* [2005]).

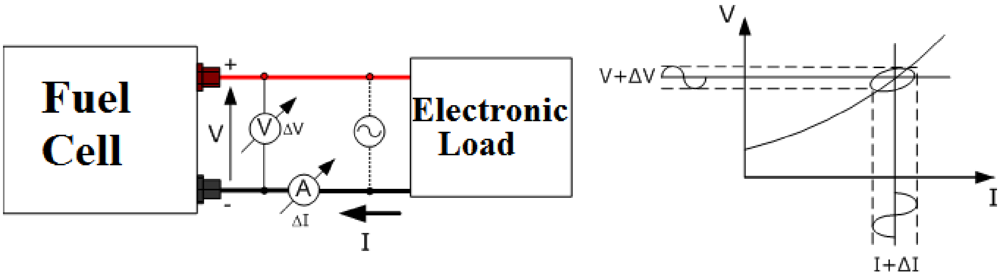

(a) Simplified Scheme

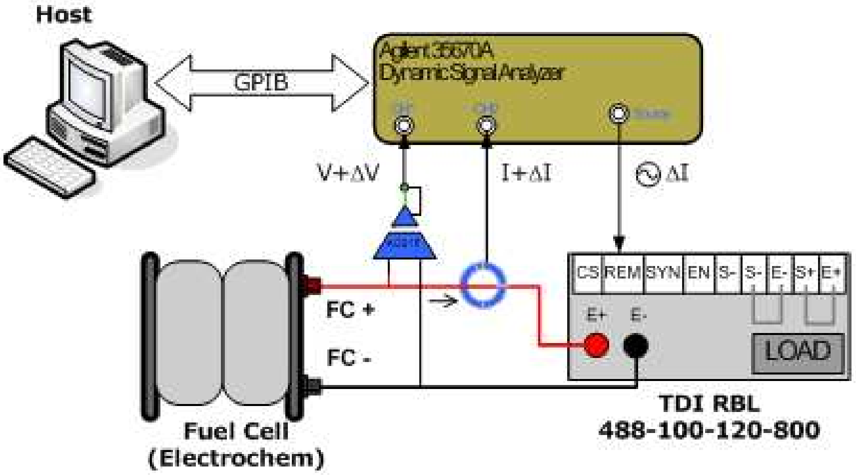

(b) Test Station 1 (IRII)

Figure 3.4: Implementation of EIS technique

EIS studies the system response to the imposition of a small amplitude AC signal (sinusoidal) over a DC operating point. A simple scheme of the experimental implementation is shown in figure 3.4 (in figure 3.4(a) a simplified concept and in figure 3.4(b), the experimental implementation in the IRII laboratory). Usually, the nominal operating point is obtained by the imposition of a constant current (I_{FC}) to the fuel cell through an electronic load, and its corresponding fuel cell voltage (V_{FC}). If the AC sinusoidal perturbation (ΔI_{FC}) is applied, the total current (i_{FC}) is:

$$i_{FC} = I_{FC} + \Delta I_{FC} = I_{FC} + I_{\Delta I_{FC}} \sin(wt) \tag{3.1}$$

The resulting AC voltage of the fuel cell has a phase difference (φ) respect to the current imposed:

$$v_{FC} = V_{FC} + \Delta V_{FC} = V_{FC} + v_{\Delta I_{FC}} \sin(wt + \varphi) \tag{3.2}$$

The impedance of the system $Z(\omega)$ is defined as the ratio of the resulting AC voltage to the imposed AC current on frequency domain ($s = i\omega$, Laplace variable):

$$Z(s) = \frac{\Delta V_{FC}(s)}{\Delta I_{FC}(s)} \tag{3.3}$$

The impedance is a complex number:

$$Z(s) = Z'(s) + iZ''(s) = \Re[Z(jw)] + i\Im[Z(jw)] \tag{3.4}$$

The magnitude $|Z(s)|$ and phase $\varphi(s)$ of impedance are defined as:

$$|Z(s)| = \sqrt{(Z'(s))^2 + (Z''(s))^2} \tag{3.5}$$

$$\phi(s) = -\tan^{-1}\left(\frac{Z''(s)}{Z'(s)}\right) \tag{3.6}$$

Impedance data is typically presented in two types of plot: Nyquist plot and Bode plot. Nyquist plot is a polar graphical representation of complex numbers, where the X-axis represents the real part and the Y-axis represents the imaginary part of the complex number. Bode plot consists of two graphs: one with the logarithm of the magnitude of the impedance ($20log_{10}|Z(\omega)|$) on the Y-axis in a logarithmic frequency ($log_{10}(\omega)$) X-axis; the second graph is the phase of impedance $\varphi(\omega)$ on the Y-axis and the frequency in a logarithmic ($log_{10}(\omega)$) X-axis.

An important characteristic of the EIS technique is its possibility to be applied “in situ” and “ex situ” (Yuan et al. Yuan *et al.* [2007]). “In situ” applications are convenient when the system has to be analysed while it is working, overimposing a small AC current (or voltage) to obtain the frequency response of the system. The data obtained can be used for control and diagnosis of the system online. “Ex situ” mode is used for material and component characterisation.

3.3 Experimental Results

In this section the system response for different operating conditions is studied. Experimental results were obtained at two different places: CEA (French Atomic Energy Commission) - Grenoble/ DTH/ PEFC Components Laboratory and at IRII fuel cell laboratory.

The results that are presented in this section correspond to the experiments performed with H_2 and O_2 as gas reactants at CEA and with H_2 and *Air* at CEA and IRII. The experiments carried out at IRII laboratory employed Electrochem®humidifiers until they were substituted by Cellkraft®humidifiers.

3.3.1 Nominal Operating Point Variations

In the following, the response of the fuel cell system at different nominal operating points are described.

The *nominal operating conditions* used in the CEA laboratory are defined in table 3.1.

	I_{FC} **[A]**	T_{FC} **[°C]**	P_{FC} **[Bar]**	Φ_{FU} **[NL/h]**	Φ_{OX} **[NL/h]**	RH_{FC} [%]
Oxygen	2.0	80	1.5	20.9	10.4	100
Air	1.0	60	1.0	20.9	49.4	100

Table 3.1: Nominal operating conditions at CEA laboratory

Where: T_{FC} is the fuel cell temperature, P_{FC} is the fuel cell pressure (considering that the anode and the cathode outlet pressures are equal, $P_{ca,out}$=$P_{an,out}$), Φ_{FU} is the fuel mass flow (H_2), Φ_{OX} is the oxidant mass flow (O_2 and Air) and RH_{FC} is the relative humidity of the inlet gases at cathode side (keeping the anode side at the maximum level RH_{an}=100 %).

In the IRII laboratory, the conditions presented in table 3.2 were applied as "nominal operating point".

	I_{FC} **[A]**	T_{FC} **[°C]**	P_{FC} **[Bar]**	Φ_{FU} **[SLPM]**	Φ_{OX} **[SLPM]**	RH_{FC} [%]
Air	1.0	60	1.0	0.324	0.823	100

Table 3.2: Operating conditions at IRII experiments

The following variables that define the operating conditions have been selected for the study:

- DC current (I_{FC})
- Fuel Cell Temperature (T_{FC})
- Fuel Cell Pressure (P_{FC})
- Fuel Cell Relative Humidity ($RH_{FC,Ca}$)

The first experiments are done imposing to the fuel cell the operating conditions (current, pressure, temperature and relative humidity) corresponding to the values defined as *nominal* in the tables 3.1 and 3.2. Then, the *operating variable* under study is established at the desired value, keeping all other variables at the nominal values. Once the system is stabilized, an EIS test is done and all data are saved. After the data saving process, the next value of the studied variable is established, maintaining all the other variables at the nominal values. A new EIS test is done and all the results are stored.

It is important to remark that the EIS is done adding a small AC current ($\Delta I_{FC,p-p} = 5\% I_{FC}$), where "*p-p*" is "peak to peak", to the DC **nominal** current (I_{FC}) and analysing the resulting voltage variation. That is to say that the *nominal operating condition* is defined by the *DC current*, normally imposed by an electronic load (I_{FC}) and must be "constant". The small variation of current (ΔI_{FC}) needed to obtain the EIS results is usually made by a frequency response analyser, connected in parallel to electronic load. This small perturbation can be considered an information signal and not an operating variable. The frequency range for the EIS test is: 0.1 [Hz] → 10 [kHz]

For example, if the "fuel cell temperature (T_{FC})" at the *IRII laboratory* is the operating variable under study, the fuel cell pressure is imposed to the nominal value P_{FC}=1.0 [Bar], the DC current, to the nominal value I_{FC}=1.0 [A] and the fuel cell relative humidity to RH_{FC}=100 %. Then, the first temperature is fixed (for example, T_{FC}=40 [°C]) and after the stabilisation time, the EIS test is done. After the EIS completion, all data can be stored and the next test can be started (for example, by setting the fuel cell temperature to T_{FC}=50 [°C]).

3.3.1.1 Operating DC Current Variations

In this section, the operation of the fuel cell at different the nominal operating DC currents, studied at CEA and IRII laboratories, is presented. A nominal DC current I_{FC} is fixed and EIS is determined with the small current variation $\Delta I_{FC,p-p} = 5\% I_{FC}$.

The response of the system when **oxygen** is used as oxidant is presented in figure 3.5. After an analysis of the response, it is seen that the frequency response can be divided in three different zones:

- *First zone, "Activation losses"*:

For a DC current, from low to medium currents (0.2 [A] to 1.2 [A]), see figures 3.5(a) and 3.5(b) and table 3.3. In this zone, the influence of the energy needed to get electrochemical reaction is relevant.

I_{FC} [A]	0.2	0.4	0.6	0.8	1.0	1.2	1.4
V_{FC} [V]	0.86	0.82	0.78	0.75	0.72	0.69	0.66

Table 3.3: DC current variation, 1st Zone ,H_2/O_2

This effect is stronger than other losses at these current levels and is reflected as a predominant low frequency arc. This arc diminishes as current increases and arrives to a certain minimum, where the other effects take more relevance.

- *Second zone, "Ohmic losses"*:

From medium to high currents (1.2 [A] to 2.2 [A]), see figures 3.5(c) and 3.5(d) and table 3.4.

I_{FC} [A]	1.4	1.6	1.8	2.0	2.2	2.4	2.6	2.8	3.0
V_{FC} [V]	0.66	0.65	0.61	0.58	0.55	0.52	0.49	0.46	0.43

Table 3.4: DC current variation, 2nd Zone, H_2/O_2

In this zone the resistance of charge transport (electrons and ions) is the main loss. It is reflected as small variations of the low and high frequency resistances.

- *Third zone, "Concentration losses"*:

At high currents (2.2 [A] to 4 [A]), the evolution is detailed in figure 3.5(e) and 3.5(f) and table 3.5.

I_{FC} [A]	3	3.2	3.4	3.6	3.8	4	4.2
V_{FC} [V]	0.43	0.39	0.35	0.31	0.26	0.21	0.16

Table 3.5: DC current variation, 3rd Zone, H_2/O_2

The main phenomena observed is associated to the fuel cell mass transport limitations, specially *oxygen* replacement after the reaction at the catalyst layer. In this case, oxygen and hydrogen concentrations play an important role and the frequency response shows that the low frequency arc increases while a second arc appears (at middle range frequencies) and starts to increase.

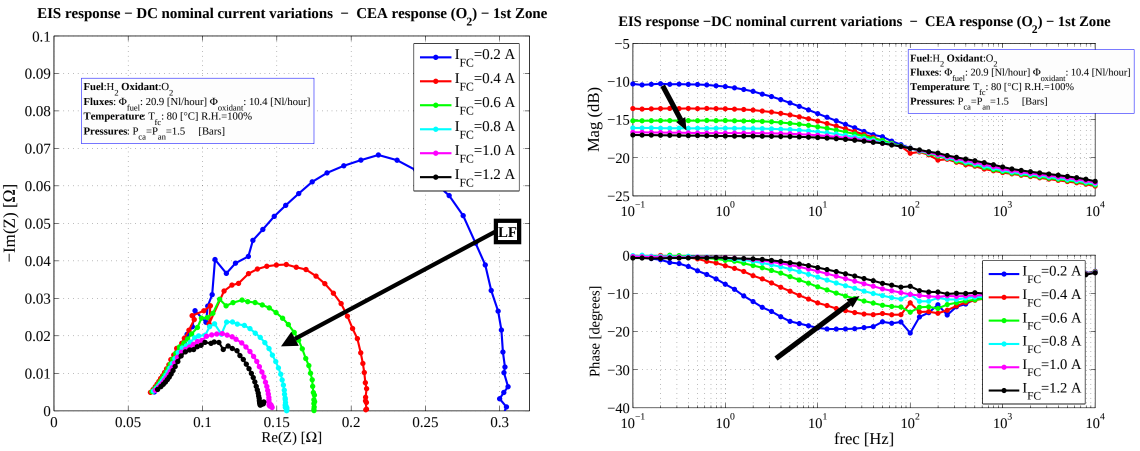

(a) Nyquist (1° Zone)

(b) Bode (1° Zone)

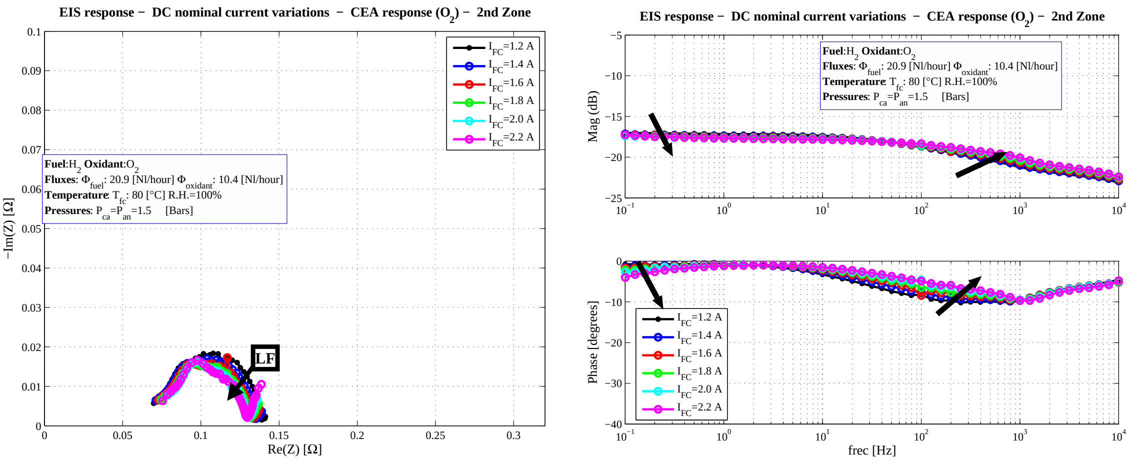

(c) Nyquist (2° Zone)

(d) Bode (2° Zone)

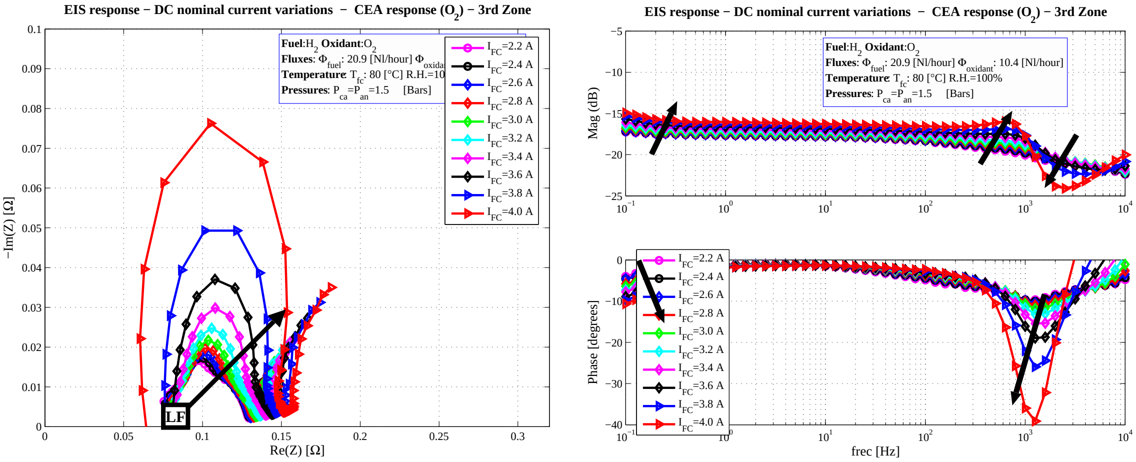

(e) Nyquist (3° Zone)

(f) Bode (3° Zone)

Figure 3.5: DC nominal current, H_2/O_2, CEA lab

The response of the system when the **air** is used as oxidant is presented in figure 3.6, where a comparison of the responses with *Electrochem®* and *Cellkraft®* humidifiers is done.

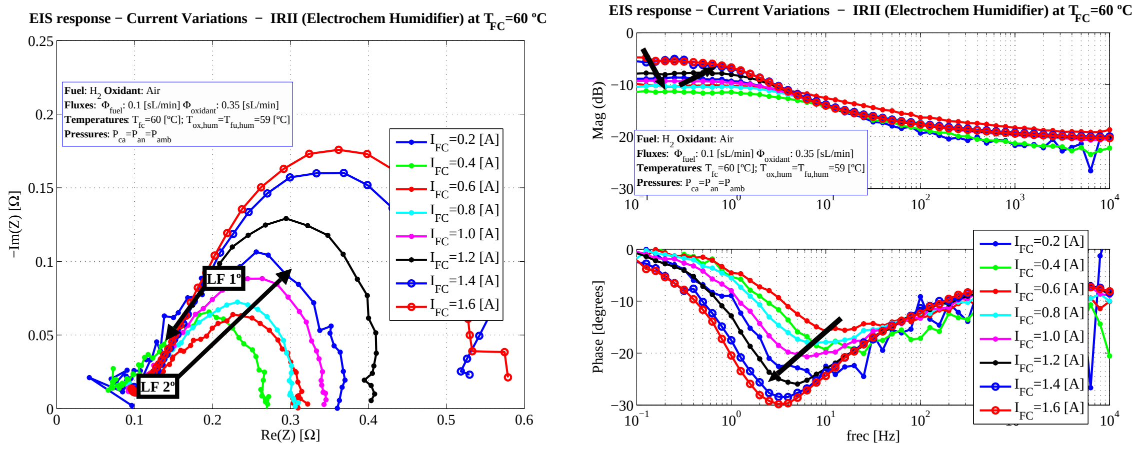

(a) Nyquist (Electrochem)
(b) Bode (Electrochem)

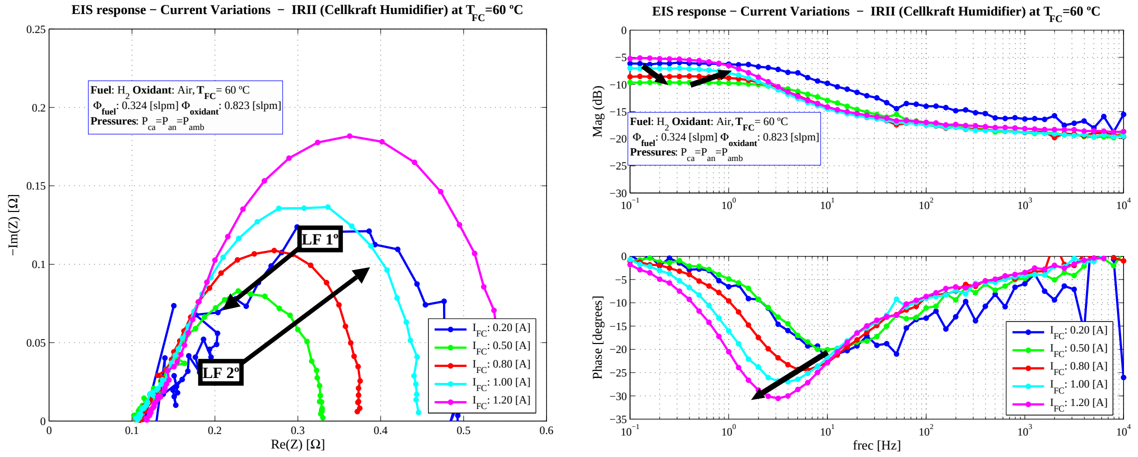

(c) Nyquist (Cellkraft)
(d) Bode (Cellkraft)

Figure 3.6: DC nominal current variation, H_2/Air, IRII lab

The frequency response of the DC current variation when the *Electrochem* humidifier is used is presented in figures 3.6(a) and 3.6(b) and details of the voltage values can be found in table 3.6. Also, the frequency response of the DC current variation when the *Cellkraft* humidifier is used is presented in figures 3.6(c) and 3.6(d) and details of the voltage values can be found in table 3.7.

Observing the response for both humidifiers, it can be seen that the frequency evolution has also three zones: *activation*, *ohmic* and *concentration*.

The first part of the evolution is from low to medium currents, marked as *LF 1º* in both Nyquist plots (figures 3.6(a) and 3.6(c)) and grouped as *Zone 1º* in both information tables 3.6 and 3.7. In this part the *activation losses* are relevant and when the current increases its influence is reduced.

The second zone is defined as *ohmic losses* zone, where the low and high frequency resistances show small variations. This zone is grouped as *Zone 2º* in both information tables

Zone	1°		2°			3°			
I_{FC} [A]	0.2	0.4	0.6	0.8	1.0	1.2	1.4	1.6	1.8
V_{FC} [V]	0.81	0.74	0.69	0.65	0.60	0.54	0.45	0.36	0.27

Table 3.6: DC current variation, Electrochem Humidifier

3.6 and 3.7.

Zone	1°		2°		3°
I_{FC} [A]	0.2	0.5	0.8	1.0	1.2
V_{FC} [V]	0.76	0.69	0.57	0.49	0.38

Table 3.7: DC current variation, Cellkraft Humidifier

The third zone of evolution is named *concentration losses*. In this zone, an increment of the low frequency resistance value is observed. This effect is related to a faster consumption of oxygen due to the higher current demanded. The *concentration losses* are marked as *LF 2°* in both Nyquist plots (figures 3.6(a) and 3.6(c)) and grouped as *Zone 3°* in both information tables 3.6 and 3.7.

3.3.1.2 Operating Pressure Variations

The absolute pressures on the cathode and the anode side are incremented at the same time, in order to avoid pressure difference between anode and cathode that could cause membrane problems (holes, deformation, etc.).

The response of the fuel cell at CEA laboratory, when H_2/O_2 are applied as reactants, can be seen in figure 3.7 and table 3.8.

In this case, the pressure starts at the atmospheric conditions and then is increased in steps by $\Delta P = 0.1$ [Bars], until 1.5 [Bars].

P_{FC} [Bar]	1	1.1	1.2	1.3	1.4	1.5
V_{FC} [V]	0.58	0.59	0.60	0.60	0.61	0.62

Table 3.8: Pressure variations, H_2/O_2, CEA lab

The influence of the pressure increments can be seen as a reduction of the low frequency arc. This effect denotes an improvement of the diffusion process, which provides an increased availability of reactants at the reaction sites.

P_{FC} [bar]	1.07	1.66	2.33	3.03
V_{FC} [V]	0.52	0.57	0.59	0.62

Table 3.9: Pressure variations, H_2/Air, IRII lab

The response of the fuel cell at the IRII laboratory using H_2/Air as reactants, is presented

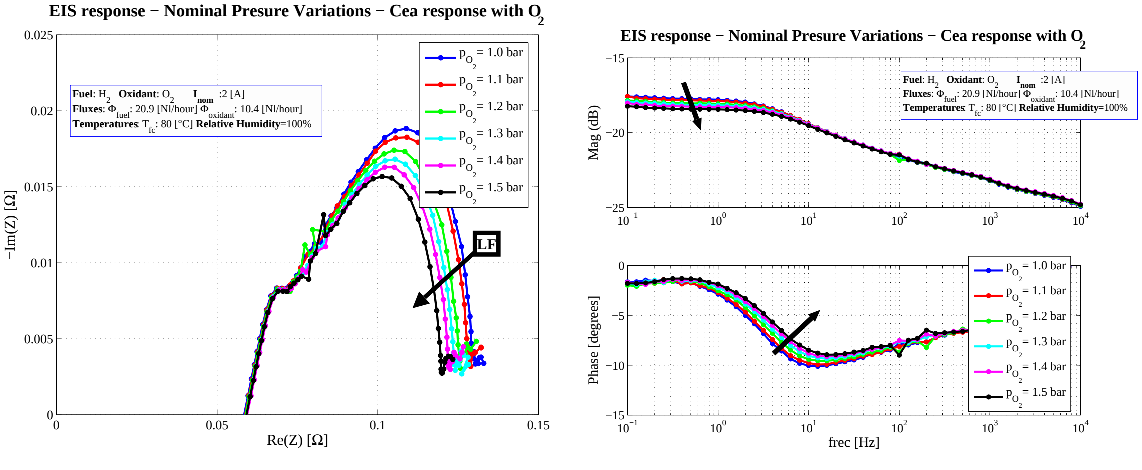

(a) Nyquist (O_2)

(b) Bode (O_2)

Figure 3.7: Pressure variations, H_2/O_2, CEA lab

in figure 3.8 and in table 3.9 (using **Cellkraft** humidifier). The nominal pressure starts with an atmospheric condition and is increased by steps of 10 [PSI] (≈ 0.67 [Bars]) up to 3.03 [Bars].

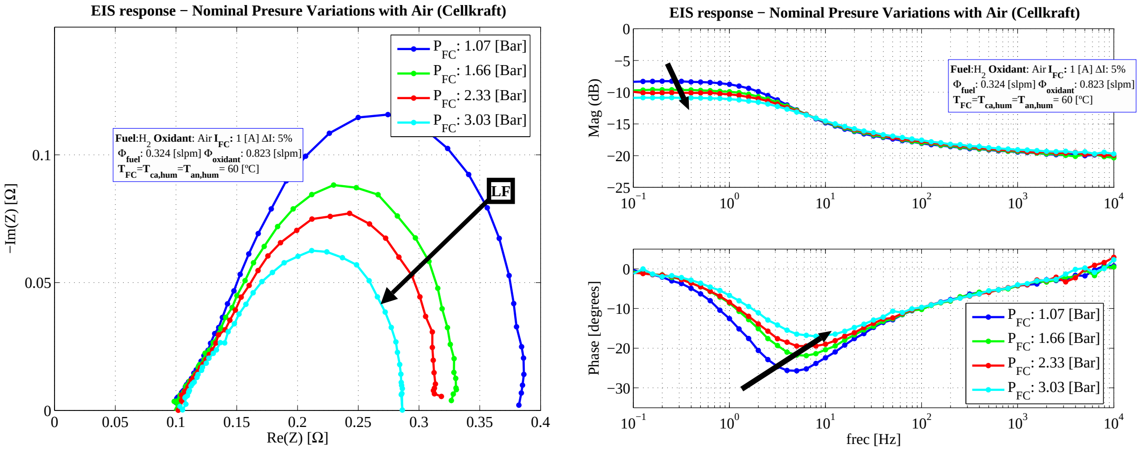

(a) Nyquist

(b) Bode

Figure 3.8: Pressure variation, H_2/Air, IRII lab

Also in this case, the increases of the pressure make that the concentrations of the reactants are higher at the channels (improvement of diffusion process). This effect is reflected in a reduction of the low frequency arc while at high frequency the response maintains its values.

3.3.1.3 Operating Temperature Variations

A fuel cell *nominal temperature variation* is done by increasing its temperature by steps of $\Delta T_{FC} \approx 10$ [°C] from 40 [°C] , to T_{FC} =80 [°C] in the case of **oxygen** response (at the CEA laboratory) and to T_{FC} =60 [°C] in case of the **air** response (at the IRII laboratory).

The EIS response of the fuel cell at the CEA laboratory using H_2/O_2 as reactants, can be seen in figure 3.9 and in table 3.10.

The influence of temperature is manifested at the low and the high frequency arcs. The reduction of the high frequency arc is due to the increasing membrane conductivity when the temperature increases (Larminie & Dicks [2003]). The reduction of the low frequency arc is due to the improvement of the diffusional process (diffusion coefficient variations, Barbir [2005]).

T_{FC} [°C]	40	50	60	70	80
V_{FC} [V]	0.53	0.56	0.58	0.59	0.57

Table 3.10: Nominal temperature variations, H_2/O_2, CEA lab

Both evolutions maintain this trend from 40 [°C] to 70 [°C]. At the T_{FC}=80 [°C] the response changes its tendency, probably due to the achievement of a physical limitation where it is possible that the membrane conductivity arrives to its limit and the high amount of energy present in the fuel cell causes water evaporation at the catalyst layer (reducing the available reaction sites).

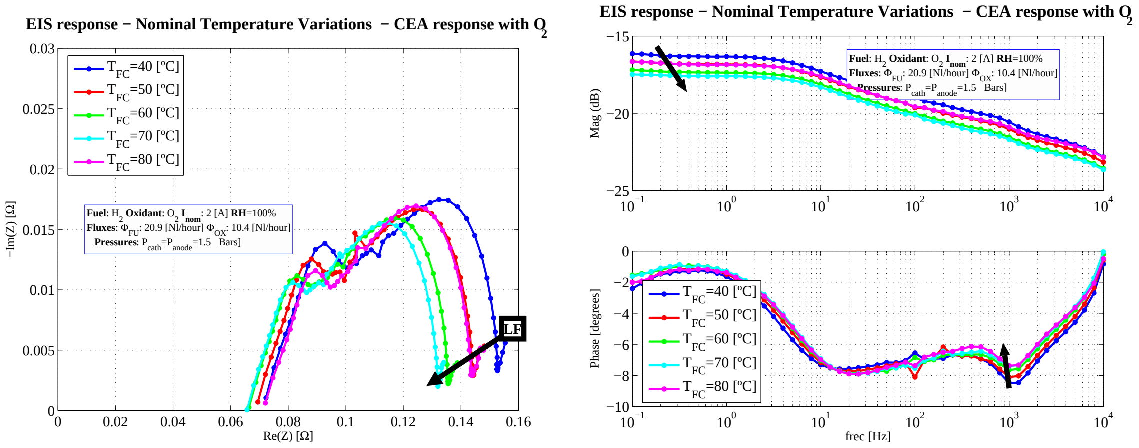

(a) Nyquist (O_2)

(b) Bode (O_2)

Figure 3.9: Temperature variation, H_2/O_2, CEA lab

The response of the fuel cell under nominal temperature variations when H_2/Air are applied as reactants (at the IRII laboratory, using the Cellkraft humidifiers), can be seen in figure 3.10 and in table 3.11.

T_{FC} [°C]	40	50	60
V_{FC} [V]	0.39	0.44	0.48

Table 3.11: Nominal temperature variations, H_2/Air, IRII lab

Again, the influence of the temperature can be seen at the low frequency resistance and at the high frequency resistance. The reduction of the low frequency resistance is due to the

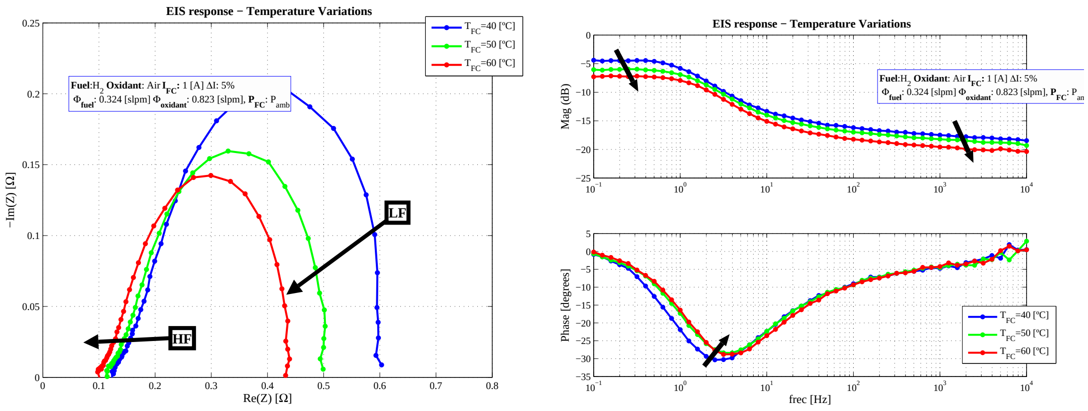

(a) Nyquist (b) Bode

Figure 3.10: Temperature variation, H_2/Air, IRII lab

improvement of the diffusional process and the reduction of the high frequency resistance is due to the improvement of the membrane conductivity when the temperature rises (reducing the membrane resistance the Nyquist plot shifts to the left).

3.3.1.4 Operating Relative Humidity Variations

The relative humidity (RH_{FC}) is the ratio between the water vapour partial pressure p_v and the water saturation pressure p_{vs}, which is the maximum amount of water vapour at cell temperature (see reference Barbir [2005]:

$$RH_{FC} = \frac{p_v}{p_{vs}} \tag{3.7}$$

The relationship between the saturation pressure p_{vs} and the temperature T_{FC} is given by the equation (see Barbir [2005]):

$$p_{vs}(T_{FC}) = e^{aT_{FC}^{-1}+b+cT_{FC}+dT_{FC}^2+eT_{FC}^3+f\ln(T_{FC})} \tag{3.8}$$

Where the coefficients of this equation are $a = -5800.22$,$b = 1.39$,$c = -0.048$, $d = 0.41 * 10^{-4}$,$e = -0.14*10^{-4}$, $f = 6.55$. The relative humidity variation is obtained by modifying the **cathode** humidifier temperature compared with the fuel cell nominal operating temperature, while maintaining the anode humidifier temperature in order to keep the relative humidity at the anode (RH_{an}) at 100 [%].

Figure 3.11 and table 3.12 show the response of the relative humidity variations at the CEA laboratory, where H_2/O_2 are applied as reactants.

RH_{FC} [%]	80	90	100
V_{FC} [V]	0.65	0.66	0.68

Table 3.12: Nominal relative humidity variations, H_2/O_2, CEA lab

The high frequency resistance is higher at low relative humidity ratios, because this implies a reduction of the water presence at the catalyst layer. This causes a reduction of the active area (less active reaction sites available) and also a membrane drying (see Fouquet *et al.* [2006]).

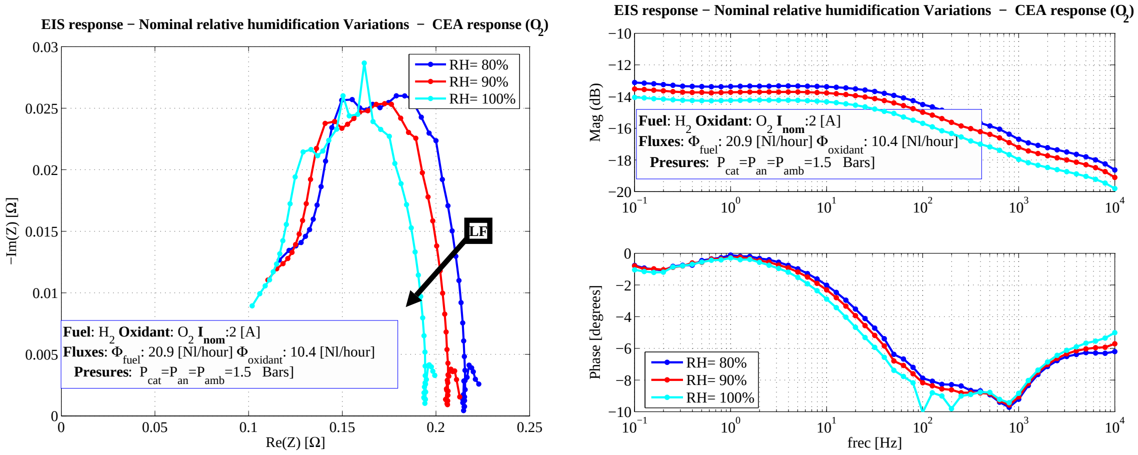

(a) Nyquist (O_2)

(b) Bode (O_2)

Figure 3.11: Relative Humidity variation, H_2/O_2, CEA

Figure 3.12 and table 3.13 show the response of the fuel cell at the IRII laboratory, when H_2/Air are applied as reactants. The high frequency resistance increases at the low relative humidity ratios, because the reduction of the water presence at the catalyst layer reduces the active area (less active reaction sites) and also dries the membrane.

RH_{FC} [%]	50.0	65.0	85.0	100.0
V_{FC} [V]	0.50	0.54	0.57	0.54

Table 3.13: Nominal relative humidity variations, H_2/Air, IRII lab

The low frequency resistances reduces its value as relative humidity increases in both test (CEA and IRII). This is true, except for RH=100 %, where the low frequency resistance increases due to the water presence at the catalyst layer. This effect can be related with an "excessive" presence of water slowing (or blocking) the oxygen arrival to the reaction sites.

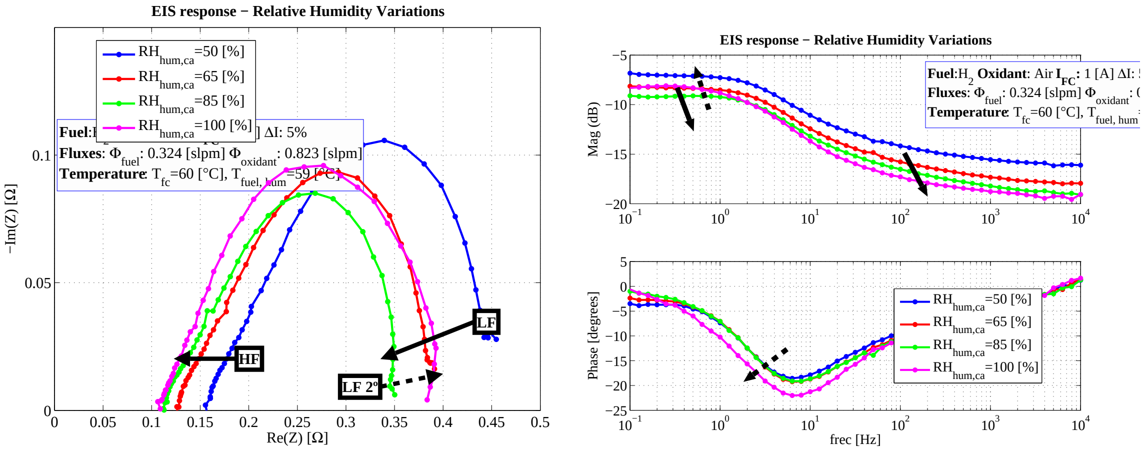

(a) Nyq. (Air)

(b) Bode (Air)

Figure 3.12: Relative Humidity variation, H_2/Air, IRII

3.4 Relevant Characteristics

In this section and in the following one, a pathway between the experimental EIS response and equivalent circuit models of the PEMFC is presented. The objective is to propose a set of *relevant characteristics* of the frequency response that can be used as the starting point of the modelling task. One important thing is that these characteristics should be extracted in an easy way from the EIS response of the system.

Also, the relevant characteristics sensitivity to the operating conditions is analysed and and a search in the defined indicators to find the most suitable ones to compare and distinguish the effects of nominal operating conditions over the frequency response.

From a typical EIS response of the fuel cell, as can be seen in figure 3.13, the introduction of the *relevant characteristics* is done.

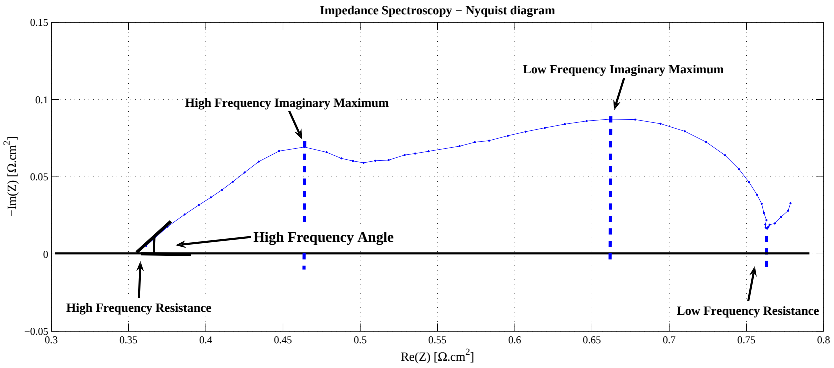

(a) Nyquist response

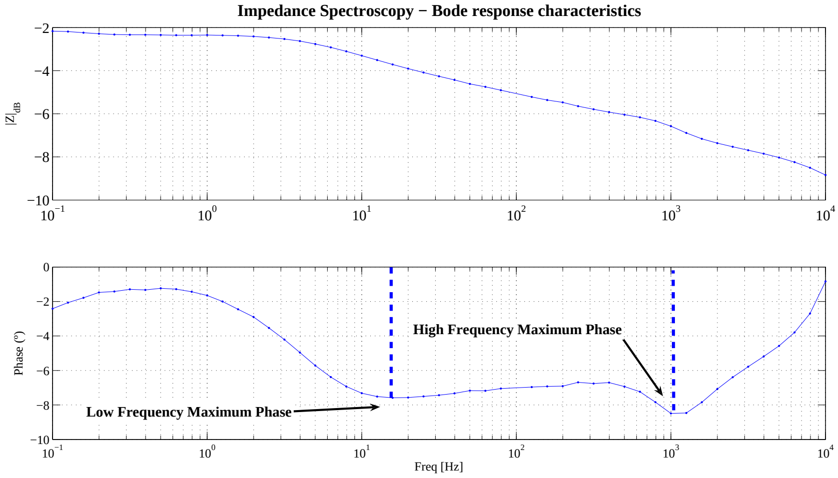

(b) Bode response

Figure 3.13: Relevant characteristics from EIS response

These *relevant characteristics* may be defined as:

From Nyquist response (see figure 3.13(a)):

- Low frequency Resistance (R_{LF}).
- Low frequency Imaginary Maximum ($Im_{Imax,LF}$), and its corresponding frequency and real part ($f_{Imax,LF}$ and $Re_{Imax,LF}$).
- High frequency Imaginary Maximum ($Im_{Imax,LF}$), and its corresponding frequency and real part ($f_{Imax,LF}$ and $Re_{Imax,LF}$).
- High frequency Resistance (R_{HF}).
- High frequency angle (φ_{HF}).

From Bode response (see figure 3.13(b)):

- Low frequency Maximum Phase ($\phi_{\phi max,LF}$), and its corresponding frequency and module ($f_{\phi max,LF}$ and $|Z|_{\phi max,LF}$).
- High frequency Maximum Phase ($\phi_{\phi max,HF}$), and its corresponding frequency and module ($f_{\phi max,HF}$ and $|Z|_{\phi max,HF}$).

These characteristics of the frequency response are selected after the observation of the EIS evolution for different operating conditions and cast for its possible use as indicators of fuel cell operation status. Also, as will be explained in the next section, the relevant characteristics can be used in order to search the coefficient values of the equivalent circuit elements.

3.4.1 Pressure variation

The relevant characteristics previously defined corresponding to different pressures can be extracted from the EIS results presented in section 3.3.1.2. The *most sensitive* relevant characteristics are resumed in tables 3.14 (for H_2/O_2) and 3.15 (for H_2/Air). Also, some of the characteristics and the fuel cell voltage are presented in the figures 3.14 and 3.15.

Table 3.14: Evolution of the some Relevant Characteristics with pressure variations (H_2/O_2)

P_{FC}[Bar]	V_{FC}[V]	R_{LF}[Ω]	$Im_{Imax,LF}$ [Hz]	$f_{Imax,LF}$[Hz]	$\phi_{\phi max,LF}$ [°]	$f_{\phi,maxlf}$[Hz]	R_{hf}[Ω]
1	0.582	0.132	-0.019	7.9	-10.1	12.6	0.058
1.1	0.587	0.132	-0.019	7.9	-9.9	12.6	0.059
1.2	0.597	0.128	-0.017	10.0	-9.6	15.9	0.059
1.3	0.604	0.127	-0.017	10.0	-9.3	15.9	0.059
1.4	0.611	0.126	-0.016	12.6	-9.1	15.9	0.059
1.5	0.620	0.123	-0.016	12.6	-8.9	15.9	0.059

The pressure variation affects specially the low frequency response. That is the low frequency resistance, the low frequency maximum arc and the low frequency maximum phase. This evolution is probably due to changes in the diffusion processes and in the reactants concentration. An increment of the total pressure gives an increment on the partial pressure

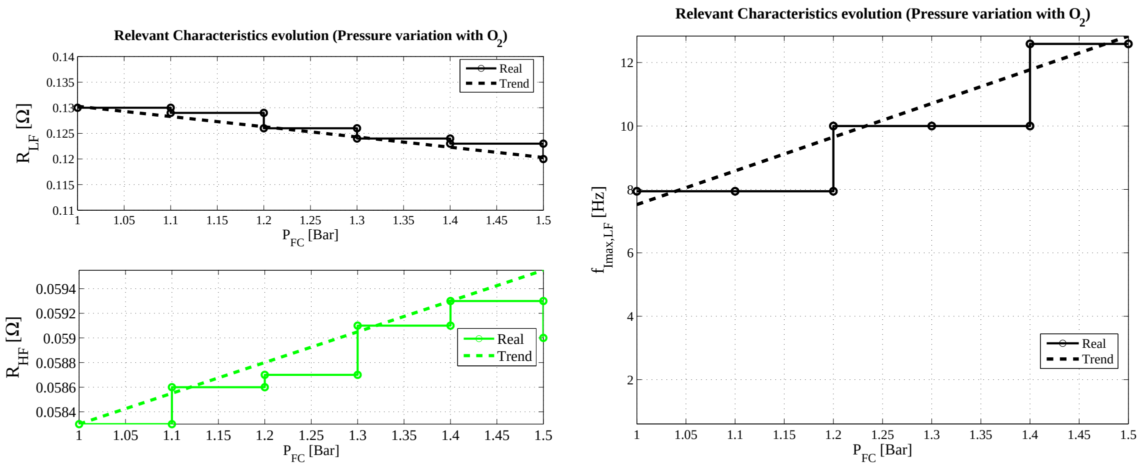

(a) Resistances (b) Frequency

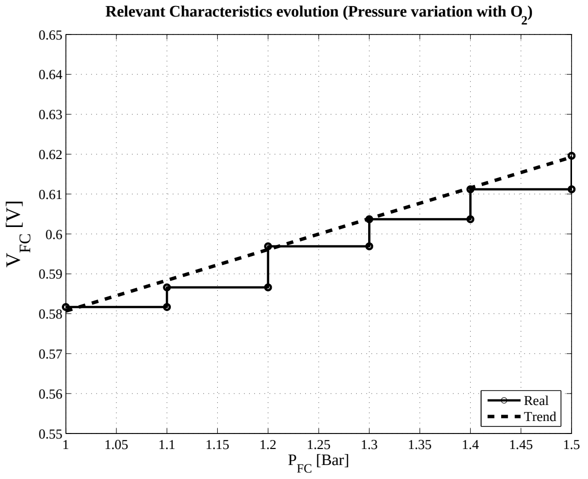

(c) Voltage

Figure 3.14: Relevant characteristics obtained for nominal pressure variation, H_2/O_2

Table 3.15: Evolution of the Relevant Characteristics with pressure variations (H_2/Air)

P_{FC}[Bar]	V_{FC}[V]	$R_{LF}[\Omega]$	$Im_{Imax,LF}[\Omega]$	$f_{Imax,LF}$[Hz]	$\phi_{\phi max,LF}$ [°]	$f_{\phi,maxlf}$[Hz]	$R_{hf}[\Omega]$
1.067	0.523	0.391	-0.116	2.512	-25.704	5.012	0.098
1.663	0.573	0.333	-0.088	3.981	-21.880	6.310	0.097
2.333	0.594	0.315	-0.077	3.162	-19.469	6.310	0.103
3.034	0.617	0.286	-0.063	5.012	-16.999	7.943	0.105

of gases and the refilling of reacting gases is faster, resulting in a reduction of the concentration losses.

In figures 3.14 and 3.15, significant variations of the relevant characteristics due to changes in the operating pressure can be observed. A pressure variation affects the low frequency behaviour either with H_2/Air or H_2/O_2 reactants. Both reactants conditions have similar trends for the low frequency resistance (R_{LF}, figure 3.14(a) and 3.15(a)), reducing its value as the operating pressure increases, due to an increase of the reactants concentration in the active layer.

In both conditions, the voltage evolution increases its values, as can be seen in the figures 3.14(c) and 3.15(c).

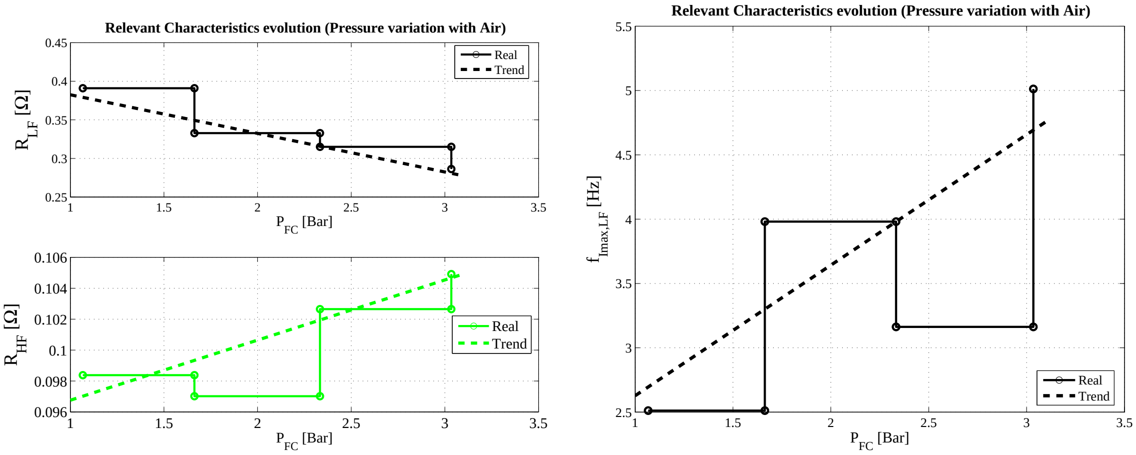

(a) Resistances (b) Frequency

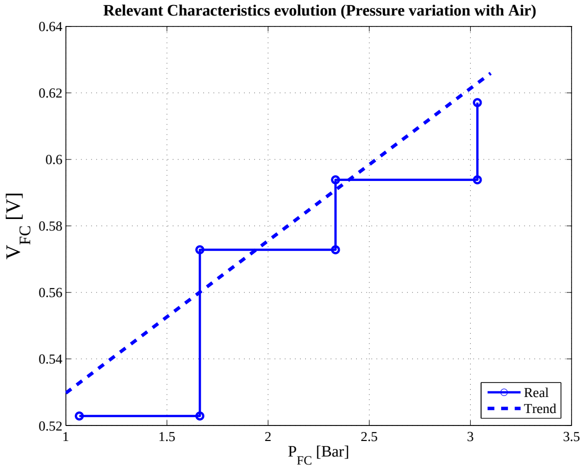

(c) Voltage

Figure 3.15: Relevant Characteristics obtained for nominal pressure variation, H_2/Air

It can be concluded that R_{LF} (decreasing trend), $f_{Imax,LF}$ (increasing trend) and voltage v_{FC} (increasing trend) can be used as *pressure variation indicators* in both cases (H_2/O_2 and H_2/Air).

3.4.2 Temperature variation

The variation of the Relevant Characteristics when the fuel cell nominal operating temperature changes are studied in the CEA laboratory (H_2/O_2) and the IRII laboratory (H_2/Air). Results are detailed in the tables 3.16 and 3.17 and in the figures 3.16 and 3.17

The temperature variation affects the low and the high frequency response. This evolution is due to the changes of the diffusion coefficients with temperature (low frequency changes)

Table 3.16: Evolution of relevant characteristics, temperature variation (H_2/O_2)

T_{FC}[°C]	V_{FC}[V]	R_{FC}[Ω]	$Im_{Imax,LF}$ [Hz]	$f_{Imax,LF}$[Hz]	$\phi_{\phi max,LF}$ [°]	$f_{\phi,maxLF}$[Hz]	R_{HF}[Ω]
40	0.53	0.15	-0.017	12.6	-7.6	15.8	0.072
50	0.56	0.14	-0.017	12.6	-7.7	19.9	0.069
60	0.58	0.13	-0.016	15.8	-7.9	19.9	0.066
70	0.59	0.13	-0.016	15.8	-7.9	25.1	0.065
80	0.57	0.14	-0.017	15.8	-7.9	25.1	0.072

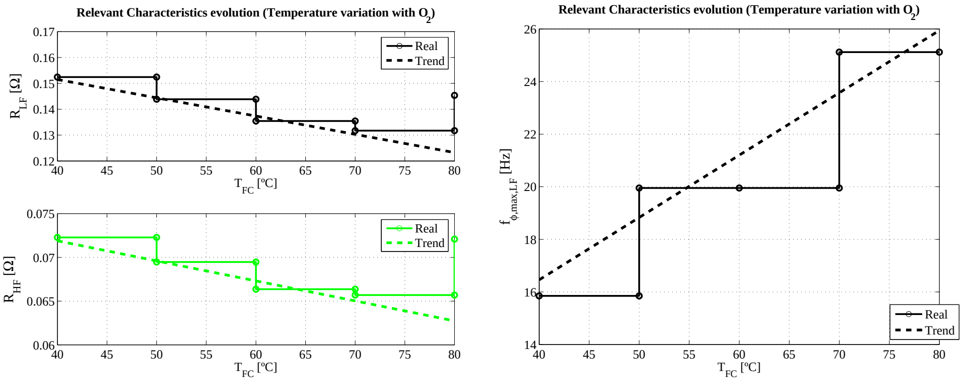

(a) Resistances (b) Frequencies

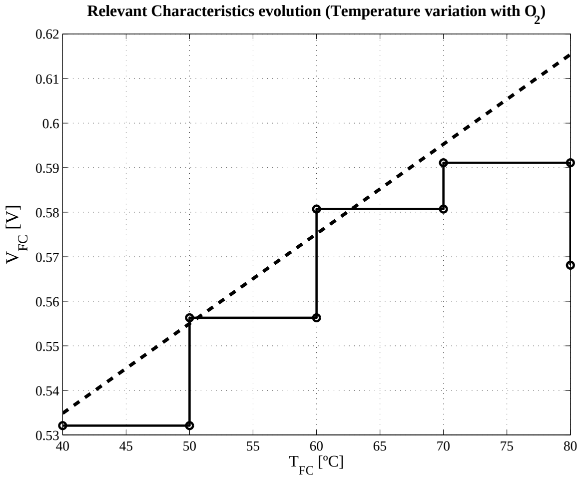

(c) Voltage

Figure 3.16: Relevant characteristics, temperature variation, H_2/O_2

and the membrane conductivity and the electrons movement improvement (high frequency changes), see Barbir [2005].

In figures 3.16 and 3.17, a significant variation of the relevant characteristics most affected by the operating temperature can be observed. Temperature variation affects the low and the high frequency behaviour without distinction of working with H_2/Air or H_2/O_2 as reactants. Both working situations give similar trends to the resistances (R_{LF} and R_{HF}), reducing its values as the temperature increases see tables 3.16 and 3.17.

Analysing the Relevant Characteristics, the possible *temperature variation indicators* are:

Table 3.17: Evolution of relevant characteristics with temperature variation (H_2/Air)

T_{FC}[°C]	V_{FC}[V]	R_{LF}[Ω]	$Im_{Imax,LF}$	$f_{Imax,LF}$[Hz]	$\phi_{\phi max,LF}$[°]	$f_{\Phi,maxLF}$[Hz]	R_{HF}[Ω]
40	0.39	0.60	-0.20	1.26	-30.3	2.5	0.12
50	0.44	0.51	-0.16	1.99	-28.4	3.9	0.11
60	0.48	0.44	-0.14	1.99	-28.8	3.2	0.096

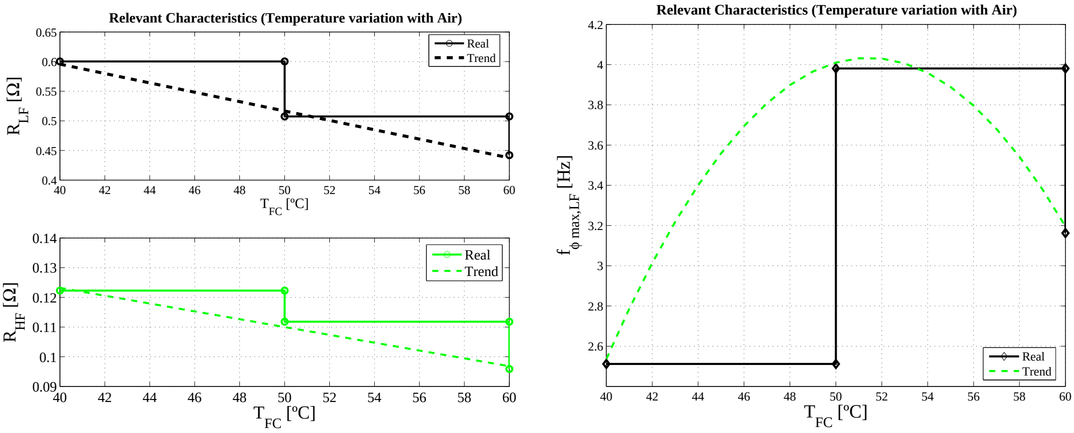

(a) Resistances (b) Frequency

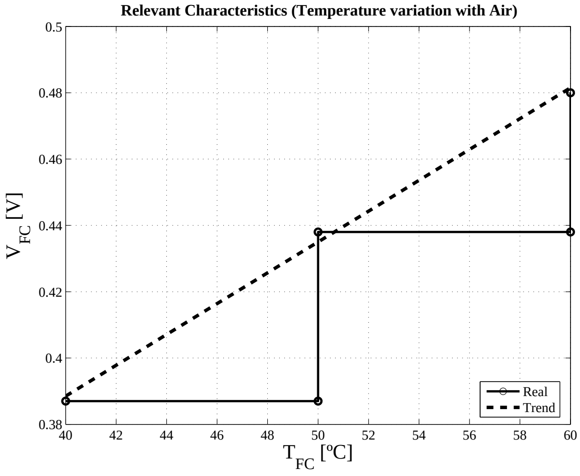

(c) Voltage

Figure 3.17: Relevant characteristics, temperature variation, H_2/Air

R_{LF} (decreasing trend), R_{HF} (decreasing trend) and $f_{\phi max,LF}$ (parabolic trend) and also voltage v_{FC} (increasing with temperature), for both cases H_2/O_2 and H_2/Air.

A special comment must be done for T_{FC}= 80 [°C] with H_2/O_2 feeding, see figure 3.16: an inversion of trend occurs for this temperature. One could expect that the higher temperature the higher is the cell performance. However, for each fuel cell design and components there is an optimal temperature working point. From the fuel cell employed (see Appendix 1), it seems that the optimal temperature is around 70-75 [°C].

3.4.3 Relative Humidity variation

The variation of the Relevant Characteristics when the operating relative humidity at the cathode and the anode side (both at same level) changes in the CEA (H_2/O_2) and the IRII (H_2/Air) laboratories are detailed in the tables 3.18 and 3.19 and in the figures 3.18 and 3.19.

Table 3.18: Evolution of the Relevant Characteristics with Relative Humidity variation (H_2/O_2)

RH_{FC}[%]	V_{FC}[V]	R_{LF}[Ω]	$Im_{Imax,LF}$ [Ω]	$f_{Imax,LF}$[Hz]	$\phi_{\phi max,LF}$ [°]	$f_{\phi,maxLF}$[Hz]	R_{HF}[Ω]
80	0.652	0.223	-0.026	125.89	-1.084	0.200	0.116
90	0.664	0.213	-0.025	125.89	-1.044	0.200	0.111
100	0.679	0.199	-0.025	125.89	-1.210	0.158	0.102

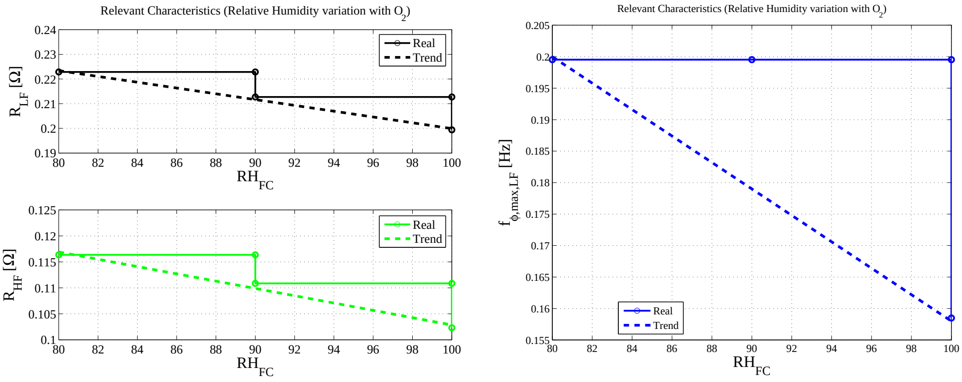

(a) Resistances (b) Frequencies

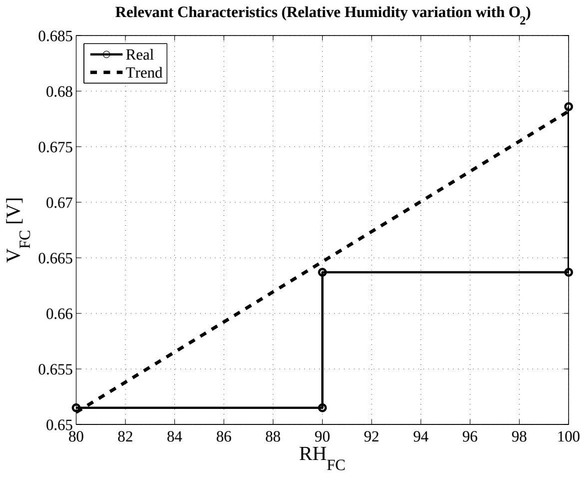

(c) Voltage

Figure 3.18: Relevant characteristics, evolution with relative humidity variations, H_2/O_2

In the figures 3.18 and 3.19, significant variations of the Relevant Characteristics most affected by the operating relative humidity can be observed. Relative humidity affects the low and the high frequency behaviour without distinction of working with H_2/Air or H_2/O_2 as reactants.

Both working situations give similar trends to the resistances (R_{LF} and R_{HF}, figures 3.18(a) and 3.19(a)), reducing their values as the relative humidity increases. This is due to the increase of the water presence, which improves the H_2 transport and membrane hydration. In the low frequency resistance, the evolution can be explained with the improvement of diffusion coefficients as the relative humidity increases (see Barbir [2005]).

Table 3.19: Evolution of relevant characteristics with relative humidity variation (H_2/Air)

RH_{FC}[%]	V_{FC}[V]	R_{LF}[Ω]	$Im_{Imax,LF}$	$f_{Imax,LF}$[Hz]	$\phi_{\phi max,LF}$[°]	$f_{\phi,maxLF}$[Hz]	R_{HF}[Ω]
50	0.495	0.442	-0.106	3.98	-18.56	6.31	0.157
65	0.541	0.386	-0.093	3.98	-19.25	6.31	0.127
85	0.571	0.350	-0.085	3.98	-19.12	6.31	0.113
100	0.535	0.398	-0.096	3.16	-22.03	6.31	0.108

Special situation arises at H_2/Air with a relative humidity of 100 %, where the trend of R_{LF} and v_{FC} is inverted. This effect can be explained for the similar values of the humidifiers and fuel cell temperatures, that create water condensation zones which cause an overall reduction of performance (transport problems for the oxygen to get the reaction sites).

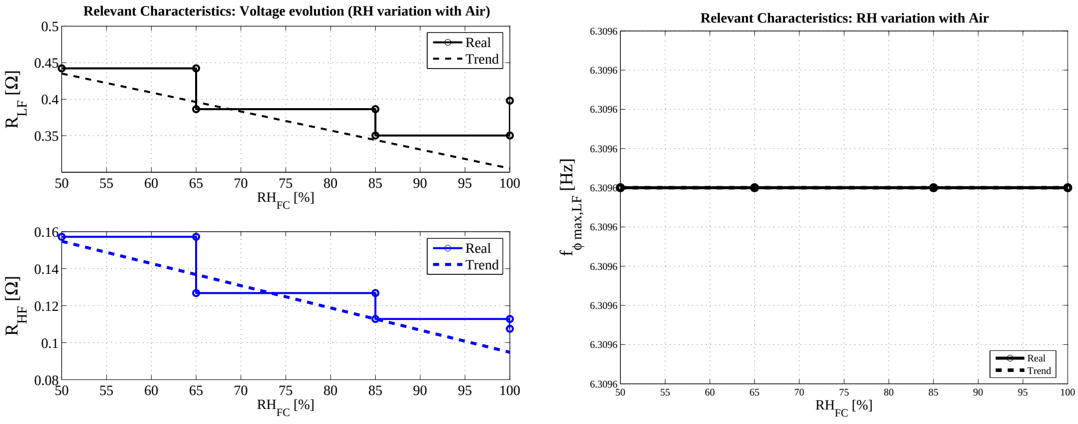

(a) Characteristics (1°)

(b) Characteristics (2°)

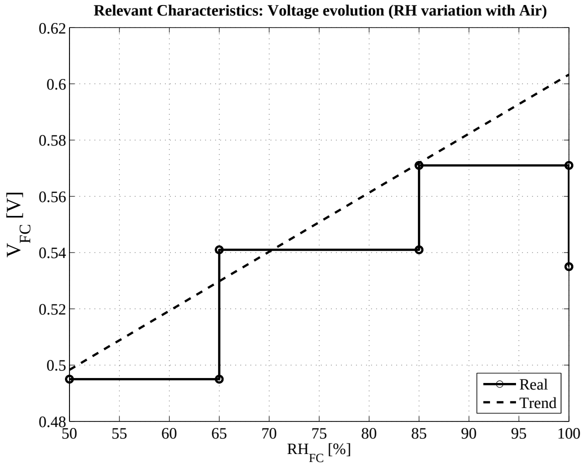

(c) Voltage

Figure 3.19: Relevant characteristics evolution with Relative Humidity variations, H_2/Air

As done for the other operating conditions variations, the Relevant Characteristics are analysed as possible performance indicators. The characteristics that are interesting are: R_{LF} (decreasing trend),R_{HF} (decreasing trend) and voltage v_{FC} (increasing trend). They can be used as *relative humidity variation* indicators in both cases: H_2/O_2 and H_2/Air.

3.5 Equivalent Circuits

Many authors have studied a modelling methodology of the fuel cell response based on the search of electrical circuits, named ”equivalent circuits”, consisting of an arrangement of different electrical components presenting the same frequency response than the obtained by PEMFC EIS tests (see reference Macdonald & Barsoukov [2005]). Some works make use of circuits combining electrical elements: like resistance (R), capacitance (C) or inductance (L), whereas other works use additional elements that represent the electrochemical or mass and ionic distributed transport phenomena (see table 3.20). For example, the Warburg element represents the impedance of one-dimensional finite distributed diffusion of a species in an electrode. Here, a Finite Length Warburg element is used (see equation 3.9), which has the following transfer function:

$$W(s) = \frac{R_W \tanh((s.T_W)^{P_W})}{(s.T_W)^{P_W}} \tag{3.9}$$

Where “s” is the Laplace complex variable, “R_W” is the finite resistance at low frequencies, “T_W” is a time constant related to the diffusion effects by some authors (see Bautista *et al.* [2002] and Diard *et al.* [2005]) with the following equation:

$$T_W = \frac{L^2}{D} \tag{3.10}$$

where “L” is the effective diffusion media thickness, and “D” is the effective diffusion coefficient of a gas trough a media. “P_W” is an exponent related with the roughness of the diffusion media (see reference Podlubny [1999]).

Another example is a Constant Phase Element (CPE), used to describe a distributed charge accumulation in a rough irregular electrode surface, an inhomogeneus reaction rate on a surface or a non-uniform current distribution (see reference Podlubny [1999]). The impedance of this element is:

$$Z_{CPE}(s) = \frac{1}{(sC_{CPE})^{P_{CPE}}} \tag{3.11}$$

Where C_{CPE} is an equivalent capacitor and P_{CPE} is the exponent related with the roughness of the electrode surface.

The different components and parameters of the equivalent circuits often have an easy correspondence with the characteristics and behaviour of a real system. However, to obtain this correspondence can be a complicated task.

Table 3.20: Typical elements and transfer functions used in equivalent circuits

Element	**Transfer Function**
Resistance	Z(s)=R
Capacitance	Z(s)=$\frac{1}{s.C}$
Inductance	Z(s)=s.L
Constant Phase Element (CPE)	Z(s)=$\frac{1}{s.C^P}$
Warburg	Z(s) = $\frac{R.tanh(s.T)^P}{(sT)^P}$

Andreaus et al. (2002 Andreaus *et al.* [2002], 2004 Andreaus & Scherer [2004], see figure 3.20(a)) have proposed a model of a fuel cell behaviour by means of an equivalent circuit that uses the following elements: R_∞, assumed to be the membrane resistance (estimated from high frequency resistance of EIS tests), $R_{ct,total}$, modelling the charge transfer resistance, C_{dl}, the double layer capacitance and N, the Nernst impedance (Warburg element) related to the mass transport limitations. Apart from the membrane resistance R_∞ estimated value, in the work it is not detailed how the other parameters are obtained.

Ciureanu et al. ((2001) Ciureanu & Roberge [2001] and (2003) Ciureanu *et al.* [2003], see figure 3.20(b), propose several circuit models that describe the fuel cell behaviour. In this case, they start with an ohmic resistance and two parallel RC circuits in series. C_1 is the double layer capacitance, R_1 is the charge transfer resistance, R_2 and C_2, stand for the diffusion process. Introducing a variation of this circuit, they replace the capacitors (C_1 and C_2) with CPE elements (T_1 and T_2), because in a porous electrode the capacitance due to the double layer charge is distributed along the length of the pores. All parameters are obtained from an EIS curve fitting software.

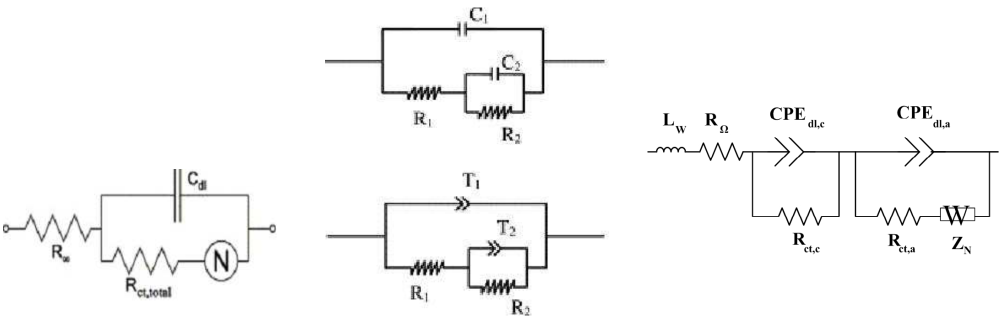

(a) Andreaus (b) Cireanu (c) Schiller

Figure 3.20: Equivalent circuit models

The articles Schiller *et al.* [2001b] and Schiller *et al.* [2001a], (see figure 3.20(c)), propose a model that represents the impedance response of a fuel cell during normal operating conditions. In this model, L_W is an inductance attributed to wiring, R_Ω is the membrane resistance, $CPE_{dl,c}$ and $CPE_{dl,a}$ are the approximations of the double layer capacitances at the cathode and anode, respectively. $R_{ct,c}$ and $R_{ct,a}$ are the charge transfer resistances associated with the cathode and anode reactions. Finally, the Nernst impedance (finite Warburg element) Z_N is used to represent the finite diffusion impedance. The adjustment of the equivalent circuit elements to the EIS response is done using a specific curve fitting algorithm.

A well known equivalent circuit for a single-step charge transfer reaction in the presence of diffusion is the ”Randles equivalent circuit” (see J. Ross Macdonald et al. Macdonald & Barsoukov [2005] and figure 3.21), where R_m is the electrolyte resistance, C_{dl} is the double layer capacitance, R_{ct} is the charge transfer resistance and Z_d is the diffusion impedance, generally represented by a Warburg. This is the starting point of most of the equivalent circuits presented in the literature.

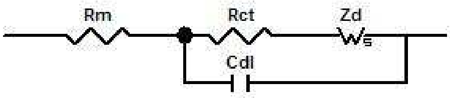

Figure 3.21: Randles equivalent circuit

After the analysis of the state of the art about the use of an equivalent circuit as an equivalent model in order to represent the PEMFC EIS response, it can be concluded that is possible to use them to represent the PEMFC response. But, there are some issues that must be solved: the circuit topology selection and the parameter tuning procedure. For the first issue, there are a lot of possible equivalent circuits and the criteria used in this thesis is the selection of the most simple as possible one presenting a good frequency response fitting for the different operating conditions. For example, when using air as oxidant, there is only one arc in the frequency response (see figure 3.10) and a simple equivalent circuit can be used. On the other hand, when using oxygen the frequency response shows two arcs (see figure 3.7(a)) and a more complex circuit must be used. For the second issue, the author has not found in the literature a clear analytical procedure to adjust the equivalent circuit parameters.

In the following, the author tries to overcome this issues proposing procedures useful to select and tune an equivalent circuit that fits the EIS experimental data.

In section 3.5.2 a simple equivalent circuit is presented and in section 3.5.4 the procedure for the initial values calculation is introduced for oxygen response. Then, the parameters of this circuit are adjusted using the specialized software (Z-View®, see reference Scribner Associates [2004]). After that, a more complete equivalent circuit model is described and its parameters are determined. In sections 3.5.3 and 3.5.4 topologies suitable when using air as oxidant are selected.

3.5.1 Equivalent circuit for Oxygen response

The first proposal is a simple equivalent circuit that is a combination of few elements (see figure 3.22). It contains two resistances (R_m and R_{tc1}), a capacitance (C_{dc1}) and a Warburg element (W_1). These elements are selected in order to represent the membrane proton conduction resistance (element R_m), the charge transfer resistance and accumulation (R_{tc1} in parallel with C_{dc1}), and the diffusion effects (Warburg element, W_1).

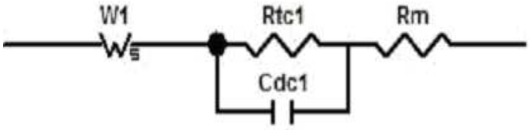

Figure 3.22: Simple equivalent circuit

If the diffusion effects are considered influential at low frequency range, the Warburg element is adjusted using the low frequency information extracted from Relevant characteristics defined in section 3.4. If the accumulation and transfer of charge is reflected at high frequency range, the parallel circuit between R_{tc1} and C_{dc1} can be determined from high frequency information of section 3.4. Also, resistive effects at high frequency can be associated with membrane resistance R_m, among other ohmic effects.

3.5.2 General procedure for equivalent circuit parameters adjustment

Once the EIS test is done with H_2/O_2 as reactants, the relevant characteristics of this response are calculated. Then, considering the equivalent circuit of figure 3.22 and making a separation of the different effects in function of their frequency range, the Relevant characteristics help to find some of the parameter values of the selected equivalent circuit. In order to illustrate the general procedure used to obtain the parameters of the simple equivalent circuit from the Relevant characteristics, an example with all necessary steps is presented.

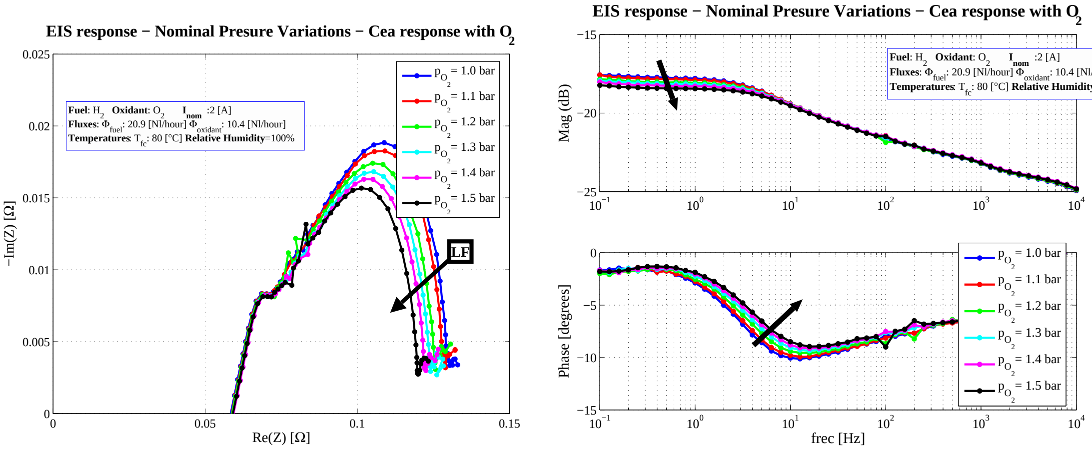

(a) Nyquist (O_2) (b) Bode (O_2)

Figure 3.23: CEA response with pressure variations (O_2)

The procedure is applied to the first experiments: pressure variation in H_2/O_2 supply (see Primucci *et al.* [2008]). The resulting frequency response is showed in figure 3.23 and the corresponding relevant characteristics are showed in table 3.14. The arrows indicate the most important variations in both graphs (LF denotes the low frequency evolution), of the fuel cell system variations.

Also, the Relevant Characteristics in the Nyquist plot, useful to calculate the equivalent circuit parameters are presented again in figure 3.24.

The following steps are aimed to relate the relevant characteristics and the equivalent circuit parameters:

- The high frequency resistance (R_{HF}) is an estimation of the ohmic effects, mainly proton conduction resistance of the membrane:

$$R_m \approx R_{HF} \approx 0.058\ \Omega \tag{3.12}$$

- The high frequency imaginary maximum frequency ($f_{Imax,HF}$) helps to find the charge accumulation and transfer time constant(τ_{dc1})

$$f_{Imax,HF} \approx \frac{1}{2\pi(R_{ct1}C_{dc1})} \rightarrow \tau_{dc1} = R_{ct1}C_{dc1} \approx \frac{1}{2\pi f_{Imax,HF}} \approx 200\mu s \tag{3.13}$$

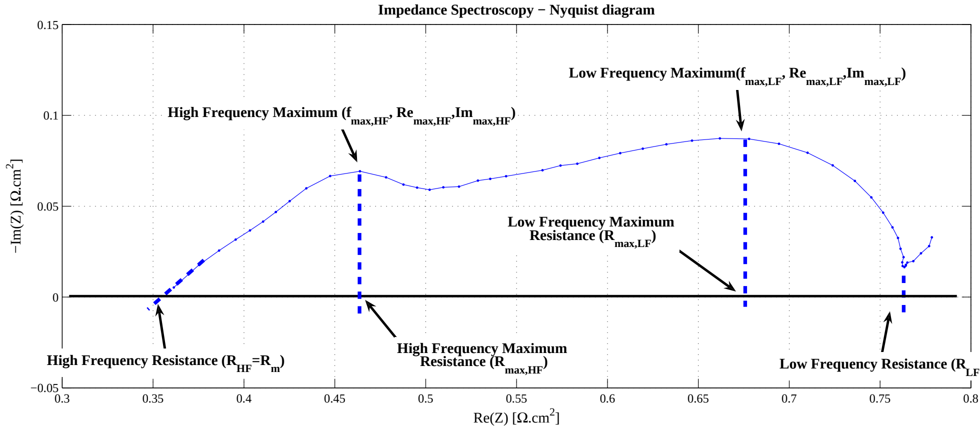

Figure 3.24: Nyquist relevant characteristics

- Using the resistance associated with this high frequency arc ($Re_{Imax,HF}$), the charge transfer resistance (R_{ct1}) is calculated as follows:

$$R_{ct1} \approx Re_{I\,\max,HF} - R_m \approx 0.009\ \Omega \tag{3.14}$$

- Combining the information of the charge transfer resistance (R_{ct1}) and the charge accumulation and transfer time constant (τ_{dc1}), the double layer capacitance is determined:

$$C_{dc1} \approx \frac{\tau_{dc1}}{R_{ct1}} \approx 22\ mF \tag{3.15}$$

- The Warburg resistance (R_{W1}) is established from the resistance difference between the low frequency resistance (R$_{LF}$) extracted from 3.14, the membrane and the charge transfer resistance:

$$R_{W1} \approx R_{LF} - R_m - R_{ct1} \approx 0.13\ \Omega \tag{3.16}$$

- The Warburg exponent (P_{W1}) is determined using a combination of one of the relevant characteristics ($Im_{Imax,LF}$, imaginary part of low frequency maximum) and a trigonometric expression of theWarburg transfer function (equation 3.9):

$$\begin{aligned} &\tanh(z) \approx \frac{z^2}{1+\frac{z}{3}^2}\ (linear\ approx.\ 1st\ order) \\ &W_{W1}(s) = \frac{R_{W1}\tanh((sT_{W1})^{P_{W1}})}{(sT_{W1})^{P_{W1}}} \approx \frac{R_{W1}\left(1+\frac{\left((sT_{W1})^{P_{W1}}\right)^2}{\pi}\right)}{\left(1+\frac{4\left((sT_{W1})^{P_{W1}}\right)^2}{\pi}\right)} \end{aligned} \tag{3.17}$$

Then, replacing $s = i\omega$ and searching the *Imaginary maximum*, evaluating $\frac{dW_{w1}}{d\omega} = 0$, the following expression is obtained:

$$\begin{aligned} Im_{Imax,LF} &= -\frac{R_{W1} sen(\frac{P_{W1}\pi}{2})}{2.(\cos(\frac{P_{W1}\pi}{2})+1)} = -\frac{3}{8} R_{W1}.\tan(\frac{P_{W1}\pi}{2}) \\ \Rightarrow P_{W1} &= -\frac{4}{\pi} \arctan\left(-\frac{2.Im_{I\max,LF}}{R_{W1}}\right) \approx 0.4 \end{aligned} \tag{3.18}$$

- Finally, the Warburg time constant (T_{W1}) can be extracted from the frequency at the low frequency maximum $f_{Imax,LF}$, extracted from equation 3.18, and is:

$$T_{W1} \approx \frac{1}{R_{W1}(2\pi f_{I\max,LF})^{P_{W1}}} \approx 0.099\ [s] \tag{3.19}$$

From the Relevant Characteristics of the frequency response and for the proposed equivalent circuit, this procedure can be applied to all working situations in order to obtain the parameters of the equivalent circuit.

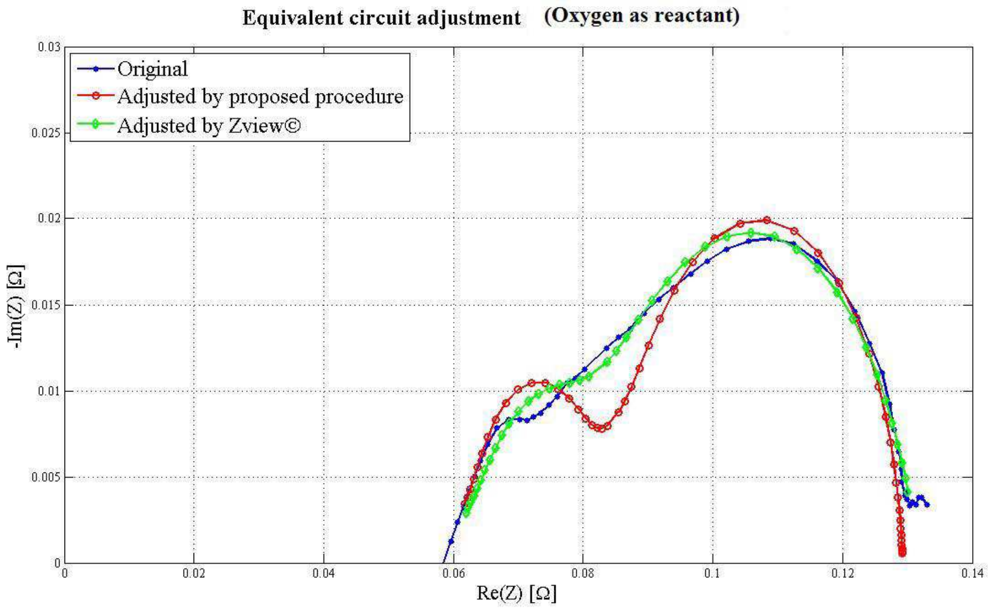

Figure 3.25: Comparison of simple equivalent circuit result effect

After this parameter estimation, the equivalent circuit is constructed in Zview®software in order to compare its corresponding Nyquist plot with that of the real response. Also, this tool allows the curve fitting with Non Linear Least Squares algorithm, which allows refining the initial values of the equivalent circuit parameters to new ones. In table 3.21 and figure 3.25, a comparison is made between the response obtained with the initial parameters provided by the procedure and the parameters estimated by Zview®.

The comparison shows that the initial parameter estimation based on the described procedure is a good tool for curve fitting of the EIS frequency response. However, using the

Table 3.21: Simple equivalent circuit adjustment for H_2/O_2 situation (P_{FC}=1 [Bar])

Element	**Initial procedure**	**Zview®**
$\mathbf{R}_{W1}[\Omega]$	0.13	0.135
$\mathbf{T}_{W1}$**[sec]**	0.099	0.092
$\mathbf{P}_{W1}$	0.4	0.42
$\mathbf{R}_{tc}[\Omega]$	0.009	0.0085
$\mathbf{C}_{dc}$**[F]**	0.022	0.035
$\mathbf{R}_{m}[\Omega]$	0.058	0.056

Zview®software, the parameters obtained from the relevant characteristics are improved giving a better curve fitting.

3.5.3 Complete equivalent circuit

In order to obtain a better adjustment of the frequency response, a complete equivalent circuit is proposed.

Considering one "Randles equivalent circuit" (presented in figure 3.21) for the anode and another for the cathode, a proposal of a complete equivalent circuit to study the experimental EIS response is done (see figure 3.26). Here, taking into account the influence of the electrode roughness on charge accumulation, a CPE (Constant Phase Element) is used in replacement of planar capacitance.

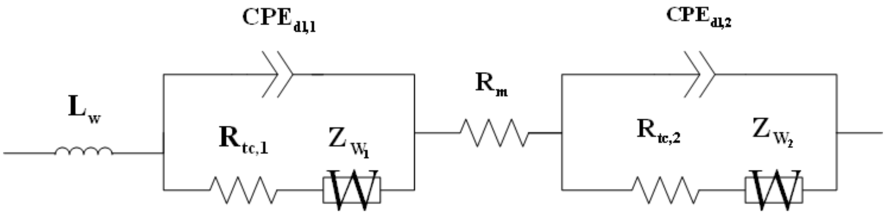

Figure 3.26: Complete equivalent circuit proposes

The elements of the complete equivalent circuit are: L_W, which represents the wiring inductance, $R_{tc,1}$ and $R_{tc,2}$ which are the representation of the charge transfer resistances (for the anode and the cathode). $CPE_{dl,1}$ and $CPE_{dl,2}$ are the double layer charge representation, Z_{W1} and Z_{W2} are the diffusion impedances, and R_m is the membrane resistance.

In this case, for the Randles circuit corresponding to the cathode side, the calculated values of the simple equivalent circuit procedure are used as initial. In the other cases, similar values are proposed and they are setted as free to be adjusted by the curve fitting software Zview®.

The main advantages of this complete equivalent circuit are the symmetry and the high quality of the adjustment for all operating condition variations. The principal disadvantages are the higher number of parameters to adjust, in comparison with the Relevant characteristics, and the difficulty for phenomena separation in frequency range. As the experimental information has only two relevant frequency zones, and the equivalent circuit has four frequency variable elements (2 CPE and 2 Warburg elements), there is an overlapping of the frequency responses of these effects.

The comparison between the responses obtained with the simple equivalent circuit and with the new proposed circuit structure can be seen in figure 3.27. The fitting of the complete equivalent circuit is much better than the simple equivalent circuit, mainly due to a higher number of free parameters to adjust the response.

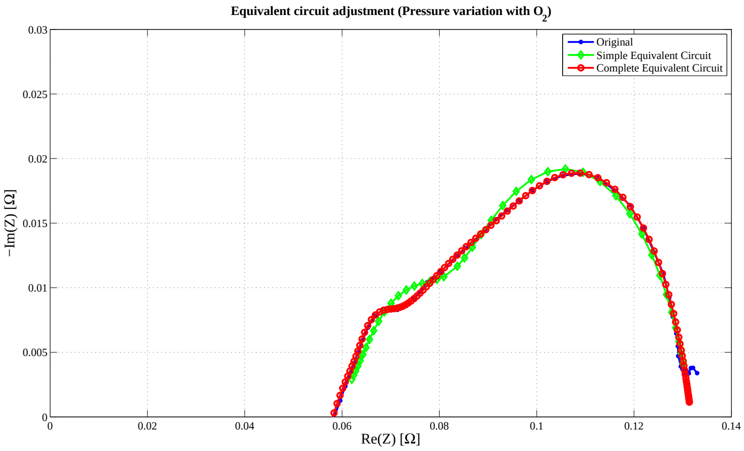

Figure 3.27: Comparison between simple and complete equivalent circuit responses

Table 3.22: Parameter evolution of complete equivalent circuit with pressure (H_2/O_2)

Element	**FC pressure, P_{FC}, in Bar**					
	1.0	1.1	1.2	1.3	1.4	1.5
R$_{tc1}$	0.063	0.063	0.063	0.064	0.065	0.064
R$_{W1}$	0.036	0.034	0.031	0.029	0.027	0.026
T$_{W1}$	0.020	0.017	0.014	0.013	0.011	0.011
P$_{W1}$	0.31	0.32	0.33	0.33	0.34	0.35
T$_{CPE,1}$	0.002	0.002	0.002	0.002	0.002	0.002
P$_{CPE,1}$	0.65	0.67	0.69	0.66	0.66	0.67
R$_m$	0.058	0.058	0.058	0.058	0.058	0.058
L$_W$	0.000021	0.000021	0.000022	0.000021	0.000021	0.000021
T$_{CPE,2}$	0.0001	0.0002	0.0002	0.0002	0.0002	0.0003
P$_{CPE,2}$	1.65	1.61	1.60	1.59	1.60	1.54
R$_{tc2}$	0.00012	0.00015	0.00016	0.00016	0.00015	0.00019
R$_{W2}$	0.035	0.032	0.031	0.030	0.031	0.029
T$_{W2}$	0.064	0.060	0.055	0.051	0.048	0.045
P$_{W2}$	0.48	0.48	0.48	0.48	0.47	0.48
SSE	0.012	0.058	0.025	0.057	0.097	0.022

In table 3.22, all adjusted parameters for the different operating pressures are shown. Also, the Sum of Squared Error (SSE) is calculated as:

$$SSE = \sum_{i=1}^{n} \frac{(Z_m^{'} - Z_c^{'})^2 + (Z_m^{''} - Z_c^{''})^2}{(Z_c^{'})^2 + (Z_c^{''})^2} \tag{3.20}$$

where n is the number of measured points, Z_m is the measured and Z_c the calculated impedance and $Z^{'}$ and $Z^{''}$ are the real and imaginary part.

Using the complete equivalent circuit, the parameters that are more influenced by the pressure changes are searched. With the information collected in table 3.22, the parameter behaviour is studied. In order to find out the most sensitive parameters, an iterative process is applied.

Starting with the parameters that have small value variations with pressure changes, the curve fitting is repeated maintaining their values fixed to their mean values. These parameters are maintained fixed if the total response is not qualitative degraded. Then, other parameters are tested and the process continues until a minimal set of parameters having a significant influence in the EIS is attained, while the equivalent circuit still presents a good fitting with the experimental response for all pressures.

Table 3.23: Circuit parameter reduction with pressure, H_2/O_2

Element	**FC pressure, P_{FC}, in Bar**					
	1.0	1.1	1.2	1.3	1.4	1.5
R_{tc1}	0.063					
R_{W1}	0.031					
T_{W1}	0.014					
P_{W1}	0.33					
$T_{CPE,1}$	0.0021					
$P_{CPE,1}$	0.67					
R_m	0.058					
L_W	2.1E-07					
$T_{CPE,2}$	0.00018					
$P_{CPE,2}$	1.6					
R_{tc2}	0.00015					
R_{W2}	0.036	0.034	0.031	0.029	0.028	0.026
T_{W2}	0.064	0.060	0.055	0.050	0.047	0.045
P_{W2}	0.48					
SSE	0.044	0.069	0.087	0.097	0.12	0.086

In table 3.23, the final result is presented: after the described iterative process, R_{W2} and T_{W2} parameters are found to be representative of the evolution of the system when pressure changes. These are two of the three parameters of one Warburg of the equivalent circuit. In figure 3.28, the selected parameter evolutions are shown and both present similar trends when the pressure changes.

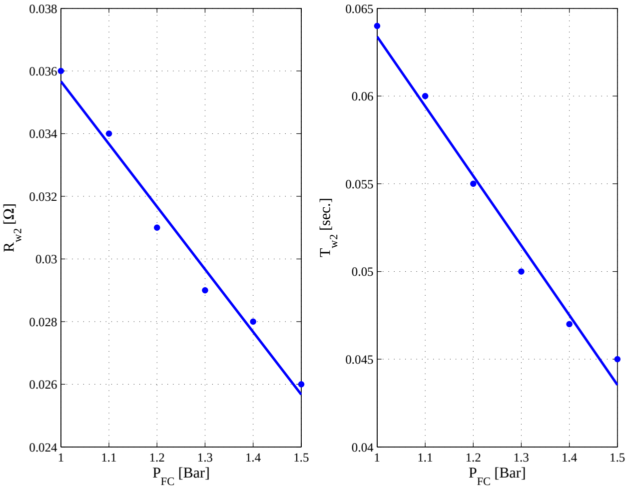

Figure 3.28: Complete circuit parameters R_{w2} and T_{w2} evolution with operating pressure, H_2/O_2

3.5.4 Equivalent circuit for Air response

The impedance spectrum of a PEMFC, specially when Air is used as a oxidant, contains only a *single impedance arc* in the Nyquist plot (see reference Yuan *et al.* [2007]). The single semicircle loop, often called the “kinetic loop”, occurs when the electrode process is dominated only by the interfacial kinetics of the ORR (Oxygen Reduction Rate) process.

In the figure 3.29, the experimental response of the single fuel cell in the IRII laboratory is presented. It can be seen that a single impedance arc is notable.

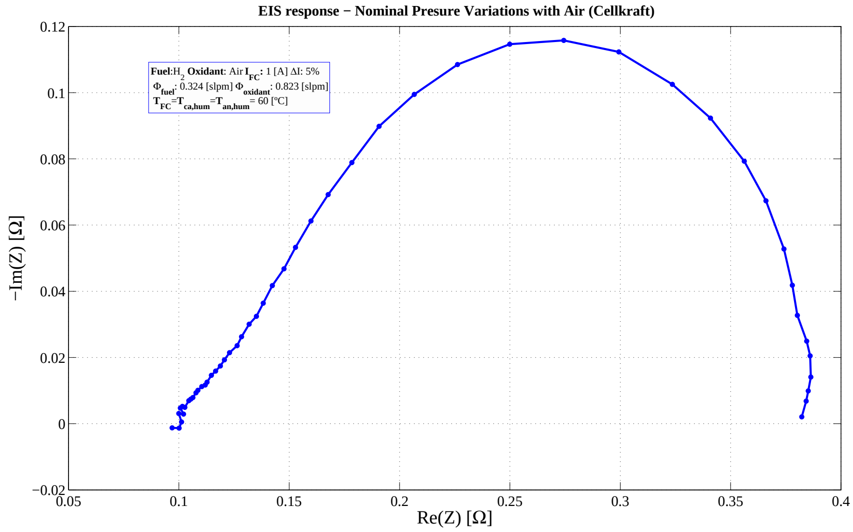

Figure 3.29: Single impedance spectra (H_2/Air, P_{amb})

In this case, the equivalent circuit model could be reduced to a simple configuration. The chosen configuration only includes an ohmic resistance and a Warburg impedance, see figure 3.30.

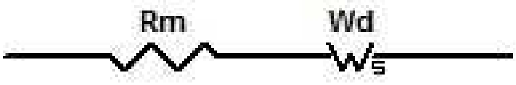

Figure 3.30: Simple equivalent circuit selected to represent H_2/Air response

Here, a procedure to obtain the parameters of this simple equivalent circuit from the Nyquist relevant characteristics is also proposed. The steps followed in order to relate the EIS relevant characteristics and the equivalent simple circuit parameters are:

- The high frequency resistance (R_{HF}) is an estimation of the ohmic effects, mainly proton conduction resistance of the membrane:

$$R_m \approx R_{HF} \tag{3.21}$$

- The Warburg resistance (R_{W1}) is established from the difference between the low frequency resistance (R$_{LF}$) and the membrane resistance:

$$R_{W1} \approx R_{LF} - R_m \tag{3.22}$$

- The Warburg time constant (T_{W1}) is given by the following equation, using the relevant characteristic $f_{\phi\,\max,LF}$:

$$T_{W1} \approx \frac{1}{2\pi f_{\phi\,\max,LF}} \tag{3.23}$$

- The Warburg exponent (P_{W1}) is determined using a combination of one of the relevant characteristics ($Im_{Imax,LF}$, imaginary part of low frequency arc) and a trigonometric expression from the Warburg transfer function (equation 3.10):

$$\begin{gathered} Im_{Imax,LF} = -\frac{R_{W1} sen(\frac{P_{W1}\pi}{2})}{2.(\cos(\frac{P_{W1}\pi}{2})+1)} = -\frac{3}{8} R_{W1}.\tan(\frac{P_{W1}\pi}{2}) \\ \Rightarrow P_{W1} = -\frac{4}{\pi}\arctan\left(-\frac{2.Im_{I\,\max,LF}}{R_{W1}}\right) \end{gathered} \tag{3.24}$$

From the relevant characteristics and for the proposed equivalent circuit, this procedure can be applied to all working situations in order to obtain a first approach to the parameters of the equivalent circuit.

After this initial parameter estimation, the equivalent circuit is constructed in Zview®software in order to compare with the real response. Also, this tool allows curve fitting with Non Linear Least Squares algorithm, refining the initial values of the equivalent circuit to new ones. In the following sections, the estimation of the equivalent circuit parameters following the described procedure for *pressure*, *temperature* and *Relative Humidity* variations is done.

3.5.4.1 Pressure variation

The H_2/Air response with pressure variation is showed again in figure 3.31.

Following the procedure detailed in section 3.5.4, the initial equivalent circuit parameters are obtained. They are showed in the table 3.24, as well as the sum of squared error, SSE (defined in equation 3.20).

After this first tuning, a better curve fitting is done using Zview®software. The resulting parameters are presented in table 3.25.

In order to compare the results, the frequency response for $P_{FC} = 1.066$ [bar] is showed in figure 3.32. From the graphical response, one can see that Zview®adjustment is better and this is confirmed by the SSE comparison.

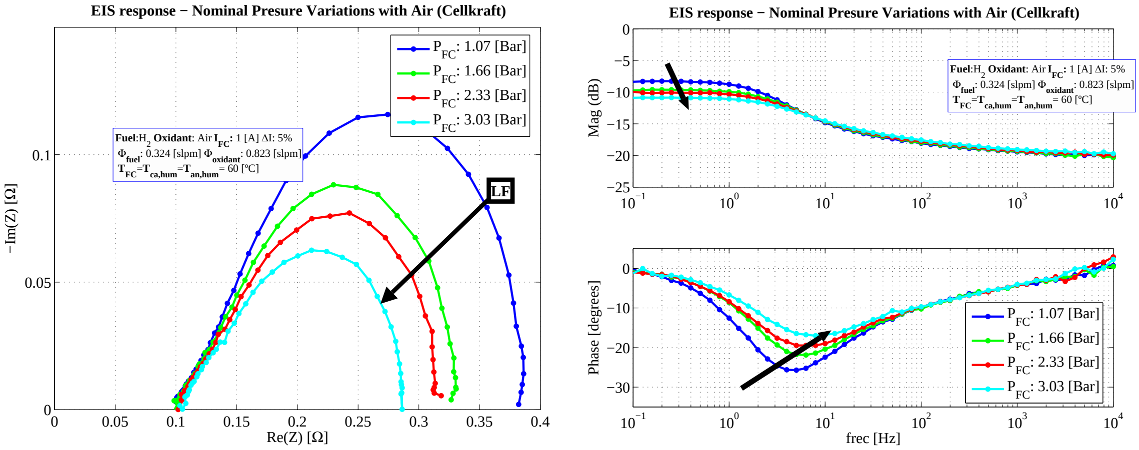

(a) Nyquist (*Air*) (b) Bode (*Air*)

Figure 3.31: IRII response with pressure variations (*Air*)

Table 3.24: First approach by simple equivalent circuit procedure, H_2/Air with Pressure variation

P_{FC} [bar]	$R_m[\Omega]$	$R_{W1}[\Omega]$	$T_{W1}[s]$	P_{W1}	SSE
1.067	0.098	0.293	0.200	0.480	0.076
1.663	0.097	0.236	0.158	0.456	0.065
2.333	0.103	0.212	0.158	0.444	0.215
3.034	0.105	0.181	0.126	0.423	0.113

Next step has been the research of the possible minimal set of free parameters that are able to fit (approximately) the frequency response for all pressures.

When the operating pressure is varying, the low frequency response is affected, then it is a very straight selection to maintain the high frequency resistance ($R_{HF} = R_m$) at a fixed value. After this first parameter is considered constant, which other can be considered also constant? There are two options: P_{w1} (called "reduction 1") or T_{w1} (called "reduction 2").

When the relevant characteristics are analysed (table 3.15 and figure 3.15), it is seen that low frequency resistance R_{LF} and frequencies $f_{Imax,LF}$ and $f_{\phi max,LF}$ have a clear variation with pressure variations (R_{LF} has a decreasing trend, while the frequencies $f_{Imax,LF}$ and $f_{\phi max,LF}$ have an increasing trend).

Then, considering the information extracted from the relevant characteristics, it is more

Table 3.25: Parameter adjusted by Zview, H_2/Air with pressure variation

P_{FC} [bar]	$R_m[\Omega]$	$R_{W1}[\Omega]$	$T_{W1}[s]$	P_{W1}	SSE
1.067	0.099	0.289	0.152	0.485	0.006
1.663	0.098	0.235	0.115	0.459	0.006
2.333	0.099	0.221	0.113	0.435	0.016
3.034	0.101	0.191	0.093	0.415	0.014

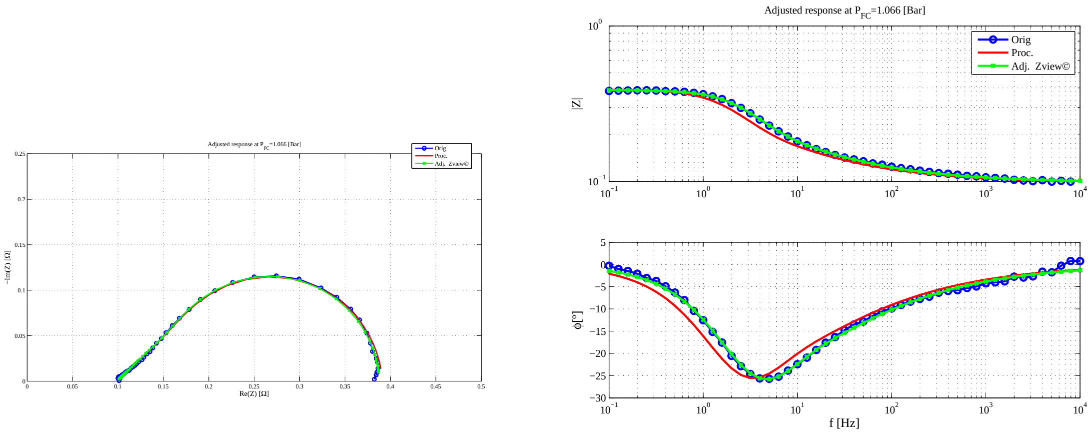

(a) Nyquist (*Air*) (b) Bode (*Air*)

Figure 3.32: Comparison of responses: procedure and Zview, $P_{FC} = 1.066$ [bar]

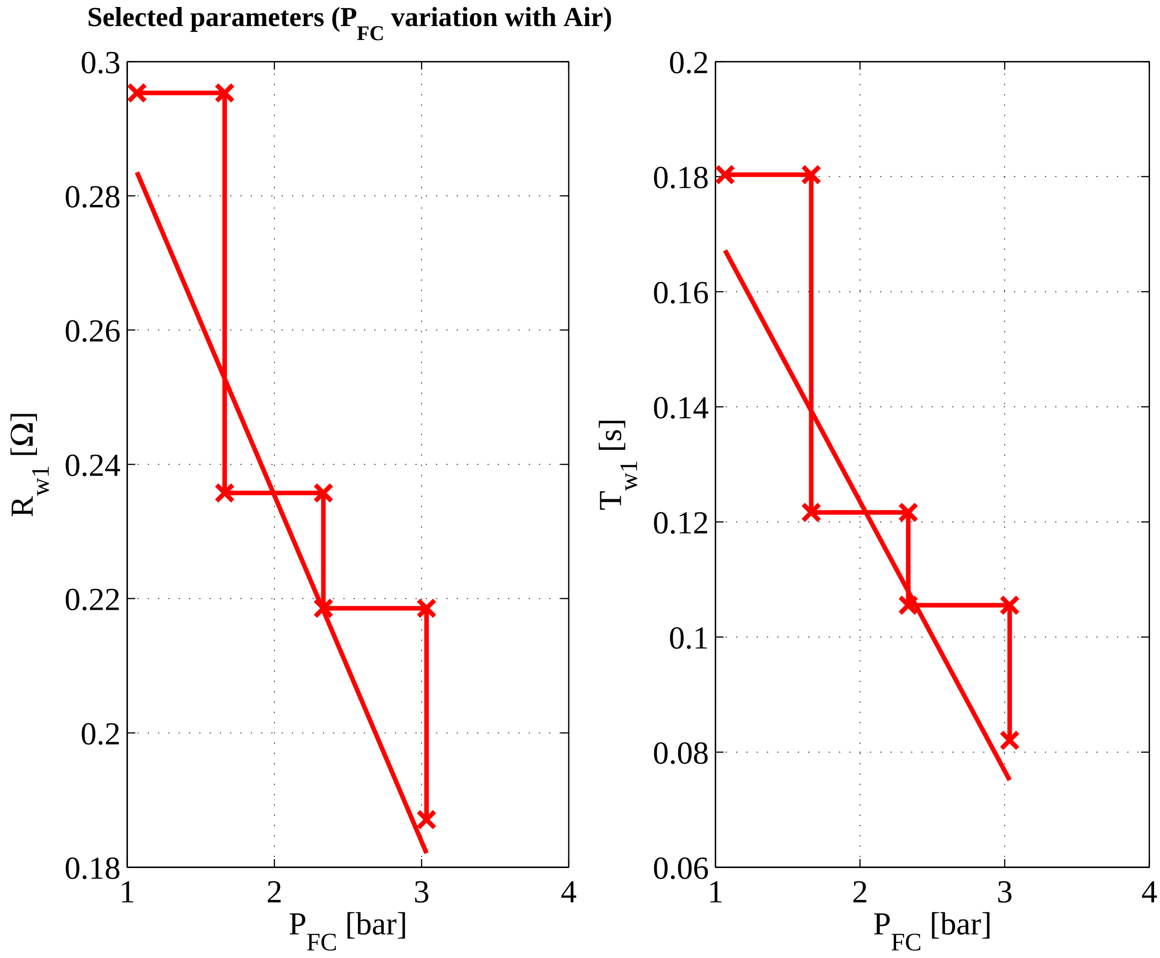

Figure 3.33: Selected parameter evolution with P_{FC} variation

suitable the *reduction 1*, keeping as free parameters the R_{W1} and T_{W1}, which can be related to R_{LF} and the frequencies $f_{Imax,LF}$ and $f_{\phi max,LF}$.

Finally, it has been proven that the selected free circuit parameters R_{W1} and T_{W1} are a good choice to reflect the pressure effects in the responses. Their dependence on pressure can be seen in figure 3.33.

3.5.4.2 Temperature variation

The H_2/Air supply response with temperature variation is shown again in the figure 3.34.

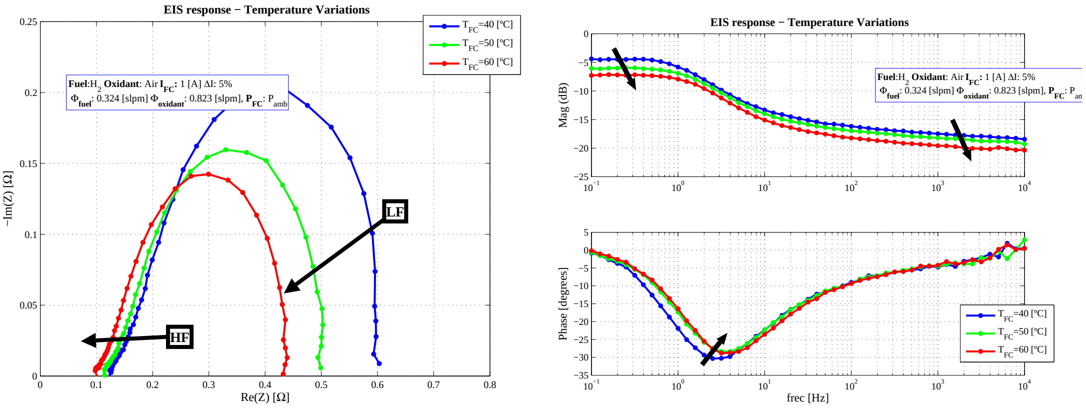

(a) Nyquist

(b) Bode

Figure 3.34: Temperature variation, H_2/Air, IRII lab

Following the same procedure detailed in section 3.5.4, the initial equivalent circuit parameters are obtained and shown in the table 3.26 along with the sum of the squared error, SSE.

Table 3.26: First approach to simple equivalent circuit parameters with H_2/Air, Temperature variation

T_{FC} [ºC]	$R_m[\Omega]$	$R_{W1}[\Omega]$	$T_{W1}[s]$	P_{W1}	SSE
40.0	0.122	0.478	0.398	0.511	0.017
50.0	0.112	0.396	0.251	0.488	0.027
60.0	0.096	0.346	0.316	0.497	0.032

As it was already done in the other cases, the obtained parameters are used as the initial parameters to Zview® adjustment. The results of this adjustment are presented in table 3.27.

Table 3.27: Parameter adjustment by Zview®, H_2/Air, Temperature variation

T_{FC} [ºC]	$R_m[\Omega]$	$R_{W1}[\Omega]$	$T_{W1}[s]$	P_{W1}	SSE
40.0	0.125	0.479	0.265	0.509	0.016
50.0	0.114	0.386	0.210	0.503	0.013
60.0	0.098	0.338	0.190	0.508	0.012

Reducing the number of free parameters in order to get approximately the same frequency response for all temperatures, allows to characterize the evolution with some parameters hold as a constant. When the operating temperature is varied, low and high frequency responses are affected. In this case, it is not clear which parameters can be selected as constant. Two alternatives are evaluated: "P_{W1}" or reduction 1 and "T_{W1}" or reduction 2. Results of both reductions are presented in table 3.28 and 3.29.

Table 3.28: Parameter "reduction 1" with temperature, H_2/Air

Element	T_{FC} [°C]		
	40	50	60
R_m	0.124	0.115	0.098
R_{W1}	0.480	0.385	0.339
T_{W1}	0.268	0.207	0.191
P_{W1}		0.507	
SSE	0.017	0.013	0.012

Table 3.29: Parameter "reduction 2" with temperature, H_2/Air

Element	T_{FC} [°C]		
	40	50	60
R_m	0.126	0.114	0.097
R_{W1}	0.457	0.392	0.351
T_{W1}		0.222	
P_{W1}	0.530	0.496	0.488
SSE	0.029	0.015	0.023

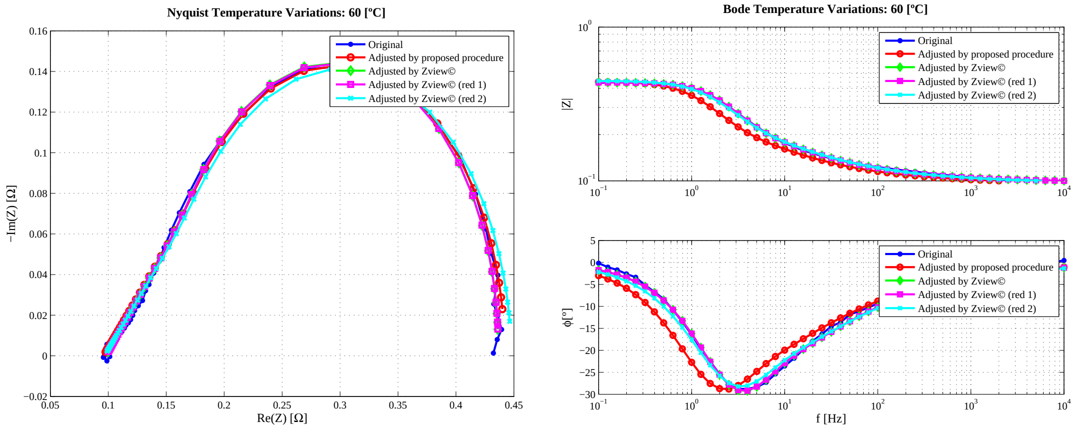

(a) Nyquist (*Air*)

(b) Bode (*Air*)

Figure 3.35: Responses: Procedure, Zview and Reduced

The frequency response employing the initial tunning procedure, the Zview®tuning and the "reduced" circuits tuning("reduced 1" and "reduced 2") with $T_{FC} = 60$ [°C] are shown in the figure 3.35. All responses have similar evolution and both "reductions" are really good. However, the "reduction 1" gives better results comparing the SSE values.

The selected free parameters of "reduction 1" (P_{W1} as constant) are presented in figure 3.36 where their evolution under temperature variation are shown.

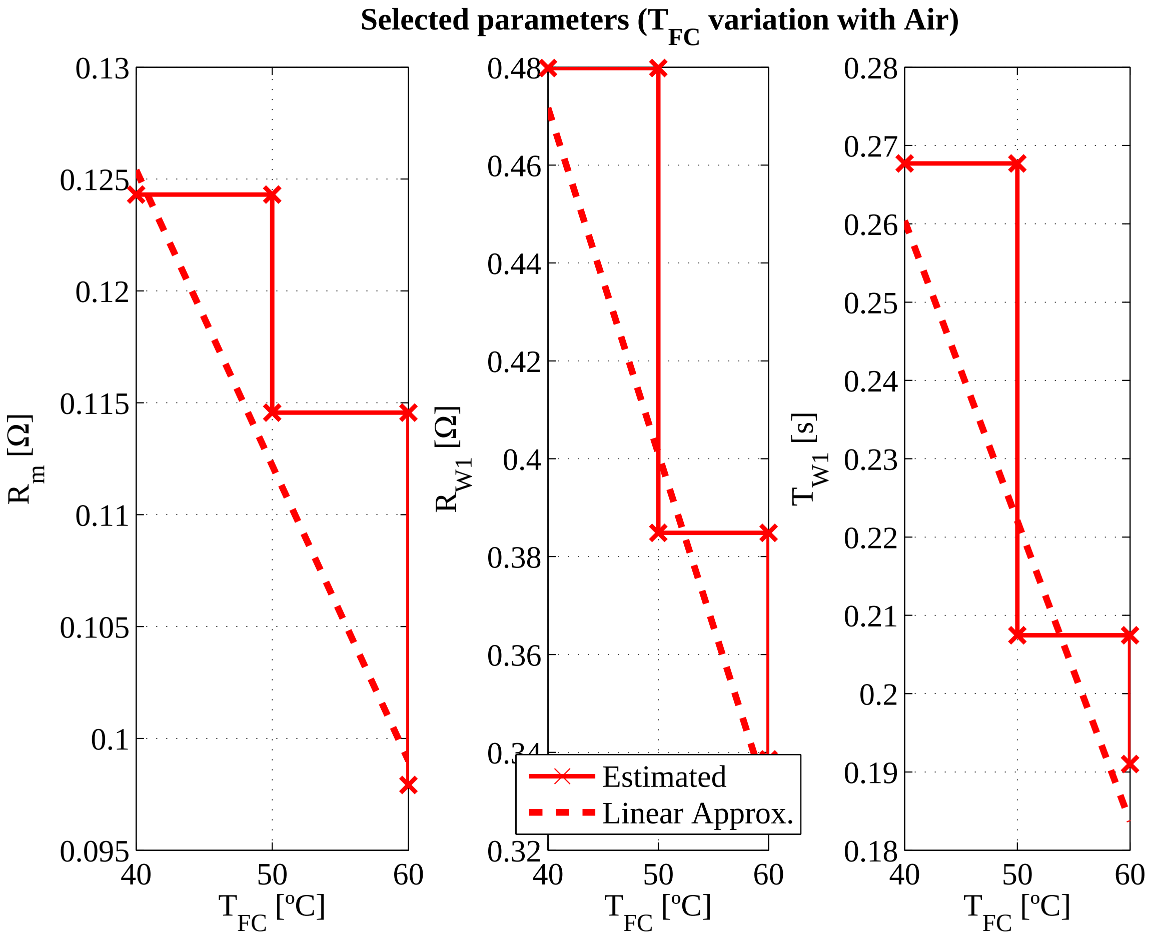

Figure 3.36: Selected temperature parameter representation, H_2/Air

3.5.4.3 Relative Humidity Variation

The H_2/Air supply response with relative humidity variation is showed again in figure 3.37.

Following the same procedure detailed in section 3.5.4, the equivalent circuit parameters are obtained and presented in the table 3.30 along with the sum of squared error (SSE).

Table 3.30: First approach to simple equivalent circuit parameters with H_2/Air, RH variation

RH_{FC} [%]	$R_m[\Omega]$	$R_{W1}[\Omega]$	$T_{W1}[s]$	P_{W1}	SSE
50.0	0.157	0.285	0.097	0.452	0.019
65.0	0.127	0.259	0.097	0.439	0.012
85.0	0.113	0.237	0.097	0.438	0.015
100.0	0.108	0.291	0.106	0.406	0.017

After this first adjustment, using Zview®software, a curve fitting is done and the resulting parameters at different relative humidity operating conditions are presented in table 3.31.

In order to compare the fittings, the Nyquists of the system for $RH_{FC} = 100.0[\%]$ are

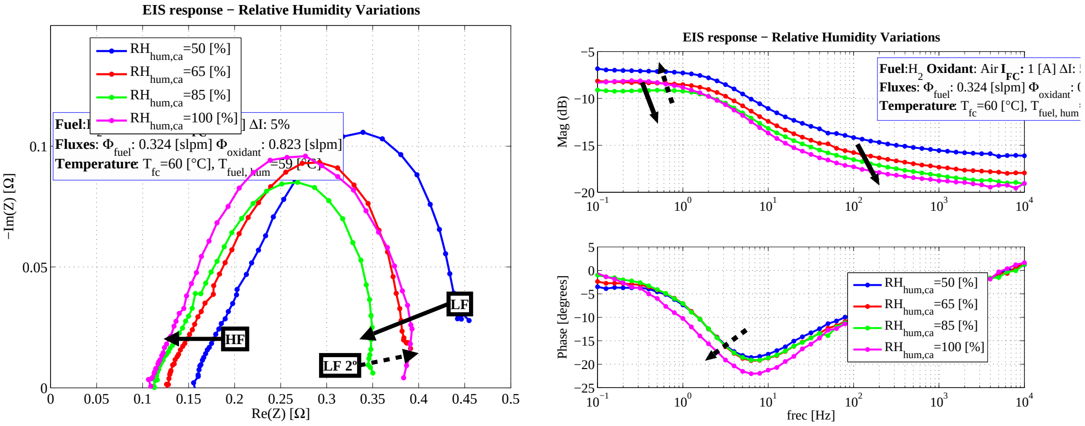

(a) Nyquist (b) Bode

Figure 3.37: Temperature variation, H_2/Air, IRII lab

Table 3.31: Parameter adjusted by Zview, H_2/Air, Relative Humidity variation

RH_{FC} [%]	$R_m[\Omega]$	$R_{W1}[\Omega]$	$T_{W1}[s]$	P_{W1}	SSE
50.0	0.152	0.303	0.103	0.426	0.014
65.0	0.122	0.272	0.101	0.424	0.011
85.0	0.109	0.250	0.096	0.422	0.011
100.0	0.104	0.289	0.136	0.445	0.028

shown in figure 3.38.

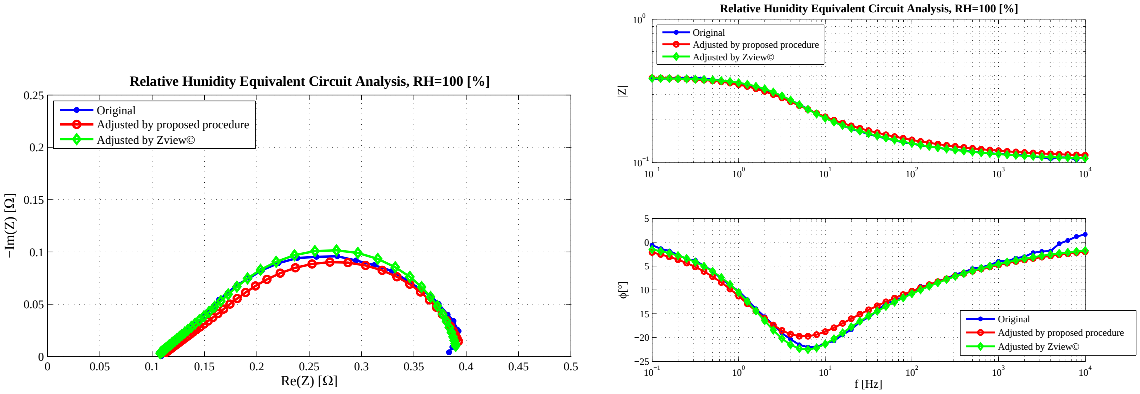

(a) Nyquist (Air) (b) Bode (Air)

Figure 3.38: Comparison of responses: procedure and Zview, $RH_{FC} = 100.0$ [%]

Reducing the number of free parameters maintaining approximately the same frequency response, allows to characterise the evolution with less parameters. Varying the operating relative humidity of the cathode, the low and the high frequency relevant characteristics are affected, what makes it more difficult to choose a reduction. In this case, the proposed reductions are the following: *reduction 1* is done keeping P_{W1} and *reduction 2* is done keeping T_{W1} constant.

Keeping P_{W1} fixed and using the values of table 3.31 as initial values for the other parameters, a new fitting is done. The results are shown in the table 3.32.

Table 3.32: Parameter *reduction 1* with RH variation, H_2/Air

Element	RH_{FC} [%]			
	50.0	65.0	85.0	100.0
R_m	0.153	0.123	0.111	0.103
R_{W1}	0.301	0.269	0.247	0.292
T_{W1}	0.100	0.097	0.092	0.144
P_{W1}	0.434			
SSE	0.014	0.011	0.011	0.016

Also, keeping T_{W1} fixed and using the same procedure used for *reduction 1*, results of the *reduction 2* fitting are obtained and shown in the table 3.33.

Table 3.33: Parameter *reduction 2* with RH variation, H_2/Air

Element	RH_{FC} [%]			
	50.0	65.0	85.0	100.0
R_m	0.15	0.12	0.11	0.11
R_{W1}	0.31	0.28	0.26	0.27
T_{W1}	0.11			
P_{W1}	0.42	0.42	0.41	0.468
SSE	0.013	0.012	0.013	0.020

In order to compare the results of all the parameter fittings, the evolution of all parameters facing RH changes are shown in the figure 3.39. Also, in the figure 3.40 all frequency responses are graphed for $RH_{FC} = 100$ [%] condition.

From the evolution of the parameters it is seen that both low and high frequency characteristics are affected by the variation of the relative humidity. Physically, the high frequency response is closely related with the membrane water content, so it is explained that increasing the cathode humidification, the high frequency resistance reduces. The low frequency response is related to the water presence at the reaction sites in the catalyst layer . When the RH is low, the water presence is not enough to get all the reaction sites available for hydrogen protons, even if for oxygen particles it is more easy to get these reaction sites.

However, when RH is close to 100 [%], R_W and T_W change their trend and indicate an impedance increase. This can be explained through a blocking effect: excess of water blocks the oxygen way to the reaction sites.

Referring to the resulting reduced set of parameters, at least three parameters are needed in order to capture this variation. The most appropriate are: R_{W1}, R_m and the other can be selected between: T_{W1} or P_{W1}. The "reduction 1" is a more suitable choice due to the relationship of T_{W1} with frequency. The Selected parameters evolution under RH changes is shown in figure 3.41.

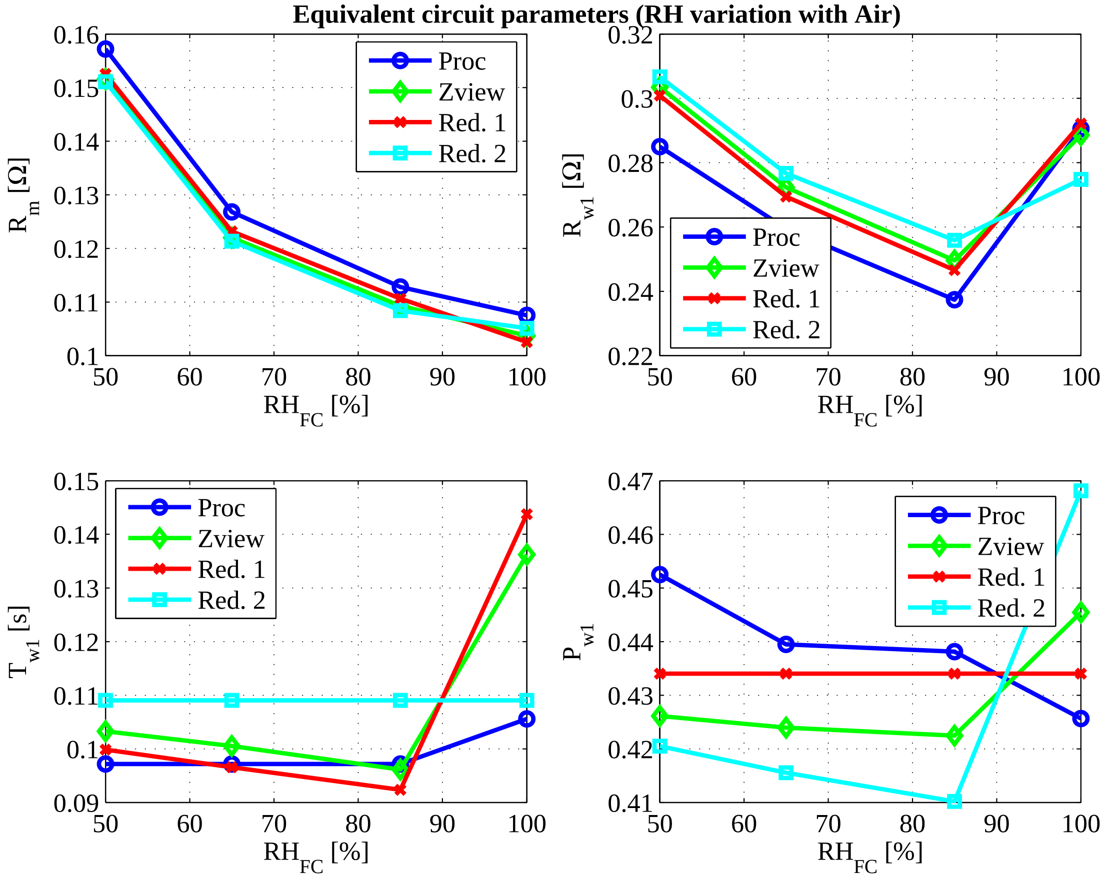

Figure 3.39: Parameter comparison: procedure, Zview and reduced

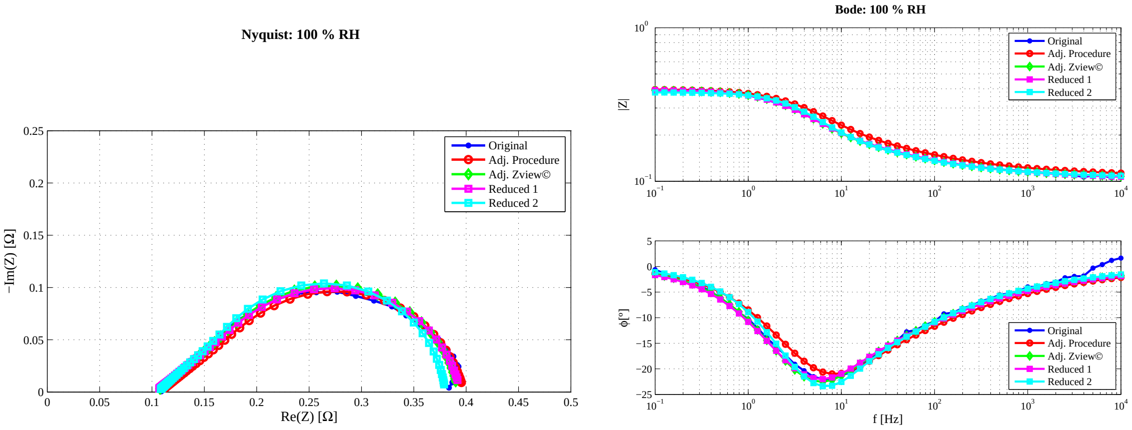

(a) Nyquist (*Air*)

(b) Bode (*Air*)

Figure 3.40: Comparison of responses: procedure, Zview and reduced $RH_{FC} = 100.0$ [%]

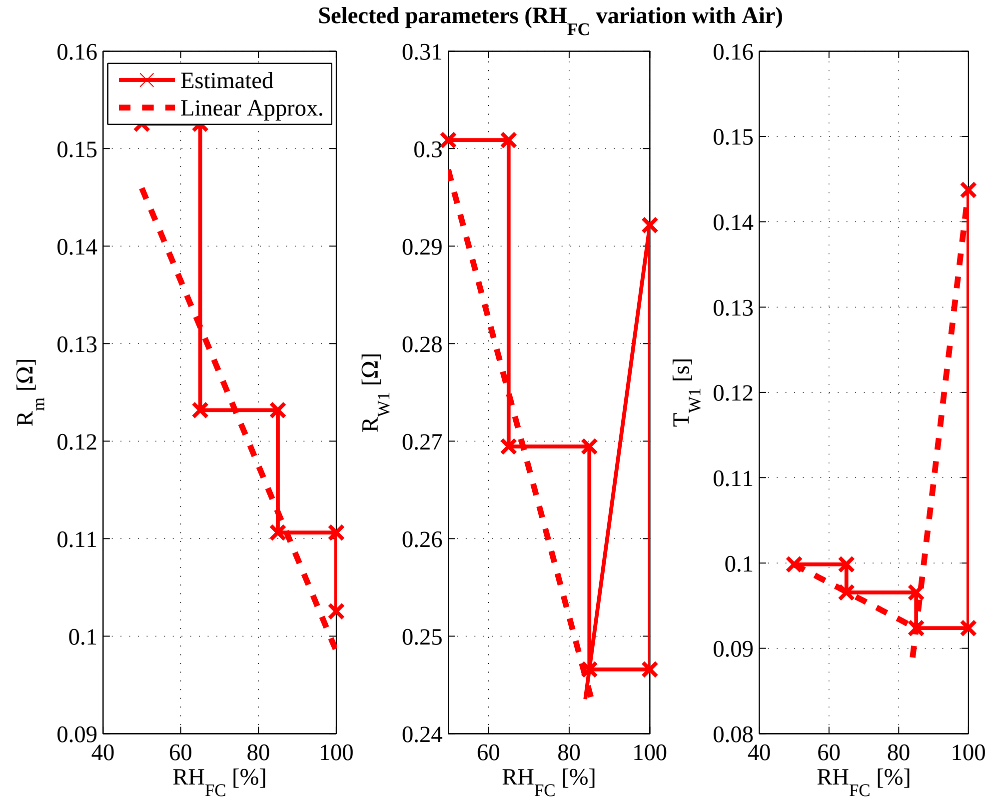

Figure 3.41: Selected parameter evolution with RH_{FC}, H_2/Air

3.6 Effective coefficients estimation

After studying the effect of different operating conditions in the frequency and time responses, the interest is focused on searching the way of reflecting those effects by means of some parameter or an *effective coefficient* that could be used as a diagnosis tool. In particular, in this section, the *effective active area* and *effective diffusion coefficient* are calculated and analysed, from the "Relative Humidity" variation response (presented in section 3.5.4.3).

First, the analysis starts using a part of the model presented by Fouquet *et al.* [2006]. In this article, a general expression for the impedance of a finite length diffusion layer, deduced from Butler-Volmer equation and Fick's second law, is presented as follows:

$$Z_\delta = \frac{RT}{n^2F^2S\sqrt{j\omega}} \frac{\tanh\sqrt{\left({}^{j\omega}/_{D}\right)}\delta}{C\sqrt{D}} \tag{3.25}$$

Equation 3.25 can be rewritten as:

$$Z_\delta = \frac{RT}{n^2F^2S\sqrt{j\omega}} \frac{1}{C} \frac{1}{D} \delta \frac{\tanh\sqrt{j\omega\left({}^{\delta^2}/_{D}\right)}}{\sqrt{{}^{\delta^2}/_{D}}} = R_d \frac{\tanh\sqrt{j\omega\tau_d}}{\sqrt{\tau_d}} \tag{3.26}$$

The equation 3.26, allows the definition of two parameters. One is a time constant τ_d:

$$\tau_d = \frac{\delta^2}{D} \tag{3.27}$$

And there is a resistance, R_d:

$$R_d = \frac{RT\delta}{n^2 F^2 SCD} \tag{3.28}$$

where R is the universal gas constant, F is the Faraday constant, n is the number of electrons involved in the reaction (four), δ is the width of the diffusion layer, T is the fuel cell temperature, S is the active area, C is the oxygen concentration at the catalyst surface and D is the diffusion coefficient.

An "effective area coefficient" is defined as:

$$\lambda_{eff} = \frac{S_{eff}}{S_{FC}} \tag{3.29}$$

where S_{eff} is the estimated active area and S_{FC} is the geometrical active area surface (for the single cell used in this thesis, $S_{FC} = 5$ $[cm^2]$).

A procedure to obtain this coefficient is proposed as follows:

- Perform an electrochemical impedance spectroscopy at the desired working conditions.
- Deduce the "relevant characteristics" as is described in section 3.4.
- Obtain the simple equivalent circuit parameters as is detailed in section 3.5.4 (R_{W1}, T_{W1}, P_{W1} and R_m).
- Refine the circuit parameters using Zview®.
- Obtain the effective diffusion coefficient from equation 3.27, as:

  $$D_{eff} = \frac{\delta^2}{\tau_d} \tag{3.30}$$

  where the $\delta = \delta_{GDL}$=0.019 [cm], and $\tau_d = T_{W1}$ (for the IRII single fuel cell).
- Obtain the oxygen concentration (in $[mol/cm^3]$) at the channel of the fuel cell, using the following relationships:
- The ideal gas law is used to obtain the total gas concentration at the humidifier:

  $$c_{tot,hum} = \frac{P_{FC}}{RT_{hum}} \tag{3.31}$$

  - The water concentration at the humidifier is obtained as follows:

    $$c_{H_2O,hum} = \frac{n_{H_2O,hum}}{V_{hum}} = \frac{p_{sat}(T_{hum})}{RT_{hum}} \tag{3.32}$$

    where $p_{sat}(T_{hum})$ is the saturation pressure at the humidifier temperature.

- The oxygen concentration at the humidifier is calculated using the relationship between nitrogen and oxygen $\frac{c_{O_2}}{c_{N_2}} = \frac{0.21}{0.79}$ as follows:

$$c_{O_2,hum} = \frac{(P_{hum} - p_{sat}(T_{hum}))}{RT_{hum}} \frac{1}{(1 + (^{0.79}/_{0.21}))} \tag{3.33}$$

- The relationship between $c_{O_2,hum}$ and $c_{tot,hum}$ is obtained as:

$$k_{O_2,hum} = \frac{c_{o_2,hum}}{c_{tot,hum}} \tag{3.34}$$

- The total concentration at the fuel cell channel is:

$$c_{tot,FC} = \frac{P_{FC}}{RT_{FC}} \tag{3.35}$$

- The oxygen concentration at fuel cell channel is:

$$c_{O_2,ch} = k_{O_2,hum} c_{tot,FC} \tag{3.36}$$

- Using the Fick's law of diffusion, and considering a linear concentration decay inside the GDL, allows to obtain the relationship between the concentration at the channel and at catalyst layer:

$$j = D_{eff} \nabla c \Rightarrow j = \frac{I_{FC}}{4FS_{eff}} = D_{eff} \frac{\Delta c}{\Delta z} = D_{eff} \frac{(c_{O_2,ch} - c_{O_2,cat})}{\delta} \tag{3.37}$$

- Combining equations 3.36 and 3.37 with equation 3.28 ($R_d = R_{W1}$), an estimation of the active area is calculated as follows:

$$R_{W1} = \frac{RT_{FC}\delta}{n^2 F^2 S_{est} c_{O_2,Cat} D_{eff}} \tag{3.38}$$

$$j = \frac{I_{FC}}{4FS_{eff}} = \frac{D_{eff}(c_{O_2,CH} - c_{O_2,Cat})}{\delta} \Rightarrow c_{O_2,Cat} = c_{O_2,CH} - \frac{I_{FC}\delta}{4FS_{eff}D_{eff}} \tag{3.39}$$

$$S_{eff} = \frac{\delta}{n^2 F^2 R_{w1} D_{eff} C_{O_2,Ch}} (RT_{FC} + I_{FC} R_{w1} F) \tag{3.40}$$

- Finally the effective area coefficient λ_{eff} is calculated from equation 3.29:

$$\lambda_{eff} = \frac{S_{eff}}{S_{FC}} \tag{3.41}$$

Applying this procedure to the Relative Humidity variation study, see section 3.5.4.3, the following data are obtained:

First, the effective diffusion coefficient, using equation 3.30 is calculated. Two values are obtained depending on the τ_d value (τ_d from initial procedure or τ_d from "reduction 1" fitting), shown in the table 3.34 and figure 3.42. The values and the trend are similar, and

Table 3.34: Effective diffusion coefficient, H_2/Air, Relative Humidity variation

RH_{FC} [%]	$D_{eff}[cm^2/s]$ (PROC.)	$D_{eff}[cm^2/s]$ (RED. 1)
50.0	6.64E-03	6.46E-03
65.0	6.64E-03	6.68E-03
85.0	6.64E-03	6.98E-03
100.0	6.11E-03	4.49E-03

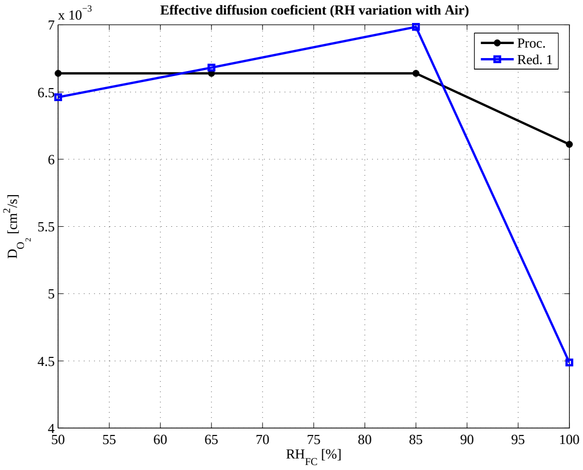

Figure 3.42: Effective diffusion coefficient

Table 3.35: Oxygen channel concentration, H_2/Air, Relative Humidity variation

RH_{FC} [%]	$c_{O2,channel}[mol/cm^3]$
50.0	7.35E-06
65.0	7.14E-06
85.0	6.81E-06
100.0	6.12E-06

Table 3.36: Effective area coefficient, H_2/Air, Relative Humidity variation

RH_{FC} [%]	$\lambda_{eff}[\%]$ (PROC.)	$\lambda_{eff}[\%]$ (RED. 1)
50.0	29.695	30.364
65.0	30.814	30.504
85.0	32.605	30.868
100.0	38.702	52.665

it is clear that diffusion grows a little bit until the water presence is strong enough to reduce its value.

Second, from the information of the different experimental situations, oxygen concentration at the channel is calculated and presented in table 3.35.

Finally, the effective area coefficient is obtained and shown in the table 3.36 and the figure3.43.

After calculating this values, it is clear that the effective area coefficient has an increasing trend either using *reduced 1* or *procedure* methodologies. It is intuitive that the effective active area grows up when the humidification increases. This evolution can be related to the availability of reaction sites for the hydrogen from the membrane (due to an increase of water paths) at cathode side.

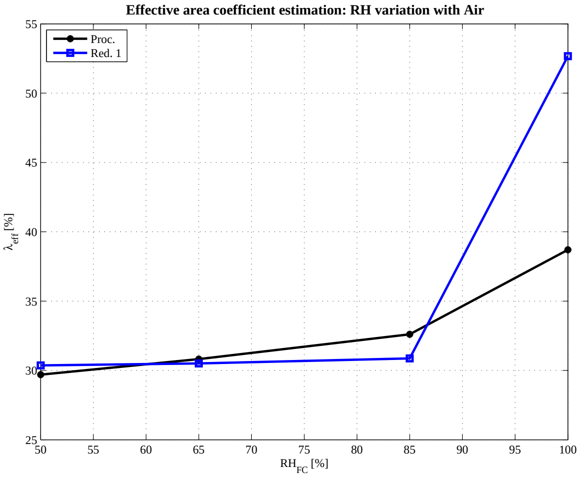

Figure 3.43: Effective area coefficient, RH variation

The low frequency response is assimilated to the diffusion process in the fuel cell (Macdonald & Barsoukov [2005]), specially at cathode side. When the RH is low, the water presence inside the GDL is low and the diffusion of the gases have better conditions. However, when RH is close to 100 [%], R_W and T_W change their trend and indicate a low frequency impedance increase. This can be explained through a "blocking" effect: excess of water blocks some of the oxygen pathways to the reaction sites, and makes the diffusion worse. These described effect can be seen in the "effective diffusion coefficient (D_{eff})", in figure 3.42.

On the other hand, when the RH is low, the water presence at catalyst layer is not enough to get all the reaction sites available for hydrogen protons, even if for oxygen particles it is more easy to get these reaction sites. Then, if the water presence increases (RH has a higher value), the reaction sites available also increase, reaching the better performance at RH=100 [%]. These described effects are reflected in the *effective area coefficient,* λ_{eff} (see figure 3.43).

Then, one of the conclusions is: even that the diffusion process can deteriorate by an excessive presence of water, this effect helps to increase the effective active area due to the recovery of the protons water paths to the reaction sites.

In this case, *effective diffusion coefficient,* D_{eff} and *effective area coefficient,* λ_{eff} seems a good choice of the fuel cell status indication, due to its relationship with water presence at GDL and catalyst layer and its reflection in EIS response.

3.7 Conclusions

In this chapter, a systematic use of **EIS** characterization technique results are presented and studied in order to analyse the influence of different operating conditions over the fuel cell response. The operating conditions under analysis includes: the DC load current, the fuel cell pressure, the fuel cell temperature and the cathode relative humidity. Also, all these operating conditions are applied with different inlet gases situation H_2/O_2 and H_2/Air.

The response of the system when H_2/O_2 are used as inlet gases, show two impedance arcs, one of them appears in the low frequency range and the other appears at the high frequency range. On the other hand, in the H_2/Air gas feeding situation, there is only one single predominant arc. This fact is repeated over all the operating conditions.

The EIS response of the fuel cell system when the DC load current is increased, presents three different zones of evolution. In the low current range there is a reduction of the low frequency arc. In the medium current range, the EIS response shows negligible variations over all frequency range. In the high current range, the low frequency arc increases significantly its values. The EIS value for high frequencies is independent of the current values. When the operating pressure of the fuel cell system increases, only the low frequency arc is affected reducing its value. If the fuel cell temperature or the relative humidity are augmented, all the values of the frequency response are shifted to the left and hence take lower values. All the conclusion detailed for the nominal operating conditions, are the same under the different inlet gases situation, H_2/O_2 and H_2/Air.

Identification of seven **relevant characteristics** from the EIS (Nyquist and Bode diagram) response is done, three of them are related with the low frequency zone of response and the other four are related with the high frequency zone of response. Two of them are the more significant ones: the high and the low frequency resistances. The variation of relevant characteristics with the operating conditions is analysed. The low frequency resistance is the most sensitive relevant characteristic.

Several equivalent circuit have been analysed and those that have the best fitting with the experimental EIS data have been selected. When *Air* is used as oxidant, a simple equivalent circuit with a resistance and Warburg elements is proposed. When *Oxygen* is used as oxidant, a more complex equivalent circuit is necessary, it is composed by one resistance, one inductance and two Randles-type circuit in series. The Warburg elements are helpful to model the diffusion phenomena, the CPE are useful to model the charge accumulation phenomena, while the serial resistance models the membrane resistance.

The EIS relevant characteristics have been related to the parameter of the equivalent circuits. For example, the R_{HF} is assigned to the R_m and, in the *Air* as oxidant case, $R_{LF} - R_{HF}$ is assigned to Warburg resistance element. A complete procedure for the fine tuning of these parameters, that takes advantage of the Zview tool, has been presented. Regarding SSE, it can be concluded that a good fittings of response are always obtained.

A detailed sensitivity analysis is performed allowing to select those parameters that capture the influence of the operating conditions. It is concluded that good fittings are still possible in spite of maintaining some of the parameters at constants values. For instance, R_m is not affected by pressure changes or P_W it is not affected by the studied operating condition variations.

An effective area coefficient relating the geometrical active area (nominally, 5 cm^2) with the effective active area is proposed and the procedure to obtain this coefficient is detailed. This procedure is specially interesting because distinguishes the effective diffusion coefficient, which is a property of the material, from the effective area coefficient, which indicates the useful reaction area. While the effective diffusion coefficient indicates the problems created by the increase of the water presence in the GDL (concentration losses), the effective area represents the reaction sites that fulfil the suitable conditions for protons to arrive to this sites.

Chapter 4

Design of experimental techniques for PEMFC characterisation

4.1 Introduction

In this chapter a description of new PEMFC characterisation tests is done. Viewing the influence of the water presence and its balance on the fuel cell behaviour, an investigation of the gas humidity requirements and its related problems is carried out. Combining EIS technique and water balance studies, a new technique named “humidification interruption” is proposed. It consists in applying on anode or cathode humidification an ON-OFF-ON sequence, performing at the same time “reduced” EIS’s. They are named “reduced” because the number of selected frequencies is lower than “complete” EIS tests, commonly used in chapter 3.

In the first part of this chapter, the state of the art and the objectives of the study are presented. Next, the experimental layout and the application description is done. Finally, temporal evolution investigation of the humidification interruption applied under different operating conditions is detailed.

4.2 State of art

This section is dedicated to show the state of the art in water management and its influence into fuel cell response.

As is described in chapter 2 “PEMFC system description”, the core of a Proton Exchange Membrane Fuel Cell is the polymeric membrane (see Larminie & Dicks [2003]). The most well known and well established polymeric membrane used in PEMFC is the Nafion(® Dupont), which has been developed trough several variants since the 1960s.

The construction of the electrode material is as follows: the starting point is the basic polymer: polyethylene. This basic polymer is modified substituting fluorine by hydrogen. This process is called “perfluorination” and the result is a modified polymer named polytetraflouroethylene or PTFE (see figure 4.1). This material is highly hydrophobic. However, to make an electrolyte, a further stage is needed. The PTFE polymer is ’sulphonated’, what means that a side chain ending with a sulphonic acid HSO_3 is added. And now, a key

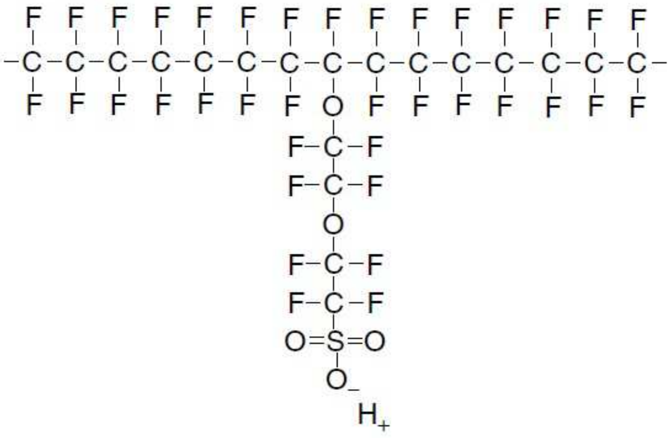

Figure 4.1: Example of structure of perfluorosulphonic acid PTFE copolymer (from reference Barbir [2005])

property of sulphonic acid is that it is highly hydrophyllic (it attracts water). That is to say, in Nafion® polymers, there are hydrophyllic regions inside a hydrophobic substance. This hydrophyllic regions around the clusters of sulphonated side chains can lead to the absorption of large quantities of water and the result is that H^+ ions are weakly attracted to SO_3^- and are able to move.

It **is important that the hydrated regions must be as large as possible**. In a well hydrated electrolyte, there will be about 20 water molecules for each SO_3^- side chain. Tipically, this gives a proton conductivity about $0.1[Scm^{-1}]$ that falls linearly as the water content falls. However, there must not be so much water presence that the electrodes that are bonded to the electrolyte flood block the pores in electrode or the gas diffusion layer.

According to Barbir [2005], an electrode is essentially a thin catalyst layer pressed between the ionomer membrane and the porous, electrically conductive substrate. This is the layer where the electrochemical reactions take place. More precisely, the electrochemical reactions take place on the catalyst surface. Because there are three kinds of species that participate in the electrochemical reactions, namely gases, electrons and protons, the reactions can only take place on a portion of the catalyst surface where all three species have access. Electrons travel through electrically conductive solids, including the catalyst particles that are somehow electrically connected to the substrate. Protons travel through ionomer, and hence, the catalyst must be in intimate contact with the ionomer. And finally, the reactant gases travel only through the voids of the substrate. Therefore, the electrode must be porous to allow gases to travel to the reaction sites. At the same time, the produced water must be effectively removed; otherwise the electrode would flood and prevent oxygen access. The most common catalyst in PEMFC for both oxygen reduction and hydrogen oxidation reactions is platinum. To minimize the cell potential losses due to the rate of proton transport and reactant gas permeation in the depth of the electrode-catalyst layer, this layer should be reasonable thin. At the same time, the catalyst active surface area should be maximized, for which the Pt particles should be as small as possible.

In general, higher Pt loading results in voltage gain, as shown in figure 4.2, assuming

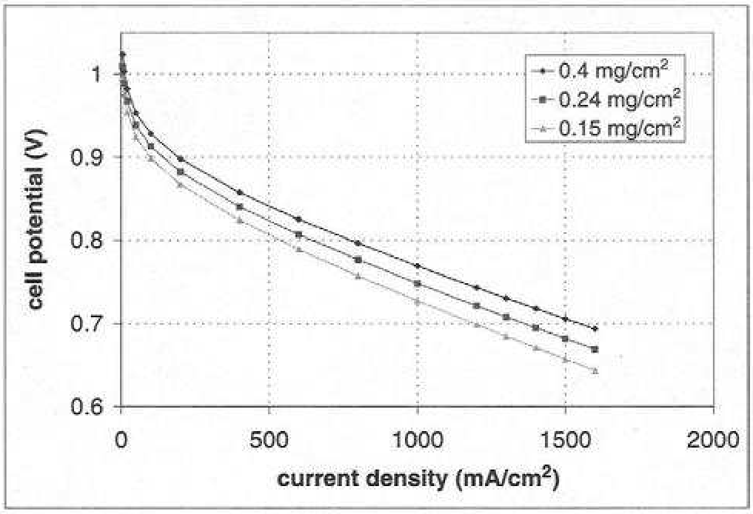

Figure 4.2: Active area influence of Pt loading (extracted from reference Barbir [2005])

equal utilization and reasonable thickness of the catalyst layer. The key to improve the PEM fuel cell performance is not to increase the Pt loading, but rather to increase Pt utilization in the catalyst layer.

In the PEMFC, water forms at the cathode catalyst layer where the reactions occurs. In an ideal situation, this water would keep the electrolyte at the correct level of hydration (reference Barbir [2005]); air would be blown over the cathode, and apart from supplying the necessary oxygen it would dry out any excess water; because the electrolyte membrane is so thin, water would diffuse from the cathode side to the anode, and throughout the whole electrolyte a suitable state of hydration would be achieved without any special difficulty. But this is only an **ideal situation**.

There are several complications:

- During the operation of the cell the H^+ ions move from the anode to the cathode. One ion can pull with it from one to five water molecules (this phenomena is called “electro-osmotic drag”).
- There is an added drying effect of the air at high temperatures.
- Water may be not well distributed throughout the electrolyte: some parts may be just hydrated, others too dry and others too flooded.

One common way to solve these problems is to humidify the air, the hydrogen or both, before they enter the fuel cell. This humidification can cause water flooding over channels, the gas diffusion layer and other parts. However, humidification is sometimes needed and greatly improves fuel cell performance.

Water movement inside PEMFC is showed in figure 4.3. The water production at the cathode catalyst layer is directly proportional to the current and the water drag is related with the flow of the protons moving from anode to cathode (electro-osmotic drag). The back diffusion of water from cathode to anode depends on the thickness of the electrolyte membrane

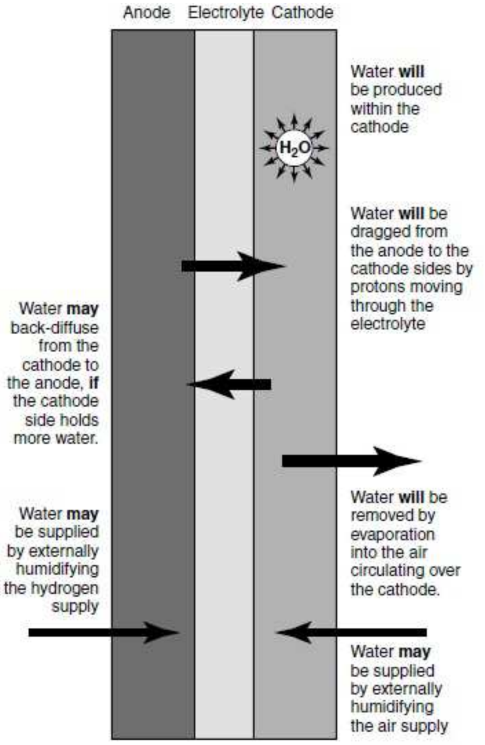

Figure 4.3: Water movement within inside PEM fuel cell (from reference Larminie & Dicks [2003])

and the relative humidity of each side. Finally, if external humidification of reactant gases is used, its control can be used to influence the water movement inside the PEMFC.

A series of the articles : Owejan *et al.* [2009],Lu *et al.* [2009] and Lu *et al.* [2010], presents a water management studies with the physical influence of different constitutive part of fuel cells, flow maldistribution, gas channel design and water drainage characteristics. In the first article of the series, Owejan *et al.* [2009], a design of a test set up that enables investigation of two-phase channel flow within PEMFC is presented. It includes water from the porous gas diffusion layer (GDL) into the channel gas flows, the flow of water within the bipolar plate channels themselves and the dynamics of flow trough multiple channels connected to common manifolds which maintain a uniform differential pressure across all possible flow paths. Also, these effects are investigated at relatively low operating temperatures, steady-state conditions and during transient air purging sequences. The main aspects elucidated are the dynamics during cathode air purge, where rapid elimination of anode channel water by system pressure release occurs, followed by a relative slow evaporative removal of water from the gas diffusion layer. Water removal from the membrane-electrode assembly appears to begin once the drying front in GDL moves beyond the edge of the active area. If significant evaporative water removal from the GDL and MEA is required to prepare the fuel cell for the subsequent start-up under freezing conditions, long cathode air purges could be required, specially at low shut-down temperatures.

In Lu *et al.* [2009], an ex-situ experimental setup is designed to investigate the two-phase water transport in PEMFC parallel cathode gas channels. The two phase flow dynamics is studied in terms of the instantaneous airflow rate in each channel, the total pressure drop across the entire flow field, and high-speed video observation of the water flow distribution, all measured simultaneously. At low airflow rates the two phase flow is dominated by slug flow. The individual channel flow rate measurements indicate that a water slug causes flow maldistribution or even blocks a channel, causing a PEMFC performance degradation and possible durability problems. At higher airflow rates, the two-phase flow is dominated by annular/film flow for the hydrophilic channel walls. Liquid water collects on the channel walls in the form of large droplets which are removed in a film-like structure along the sidewalls by the drag forces of the core airflow and gravity. Since the channel is not significantly blocked by the water film, severe flow maldistribution is not found under film flow pattern. Finally, it is found that water build up in the gas channels and the channel-exit manifold interface can be quantitatively described by a two phase pressure drop factor, which is defined as the ratio of the two phase pressure drop to the single-phase pressure drop. This factor decreases with increasing airflow rates.

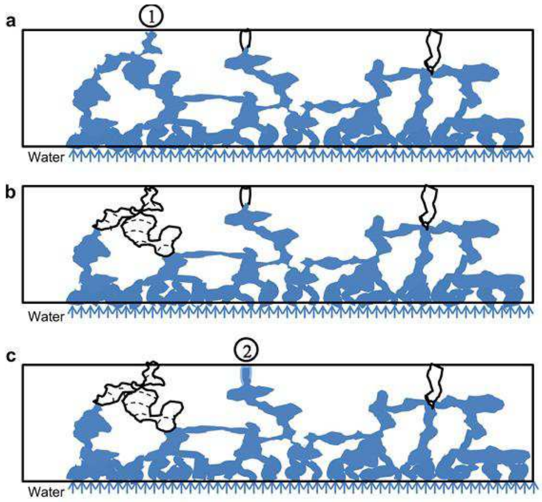

Fig. 11 – A schematic of water drainage process of a model capillary system as water emerges from GDL surface. a) 1st water breakthrough at a preferential location; b) the "choke-off" leaves empty pores in GDL and breaks down the water paths; c) spontaneous redistribution of water occurs inside GDL, which may make breakthrough at 2nd location possible.

(a) Water drainage process at GDL

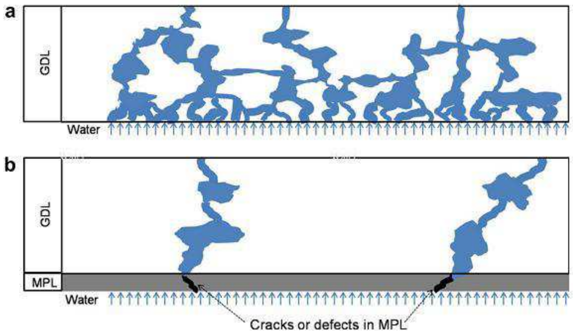

Fig. 12 – Schematic of water drainage in GDL (a) without MPL, displaying a large number of water entry points into the GDL; and (b) with MPL, restricting water entry into GDL only at the crack/defect locations in the MPL.

(b) Water drainage process with MPL

Figure 4.4: Water drainage process in GDL with and without MPL (extracted from Lu *et al.* [2010])

In the last article of this serial, reference Lu *et al.* [2010], the liquid water breakthrough across gas diffusion layer (GDL) with and without microporous layer (MPL) are studied in an ex-situ setup which closely simulates a real fuel cell configuration and operating conditions. The following several points can be concluded from the results:

- The capillary pressure inside the GDL is dynamic even after breakthrough and recurrent water breakthroughs are always observed (see figure 4.4(a)). This indicates a breakdown and re-build of water paths caused by an intermittent water drainage process from the GDL surface.
- From GDL samples without MPL a dynamic changing of breakthrough locations is observed, while for GDL samples with MPL no such phenomenon can be found. At the same time, the water saturation for GDLs with MPLs is significantly lower than in the samples without MPLs. This result suggest that MPL limits the number of water entries into GDL and stabilizes the water paths (see figure 4.4(b)).
- The effect of MPL on the two phase flow dynamics in gas channels with multi-channels is analysed. The most important result is that GDL without MPL promotes film flow and shifts the slug-to-film flow transition to the lower flow rates, compared with the case of GDL with MPL.

On the other hand, in the last years efforts in modelling the water transport in polymer electrolyte membrane fuel cells are done. In article Wu *et al.* [2009], a 3-D model with a single straight flow channel has been developed which incorporates transport phenomena in PEMFCs, such as multi-species transport, heat transfer, and electrochemical reactions as well as product water in dissolved ionomer phase. The model of the equilibrium for the membrane sorption/desorption processes tends to underestimate the cell current output even under steady conditions. A non-equilibrium model with finite sorption/desorption rates is used for the transient phenomena study. The effect of the state of the produced water during the oxygen reduction reaction (ORR) on the cell performance has also been investigated. Capillary pressure and relative permeability have significant effect on water transport, and relative permeability has more impact on the liquid water transport than capillary pressure.

In article of Das *et al.* [2010], a simplified mathematical formulation of liquid water transport in the cathode catalyst layer (CCL) of a PEMFC has been developed and one-dimensional analytical solutions have been provided for both hydrophilic and hydrophobic CCLs. It has been observed that the wetting properties of a CCL control the flooding behaviour, and hydrophilic characteristic of CCL plays a significant role on the cell performance. Based on the analysis of the presented dimensionless time constants, it is found that liquid water production from the phase change process is almost negligible compared to liquid water production from electrochemical process. However, the liquid water transport by electro-osmotic drag and back diffusion from the membrane to the CCL has significant contribution to the liquid accumulation. The effect of water flooding on the activation overpotential is found to be less sensitive if a linear reduction of active region area is assumed, whereas the higher order reduction of active region area shows a significant increase of activation overpotential due to liquid saturation. Hence, the widely used linear approximation modelling of the reduction of active reaction site due to the liquid water saturation seems to be an underestimation. The dimensionless time constants defined in this study might be a useful tool in investigating other flows in porous medium, such as ground water transport, oil transport in oil sands, and membrane filtration.

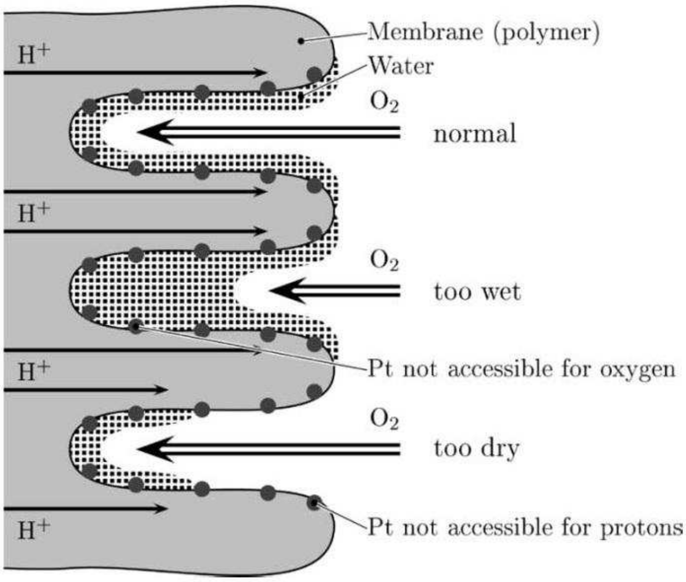

Figure 4.5: Humidity conditions at catalyst layer

From modelling and interpretation of water influence in the transient response, the paper presented by Friede *et al.* [2004], presents a mathematical model and an special experimental method to characterize the fuel cell transient behaviour. One important description of this paper is the electrode and its relation with the humidity condition. The electrodes are made of platinum particles deposited within a carbon support of the membrane surface. As a result of the membrane porosity, the particles are introduced into the membrane material. For the reaction, a small water film is necessary to ensure proton transport in the membrane while too much water can constrict the pores so that oxygen gas supply is not sufficient (see figure 4.5). On the other hand, if the catalyst layer is too dry, the oxygen gas arrives easily to the reaction sites, but protons are blocked to reach this platinum reaction sites. Modelling and experimental results under temperature, current and humidification transients are obtained. One important conclusion about the humidification conditions is the need of obtained air inlet humidification in order to obtain stable operating points. The humidity of electrode/catalyst layer is very important for a proper gas and proton transport. It has been observed that there is a strong correlation between the membrane resistance and the voltage losses.

In the article of Gebregergis *et al.* [2010], flooding and drying faults are detected from the cell voltage and the impedance response of the cell. The flooding and drying processes are forced by the difference of the temperatures of the fuel cell and the gas inlet humidification (for both reactants, H_2/O_2) during a long time (more than 120 minutes each process, see figure 4.6). To create flooding in the cell, the humidifier temperature is maintained at about 40 °C or higher than the cell temperature. Drying process is forced by keeping the cell temperature at about 40 °C or higher than the humidifier one. At the same time as these process occurs, several EIS tests are done. Some of the results are presented in figure 4.7, with a comparison of the healthy, the flooded and the dried cell response is presented. The impedance response at low frequency is used to identify the cause of the fault. The slope of the magnitude and the negative phase response of the cell impedance at low frequency is observed to allow separation of fault. A cell impedance model based on resistive capacitive

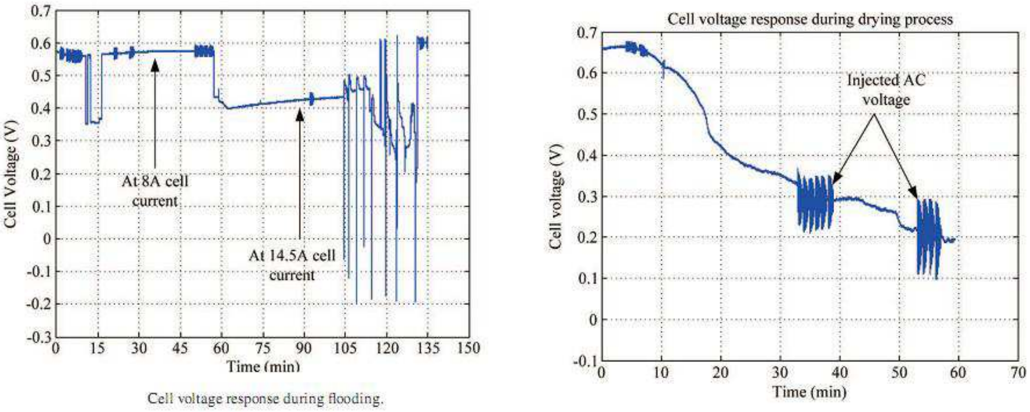

(a) Flooding procedure

(b) Drying procedure

Figure 4.6: Cell voltage during flooding and drying processes (see reference Gebregergis *et al.* [2010])

(C model) and resistive constant-phase-element (CPE model) circuits is developed. CPE model provides better adjustment, but C model is easy to implement since it is well known in most simulation tools. Also, a *cascade Boost-Buck* power converter circuit is designed (and experimentally tested) in order to mitigate the drying fault. The performance of the fuel cell is improved making pulses of the cell current to higher values (water generation is higher). The *Boost* converter controls the fuel cell operating point (inserting the current pulses) and the *Buck* converter ensures the constant power to the output.

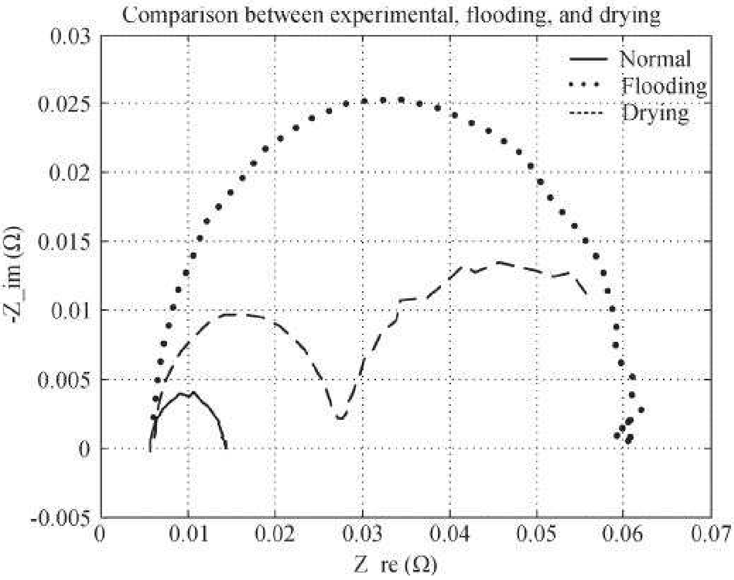

Figure 4.7: EIS response of flooding and drying processes (see reference Gebregergis *et al.* [2010])

Another important article is presented by Fouquet *et al.* [2006], with the monitoring of the flooding and drying out PEM Fuel Cell using a model-based approach coupled with AC impedance measurements (EIS) as a function of the inlet gas relative humidity . The temporal evolution of drying and flooding processes is presented in figure 4.8(a). The parameters of a Randles-like equivalent circuit are then fitted to the data. In order to improve the quality of the fit, the classical Randles cell is extended by changing the standard plane capacitor into a constant phase element (CPE).

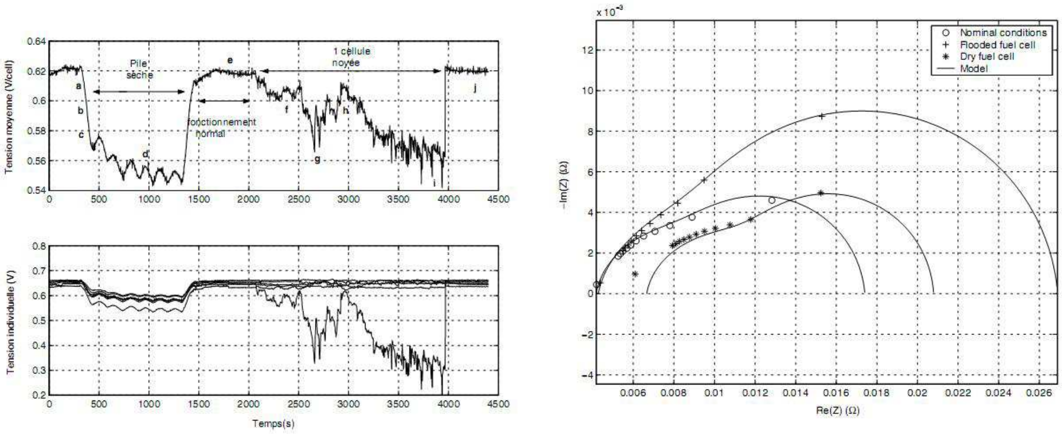

(a) Voltage evolution

(b) EIS comparison

Figure 4.8: Drying and flooding process (see reference Fouquet *et al.* [2006])

It is found that monitoring the evolution of the three resistances of this modified Randles model is an efficient and robust way of monitoring the state-of-health (SOH) of the fuel cell with respect to the water content of the membrane electrode assembly. A Qualitative interpretation of the variation of the parameters as a function of the SOH is proposed in both flooded and dry conditions.

4.2.1 Objectives

As is seen in the state of the art analysis, the water management is one of the main issues in the fuel cell operation. The performance of the polymer electrolyte membrane fuel cell is significantly affected by the liquid water presence along the channels, the GDL and in the cathode catalyst layer. Liquid water generated by the reaction or coming from an external system (humidifier) potentially causes *flooding* in the cathode catalyst layer and reduces the availability of platinum reaction sites for oxygen particles coming from air. Also, the reduction of water presence in the system, can cause the *drying* of the membrane electrode assembly and the loss of reaction sites due to absence of water needed by the protons reaching path to the reaction zone.

Even that there are models related with water presence in the fuel cell, the results are not fully validated experimentally. On the other hand, there are some experimental setups specially designed to investigate the water distribution and implies a construction of dedicated and special equipment. This fact is a disadvantage if the technique is intended to be used as "in-situ" technique. Finally, there are also interesting experimental tests, where the *flooding* and *drying* process are forced by the difference of the temperatures of the humidifier and the cell (Gebregergis *et al.* [2010] and Fouquet *et al.* [2006]). One of the main problems of these techniques is the long time needed to force the system to those situations (due to a large time constant of the temperature process). Another issue is the deterioration over the cell response and the unknown consequence of this extreme situations (keeping flooding or drying, arises in voltage unstable situations) in the physical components. These two problems denote a high intrusion to the cell operation, causing problems if it is used as "in-situ" technique.

Then, as a result of this state of the art study, in this chapter is proposed a new experimental technique that combines the results of a standard characterisation technique (EIS) with the water influence over response. This technique should be a less invasive as possible, simple to apply and studied to be applied as "in-situ" technique.

The main objectives of this chapter is :

- Propose a simple test that shows the state of the fuel cell related to water influence.
- Analyse the temporal and frequency response to propose new possible performance indicators.
- Obtain information from EIS, specially with fast and short tests.
- Study the advantages and disadvantages for an in-Situ application.

4.3 Characterisation technique based on humidification interruption

In this section, a characterisation technique based on the humidification interruption of one of the reactants is presented. In the first subsection the anode humidification influence is presented, the second subsection details the experimental set-up description of the humidification interruption test, the third sub-section shows the temporal evolution comparison of the humidification interruption responses, and finally an impedance response comparison is done.

Why is used Humidification Interruption as Characterisation technique?

The PEMFC system needs water to work with a reasonable performance. Therefore, there is saturated water vapour entering with the reactants at both sides of the cell, water creation at the cathode side due to reaction and water coming from proton flow transport from the anode side. Also, there is back diffusion from cathode to anode trough the membrane.

It is very intuitive that there is a lot of water at the cathode catalyst layer, where the reaction is generating water continuously and there is also water coming from the GDL and membrane transport. Also, under normal conditions the water is in vapour form, but it is possible that some of the water condenses and forms a liquid barrier, causing flooding in the catalyst layer and blocking platinum (Pt) reaction sites to the Oxygen.

Then, the characterisation technique proposed is done avoiding one of the inlet gas to pass through the humidifier and recording the time response and applying at the same time a set of short EIS in order to have dynamical information during the interruption.

4.3.1 First experimental reference: Anode humidifier influence

This experimental test is done with the objective to study the fuel cell response when the Anode humidifier is re-connected after the fuel cell is working a certain time without it. In the table 4.1, the initial operating conditions are showed.

Table 4.1: Starting operating conditions of anode humification test

	$\mathbf{T}_{Ca,hum}$[^{o}**C**]	$\mathbf{T}_{Ca,LH}$[^{o}**C**]	$\mathbf{P}_{Ca}$[**bar**$_a$]	Φ_{cath}[**slpm**]
Cath. (Air)	60	85	1.01	1.0
	$\mathbf{T}_{An,hum}$[^{o}**C**]	$\mathbf{T}_{An,LH}$[^{o}**C**]	$\mathbf{P}_{An}$[**bar**$_a$]	Φ_{an}[**slpm**]
Anode (H$_2$)	OFF	OFF	1.01	0.03
	$\mathbf{T}_{FC}$[^{o}**C**]	I_{FC} [A]		
Cell	60	0.6		

In figure 4.9, the fuel cell system response is showed. In the first part, the system starts with the anode humidifier disconnected, and a series of EIS at this working situation are done. Then, some changes in the cathode humidifier and in the fuel cell temperature are done. In the last part of the test, the anode humidifier is connected, working at ambient temperature and maintaining the cathode humidifier temperature at 60 [^{o}C], the same as the fuel cell temperature. In table 4.2, the EIS operating situation and conditions are summarized. The used values for EIS test are: f_{start}=0.1 [Hz], f_{stop}=10 [kHz],
I_{FC}=0.6 [A], 51 points, $\Delta I_{FC,p-p}$= 5 [%].

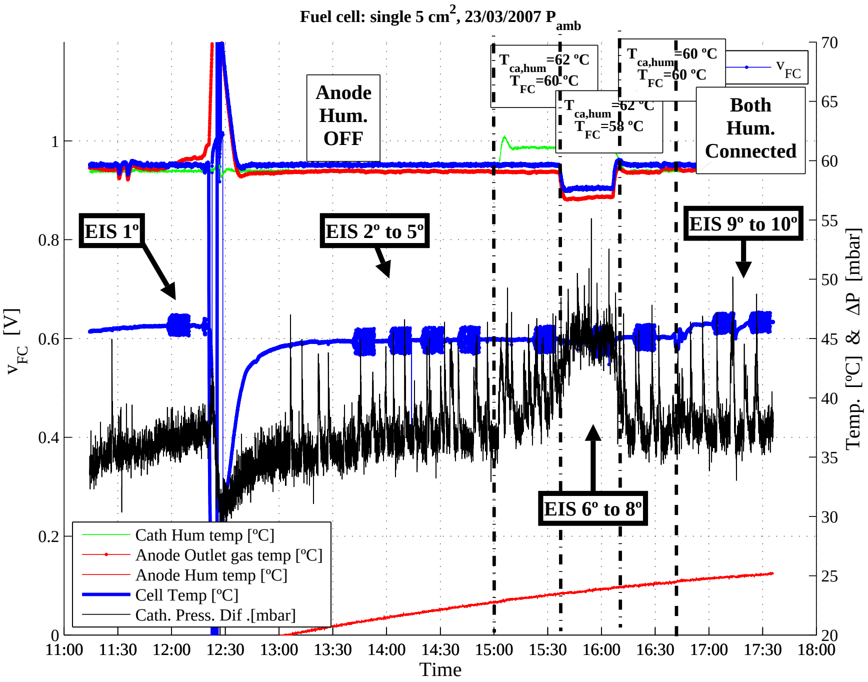

Figure 4.9: Anode humidifier connection time evolution

Table 4.2: EIS conditions of anode humidification test

EIS	T_{FC} **[°C]**	$T_{an,hum}$ **[°C]**	$T_{ca,hum}$ **[°C]**	**Comments**
1	60	OFF	60	Anode Humidifier OFF
2	60	OFF	60	Anode Humidifier OFF
3	60	OFF	60	Anode Humidifier OFF
4	60	OFF	60	Anode Humidifier OFF
5	60	OFF	60	Anode Humidifier OFF
6	60	OFF	62	Anode Humidifier OFF
7	58	OFF	62	Anode Humidifier OFF
] 8	60	OFF	60	Anode Humidifier OFF
9	60	26.5	60	Anode Humidifier ON
10	60	26.5	60	Anode Humidifier ON

In figure 4.10, the EIS responses of the fuel cell system are showed. The high frequency part is zoomed and showed in the right part of the figure.

The difference between the first and the second EIS is noticeable: high and low frequency resistance grows, making visible a degradation of the response due to the anode humidification bypass.

Then, on the sixth EIS, the cathode humidifier temperature is increased from 60 [°C] to 62 [°C], the high frequency resistance reduces its value but the low frequency resistance maintains similar values.

On the seventh EIS, the fuel cell temperature is decreased to 58 [°C], and the distance between fuel cell temperature and cathode humidifier is higher, with a higher water presence on the cathode side. But, at this point, probably a condensation of water in the cathode channels occurs. This effect can be reflected in the low frequency resistance, that increases its value.

Then, in the eighth EIS, where the temperatures of cathode humidifier and fuel cell have the same value, 60 °C, a recovery of the low and the high frequency resistances is observed.

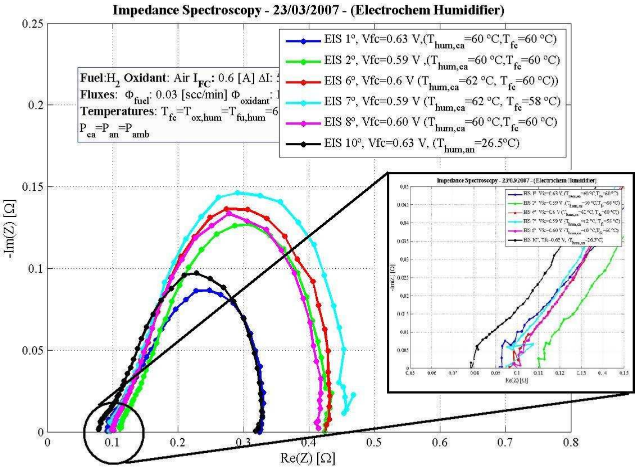

Figure 4.10: EIS response of anode humidification influence

In the last EIS, the connection of the anode humidifier is done, where the anode humidifier has ambient temperature. The low and high frequency resistances reduce its values, showing the influence of anode humidification on the fuel cell response.

The final **conclusion** is: the fuel cell system can be operated without anode humidifier, but the cell systems works better with both humidifiers connected.

4.3.2 Experimental set-up description for humidification interruption

In this section, the experimental set-up and a description of the humidification interruption is done.

To study the fuel cell response with EIS technique, different operating conditions are imposed to the fuel cell: current, temperature, pressure and relative humidity conditions. All tests are performed over the single fuel cell described in chapter 2.

In figure 4.11 a simplified scheme of the experimental set-up used to obtain the cell response is presented. The test station includes two reactant (anode and cathode) gas subsystems. Each subsystem contains: a mass flow controller, a membrane based humidification system with dew point sensors for control, inlet line heater to prevent condensation, absolute pressure transducer at the inlet, differential pressure transducer between the inlet and outlet of each reactant, and a back pressure regulator at the outlet of the fuel cell to control the system pressure. Each mass flow controller is calibrated for a specific gas (Hydrogen for the anode and synthetic air/Oxygen for the cathode).

There are also temperature readings in the fuel cell inlet and outlet gas channels, humidifiers and line heaters. These measurements are done using “K” Type thermal couples. Temperatures of the fuel cell, humidifiers and line heaters are controlled by Proportional Integral Derivative (PID) controllers. The cooling of the cell is attained by natural convection.

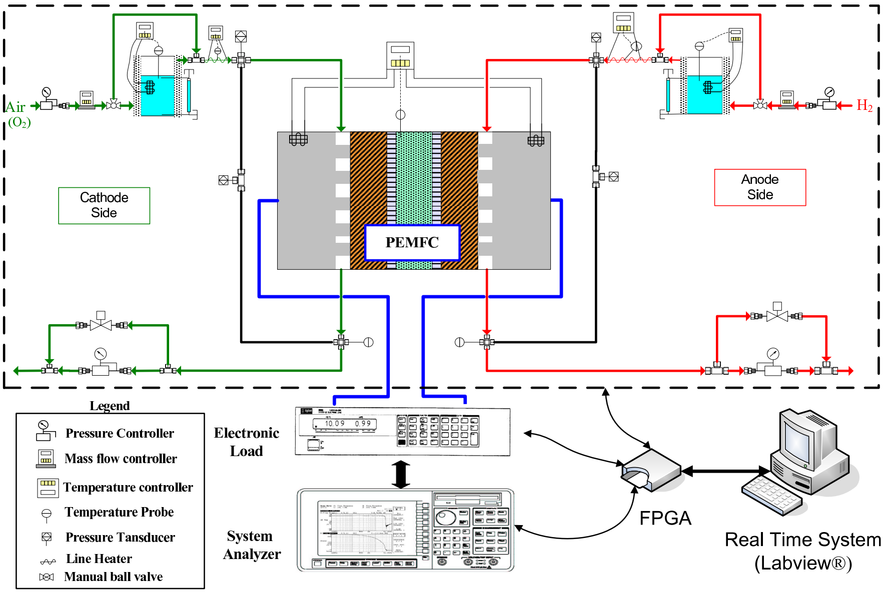

Figure 4.11: Experimental set-up description

All the measurements and the control are made in real time by means of a LabView® control system. Electrochemical Impedance Spectroscopy experiments are done controlling the imposed operating current with an electronic load (TDI®) and a system analyser (HP®).

4.3.2.1 Humidification interruption test details

The experimental set-up allows the interruption of the humidification system on both sides (cathode and anode) with a parallel connection of gas and a two ways valve. When the valve is positioned to the humidifier side, the gas pass trough the humidifier and goes to the fuel cell, when the valve is positioned to the other way, the gas by-passes the humidification and is fed to the line heater connection and then enters to fuel cell (see figure 4.12).

At the same time the humidification interruption occurs, a set of EIS is done. The interest of these EIS is the study of frequency evolution response when the humidification is interrupted. Since the EIS technique is a stationary response technique, a reduction of the time required to do the EIS is proposed in order to obtain "pseudo-stationary response" (reducing the number of frequencies, the average and settling). See appendix 3 "Humidification Interruption Results" for more details in frequency description.

The *humidification interruption technique* is summarised as follows:

1. During all the test the time evolution of the variables depicted in figure 4.11 is recorded
2. Before starting the humidification interruptions: a "Complete EIS" is performed, with the following specifications: 51 frequency points, range f:0.1[Hz]→10[kHz]
3. The humidification interruption starts
4. Several "Reduced" EIS are performed, with the following specifications: 21 frequency points, range f:0.2[Hz]→10[kHz]. Various "reduced" EIS are done during humidifier interruption. Those short EIS have approximately 12 seconds of duration

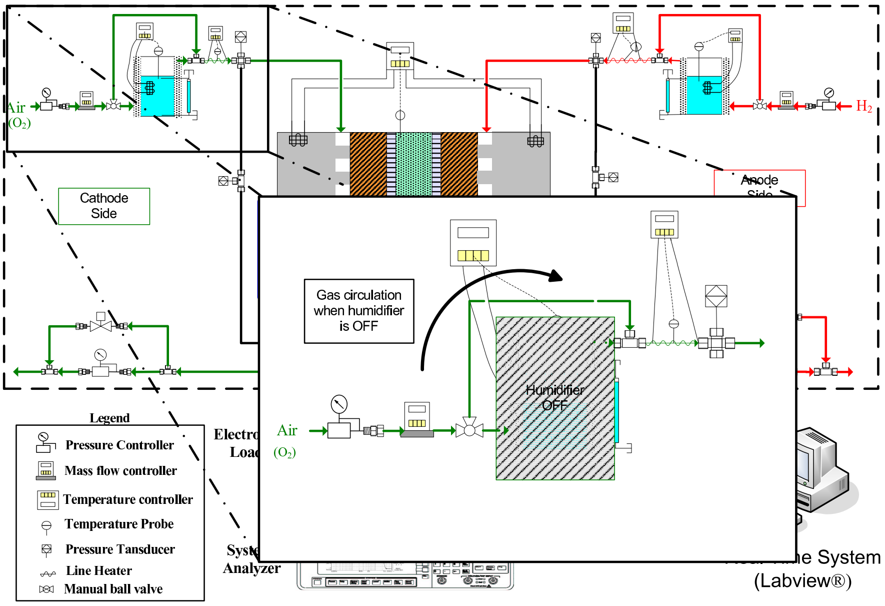

Figure 4.12: Humidification Interruption description

5. The humidifier is reconnected

6. “Reduced” EIS are performed, with the following specifications: 21 frequency points, range f:0.2[Hz]→10[kHz].These EIS are done after humidifier is reconnected in order to study the recovery of water response

7. After the system reaches the new steady state, a “Complete EIS” is done, with the following specifications: 51 frequency points, range f:0.1[Hz]→10[kHz]

4.4 Experimental results of the humidification interruption

In order to apply this characterization technique to the single fuel cell under different working situations, a “testing day” is carried on (see time evolution in figure 4.13) in order to observe the experimental results obtained.

Nominal operating conditions are: fuel cell temperature, $T_{FC} = 40$ [°C], current, $I_{FC} = 1[A]$, pressure at both sides, $P_{FC} = P_{amb}$, humidification of both sides, $RH = 100[\%]$, more details are given in table 4.3.

Table 4.3: Operating conditions of the first test day

	$\mathbf{T}_{ca,hum}[^{o}\mathbf{C}]$	$\mathbf{T}_{ca,LH}[^{o}\mathbf{C}]$	$\mathbf{P}_{ca}[\mathbf{bar}_a]$	$\Phi_{cath}[\mathbf{slpm}]$
Cath. (Air)	39.5	50	1	0.824
	$\mathbf{T}_{An,hum}[^{o}\mathbf{C}]$	$\mathbf{T}_{An,LH}[^{o}\mathbf{C}]$	$\mathbf{P}_{An}[\mathbf{bar}_a]$	$\Phi_{an}[\mathbf{slpm}]$
Anode ($\mathbf{H_2}$)	39.5	50	1	0.324
	$\mathbf{T}_{FC}[^{o}\mathbf{C}]$			
Cell	41.5			

In the first part, the stabilisation of voltage can be observed (first zone of time evolution). In the figure 4.13, the humidifiers are *both connected* (marked as **BC**).

After this part, a *Cathode humidification interruption* is tested (second zone of time evolution, named as **Cath. Hum. OFF**); details of this temporal and EIS evolution are showed in the next section. Later, the cathode humidifier is reconnected and the recovery of the system can be observed (third zone of time evolution, marked again as **BC**).

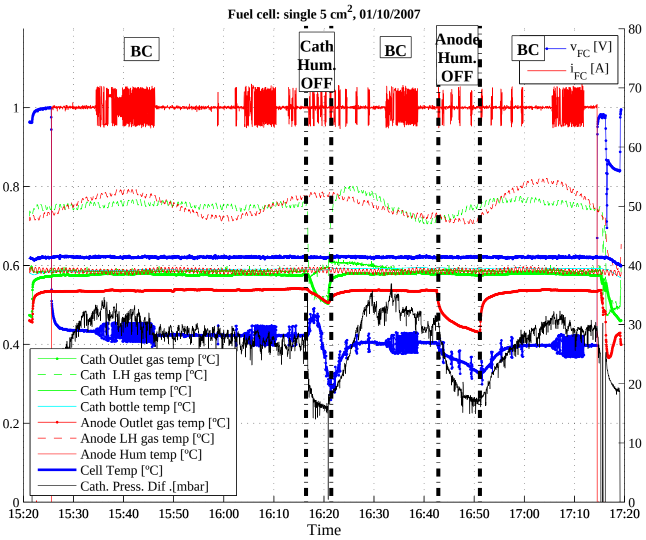

Figure 4.13: Time evolution of “test day” of Humidification Interruption

Next, *Anode humidification interruption* is done (fourth zone of the time evolution, marked as **Anode Hum. OFF**), this part is longer than the cathode humidifier interruption and shows that the influence of both humidifications are very different. Finally, after the system is stabilised, the last part of test day is performed (fifth part, marked as **BC**).

At the end of the test day, a long EIS was done in order to have another reference of the evolution along the day.

4.4.1 Cathode Humidification Interruption

In the first part of the test day, a **Cathode humidification interruption** is performed.

In figure 4.14, the time evolution details are showed. In this response, the cathode differential pressure has a decreasing trend starting when the humidifier is bypassed. This fact can be explained by the lower water content in the channel, quickly removed by air mass flow circulating without presence of water vapour.

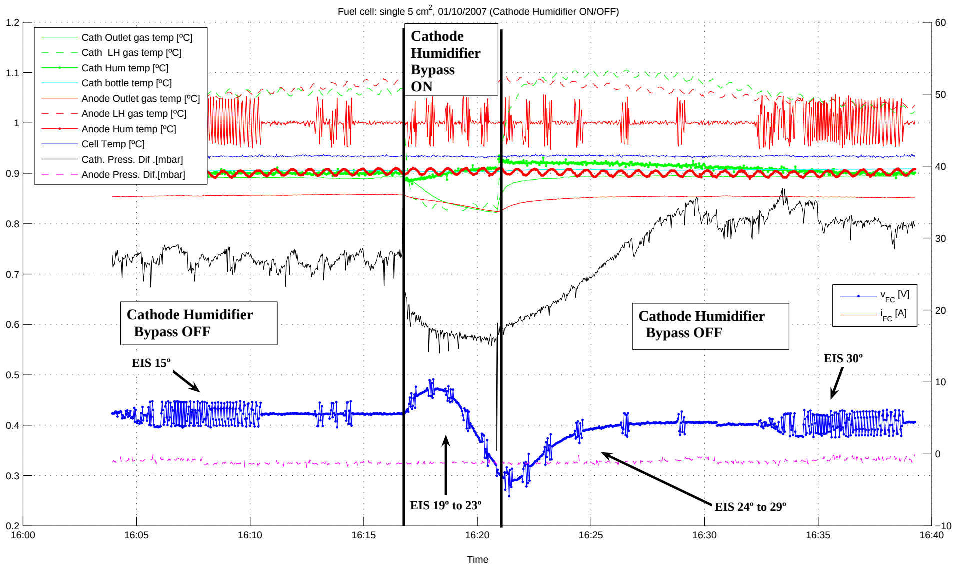

Figure 4.14: Cathode Humidification Interruption, time evolution

Also, the cathode and anode temperatures are decaying in this first part of the test. Both temperatures reflect the influence of the water presence reduction. On the cathode side, the water is moving out from the channel due to a strong and dry air flow. The cathode outlet temperature reduces its value due to absence of the heated water vapour when the humidifier is by-passed. On the other hand, in the anode side, the water is moving to cathode side (due to water concentration difference). This water flow to other side, makes also the anode outlet temperature to reduce its value.

Special attention must be given to the voltage evolution, where two different trends can be seen when the *cathode humidification is turned off*. First, an increase of the voltage occurs, caused by two main effects:

- Oxygen partial pressure increases its value due to absence of water mass flow introduced by the humidifier. As a consequence, oxygen concentration increases at the channel and also at the catalyst layer (Fick's law).
- Excess of water (in liquid or vapour form) is removed and evaporated (in case of liquid)

and Oxygen diffusion from channel to the reaction sites improves and the voltage reflects this increment.

Second, a fast falling of the voltage occurs, where again there are two main effects that cause this fall:

- Membrane water content reduces its value due to water passing from anode to cathode side, where the water concentration is low. This effect causes and increases the membrane resistance.
- There is also an active area reduction due to a loss of catalyst reaction sites. Once the water is moving out the membrane, there are unreachable platinum points for protons, due to absence of a water path for them.

After this last decay, humidification is reconnected because voltage levels are reaching unsafety values (in our case, $V_{FC,limit}$=0.2 [V]) and a possible "Short circuit" should be avoided (decreasing voltage to zero in order to keep desired current).

When the *cathode humidifier is reconnected*, the system evolution is dominated by the cathode humidification recovery that returns the system to the initial level of water vapour.

Important conclusion:

It is very clear that the ***cathode humidifier*** *is fundamental for proper operation and that the single fuel cell* ***cannot*** *work without humidification on the cathode side.*

The Nyquist plots obtained during "humidifier OFF" and "humidifier ON" are presented in figure 4.15.

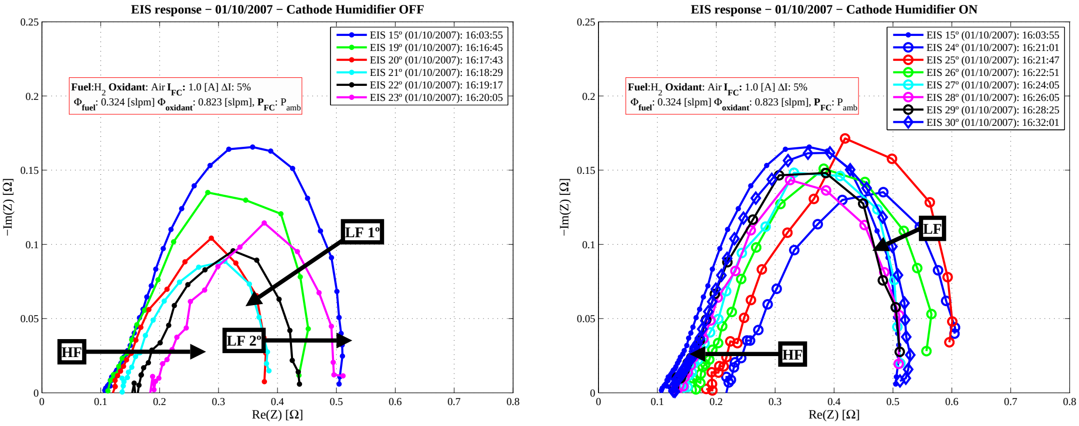

(a) Humidifier OFF

(b) Humidifier ON

Figure 4.15: EIS of Cathode humidifier ON-OFF-ON sequence,T_{FC}=40 °C, P_{FC}=P_{amb}, 1st. test

The Nyquist graphs show that the evolution of voltage is accompanied by remarkable changes in the Nyquist low and high frequency impedance evolutions. As can be seen in figure 4.15(a), the low frequency resistance has two different evolutions (denoted as "LF 1°" and "LF 2°"). In the first seconds (corresponding to EIS 19° to 21°), an increasing oxygen partial pressure and diffusion improvement reflect as decreasing values of the low frequency impedances, while the high frequency resistance does not change significantly. In the later moments (from EIS 21° to 23°) both low and high frequency resistances increase at the same time due to concurrent effects: membrane drying and active area reduction.

Once the cathode humidification is reconnected, the recovery part shows that low and high frequencies have the same trend, reducing its values and tending to values close to the starting values, (EIS 25°) as can be seen in figure 4.15(b).

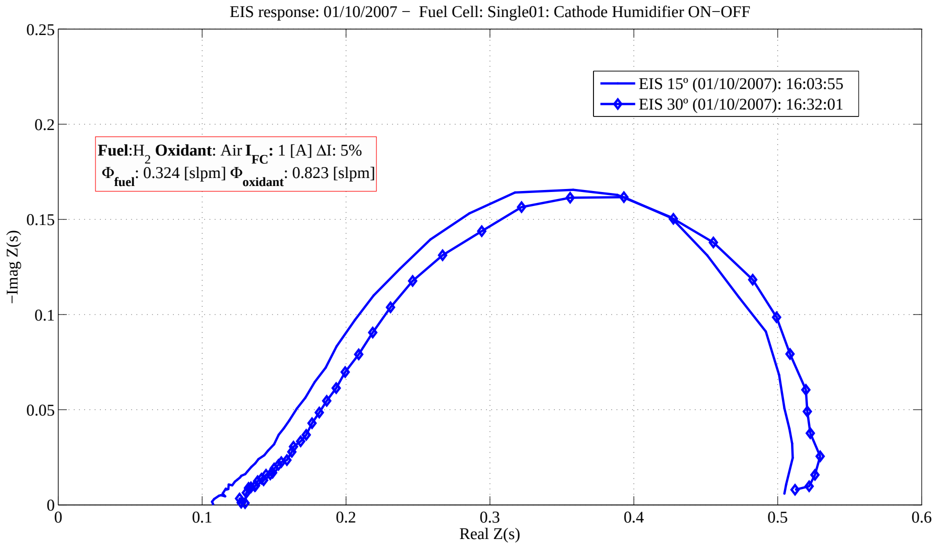

Figure 4.16: Comparison of "complete" EIS, before (15°) and after (30°) cathode humidifier ON-OFF

In figure 4.16, the comparison between "complete" EIS made before and after the anode humidification interruption is presented. The results show a good matching between both responses, remarking the fact that it is possible to recover a similar state after the humidification interruption.

In order to complete the results of the cathode humidification interruption, the time evolution of some *relevant characteristics* are presented in figure 4.17, where the described trends in the Nyquist plot are reflected in the low (R_{LF}) and the high frequency (R_{HF}) resistances. Also, the frequency of the *low frequency maximum* ($f_{Im_{max,LF}}$), has the evolution related with diffusion process (as it is described in the section "Equivalent Circuit" of chapter 3), indicating that the diffusion improves in zone 1° and is stable in zone 2°, where the membrane resistance suffers a drying effect.

On the other hand, the *low frequency maximum phase* ($\Phi_{\phi_{max,LF}}$), follows a similar trend, while in the first part of evolution increase its value (related with diffusion process improvement) and in the second zone of evolution (LF 2°) maintains its value. These effects can be related to diffusion influence, giving better results in the first zone and a stabilisation at the second zone, where the drying of the membrane does not affect the diffusion.

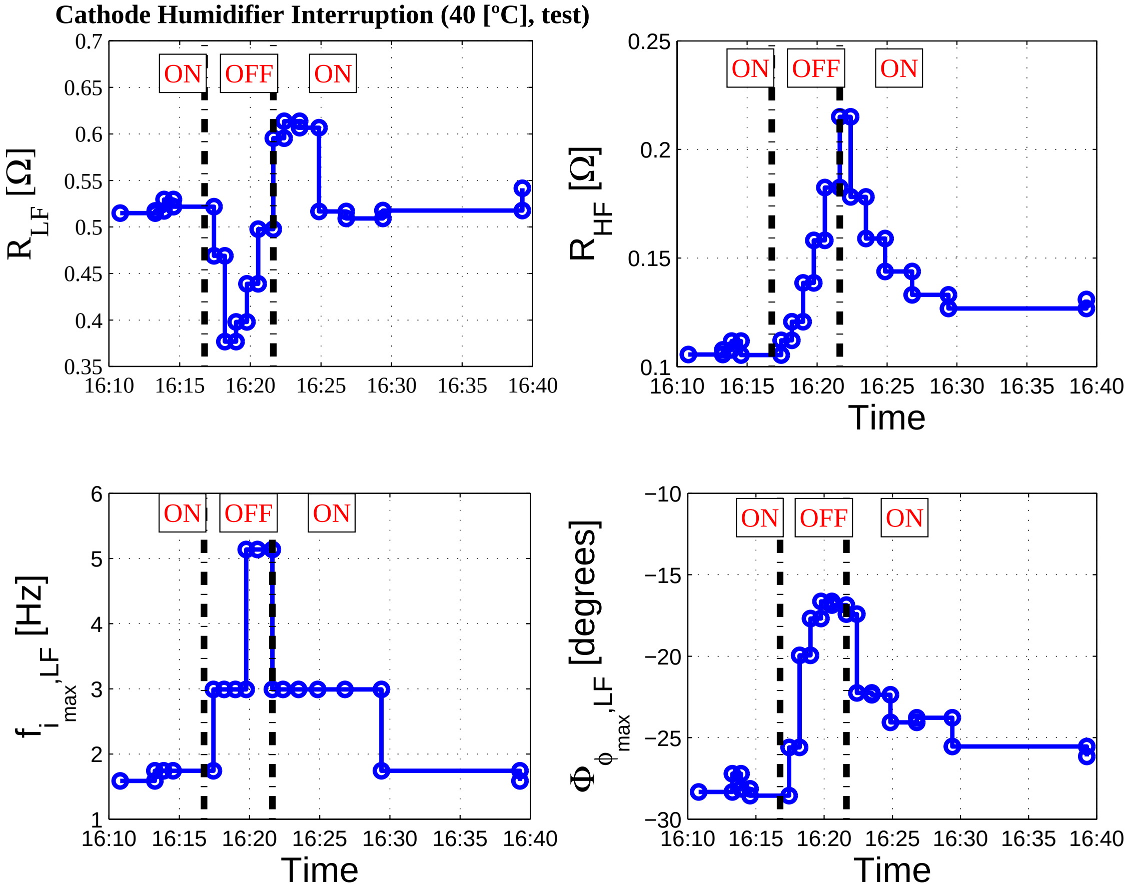

Figure 4.17: Relevant characteristics during the cathode humidification interruption

4.4.2 Anode Humidification Interruption

The *Anode humidification interruption* is showed in figure 4.18, which corresponds to she second part of the test day. In this case, the anode humidification is interrupted and the three stages of evolution are showed: anode humidification ON, where the EIS 30° is performed; the humidification is interrupted, OFF, where the "reduced" EIS 31° to 35° are done, and then the humidifier is re-connected, ON, where the "reduced" EIS 36° to 40° are done. Finally, when the system is in steady state the "complete" EIS 41° is performed.

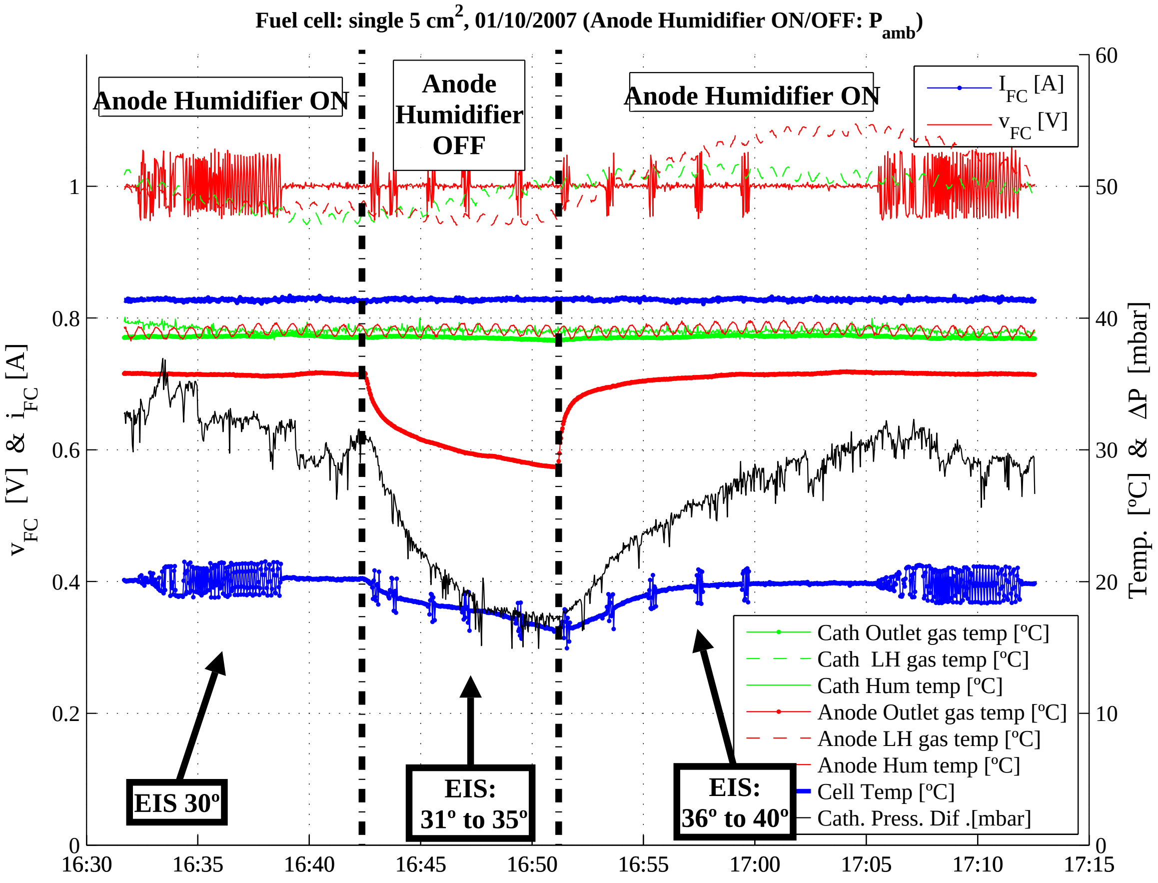

Figure 4.18: Anode Humidification Interruption, time evolution

Studying the time response, it is seen that the cathode differential pressure has a decreasing trend starting when the anode humidifier is bypassed. In this case, the water concentration differential makes that water from the cathode side moves to the membrane/anode side and reduces its presence in the cathode channel, giving this cathode differential pressure a reducing trend. Also, the cathode and the anode temperatures have lower values. In this case, the cathode outlet temperature has a lower reduction than in the cathode humidifier interruption situation. On the other hand, in the anode side, the water content reduces quickly due to the anode humidifier bypass and a consequent dry hydrogen mass flow circulation.

When *anode humidification is off*, the voltage diminishes its value at a lower rate than in the cathode humidification interruption case. It seems, confirming the precedent case presented in section 4.3.1, that if the anode humidification is closed, the fuel cell still can work, but at a lower performance.

The Nyquist plots evolution at “humidification OFF” and “humidification ON” situations are presented in figure 4.19.

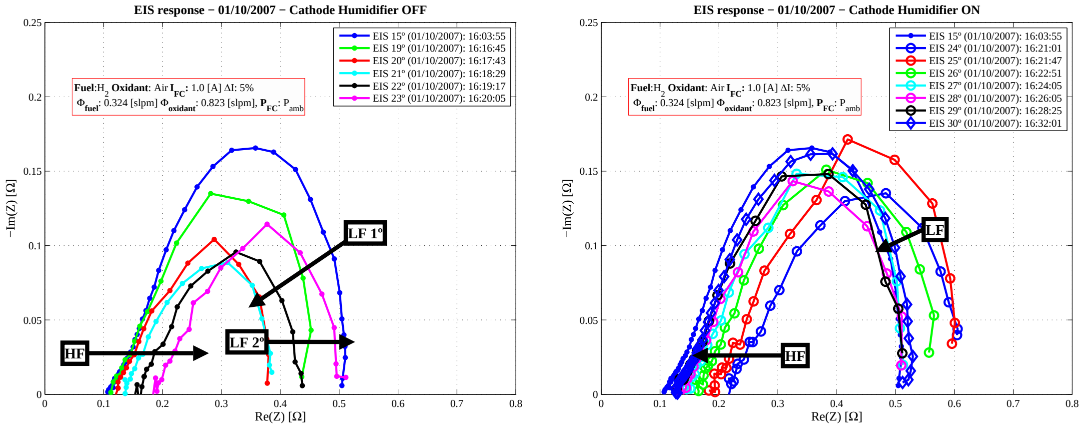

(a) Humidifier OFF

(b) Humidifier ON

Figure 4.19: EIS response of Anode humidification interruption,T_{FC}=40 °C, P_{FC}=P_{amb}

The Nyquist responses show the increment of low and high frequency resistances when the anode humidification is interrupted, see figure 4.19(a). It is important to note that the low frequency resistance grows more than the high frequency resistance. After the humidification is re-connected, both resistances have the opposite behaviour 4.19(b), tending to the values measured before the interruption.

In figure 4.20, the comparison between “complete” EIS performed before and after the anode humidification interruption is presented. The results show a good matching between both responses, indicating that it is also possible to recover a similar state after the anode humidification interruption.

The time evolution of some of the *relevant characteristics*, obtained from the results of anode humidification interruption, are presented in figure 4.21, where the described trends in the Nyquist diagram are reflected in the low and the high frequency resistances. That is, both have an increasing trend after the anode humidification interruption occurs. The frequency of the *low frequency maximum* ($f_{Im_{max,LF}}$), has a steady state value before and after the anode humidification interruption. This effect shows that the main contribution of the diffusion occurs at the cathode side.

The *low frequency maximum phase* ($\Phi_{\phi_{max,LF}}$), has a similar value before and after the interruption, confirming that the anode humidification interruption process does not affect the characteristics related with the diffusion effects.

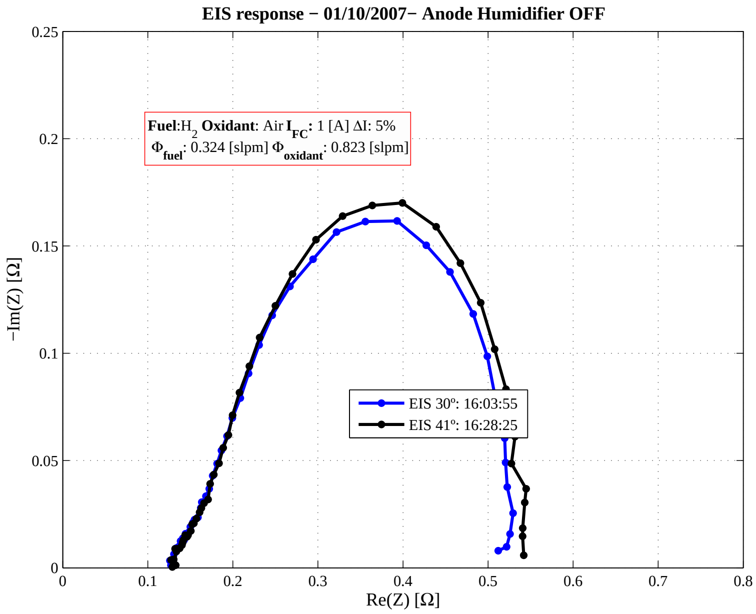

Figure 4.20: Comparison of "complete" EIS before (30°) and after (41°) anode humidification interruption

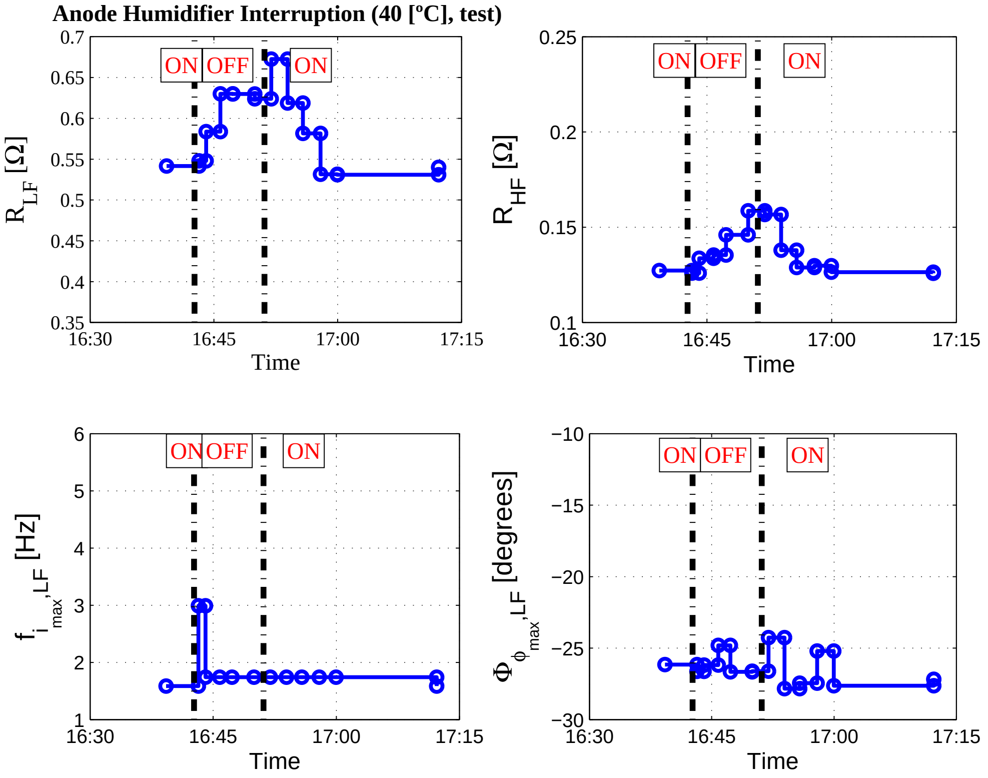

Figure 4.21: Relevant characteristics of Anode humidification interruption, 1° test

4.4.3 Comparison of the relevant characteristics: anode vs. cathode

Comparison of the relevant characteristics between anode and cathode humidification interruption responses is done in figure 4.22. In this comparison, the relevant characteristics are presented with the number of the EIS reference instead of the time evolution.

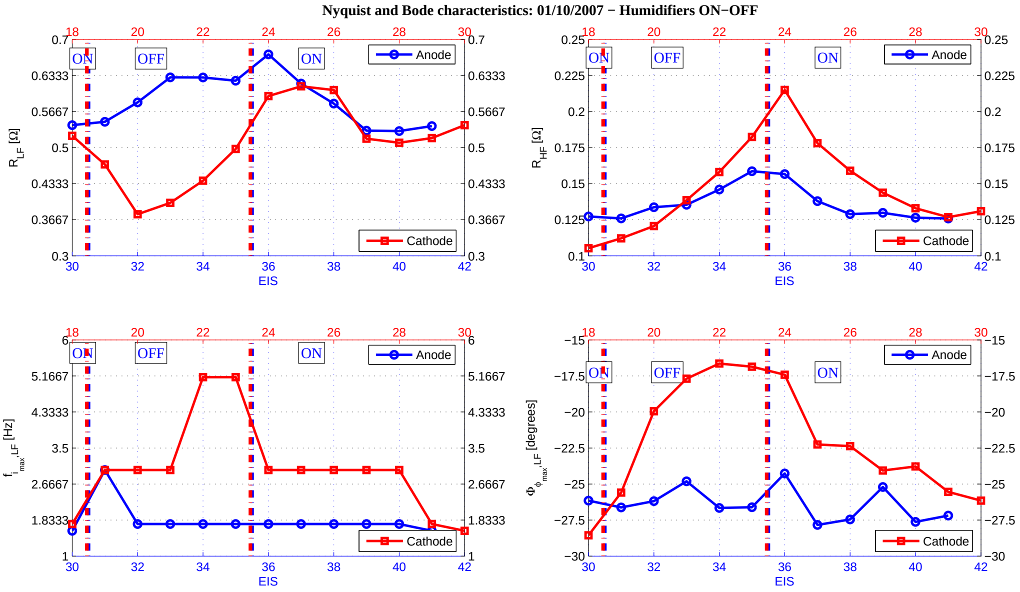

Figure 4.22: Relevant characteristics of humidifications ON-OFF

This figure is very useful to see the influence of both interruptions on the relevant characteristics. The first conclusion is that the *starting and finishing* points of all relevant characteristics are very similar. This indicates that the cell can be returned to a normal operation without important changes of the characteristics after the humidification interruption. Another important conclusion is the notabile influence of cathode humidification interruption, on both resistances (low and high frequency).

The main differences between anode and cathode humidification interruption responses are in the *low frequency* response. In the anode case, the low frequency resistance increases (R_{LF}) its value slowly and seems to tend to a steady state point. When cathode humidification is bypassed, the low frequency resistance falls, indicating an improvement of the conditions for oxygen diffusion and the increment of oxygen concentration. This fact is also confirmed by the evolution of the other two presented characteristics: the frequency of the *low frequency maximum* ($f_{Im_{max,LF}}$) and the *low frequency maximum phase* ($\Phi_{\phi_{max,LF}}$). These two values have an increasing trend coincident with the low frequency resistance falling trend. But, after a while, the reduction of active area caused by the membrane drying effect (synchronous in time with the high frequency resistance increase) affects also the the low frequency resistance, increasing rapidly its value. At the same time, the frequency ($f_{Im_{max,LF}}$) and the phase ($\Phi_{\phi_{max,LF}}$) arrive to steady state values, indicating the stabilisation of the diffusion effects.

The high frequency resistance (R_{HF}) evolution shows that when the humidification (cathode or anode) are interrupted, the resistance grows. The difference between then is the velocity. When the anode humidification is off, the resistance increases slowly and tends to stabilize. On other hand, when the cathode humidification is interrupted, the resistance grows quickly and the evolution is not stabilized.

Finally, after the reconnection of the humidification system, the relevant characteristics return to similar values to the starting ones, in both situations.

4.4.3.1 Anode vs. cathode humidification interruption, 2nd day response

In order to check the results presented in the past section, a comparison of relevant characteristics of the anode and cathode humidification interruption is done again for a second day of test (see figure 4.23). This test is carried on with the same operating conditions as the first day, described in the table 4.3.

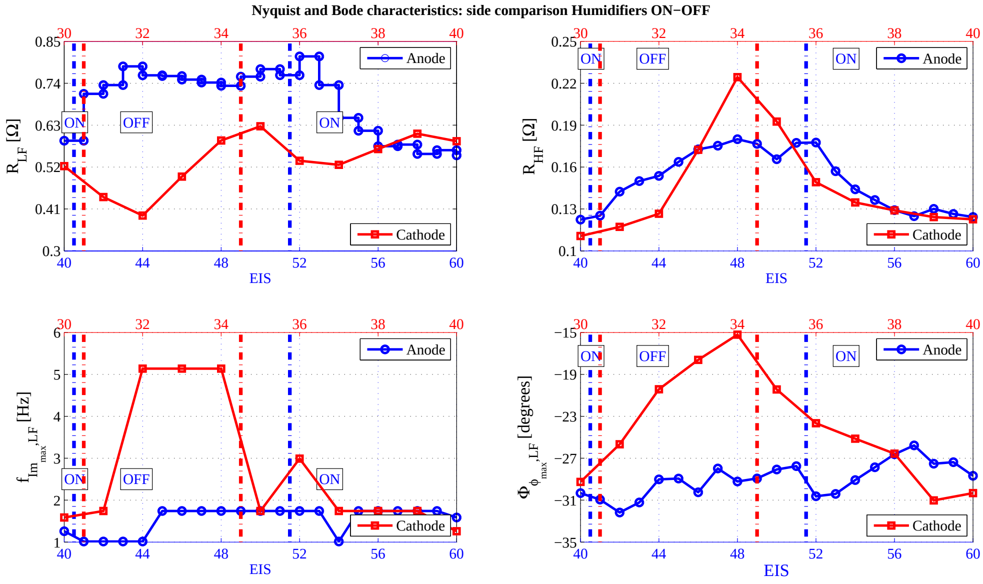

Figure 4.23: Relevant characteristics of cathode vs. anode humidification interruption (2nd. day)

In this case, the same trends seen in all relevant characteristics in the first test day (see figure 4.22) are confirmed.

As the response in the anode humidification interruption is longer in time and in the number of the EIS test, the conclusions are that the low frequency increases its value slowly to a steady state value (R_{LF}), the high frequency resistance also grows slowly and seems to be stabilized (R_{HF}). The frequency of the *low frequency maximum* ($f_{Im_{max,LF}}$) and the *low frequency maximum phase* ($\Phi_{\phi_{max,LF}}$) have similar values and confirms the conclusion about the lower influence of the anode humidification in the diffusion process.

In the cathode humidification interruption response all the evolutions described in the first test day are repeated in this second test day.

4.5 Humidification interruption under different conditions

In this section, a comparison of the humidification interruption responses under different experimental situations is done. All the experimental tests are performed with Air and H_2 as reactants and the main operating conditions are summarised in table 4.4.

Table 4.4: Operating conditions of the humidification interruption

Day	T_{FC} [°C]	N° EIS	Conditions
01/10/2007	40	40	Testing humidification interruption at I_{FC}=1[A]
02/10/2007	40	134	I_{FC}=0.5[A] and 1[A], P_{FC}=P_{amb} and 10 [PSIg]
03/10/2007	50	102	I_{FC}=0.5[A] and 1[A], P_{FC}=P_{amb} and 10 [PSIg]
04/10/2007	60	97	I_{FC}=0.5[A] and 1[A], P_{FC}=P_{amb} and 10 [PSIg]

All the time responses and frequency responses are presented in the appendix 3 “Humidification Interruption Results” and the relevant characteristics analysed in the next sections are summarized in the appendix 4 “Humidification interruption: relevant characteristics”. The comparison of the variables of interest includes:

- Current variations (cathode and anode, I_{FC}=0.5 [A] and 1.0 [A]).
- Pressure variations (cathode and anode, P_{FC}=P_{amb} and P_{amb}+10 [PSI]).
- Temperature variations (cathode and anode, T_{FC}=40 [°C], 50 [°C] and 60 [°C]).

In all cases, the comparison is done taking into account the temporal evolution of the most important variables, the Nyquist plots evolution during humidification OFF situation and the Nyquist plots evolution during the humidification ON. After this figures, comments about the responses and the comparison of the relevant characteristics are given.

4.5.1 Current variation: cathode humidification interruption

The *cathode* humidification interruption, with the same operating conditions apart from the nominal operating current which is changed from I_{FC}= 0.5 [A] to I_{FC}= 1.0 [A], is analysed in this section.

The nominal operating conditions of the experimental tests are: ambient pressure $P_{FC} = P_{amb}$, cell temperature T_{FC} = 50 [°C] and 100 [%] of relative humidity of the inlet gases (H_2/Air).

The evolution of the voltage is very similar in both situations (see figure 4.24(a) and 4.24(b)). Initially the voltage grows due to an improvement of the diffusion and the oxygen concentration increase at the channel and, after this, the voltage decreases due to the membrane drying effect and active area reduction due to unreachable platinum sites for hydrogen protons.

Anode and cathode outlet temperature decrease, indicating the reduction of water presence in both channels. The cathode differential pressure also reduces and confirms the trend. It is interesting that the values of this pressure difference are very similar for different current

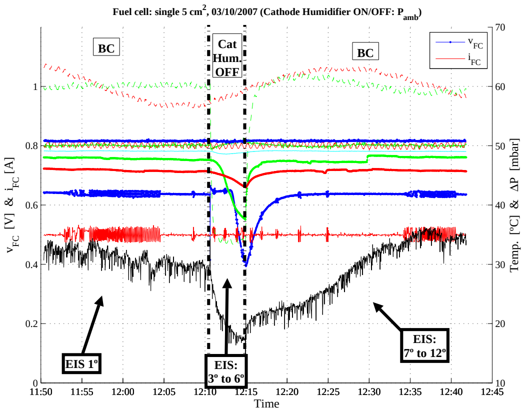

(a) I_{FC}=0.5 A　　(b) I_{FC}=1.0 A

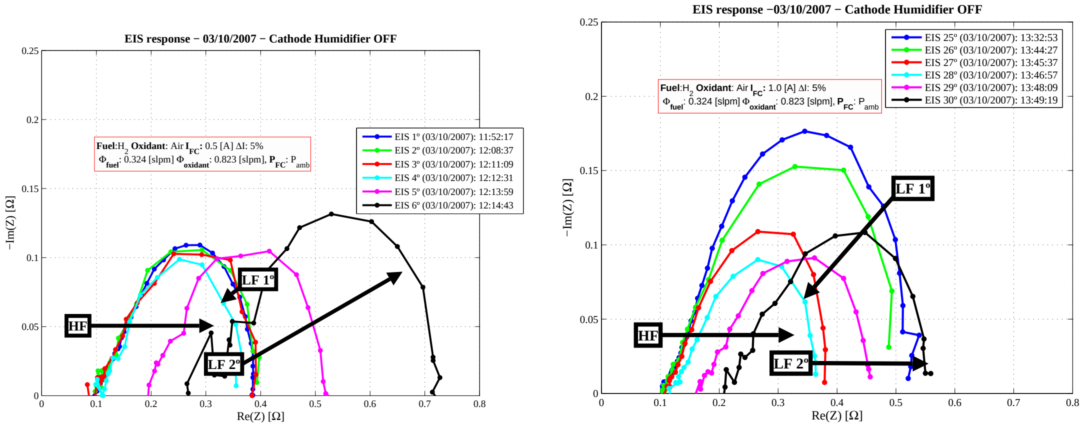

(c) Nyquist OFF, I_{FC}=0.5 A　　(d) Nyquist OFF, I_{FC}=1.0 A

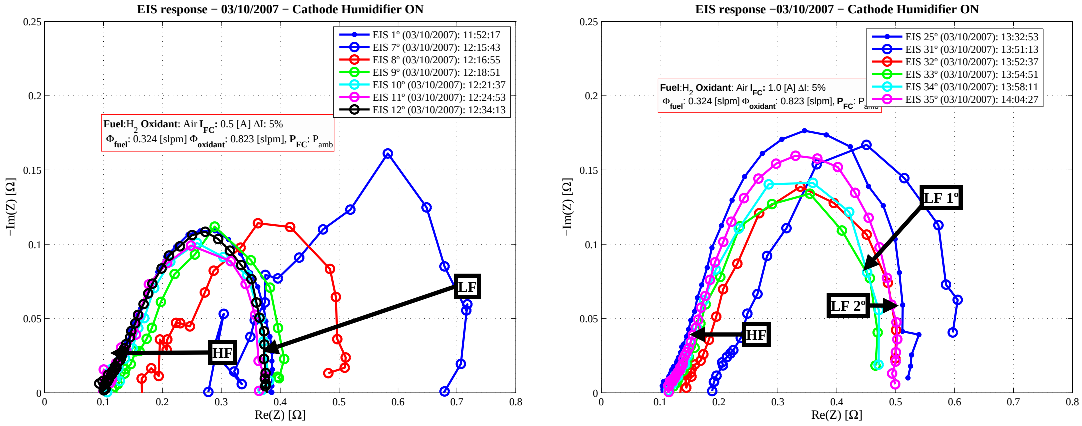

(e) Nyquist ON, I_{FC}=0.5 A　　(f) Nyquist ON, I_{FC}=1.0 A

Figure 4.24: Experimental responses of the nominal current comparison (cathode humidification interruption)

values. The rate of voltage reduction is higher at lower current. This indicates that the membrane drying effect influence on the active area reduction depends on the water generated by the reaction.

Comparison of the relevant characteristics

The relevant characteristics are presented on the same graph (figure 4.25) and are useful to indicate the difference between $I_{FC} = 0.5[A]$ and $I_{FC} = 1.0[A]$, for the cathode humidification interruption.

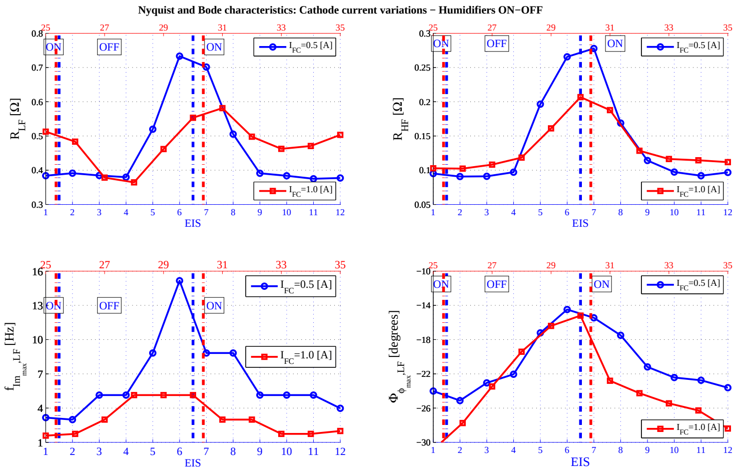

Figure 4.25: Relevant characteristics, current variation, cathode humidification interruption

Trends of both current are very similar and confirm the evolution of cathode humidification interruption presented in the figure 4.22.

When the operating nominal current is I_{FC}=0.5 [A], the starting values of the relevant characteristics are lower than with I_{FC}=1.0 [A], but the rates of the increase of the resistances values (R_{LF} and R_{HF}) and the low frequency maximum ($f_{Im_{max,LF}}$) are higher than in the other case (I_{FC}=1.0 [A]). The *low frequency maximum phase* ($\Phi_{\phi_{max,LF}}$) has a similar evolution in both cases.

4.5.2 Current variation: anode humidification interruption

In this subsection, the temporal and frequency responses of the anode humidification interruption at different nominal operating currents (I_{FC}= 0.5 [A] and I_{FC}= 1.0 [A]) are compared (figure 4.26).

The nominal operating conditions are: ambient pressure $P_{FC} = P_{amb}$, cell temperature $T_{FC} = 60$ [°C] and 100 % of relative humidity of the inlet gases (H_2/Air).

The evolution of the voltage in both situations indicates that the influence of the anode humidification interruption is similar at different currents (see figure 4.26(a) and 4.26(b)). The voltage falls in both situations, due to a membrane drying effect and to reduced transport of the hydrogen protons inside the membrane.

The anode outlet temperature shows a decreasing trend, an indication of the water reduction process at that side. The cathode outlet temperature has a small reduction trend,

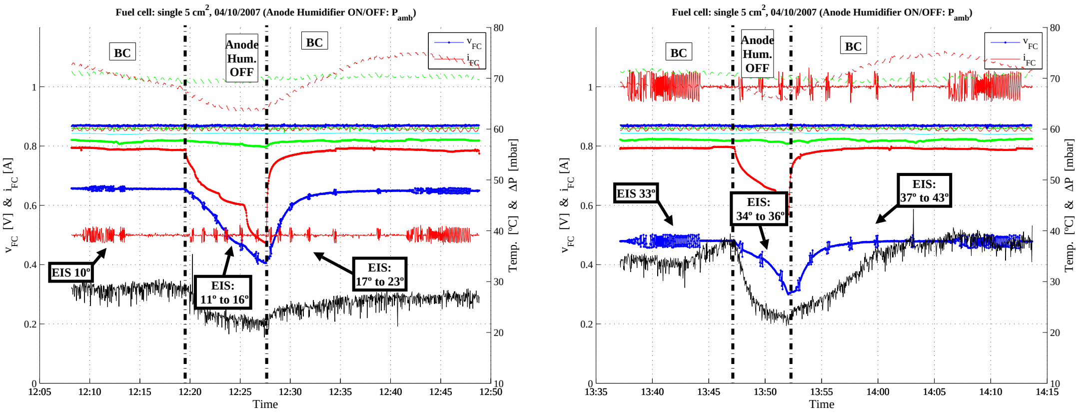

(a) I_{FC}=0.5 A (b) I_{FC}=1.0 A

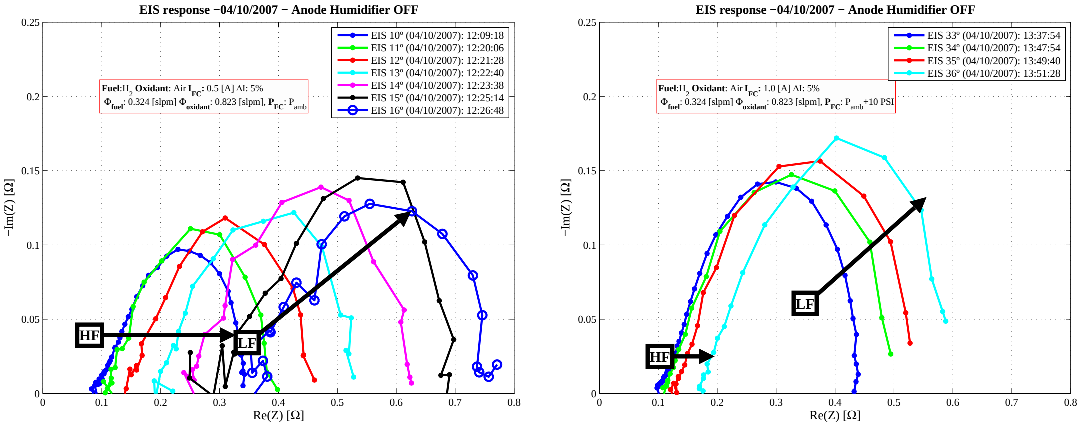

(c) Nyquist OFF I_{FC}=0.5 A (d) Nyquist OFF I_{FC}=1.0 A

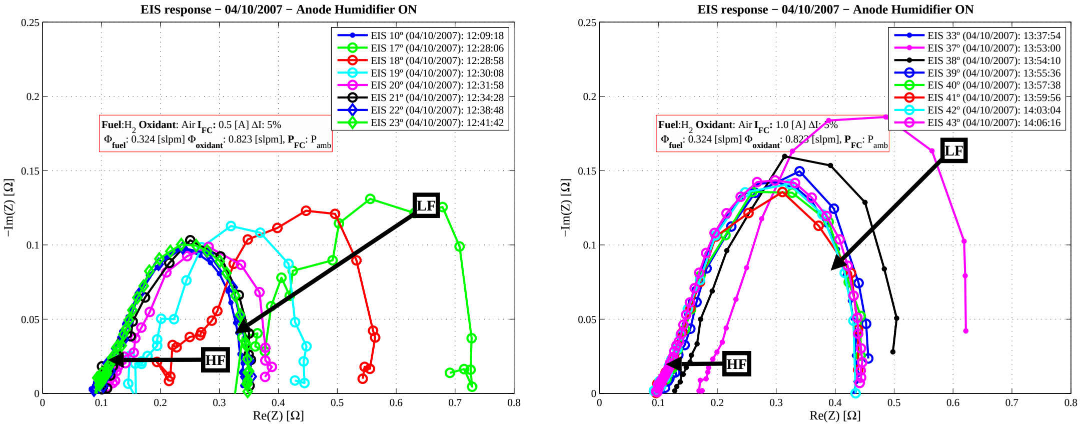

(e) Nyquist ON I_{FC}=0.5 A (f) Nyquist ON I_{FC}=1.0 A

Figure 4.26: Experimental responses of the nominal current comparison (anode humidification interruption)

reflecting the reduction of water presence in both channels. The cathode differential pressure also reduces its value and confirms the water presence reduction.

Comparison of relevant characteristics

In figure 4.27 a comparison of the *relevant characteristics* in the same graph is done, which is useful for the analysis of the nominal current influence over the anode humidification interruption responses.

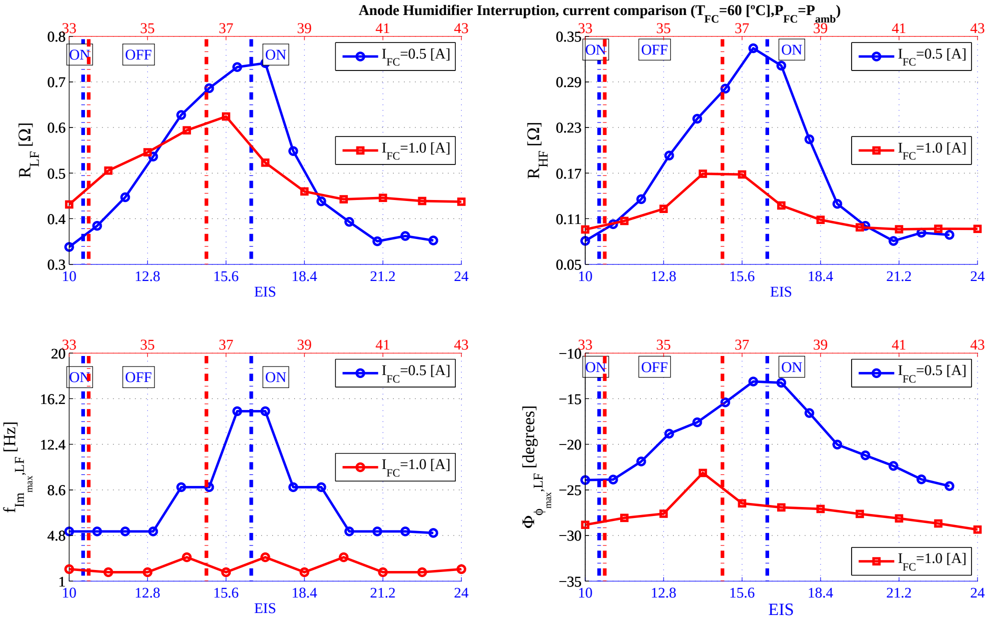

Figure 4.27: Relevant characteristics, current variation, anode humidification interruption

Similar trends can be observed under anode humidification interruption at different currents in all relevant characteristics, with the exception of the frequency of the low frequency imanaginary maximum ($f_{Im_{max,LF}}$). The $f_{Im_{max,LF}}$ is higher when the fuel cell current is I_{FC}=*0.5 [A]* and the trend is very different. At current I_{FC}=*1.0 [A]*, the values of $f_{Im_{max,LF}}$ are almost constant during the anode humidification interruption. On the other hand, when the current is I_{FC}=*0.5 [A]*, the values of $f_{Im_{max,LF}}$ increase in a similar way as the cathode. That effect could indicate the influence of the generated water by reaction in the fuel cell.

The other relevant characteristics have l*ower initial values* but a *higher increasing rate* at the lower nominal current applied (I_{FC}=0.5 [A]).

4.5.3 Pressure variation: cathode humidification interruption

In this subsection, the temporal and frequency responses of the cathode humidification interruption at different nominal operating pressures (P_{FC}=P_{amb} and P_{FC}=$P_{amb}+10[PSIg] \approx$ 1.68 [Bar]) are compared (see figure 4.28).

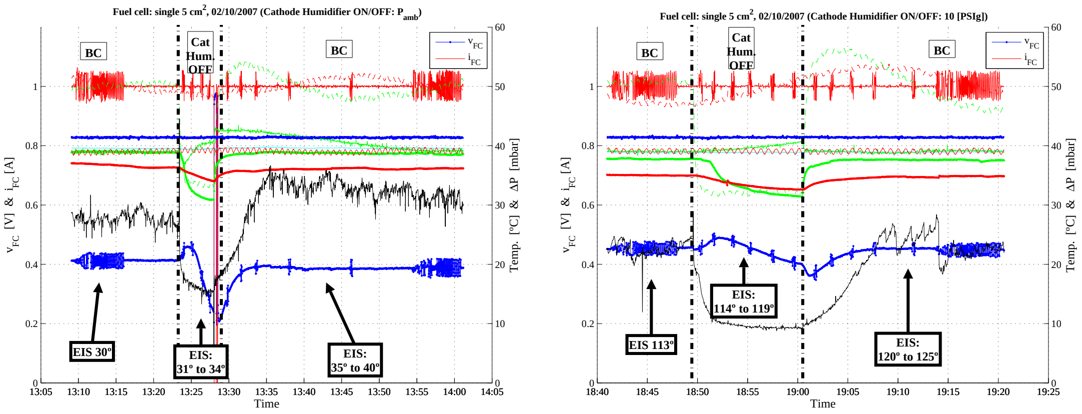

(a) P_{FC}=P_{amb} (b) P_{FC}=P_{amb}+10 PSI

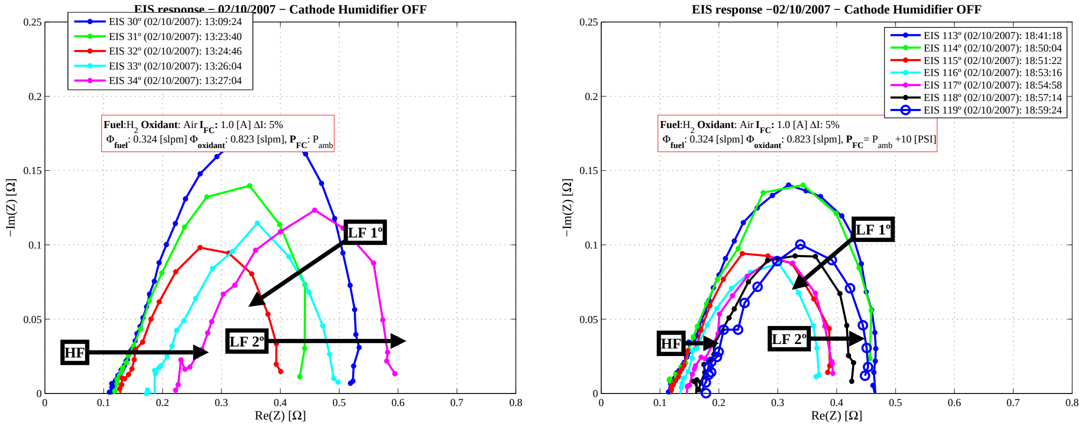

(c) Nyquist OFF, P_{FC}=P_{amb} (d) Nyquist OFF, P_{FC}=P_{amb}+10 PSI

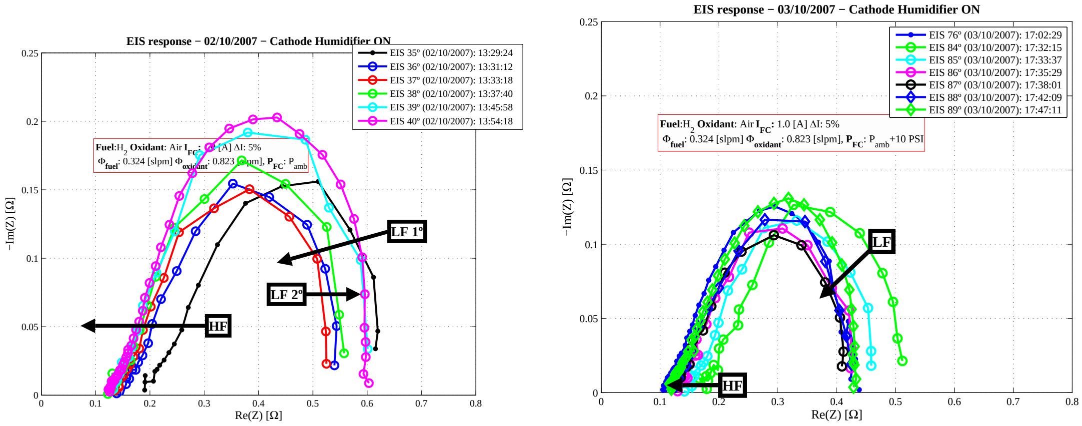

(e) Nyquist ON, P_{FC}=P_{amb} (f) Nyquist ON, P_{FC}=P_{amb}+10 PSI

Figure 4.28: Experimental responses of the nominal pressure variation, cathode humidification interruption

The nominal operating conditions are: nominal current $I_{FC} = 1.0$ [A], cell temperature $T_{FC} = 40$ [°C] and 100 [%] of relative humidity of the inlet gases (H_2/Air).

The temporal evolution of the cathode humidification interruption at different pressures can be seen in figures 4.28(a) and 4.28(b). The main difference is the time constant of the concurrent effects. For example, the anode and the cathode outlet temperatures have lower time constant in the high pressure case ($P_{FC}{=}P_{amb} + 10[PSIg] \approx 1.68$ [Bar]). It seems that the higher concentration of oxygen helps to maintain during a longer time the voltage value and makes softer the falling part due to the membrane drying and the active area reduction effects.

Comparison of relevant characteristics

In figure 4.29 a comparison of *relevant characteristics* on the same graph is done to analyse the difference of the response with one pressure or the other.

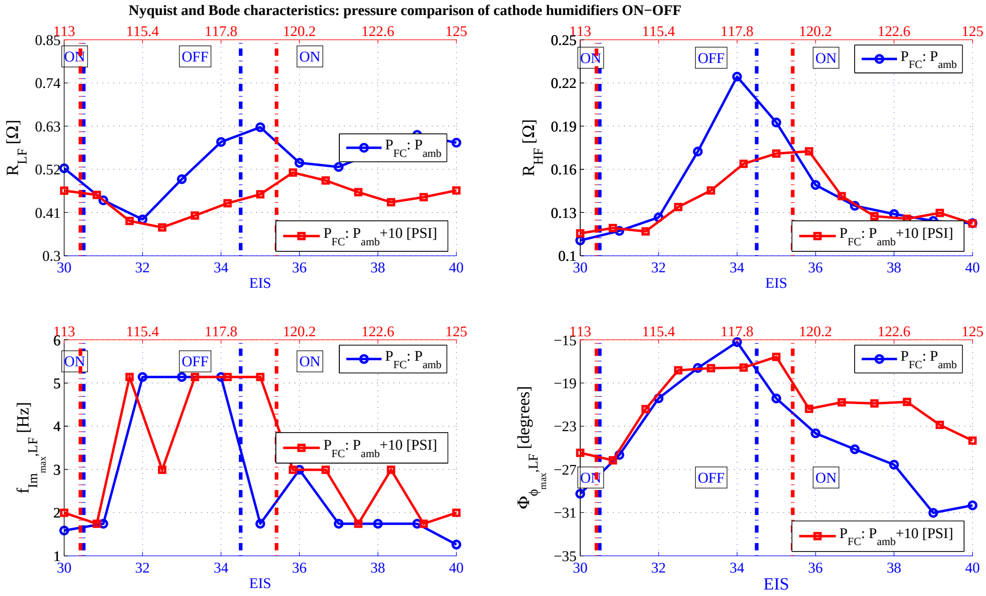

Figure 4.29: Relevant characteristics, pressure variation, cathode humidification interruption

Figure 4.29 shows the influence of the pressure in the *relevant characteristics*. The first conclusion is that the *starting and finishing* points of the high (R_{HF}) and the low frequency (R_{LF}) resistances are very similar. This indicates that the cell can be returned to normal operation without an important disturbance of these characteristics after humidification interruption.

With this comparison the conclusions obtained with the cathode humidification interruption are confirmed (see figures 4.23 and 4.22). The difference between the different pressures behaviour lies in the rates of evolution. At a higher pressure, the response has a better performance due to the higher oxygen concentration and to the diffusion process improvement with pressure.

4.5.4 Pressure variation: anode humidification interruption

The temporal and frequency responses under different pressures of the anode humidification interruption is presented (see figure 4.30).

The nominal operating conditions are: nominal current $I_{FC} = 1.0$ [A], cell temperature $T_{FC} = 40$ [^{o}C] and 100 [%] of relative humidity of the inlet gases (H_2/Air).

The time evolution of the anode humidification interruption with pressure variations can be seen in figures 4.30(a) and 4.30(b). The evolution of the anode outlet temperature, the voltage and the cathode differential pressure are very similar for both pressures. Both cases show a performance decay, but with a stable trend, indicating the possibility of *working without anode humidification*.

Comparison of relevant characteristics

In figure 4.31, a comparison of the relevant characteristics for different pressure conditions when the anode humidification is interrupted, is presented.

Figure 4.31 shows the influence of pressure in the *relevant characteristics*. One important conclusion is that the *starting and finishing* points of all relevant characteristics are very similar. This indicates, again, that the cell can be returned to normal operation without an important disturbance of characteristics after the humidification interruption.

Another important conclusion is that the influence of the anode humidification interruption is very similar at both pressures, specially the resistances R_{HF} and R_{LF}, are similar at the end of the test and with very coincident trends (increasing values and stabilisation).

The other relevant characteristics ($f_{Im_{max,LF}}$ and $\Phi_{\phi_{max,LF}}$) do not change so much, and this fact helps to understand that the low frequency characteristics are more related to the changes of the operating conditions in the cathode side.

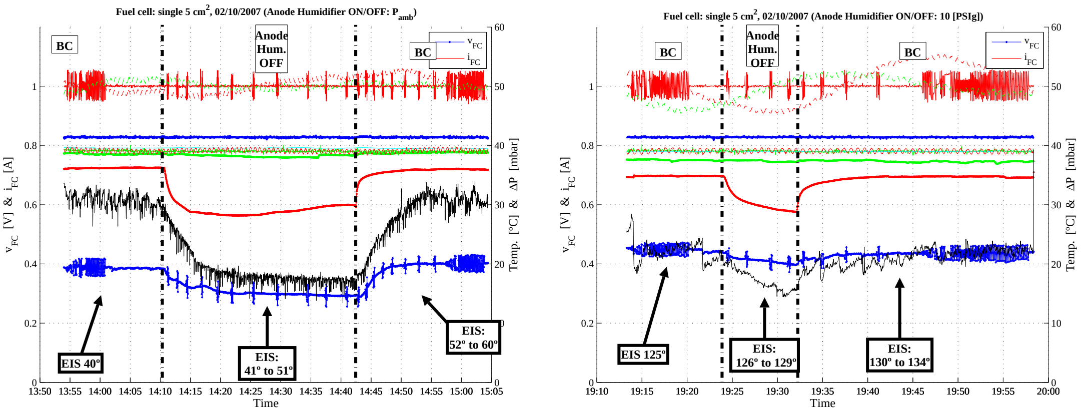

(a) P_{FC}=P_{amb}

(b) P_{FC}=P_{amb}+10 PSI

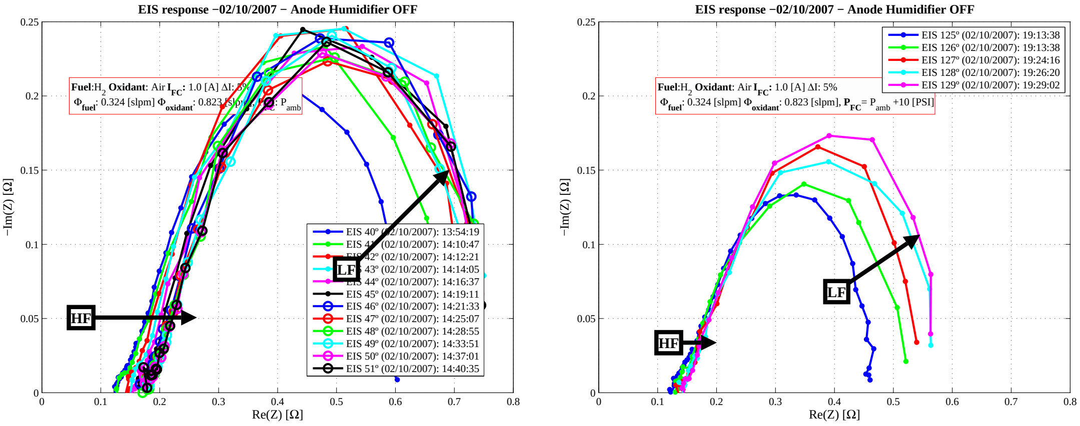

(c) Nyquist OFF, P_{FC}=P_{amb}

(d) Nyquist OFF, P_{FC}=P_{amb}+10 PSI

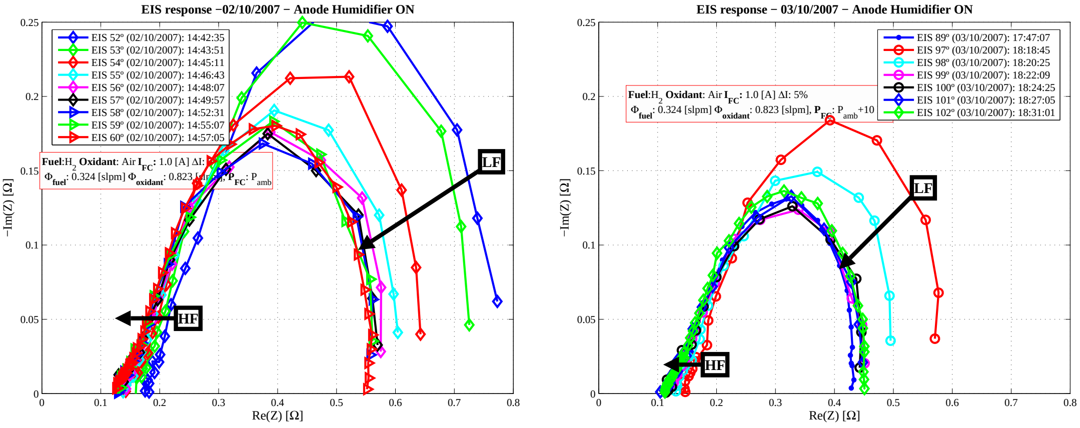

(e) Nyquist ON, P_{FC}=P_{amb}

(f) Nyquist ON, P_{FC}=P_{amb}+10 PSI

Figure 4.30: Experimental responses of the nominal pressure variation, anode humidification interruption

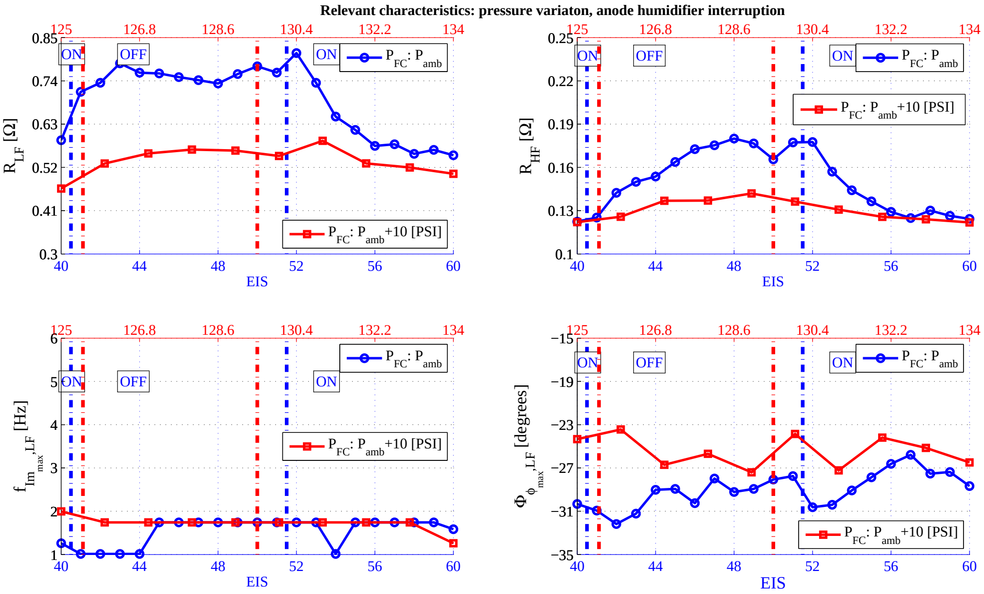

Figure 4.31: Relevant characteristics with pressure variation for anode humidification interruption

4.5.5 Temperature variation: cathode humidification interruption

In this subsection, temporal and frequency responses under temperature variations of cathode humidification interruption are compared. Figure 4.32 shows the time response at temperatures T_{FC}= 40 [°C], 50 [°C] and 60 [°C].

The frequency responses of cathode humidification interruption under temperature variation are summarized in figure 4.33.

The nominal operating conditions are: current $I_{FC} = 1.0$ [A], cell pressure $P_{FC} = P_{amb}$ and 100 [%] of relative humidity of the inlet gases (H_2/Air).

Observing figure 4.32, it is seen that there are some coincidences in the evolution of the voltage at the different temperatures, the voltage grows for a while and then falls quickly. The anode and the cathode outlet temperatures have also similar behaviours at the different temperatures, changing their magnitude due to less water concentration at both sides (removed by the bypass in cathode side). The cathode differential pressure also falls in all temperature situations.

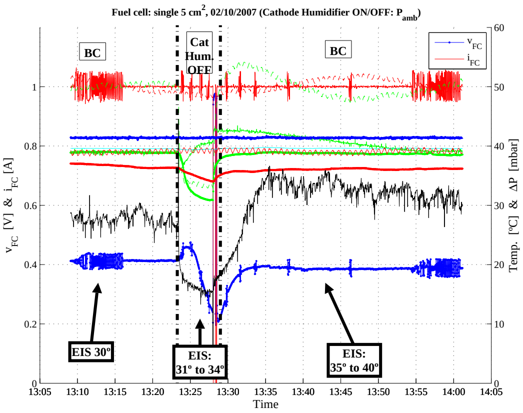

(a) T_{FC}=40 °C

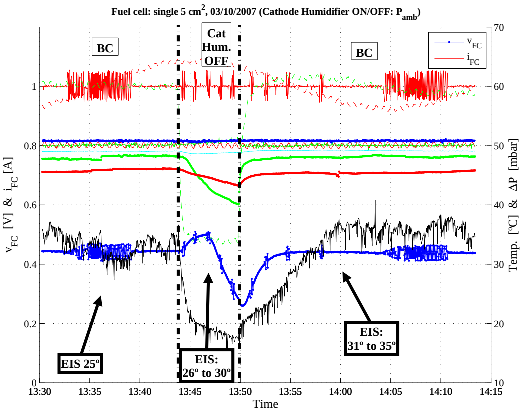

(b) T_{FC}=50 °C

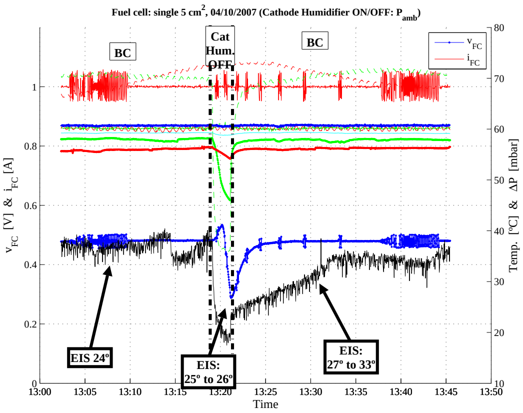

(c) T_{FC}=60 °C

Figure 4.32: Time responses of the nominal temperature variation, cathode humidification interruption

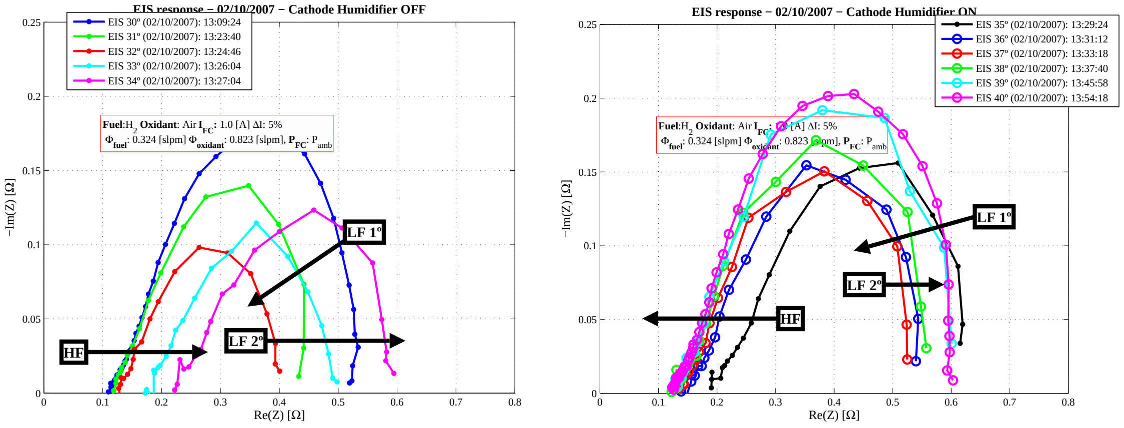

(a) Nyquist OFF, T_{FC}=40 °C

(b) Nyquist ON, T_{FC}=40 °C

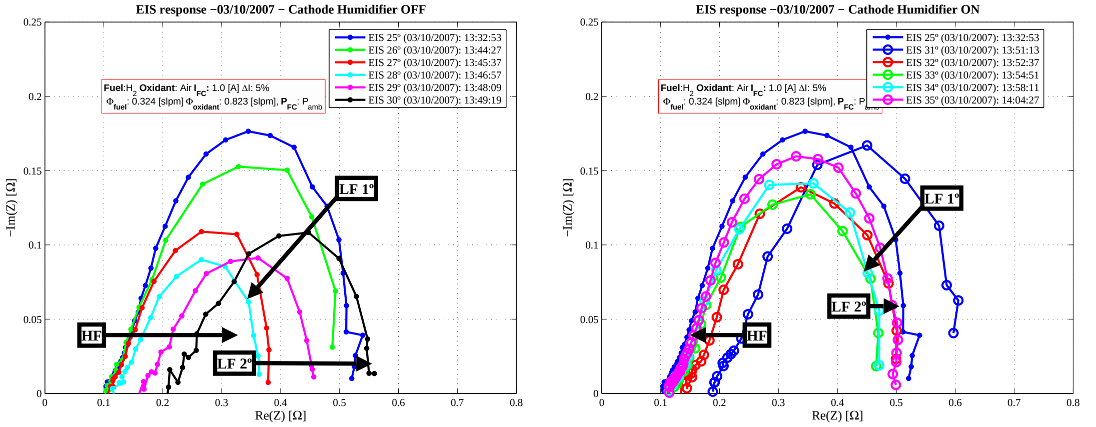

(c) Nyquist OFF, T_{FC}=50 °C

(d) Nyquist ON, T_{FC}=50 °C

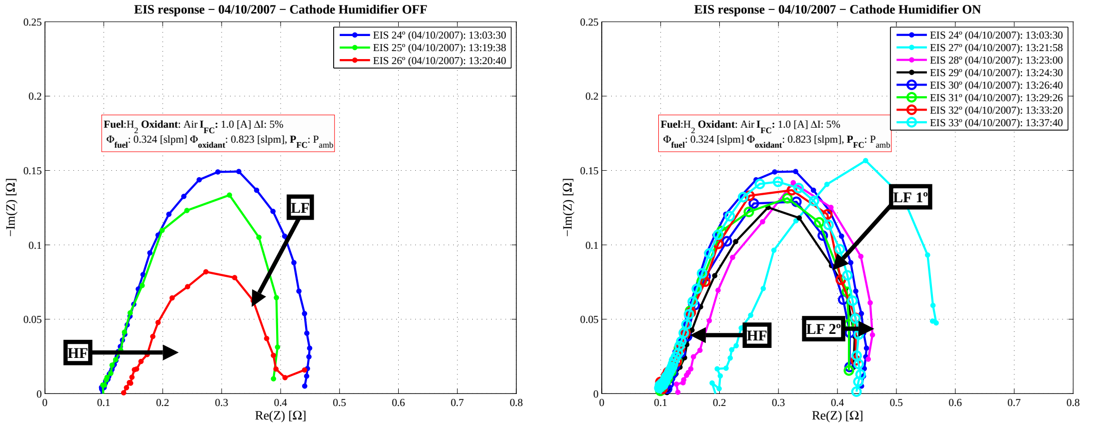

(e) Nyquist OFF, T_{FC}=60 °C

(f) Nyquist ON, T_{FC}=60 °C

Figure 4.33: Frequency responses of the nominal temperature variation, cathode humidification interruption

Comparison of the *relevant characteristics*

The comparison of the *relevant characteristics* is presented in figure 4.34. The results of the operation under different temperatures for the cathode humidification interruption are graphed.

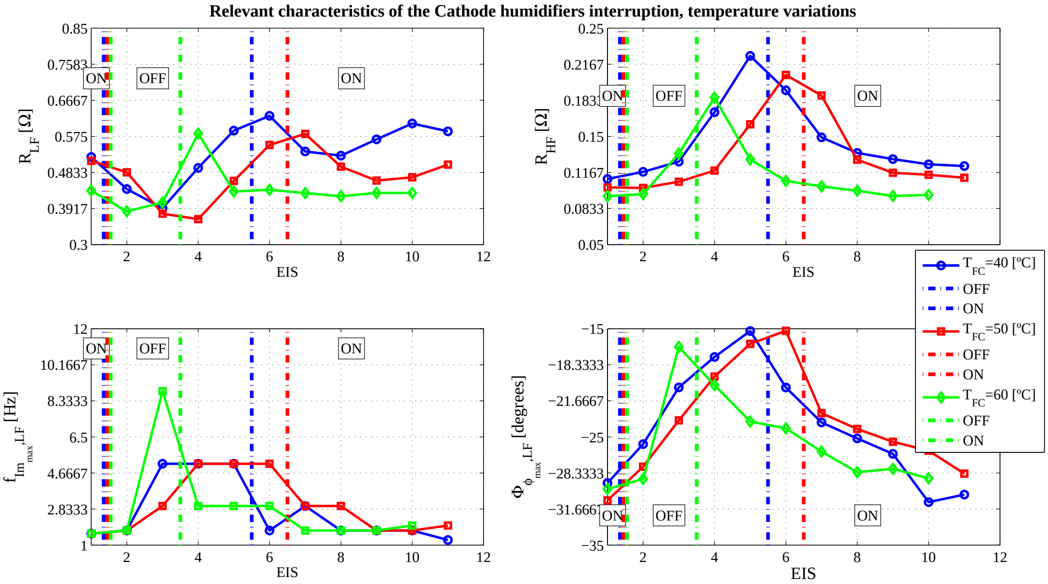

Figure 4.34: Relevant characteristics for temperature variation of the cathode humidification interruption

The first conclusion is the reproduction of the results described in figure 4.22, with the difference in the rate of the response degradation. This rate improves (understanding the improvement as a lower rate), from temperature T_{FC}= 40 [°C] to the T_{FC}= 50 [°C], but is worse when the temperature is T_{FC}= 60 [°C]. This fact can be interpreted as the influence of needed energy in order to maintain the fuel cell system at this temperature.

Another important conclusion is that the *starting and finishing* points of the low (R_{LF}) and the high (R_{HF}) frequency resistances are reflecting the influence of the temperature, the higher is the temperature the lower are the values (better diffusion of oxygen, more activity of reactants and better membrane proton transport, see reference Barbir [2005]).

The other relevant characteristics ($f_{Im_{max,LF}}$ and $\Phi_{\phi_{max,LF}}$) also show the same evolutions described in the 4.22 and confirm the conclusion about the rate of deterioration of the performance.

4.5.6 Temperature variation: anode humidification interruption

In this subsection, the temporal and the frequency responses under temperature variations of the anode humidification interruption are compared. Figure 4.35 shows the time response for temperatures T_{FC}= 40 [°C], 50 [°C] and 60 [°C].

The frequency response of the anode humidification interruption under temperature variation is summarized in figure 4.36. The nominal operating conditions are: current $I_{FC} = 1.0$ [A], cell pressure $P_{FC} = P_{amb}$ and 100 [%] of relative humidity of the inlet gases (H_2/Air).

Looking at figure 4.35, it is seen that there is a coincidence with the evolution of the voltage at the different temperatures: the voltage falls slowly, the anode outlet temperature goes down and tends to stabilize due to less water concentration at both sides (water is removed by the bypass in the anode side) and the cathode differential pressure also falls down in all cases, to similar values.

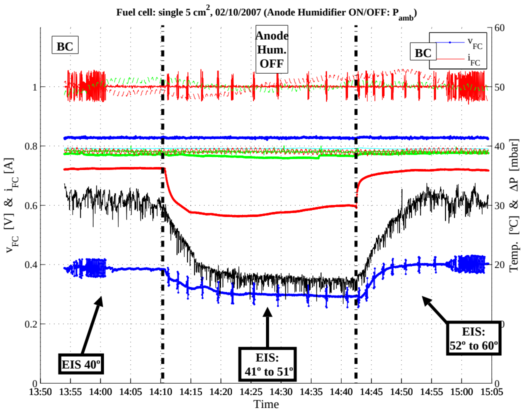

(a) T_{FC}=40 °C

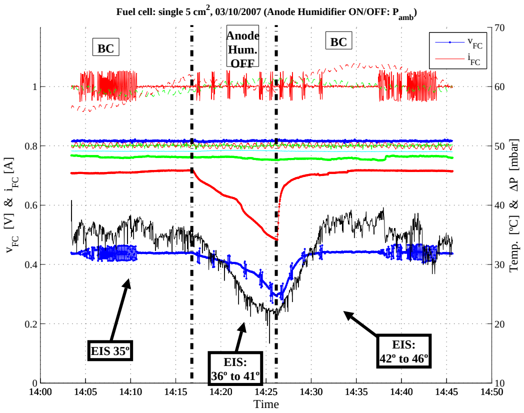

(b) T_{FC}=50 °C

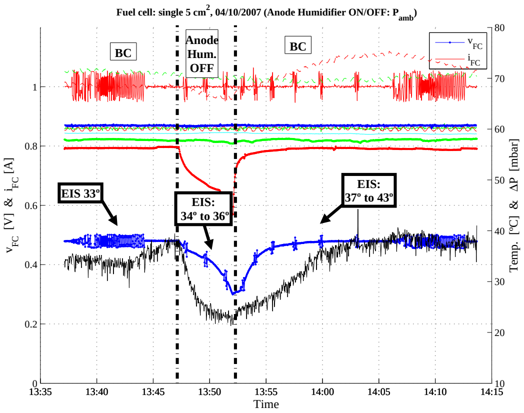

(c) T_{FC}=60 °C

Figure 4.35: Time responses of the nominal temperature variation, anode humidification interruption

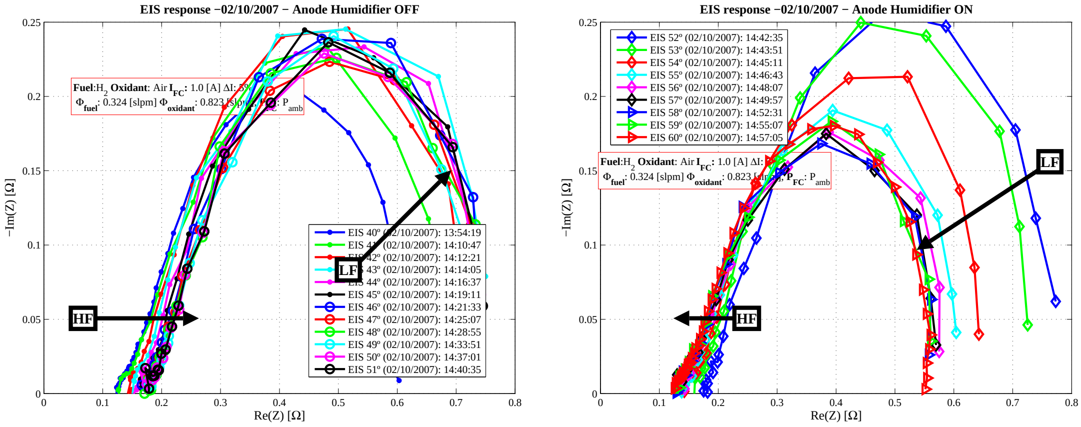

(a) Nyquist OFF, T_{FC}=40 °C (b) Nyquist ON, T_{FC}=40 °C

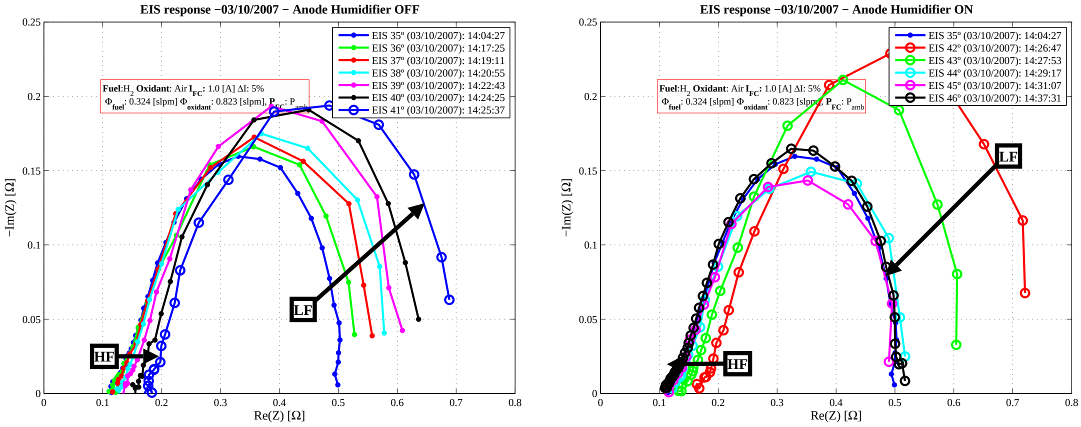

(c) Nyquist OFF, T_{FC}=50 °C (d) Nyquist ON, T_{FC}=50 °C

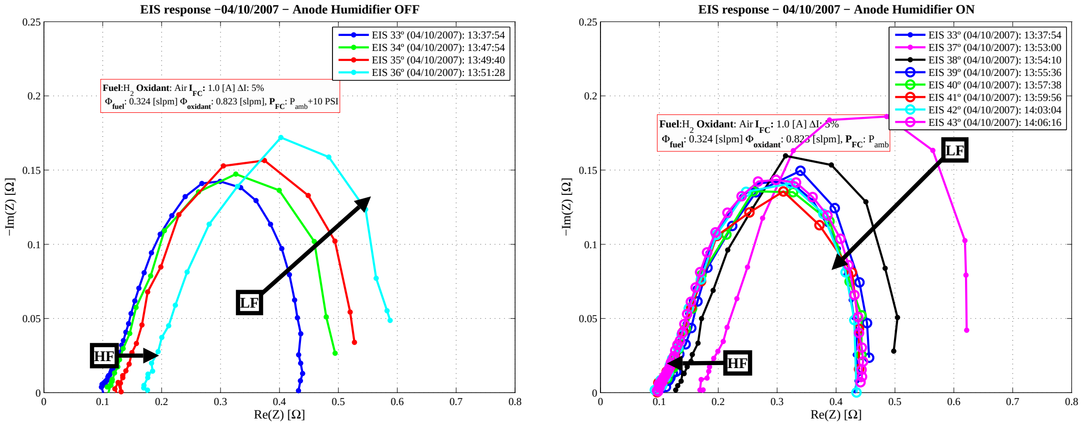

(e) Nyquist OFF, T_{FC}=60 °C (f) Nyquist ON, T_{FC}=60 °C

Figure 4.36: Frequency responses of the nominal temperature variation, anode humidification interruption

Comparison of *relevant characteristics*

In the figure 4.37, a comparison of the relevant characteristics is done for the operation at different operating temperature for the anode humidification interruption.

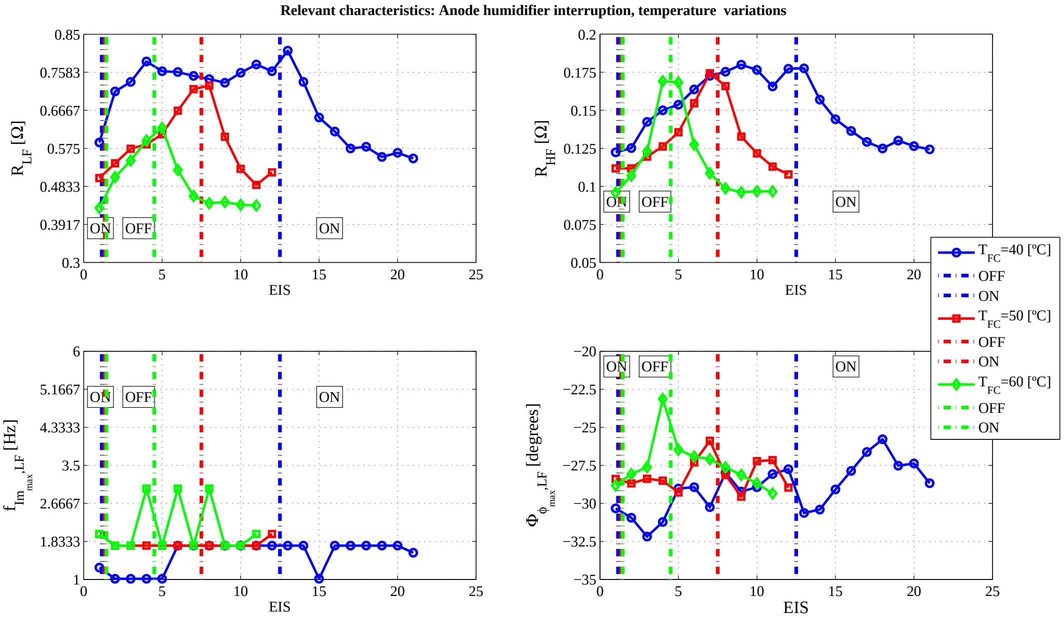

Figure 4.37: Relevant characteristics, temperature variation of anode humidification interruption

As in the cathode variation of temperature, the first conclusion is the reproduction of the results described in figure 4.22, with the difference in the rate of the degradation response. This rate improves (understanding the improvement as a lower rate) from temperature T_{FC}= 40 [°C] to the T_{FC}= 50 [°C], but is worse when the temperature is T_{FC}= 60 [°C].

The other relevant characteristics ($f_{Im_{max,LF}}$ and $\Phi_{\phi_{max,LF}}$) also show the same evolutions described in the 4.22 and confirm the conclusion about the rate of the performance deterioration.

Another important cfact is that the *starting and finishing* points of the low (R_{LF}) and the high (R_{HF}) resistances are reflecting the influence of the temperature: the higher the temperature, the lower the values (better diffusion of oxygen, more activity of reactants and better membrane proton transport, see reference Barbir [2005]).

4.6 Conclusions

In this chapter a new experimental characterisation technique, based on the inlet gases humidification interruption is proposed. This dynamic technique combines the information extracted from the standard characterisation technique, EIS, and the temporal response. The test is dedicated to study the water transport and storage effects and is performed trough the humidification interruption. The proposed experimental test is very simple to implement, it only needs a bypass valve and appropriate gas connections to implement it. Due to its hardware simplicity configuration and due to the relative low impact on the fuel cell response, the humidification interruption test can be used as an in-situ technique.

Observing the temporal response to the humidification interruption test for different operating conditions the patterns have always the same shape. For all the experimental tests performed it is remarkable that the temperature, voltage, cathode differential pressure as well as the EIS relevant characteristics before and after the test have similar values. This confirms that the test has a low distortion on the fuel cell performance.

The anode humidification interruption has a decrease in the performance, but maintains stable behaviour. On other hand, the cathode humidification interruption presents also a decrease in the performance, but is not able to maintain its behaviour.

The **cathode humidification** plays an important role in the cell behaviour. Time and frequency responses of the cathode humidification interruption show two zones of evolution that reflect in the values of the cell voltage, R_{LF} and R_{HF}. In the first zone, an improvement of the response is due to a better diffusion process and to the increase of the concentration of oxygen, due to the fact that water vapour is no more injected by the humidifier. The cell voltage and R_{LF} are good indicators of this improvement. At the same time the membrane starts to dry, this reflects in a slow increase of the R_{HF}.

In the second zone the membrane dries with a faster rate, because the water in the GDL and the cathode catalyst layer has already moved out and the membrane water content starts to decrease, and hence R_{HF} grows rapidly. Also, as a consequence of this lack of water inside the membrane, the reaction sites are more difficult to reach for the protons and a reduction of the active area occurs. The humidification must be restablished in order to avoid unacceptable voltage losses. These results are consistent with those obtained in section **3.5.5.3**, which analyses the influence of the Relative Humidity of the inlet gases on the EIS *relevant characteristics*.

As is said before, the **anode humidification** interruption response presents a much more softer and limited variations compared with the cathode side response. When the anode humidification is interrupted, R_{LF} and R_{HF} increase their values slowly and tend to new stationary ones. This new operation state allows the system continuing working without the need to restablish the humidification although with a deteriorated performance.

Summarizing, the proposed test is a simple, in-situ and low invasive technique useful to understand the behaviour of the fuel cell in front of dynamic humidity variations. This test gives a set of recognizable patterns of the evolution of the relevant characteristics. This test will also allow, in chapter 5, to identify some indicators to perform a diagnosis of the humidification state of the fuel cell.

Chapter 5

Diagnosis tools for PEMFC from humidification interruption tests

5.1 Introduction

In this chapter, diagnostic tools are derived from the combination of the time and frequency responses when an interruption of the gas inlet humidification is done.

The main objective of this chapter is to define procedures to determine the humidification fuel cell state trough *performance indicators* without forcing high intrusive conditions in the fuel cell operation. These performance indicators should be related to the physical phenomena inside the PEM fuel cell and give useful information about the possible solutions of the problems caused by inappropriate water distribution (flooding/drying effects).

5.2 State of art

One of the reviews of the diagnostic tools applied to PEM fuel cell is the two parts article: Wu *et al.* [2008a] and Wu *et al.* [2008b].

The article Wu *et al.* [2008a], review and discusses various electrochemical techniques and outlines for each one of them the experimental procedure, its capabilities and weaknesses. The experimental electrochemical techniques reviewed are *polarization curve*, *current interruption*, *electrochemical impedance spectroscopy*, *cyclic and CO stripping voltammetry* and *Linear sweep voltammetry.*

The *Polarization curve* is the representation of fuel cell performance by static current-voltage response (see chapter 3 and references Ju & Wang [2004], Srinivasan *et al.* [1991], Kim *et al.* [1995], Squadrito *et al.* [1999],Pisani *et al.* [2002],Amphlett *et al.* [1992]). This technique provides information on the performance of the cell or stack as a whole. While it gives useful information of the overall performance under specific operating conditions, it fails to give much information about the performance of individual components within the cell (see figure 5.1). The technique cannot be performed during normal operation of a fuel cell and takes significant time to be performed. In addition, it fails to differentiate internal mechanisms from each other. For example, both flooding and drying inside a fuel cell cannot be distinguished with a single polarization curve.

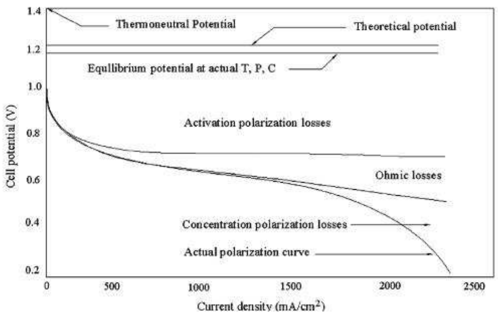

Figure 5.1: Example of polarization curve

The *Current interruption* method is mainly used for measurement of the ohmic losses in a PEM fuel cell. As is explained in chapter 3, the experiment consist in opening the load suddenly and record the voltage evolution (see figure 5.2 and references Wruck *et al.* [1987], and Larminie & Dicks [2003]). The ohmic losses vanish very quickly and the electrochemical (activation) overpotentials decline to the open circuit voltage at a slower rate. Compared to other methods like the impedance spectroscopy, the current interrupt method has the advantage of being straightforward data analysis. However, one of the weaknesses of this method it that the obtained information is limited and also that the exact point in which the voltage jumps instantaneously is required thus a fast oscilloscope has to be used to record the voltage changes. Another issue with this method is its relative high intrusion in the FC operation.

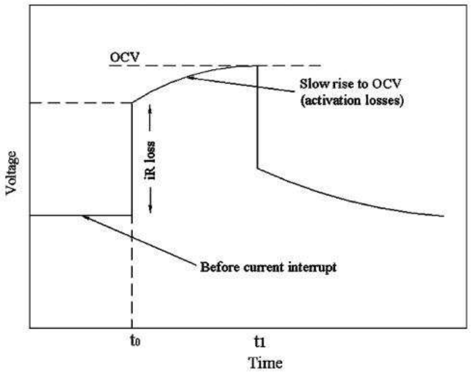

Figure 5.2: Example of Current Interruption response

The *Electrochemical Impedance Spectroscopy* is a powerful technique for fuel cell study. This dynamic method can provide more information than steady-state experiments and provide diagnostic criteria for evaluating PEM fuel cell internal state (see figure 5.3 and references Parthasarathy *et al.* [1992], Springer *et al.* [1996], Cooper *et al.* [2005] and Barsoukov & Macdonald [2005]). The main advantage of EIS as a diagnosis tool for evaluating fuel cell behaviour is its ability to resolve, in the frequency domain, the individual contributions of the various factors determining the overall PEM fuel cell power losses: ohmic, electrochemical and mass transport. Such a separation provides useful information both for optimization of the fuel cell design and for the selection of the most appropriate operating conditions. However, the interpretation of impedance spectra has some difficulties difficult due to the complexity of processes involved and there are a lot of unresolved issues regarding the explanation of impedance and the separation of anode and cathode phenomena, although it is generally considered that the main contribution of rapid kinetics and mass transport loss occurs in the cathode side. Another important characteristic of EIS is that the intrusion of the test is relatively low.

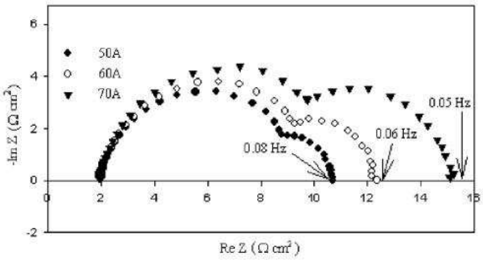

Figure 5.3: Example of EIS response

The other electrochemical methods have the voltage variation as common factor. *Cyclic voltammetry* is a voltage sweep between two voltages while the current is recorded (see figures 5.4(a) and 5.4(b) and references Oszcipok *et al.* [2005], Ticcianelli *et al.* [1988] and Wang *et al.* [2001]). This method is used to obtain information about hydrogen adsorption and desorption at catalyst surface, named Electrochemical Catalyst Area (ECA). *CO stripping voltammetry* is the measure of ECA of electrodes trough the oxidation of absorbed CO at room temperature (see references Brett *et al.* [2004] and Salagado *et al.* [2004]). *Linear Sweep Voltammetry (LSV)* is used to measure the crossover of hydrogen and oxygen through the membrane, which is considered to be one of the most important phenomena in PEM fuel cells (see references Kocha *et al.* [2006] and Ramani *et al.* [2004]). Humidified H_2 and N_2 are supplied to the anode and the cathode sides of the fuel cell and voltage scans are done. The information about crossover if there is any current generated at the given potential, is due to electrochemical oxidation of H_2 gas that crosses over the membrane from the anode side.

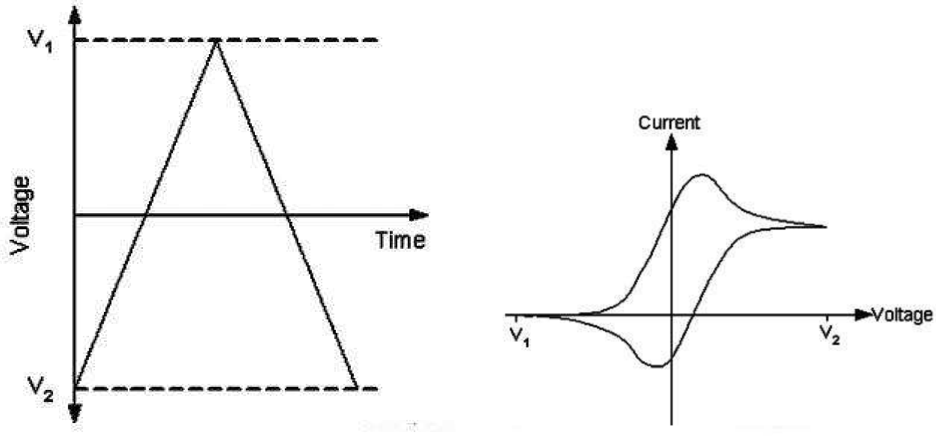

(a) Voltage variation

(b) Current-Voltage response

Figure 5.4: Cyclic voltammetry examples

Finally, *cathode discharge* is a “in situ” method to determine the MEA resistance and electrode diffusion coefficient (MRED) for a fuel cell. This method is based on the galvanostatic discharge of a fuel cell with an interrupted reactant supply (see reference Stumper *et al.* [2005b]). During a cathode discharge experiment, the cathode compartment is separated from the gas supply by closing both inlet and outlet valves, whereas the anode side is fed continuously with H_2. Then the load is switched on with constant current, and the cell voltage transient is recorded during the discharge of the fuel cell. These measurements are used to determine the ohmic resistance and the effective diffusivity of the electrodes.

The article of Wu *et al.* [2008b], reviews various physical and chemical methods and outlines their principle, experimental implementation, the associated data processing and their capabilities and weaknesses as diagnostic tools.

The *Pressure drop measurement* is an important design and diagnostic tool variable, specially at the cathode where the water is produced. The cause of the pressure drop is the friction between the reactant gases and the flow field passages and the gas diffusion layer (GDL), specially for interdigitated flow fields (see references Barbir *et al.* [2005], Görgün *et al.* [2006] and He *et al.* [2003]). If a higher pressure is needed an additional equipment is required and the parasitic power loss will be higher. In a flooding condition (too much liquid water in the flow channel) the gas flow resistance increases, hinders the reactant gas transport and lead to a performance decrease related to mass transport. The pressure drop at the cathode side increases when a cell get flooded while remains unchanged when the cell dries. Thus the pressure drop ,measurement clearly distinguishes between the two phenomena (see figure 5.5, of reference Barbir [2005]).

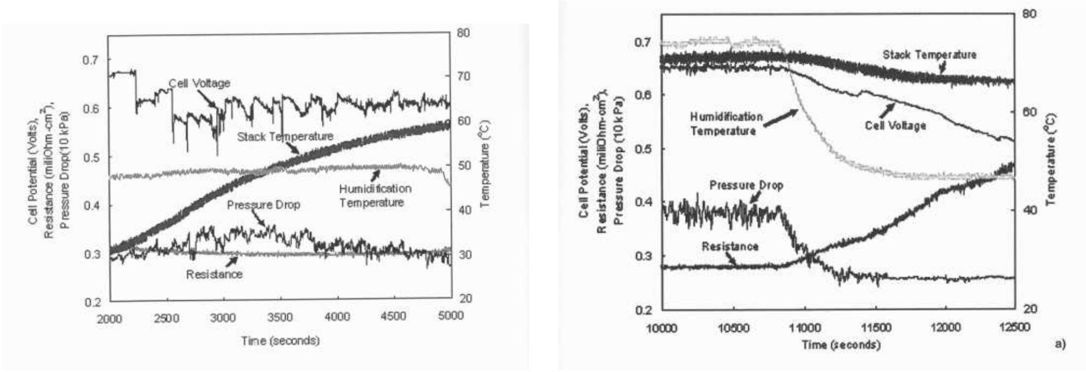

(a) Humidification variation

(b) Insufficient humidification

Figure 5.5: Pressure drop response

Other examples of using the pressure drop as diagnostic tool are the methodology and the equipment designed by General Motors (see reference Bosco & Fronk [2000]) for monitoring a H_2/O_2 fuel cell to detect and to correct its flooding using pressure drop thresholds. The article of Squadrito *et al.* [2004] studies the behaviour of a large stack of PEM fuel cells under different operating conditions. One of the variables analysed is the pressure drop within the stack and its relationship with the flow field with single and two-phase flows. The work concludes that once the current in the fuel cell stack is reduced, the pressure drop decreases slowly until it reaches a new value, attributed to the reduction of produced water by the current in the flow channels.

Another study of pressure drop in fuel cell is presented in reference Ma *et al.* [2006]: using a transparent PEM fuel cell with a single straight channel, designed to study liquid water transport in the cathode channel, the pressure drop between the inlet and outlet of the channel on the cathode side is used as diagnosis signal to monitor the liquid water accumulation.

Other physical/chemical techniques like *Gas Cromatography (GC)*, (see reference Dong *et al.* [2005]), *Neutron imaging* (references Bellows *et al.* [1999] and Satija *et al.* [2004]) and *Magnetic resonance Imaging (MRI)* (references Callaghan [1991] and Teranishi *et al.* [2006]) and other methods like partial MEA's, segmented cells and subcell approaches (references Hakenjos *et al.* [2004], Stumper *et al.* [1998] and Natarajan & Nguyen [2006]) are also described in this review paper (Wu *et al.* [2008b]), but they are out of the scope of this thesis.

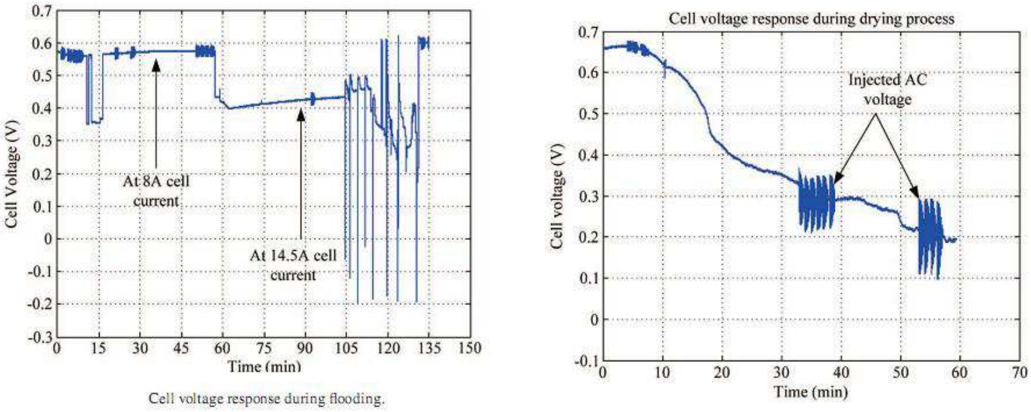

(a) Flooding procedure

(b) Drying procedure

Figure 5.6: Cell voltage during flooding and drying processes (see reference Gebregergis *et al.* [2010])

In the article of Gebregergis *et al.* [2010], flooding and drying are detected from the cell voltage and the impedance response. The flooding and drying processes are forced by the difference of the cell and the gas inlet humidifiers temperatures (for both reactants, H_2/O_2) during a long time (more than 120 minutes each process, see figure 5.6). To create flooding in the cell, the humidifier temperature is maintained at about 40 [°C] or higher than the cell temperature. Drying process is forced by keeping the cell temperature at about 40 [°C] or higher than the humidifier one. At the same time that these processes occurs, several EIS test are done. Some of the results are presented in the figure 5.7, with a comparison of the healthy, the flooded and the dried cell response. The impedance response at low frequency is used to identify the cause of the fault. The slope of the magnitude and the negative phase response of the cell impedance at low frequency is observed to allow the fault diagnosis. A cell impedance model based on resistive capacitive (C model) and resistive constant-phase-element (CPE model) circuits is developed. CPE model provides better adjustment, but C model is easier to implement since it is well known in most simulation tools. Also, a *cascade Boost-Buck* power converter circuit is designed (and experimentally tested) in order to mitigate the drying fault. The fuel cell performance is improved making pulses of the cell current to higher values (water generation is higher). The *Boost* converter controls the fuel cell operating point (inserting the current pulses) and the *Buck* converter ensures the constant power to the output.

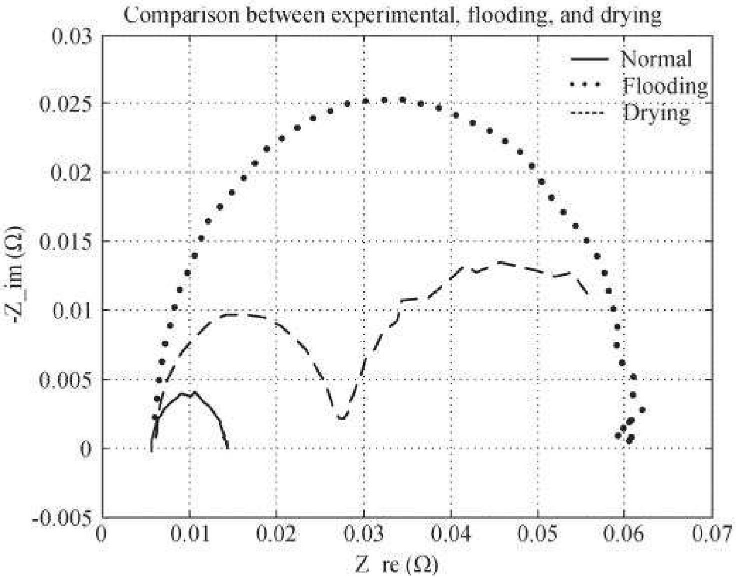

Figure 5.7: EIS response of flooding and drying processes (see reference Gebregergis *et al.* [2010])

Another important article is presented by Fouquet *et al.* [2006], with the monitoring of the flooding and drying effects using a model-based approach coupled with AC impedance measurements (EIS) as a function of the inlet gas relative humidity. The temporal evolution of drying and flooding processes is presented in figure 5.8(a). The parameters of a Randles-like equivalent circuit are then fitted to the data. In order to improve the quality of the fit, the classical Randles cell is extended by changing the standard plane capacitor into constant phase element (CPE).

It is found that monitoring the evolution of the three resistances of this modified Randles model is an efficient and robust way of monitoring the state-of-health (SOH) of the fuel cell with respect to the water content of the membrane electrode assembly. A Qualitative interpretation of the variation of the parameters as a function of the SOH is proposed in both flooded and dry conditions.

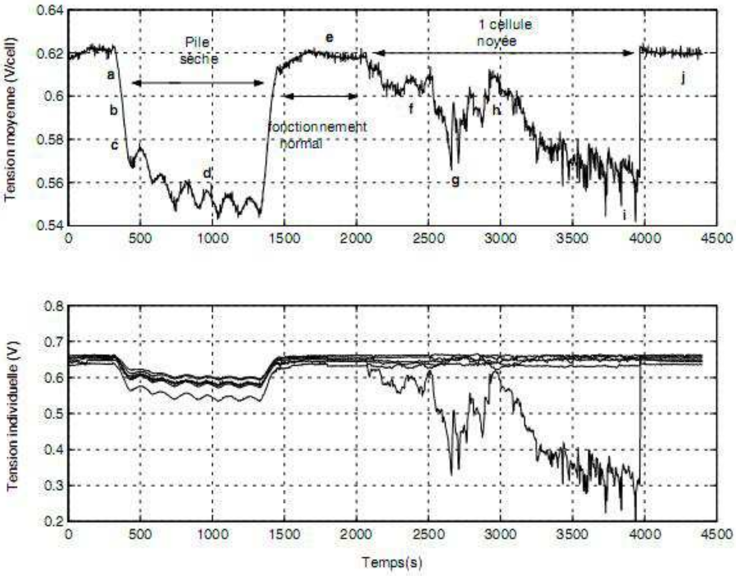

(a) Voltage evolution

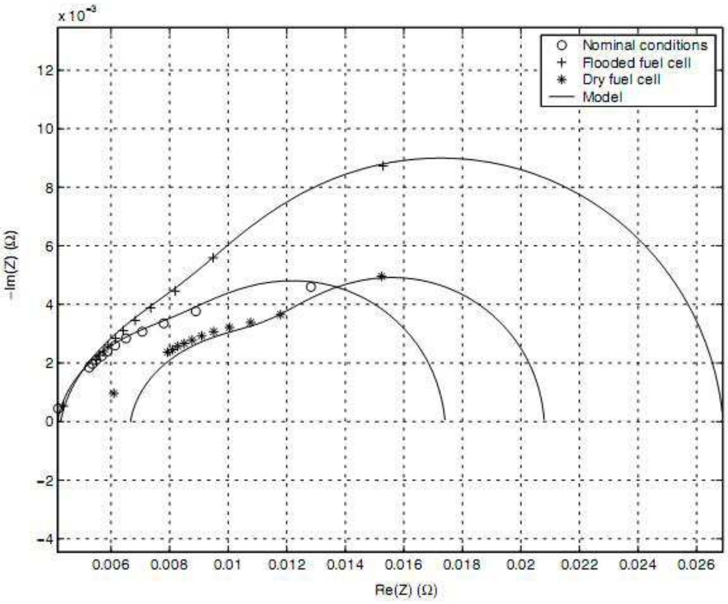

(b) EIS comparison

Figure 5.8: Cell voltage and EIS responses (see reference Fouquet *et al.* [2006])

5.3 Objective of the diagnosis tools

Operating conditions given by pressure, temperature, flow rates and humidity of reactants have a significant effect on PEMFC performance (see reference Barbir [2005]). In general, the performance of a PEM fuel cell is stable in a relatively narrow operating conditions window. This is mainly related to water management inside the cell. Although it is possible to select operating conditions to maintain a required water balance in the whole FC, flooding and drying may still take place due to uneven local conditions inside the cell. Water plays a key role in PEM fuel cells because its presence is closely linked to the functionality of the main components of the cell (Stumper *et al.* [2005a]). For example, the ionic conductivity of the most commonly used perfluorosulfonic acid (PFSA) electrolyte membrane Nafion, increases almost linearly with water content. Therefore, the water content of the membrane should be larger than a threshold value (minimum condition) under all operating conditions. The gas diffusion electrode (GDE) can be divided into the gas diffusion layer (GDL) and the catalyst active layer (CAL). The catalyst layer consists of particles, ionomer and pore spaces each of which are critical for the formation of the three-phase boundary where the electrochemical reactions take place. If the CAL contains too little water, its ionic conductivity will drop and not all of the catalyst surface will be accessible, which will contribute to increase the resistive and kinetic cell voltage losses. Too much water, on the other hand, will impede reactants transport and lead to mass transport related performance losses. Similarly, water presence in the GDL will impede gas transport from the flow channels to the catalyst layer. Consequently, the water content of the catalyst layer should lie between a minimum and a maximum value (optimum condition) and the GDL water content should be less than a maximum value (maximum condition). Finally, similar requirements must be overcome for the water presence into the gas channel.

As is seen in the state of the art, the water is a key point of the operation. There are several modelling, experimental characterisation and diagnosis methods, studying the water behaviour. Specially, there are some of the references (Gebregergis *et al.* [2010] and Fouquet *et al.* [2006]) that use the difference of the humidification temperature compared to the cell temperature, in order to analyse the response of the system. The *flooding* and *drying* processes in these references are forced during a long time over the system, and together with the degradation of the cell response and the unknown consequence of this extreme situations (keeping flooding or drying arises in voltage unstable situations) make these procedures high intrusive techniques for the fuel cell operation and cannot be used as "online" technique.

In following sections a complete test procedure is proposed to analyse the influence of the water content (humidity state of the inlet gases) over the fuel cell response. The main requirements for a proposed PEMFC diagnostic tool to be useful are:

- In-situ applicability
- Minimal invasiveness as possible
- Ability to provide localized information (about water presence in different zones)

In order to maximize the amount of information that can be extracted from an experimental test it is necessary to make use of advanced diagnostic methods and procedures. Such information can be used to:

1. Support the development of empirical correlations about the internal water state
2. Validate theoretical models useful to predict cell performance as function of operating conditions

The proposed experimental diagnosis setup in this work is an *humidification interruption test + short EIS*. This test is applied in-situ maintaining all the operational conditions (temperature, pressure and current) and forcing an humidification interruption and performing, in parallel, short duration EIS to get detailed information during the test.

Following the line of investigation of diagnosis methods presented in articles Stumper *et al.* [2005a], Barbir *et al.* [2005], Fouquet *et al.* [2006] and He *et al.* [2003], three novel experimental diagnosis tools are presented. All of them use experimental response of humidification interruption and EIS data.

They can be summarised as:

- Diagnosis based on *relevant characteristics* (see section 5.5).

In this case, a selection of the *relevant characteristics* obtained from the EIS evolution is proposed as performance indicators, and the diagnosis tool is based on this selection.

- Diagnosis based on *equivalent circuits* (see section 5.6).

In this case, a selection of the *equivalent circuit parameters* is proposed as performance indicators, and the diagnosis tool is based on these parameters.

- Model based diagnosis (see section 5.7).

In this case, indicators that are closer to the physical phenomena are introduced as key elements of the diagnosis tool. From EIS and polarisation curve data, the temporal evolution of three performance indicators (the effective active area, the diffusion coefficient and the membrane resistance) is obtained. A combination of these evolutions gives a diagnose of the fuel cell state.

The three diagnosis tools apply to H_2/Air as inlet gases, where a single impedance arc in the Nyquist response appears (see references Yuan *et al.* [2007] and Friede *et al.* [2004]).

5.4 Selected experimental test used as initial example

The selected experimental test used for the description of the diagnosis tools is the *cathode humidification interruption*, presented in section **4.5.1** with the following operating conditions: $I_{FC} = 1.0[A]$ and $P_{FC} = P_{amb}$ at $T_{FC} = 50$ [°C].

The time evolution of the selected cathode humidification interruption is presented again in figure 5.9.

The frequency response (Nyquist and Bode) of the selected cathode humidification interruption, can be seen in the figure 5.10.

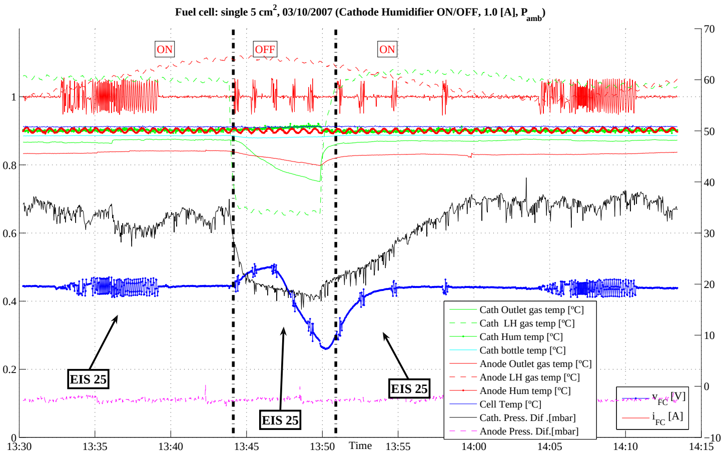

Figure 5.9: Cathode humidification OFF: T_{FC}= 50 °C, I_{FC}= 1.0 A, P_{FC}= P_{amb}

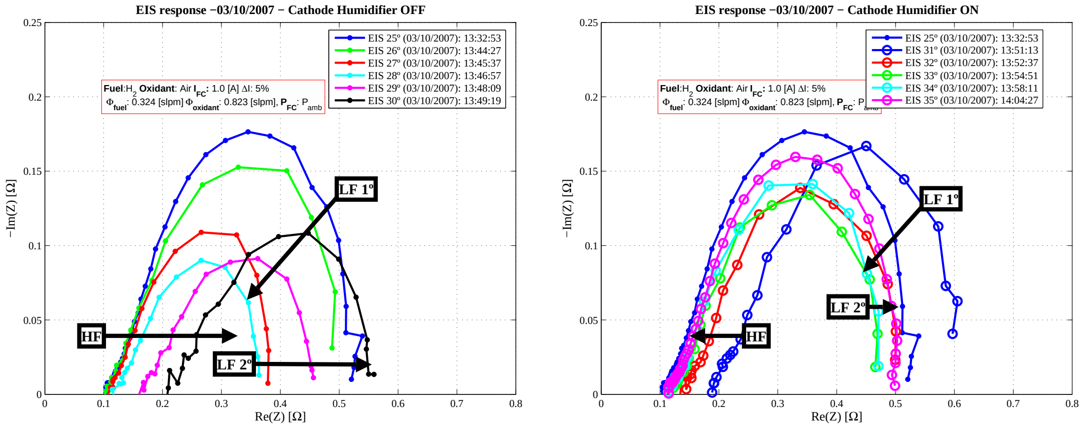

(a) Nyquist (Hum. OFF)

(b) Nyquist (Hum. ON)

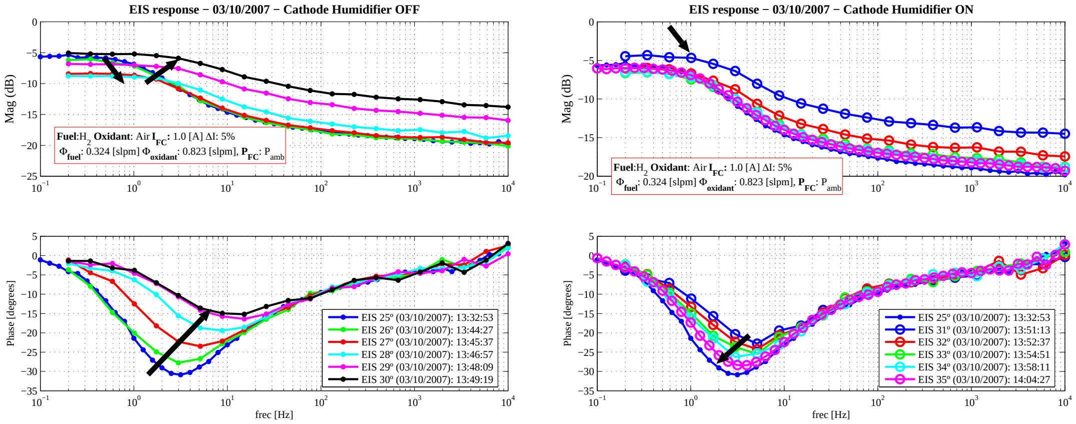

(c) Bode (Hum. OFF)

(d) Bode (Hum. ON)

Figure 5.10: Cathode humidification OFF: T_{FC}= 50 °C, I_{FC}= 1.0 A, P_{FC}= P_{amb}

5.5 Diagnosis based on relevant characteristics

Fouquet *et al.* [2006] focus on the problem of the on-line monitoring of the water content of PEM fuel cells through voltage and current measurements under dynamic conditions. The article shows how a model-based approach coupled with EIS results can help to identify a set of parameters exhibiting much greater sensitivity to flooding and drying than voltage and pressure drop does.

In this section, a diagnosis method to obtain *performance indicators* from EIS *relevant characteristics* during humidification interruption is proposed. A diagram of the steps followed in order to obtain the indicators is shown in figure 5.11.

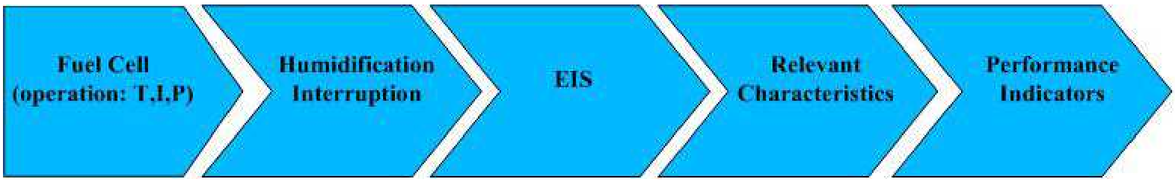

Figure 5.11: Diagnosis tool procedure based in the EIS relevant characteristics

The EIS *relevant characteristics* when H_2/Air are used as reactants (defined in section **4.5.2**) are: R_{LF}, $f_{Imax,LF}$, R_{HF}, $\phi_{max,LF}$ and $f_{\phi max,LF}$.

The relevant characteristics evolution after the cathode humidification interruption are presented in table 5.1. The most sensitive ones are: R_{LF}, R_{HF} and $f_{\phi_{max,LF}}$. These characteristics will be used as *performance indicators*. The time evolution of the voltage is presented along with the proposed performance indicators in figure 5.12.

Table 5.1: Relevant characteristics obtained of the cathode humidification interruption

EIS	Hour	V_{fc}[V]	R_{LF}[Ω]	$f_{max,LF}$[Hz]	$Im_{Imax,LF}$[Ω]	$\phi_{max,LF}$[°]	$f_{\phi_{max,LF}}$[Hz]	R_{HF}[Ω]
25	13:32	0.441	0.51	1.58	-0.18	-30.86	3.16	0.103
26	13:44	0.480	0.48	1.74	-0.15	-27.75	2.99	0.102
27	13:45	0.497	0.38	2.99	-0.11	-23.47	5.14	0.108
28	13:46	0.460	0.36	5.14	-0.09	-19.42	8.82	0.118
29	13:48	0.358	0.46	5.14	-0.09	-16.40	15.16	0.161
30	13:49	0.284	0.55	5.14	-0.11	-15.19	15.16	0.207
31	13:51	0.366	0.58	2.99	-0.17	-22.81	5.14	0.188
32	13:52	0.421	0.50	2.99	-0.14	-24.26	5.14	0.128
33	13:54	0.439	0.46	1.74	-0.13	-25.45	5.14	0.116
34	13:58	0.440	0.47	1.74	-0.14	-26.27	2.99	0.114
35	14:04	0.439	0.50	2.00	-0.16	-28.39	3.98	0.112

It is very important to see how the evolution of the selected relevant characteristics helps to understand some of the processes involved in the fuel cell performance.

Observing the evolution of the cell voltage and resistances, there are two zones of evolution **during** the cathode humidification interruption, (see figure 5.12):

- **Zone 1**

The voltage grows, the low frequency resistance decreases, the frequency of the low frequency maximum phase and high frequency resistance increases at a slower rate. As is

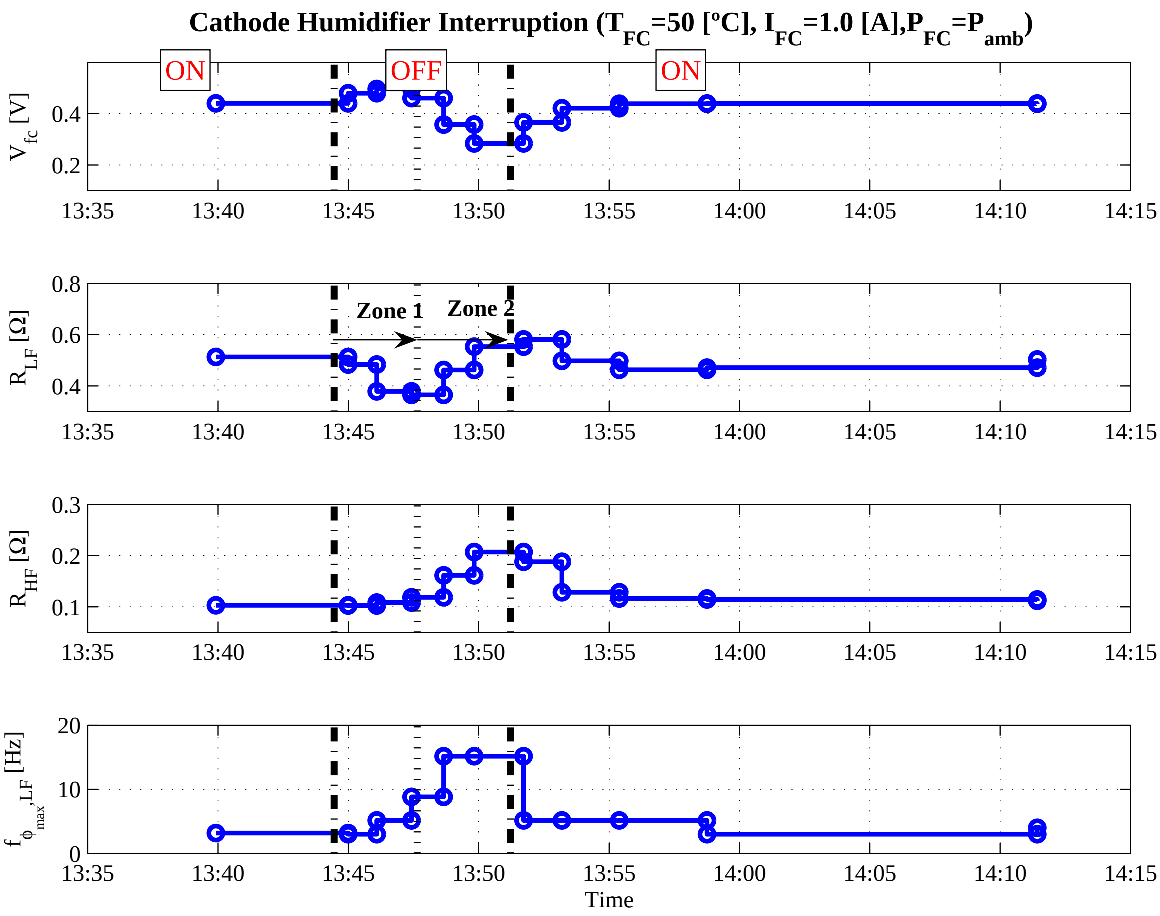

Figure 5.12: Proposed performance indicators during cathode humidification interruption

mentioned in the previous chapter, during this interval better diffusion conditions, the increasing oxygen concentration at the channel and the water liquid evaporation at the catalyst layer and at the GDL, allow more accessibility of oxygen gas particles to the reaction sites.

These effects reflect in the voltage and in the low frequency resistance. At the same time, the membrane water content starts to decrease due to a water concentration difference between the membrane and the cathode channel. As the membrane is hydrophilic, the resistance does not increase immediately because there is a water retention during this zone.

- **Zone 2**

The cell voltage falls, R_{LF} increases and R_{HF} grows at a higher rates. In this zone, the water starts to move out from the membrane to the cathode channel (due to the water concentration difference). This movement affects the membrane resistance, directly related to its water content. The membrane water losses also reduce the reaction sites for hydrogen protons connected by water paths to the membrane. These complex and coincident effects can be interpreted as the temporary difficulty to access the platinum sites. Observing that the evolution of $f_{\phi,max,LF}$, has reached a steady state in this zone, it can be concluded that the diffusion process has reached an equilibrium.

- **Humidification reconnection**

From the evolution of the selected EIS relevant characteristics at the reconnection of cathode humidification system, it can be observed that there are no maximums and minimums in none of them. Therefore a separation in two zones is not seen. This is due to two contrary simultaneous effects: diffusion deterioration and improvement of the accessibility to reaction sites.

Performance indicators from relevant characteristics

Evolution in percent of the selected relevant characteristics variation, taking as reference the initial “long EIS” values (steady state before humidification interruption) is presented in table 5.2.

Table 5.2: Variation of performance indicators for cathode humidification interruption

EIS	ΔR_{LF} [%]	$\Delta f_{\phi_{max},LF}$ [%]	ΔR_{HF} [%]
26	-5.2	-5.4	-0.4
27	-23.9	62.5	5.2
28	-28.1	179.0	15.2
29	-9.4	379.3	56.8
30	8.5	379.3	101.1
31	19.9	62.5	77.5
32	-2.4	62.5	27.4
33	-9.3	62.5	13.2
34	-7.7	-5.4	11.4
35	-10.5	25.9	8.7

For example, the variation of R_{LF} is very useful to get the separation of zones. The first zone of evolution is determined by a negative trend of R_{LF} (from 0.0% to -28.8 %) and the second zone of evolution is determined with a positive trend (from -28.8 % to 20%).

Table 5.3: Relevant characteristics trends, cathode humidification interruption

Zone	R_{LF}	R_{HF}	$f_{\phi_{max},LF}$
1^{o}	$< 0, \downarrow\downarrow$	$> 0, \uparrow$	$> 0, \uparrow$
2^{o}	from $< 0 \rightarrow > 0, \uparrow\uparrow$	$> 0, \uparrow\uparrow$	$> 0, \approx cte.$
Reconnection	$< 0, \downarrow$	$< 0, \downarrow$	$< 0, \downarrow\downarrow$

In the case of R_{HF}, its evolution has a slow rate at the first zone (from 0.0% to 15% in 3 short EIS points), changing to high rate of evolution in the second zone (from 15.0% to 101.0%, in 3 short EIS points).

Finally, $f_{\phi,max,LF}$ presents a high increasing rate in the first zone of evolution (from 0% to 379%, in 3 short EIS points) while in the second part it remains almost constant.

5.5.1 Cathode humidification interruption: temperature variation

In order to summarize the effects of the cathode humidification interruption on the performance indicator evaluation, for different operation temperatures, the evolution of R_{LF}, R_{HF} and $f_{\phi_{max,LF}}$ is shown in the figure 5.13(c)).

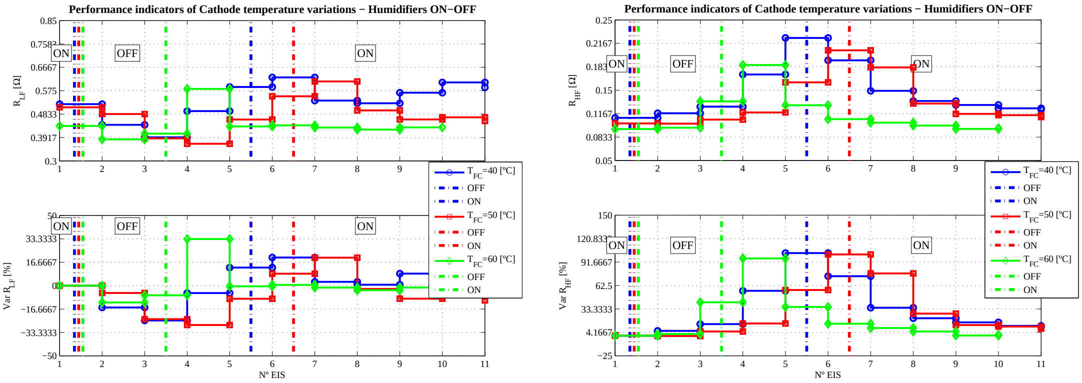

(a) R_{LF}

(b) R_{HF}

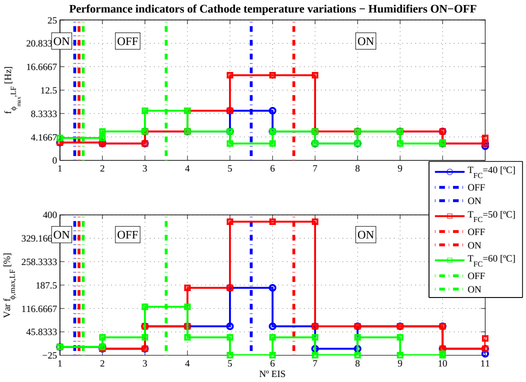

(c) $f_{\phi_{max,LF}}$

Figure 5.13: Indicator performance, temperature variation

It is very important to observe that the evolution of all the performance indicators have the same shape in all cases. This fact shows the good choice of these variables as performance indicators, because their behaviour is repetitive at similar conditions.

5.5.2 Anode humidification interruption

The evolution of the *performance indicators* with anode humidification interruption, at the same operating conditions as in the cathode humidification interruption, is studied in this section.

The time evolution of the anode humidification interruption is presented in figure 5.14.

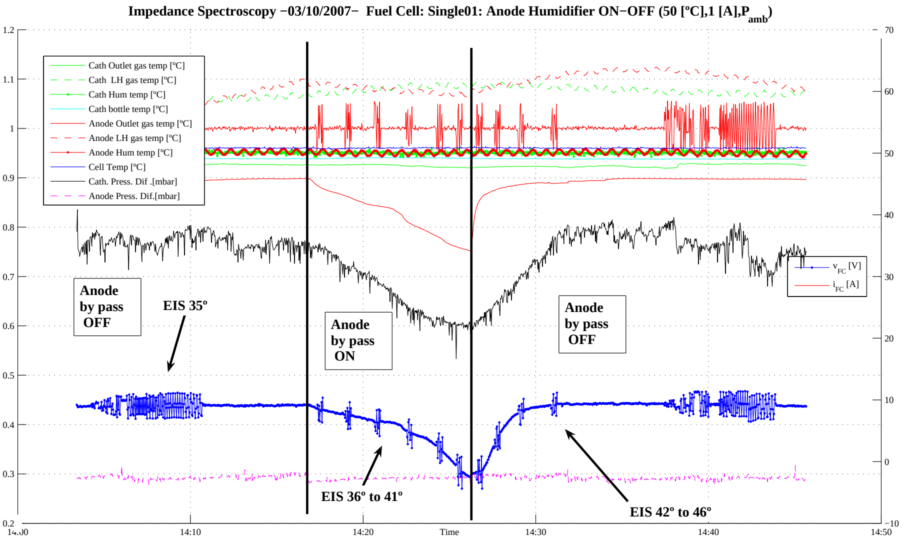

Figure 5.14: Anode humidification interruption: T_{FC}= 50 °C, I_{FC}= 1.0 A, P_{FC}= P_{amb}

The relevant characteristics of anode interruption are presented in table 5.4 and figure 5.15 shows the evolution of the selected performance indicators.

Table 5.4: Relevant characteristics of anode humidification interruption

EIS	**Hour**	V_{fc}[V]	R_{LF}[Ω]	$f_{max,LF}$[Hz]	$Im_{Imax,LF}$[Ω]	$\phi_{max,LF}$[°]	$f_{\phi_{max,LF}}$[Hz]	R_{HF}[Ω]
35	14:04	0.44	0.50	2.00	-0.16	-28.39	3.98	0.11
36	14:17	0.43	0.54	1.74	-0.17	-28.69	2.99	0.11
37	14:19	0.42	0.57	1.74	-0.17	-28.38	5.14	0.12
38	14:20	0.40	0.58	1.74	-0.17	-28.51	5.14	0.13
39	14:22	0.38	0.61	1.74	-0.19	-29.28	2.99	0.14
40	14:24	0.33	0.67	1.74	-0.19	-27.30	2.99	0.15
41	14:25	0.30	0.72	1.74	-0.19	-25.88	2.99	0.17
42	14:26	0.34	0.73	1.74	-0.23	-28.13	2.99	0.17
43	14:27	0.40	0.60	1.74	-0.21	-29.56	2.99	0.13
44	14:29	0.43	0.53	1.74	-0.15	-27.22	5.14	0.12
45	14:31	0.44	0.49	1.74	-0.14	-27.16	5.14	0.11
46	14:37	0.44	0.52	2.00	-0.16	-28.96	3.16	0.11

In this case, the voltage and the relevant characteristics are affected in a different way than in the cathode humidification interruption case. Validating the importance of cathode losses in front of anode ones, it seems that the cell can be stabilised with a lower (or inexistent) humidification on anode side.

The membrane (high frequency resistance) is obviously affected due to the migration of

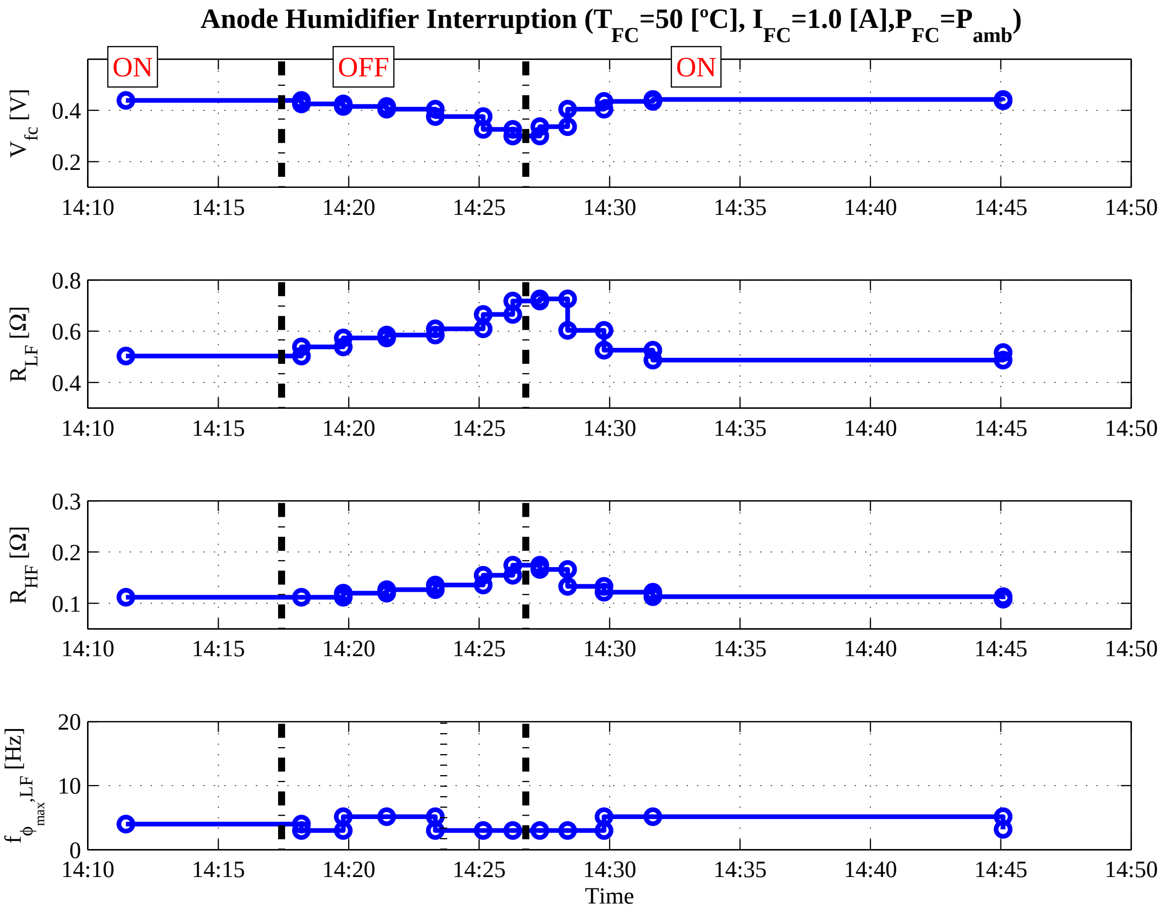

Figure 5.15: Performance indicators for anode humidification interruption

water from cathode to anode. But this effect is counteracted by the electro-osmotic drag effect. It is very important to note that the high frequency resistance (R_{HF}) increases its value at a constant rate (not so high as for the cathode humidification interruption). This indicates that the water movement from the cathode to the anode helps to maintain the water content enough to hold the rate of change at lower values.

The low frequency resistance (R_{LF}) evolution is motivated by the progressive reduction of the available water paths near the reaction sites.

The evolution of the indicators with the anode humidification interruption are presented in table 5.5. As it can be observed the low frequency resistance (R_{LF}) increases from 0% to 45% during the humidification interruption and the high frequency resistance (R_{HF}) increase from 0% to 56%, indicating the evolution to a lower performance operating state. Despite the loss of performance, it is possible to continue working without the humidification of the hydrogen at the anode side. The frequency $f_{\phi,max,LF}$ has a lower variation and does not change significantly during the humidification interruption. This fact indicates that the diffusion is almost stable during the anode humidification interruption.

The selected *performance indicators* derived from the relevant characteristics, show that the phenomena occurring during the anode humidification interruption can be interpreted as

Table 5.5: Variation of some of relevant characteristics of anode humidification interruption

EIS	ΔR_{LF} [%]	ΔR_{HF} [%]	$\Delta f_{\phi,max,LF}$ [%]
36	7.0	-24.9	0.0
37	14.0	29.0	7.0
38	16.2	29.0	13.0
39	21.0	-24.9	21.2
40	32.3	-24.9	38.3
41	42.6	-24.9	56.0
42	44.3	-24.9	48.4
43	19.8	-24.9	18.7
44	4.4	29.0	8.9
45	-3.3	29.0	1.1
46	2.7	-20.6	-3.5

Table 5.6: Relevant characteristics trends, anode humidification interruption

Zone	R_{LF}	R_{HF}	$f_{\phi_{max},LF}$
Disconnection	$> 0, \uparrow$	$> 0, \uparrow$	$> 0, \approx cte.$
Reconnection	$< 0, \downarrow$	$< 0, \downarrow$	$> 0, \approx cte.$

a drying effect of the membrane and a movement of water from the cathode side to the anode side, including the water of the cathode catalyst layer-GDL.

Then, at the same time that the membrane is drying near the anode side, at the cathode side, the water is moving out due to a concentration difference (back diffusion) and the number of reaction sites is reduced due to water paths loss for protons, causing an active area reduction in the cathode side. These effects, the membrane drying and the active area reduction, can be related to an increase of the low and the high frequency resistances.

5.5.3 Anode humidification temperature variation

In order to complete the description of the effects of the anode humidification interruption, the evolution of the low frequency resistance R_{LF}, the high frequency resistance R_{HF} and the low frequency phase maximum $f_{\phi,max,LF}$ is presented for different cell temperatures in figure 5.16.

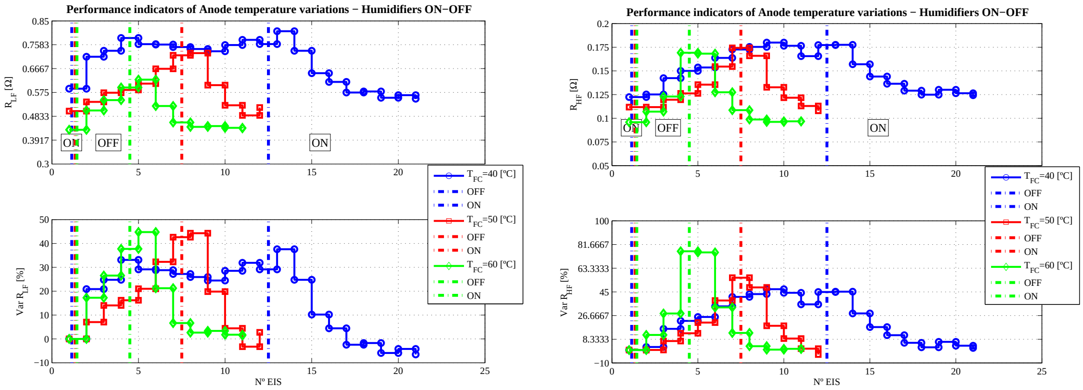

(a) R_{LF} (b) R_{HF}

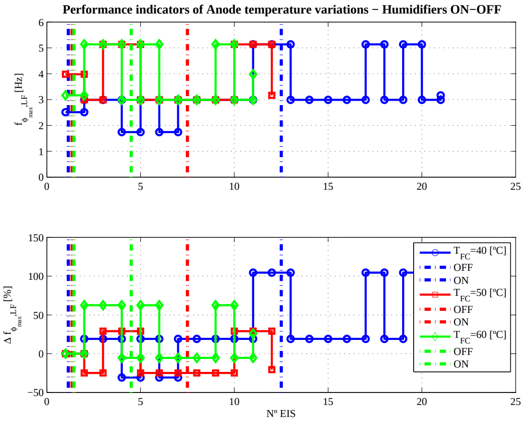

(c) $f_{\phi,max,LF}$

Figure 5.16: Indicator performance anode temperature variation

The evolution of the selected performance indicators, R_{LF}, R_{HF} and $f_{\phi,max,LF}$, has the same shape in all temperature cases. The resistances (R_{LF} and R_{HF}) increase its values after the anode humidification interruption starts. The only difference between one experimental condition and the other is the rate of increment of the values, where the test done at the temperature T_{FC}=50 [°C] has the slower rate. The $f_{\phi,max,LF}$, shows a small variation around the starting value.

The longest anode humidification interruption (with T_{FC}=40 [°C]) is very useful because shows the possibility that the system works without the anode humidification, in spite of a lower performance.

5.5.4 Use of the humidification interruption test with the EIS relevant characteristics as a diagnosis tool

A set of EIS relevant characteristics are selected as *performance indicators* which, if properly monitored can give a diagnostic of the internal state of the fuel cell. Thanks to the relative low impact of the test over the fuel cell state, this diagnosis procedure can be applied whenever it is required.

Comparing the results of the cathode and anode humidification interruption for the studied fuel cell it can be concluded that the cathode humidification interruption test gives more useful information about the humidification conditions. This result could be different for other cells, depending of the design and material, but it seems quite general because the diffusion of the hydrogen is higher than that of oxygen and it is not affected by the presence of water.

Therefore, the proposed diagnosis process, based on the cathode humidification interruption, is useful to determine if the cell with the current operating conditions is over- or under-humidified:

- If the evolution of the performance indicators after the interruption shows a large zone 1 (which is defined as the zone where R_{LF} decreases, R_{HF} increases slightly and $f_{\phi,max,LF}$ increases), the cathode is over-humidified
- If the evolution of the performance indicators after the interruption shows a very reduced zone 1, the cathode is optimally humidified
- If the evolution of the performance indicators after the interruption shows an inexisting zone 1, the cathode is under-humidified

At the same time, tables 5.3 and 5.6, are patterns that can be used to distinguish the water increase or decrease in anode or cathode sides.

5.6 Equivalent circuit parameters as diagnosis tool

The use of the EIS Relevant Characteristics as diagnosis tool has one main disadvantage: the performance indicators are not linked directly with physical parameters.

In chapter 3, the *equivalent circuits* modelling and fitting methods are presented as a good tool to match the experimental response with simplified models. Once the humidification interruption test gives some Relevant Characteristics, their link with the simple equivalent circuit arises naturally as a good option. A proposed procedure is summarized in figure 5.17, where from the humidification interruption test, the Relevant Characteristics are defined and linked to equivalent circuits parameters to get new performance indicators more related to the physical phenomena occurring inside the fuel cell.

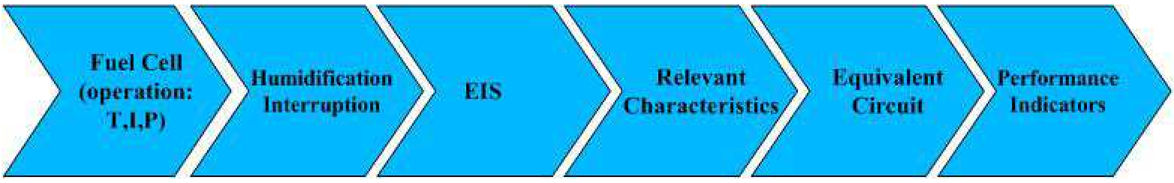

Figure 5.17: Diagnosis tool based in equivalent circuit

The study of the equivalent circuit models as diagnostic tools starts with the estimation of the parameters of an equivalent circuit from the Relevant Characteristics deduced as in section 5.5. The second step is the adjustment of the response via Zview® software, obtaining a better circuit parameter adjustment to experimental frequency response and good fitting. Finally, a selection of the most appropriate performance indicators is done.

The simple equivalent circuit employed is shown in figure 5.18, containing a resistance (representing membrane resistance) and a finite length Warburg element (representing a diffusion limited process).

Step 1: Determination of the parameters of the equivalent circuit

Next steps are followed in order to relate the Relevant Characteristics determined in the humidification interruption test and the equivalent circuit parameters:

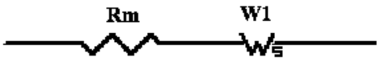

Figure 5.18: Simple equivalent circuit, H_2/Air response

- The high frequency resistance (R_{HF}) is an estimation of the ohmic effects, mainly due to the proton conduction resistance of the membrane:

$$R_m \approx R_{HF} \tag{5.1}$$

- The Warburg resistance (R_{W1}) is established from the difference between the low frequency resistance (R$_{LF}$) and the membrane resistance:

$$R_{W_1} \approx R_{LF} - R_m \tag{5.2}$$

- The Warburg time constant (T_{W1}) is given by the following equation, using the relevant characteristic $f_{\Phi\,\max,LF}$:

$$T_{W_1} \approx \frac{1}{2\pi f_{\Phi\,\max,LF}} \tag{5.3}$$

- The Warburg exponent (P_{W1}) is determined using a combination of the relevant characteristic $Im_{I,max,LF}$) and a trigonometric expression from the Warburg transfer function:

$$\begin{gathered} Im_{Imax,LF} = -\frac{R_{W_1} sen(\frac{P_{W_1}\pi}{2})}{2.(\cos(\frac{P_{W_1}\pi}{2})+1)} = -\frac{3}{8} R_{W_1}.\tan(\frac{P_{W_1}\pi}{2}) \\ \Rightarrow P_{W_1} = -\frac{4}{\pi}\arctan\left(-\frac{2.Im_{I\,\max,LF}}{R_{W_1}}\right) \end{gathered} \tag{5.4}$$

This procedure can be applied to all working situations to obtain the parameters of the equivalent circuit. Applying it to the cathode humidification interruption test explained in section 5.4 (at operating conditions: $I_{FC} = 1[A]$, $T_{FC} = 50[^oC]$ and $P_{FC} = P_{amb}$), the "procedure" estimated parameters are summarized in table 5.7.

Table 5.7: Simple equivalent circuit parameters

EIS	$R_m[\Omega]$	$R_{W1}[\Omega]$	$\tau_{W1}[s]$	P_{W1}
25	0.103	0.41	0.32	0.52
26	0.102	0.38	0.33	0.48
27	0.108	0.27	0.19	0.49
28	0.118	0.25	0.11	0.44
29	0.161	0.31	0.06	0.37
30	0.207	0.35	0.06	0.38
31	0.182	0.43	0.19	0.47
32	0.131	0.37	0.19	0.46
33	0.116	0.35	0.19	0.47
34	0.114	0.36	0.33	0.48
35	0.112	0.34	0.25	0.55

Step 2: Refining of the equivalent circuit parameters

After this first adjustment, a refining curve fitting is done using Zview® software, for all responses.

The resulting parameters are presented in table 5.8.

Table 5.8: Simple equivalent circuit adjusted by Zview

EIS	$R_m[\Omega]$	$R_{W1}[\Omega]$	$T_{W1}[s]$	P_{W1}
25	0.104	0.42	0.25	0.51
26	0.102	0.40	0.25	0.49
27	0.107	0.28	0.14	0.48
28	0.119	0.25	0.09	0.45
29	0.160	0.30	0.07	0.41
30	0.203	0.36	0.07	0.40
31	0.187	0.43	0.14	0.46
32	0.137	0.37	0.17	0.47
33	0.120	0.35	0.19	0.48
34	0.115	0.36	0.19	0.49
35	0.114	0.38	0.21	0.50

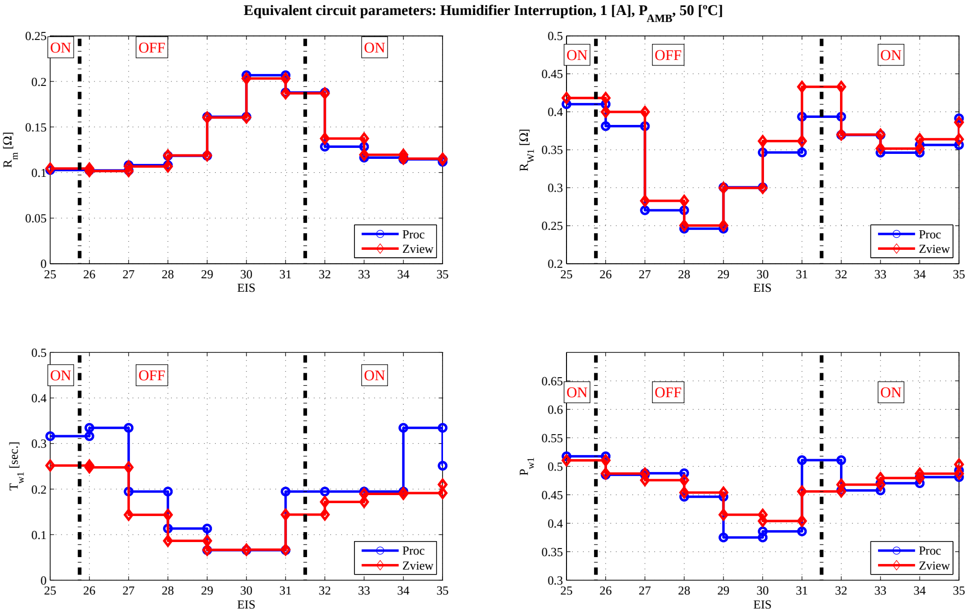

Figure 5.19: Comparison of the equivalent circuit parameters obtained from Relevant Characteristics and refined by Zview software

In figure 5.19, the comparison between the results of *procedure* parameters and *zview* parameters is presented.

All the parameters obtained follow the same profile and similar values using the "procedure" or the "zview" estimation. This indicates that the Relevant Characteristics are the procedure a good choice and a good approximation to get the value of the equivalent circuit parameters.

Relationship between the Warburg time constant and the diffusion coefficient

The Warburg time constant "$\tau_{W,d}$" gives an insight to the losses at the operating point, because there is a close relation between this parameter and diffusion processes as is described by the equation, presented in Fouquet *et al.* [2006]:

$$\tau_{W,d} = \frac{\delta_{GDL}^2}{D_{eff}} \tag{5.5}$$

Where δ_{GDL}, is the gas diffusion layer thickness (in [cm]) and D_{eff}, the effective diffusion coefficient (in $[cm^2/seg]$).

The evolution of $\tau_{W,d}$ and D_{eff} is presented in figure 5.20.

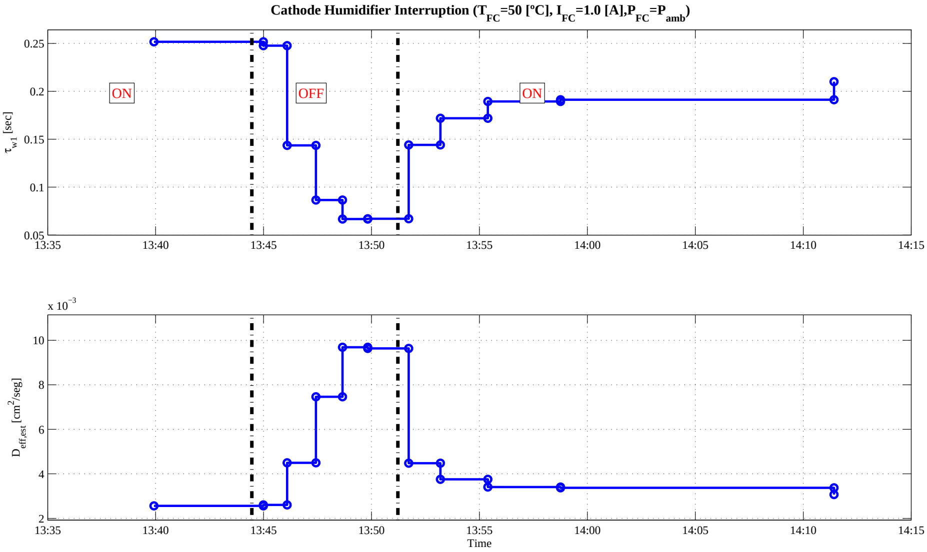

Figure 5.20: Warburg time constant and effective diffusion coefficient evolution

The $\tau_{W,d}$ parameter is directly linked with the diffusion processes and that relation can give another tool for understanding the fuel cell performance.

The trajectory of $\tau_{W,d}$ indicates that the diffusion coefficient is arriving at a constant value before the humidification is reconnected, see figure 5.20. This effect is due to an improvement of diffusion process due to water evaporation at the GDL/catalyst layer of the cathode side.

The maximum effective diffusion can be obtained from the minimum value of $\tau_{W,d}$ as follows:

$$D_{eff}|_{max} = \frac{\delta_{GDL}^2}{\tau_{W,d}|_{min}} = 0.0097 \left[\frac{cm^2}{s}\right] \tag{5.6}$$

This value is higher than the initial value of effective diffusion coefficient ($D_{eff,init}$=0.0026 $[cm^2/seg]$).

Performance indicators

Observing the response, R_m, R_W and τ_W, d can be selected as *performance indicators*. The advantage of these parameters is that they are equivalent circuit parameters.

In figure 5.21 the selected performance indicators from the equivalent circuit parameters is presented.

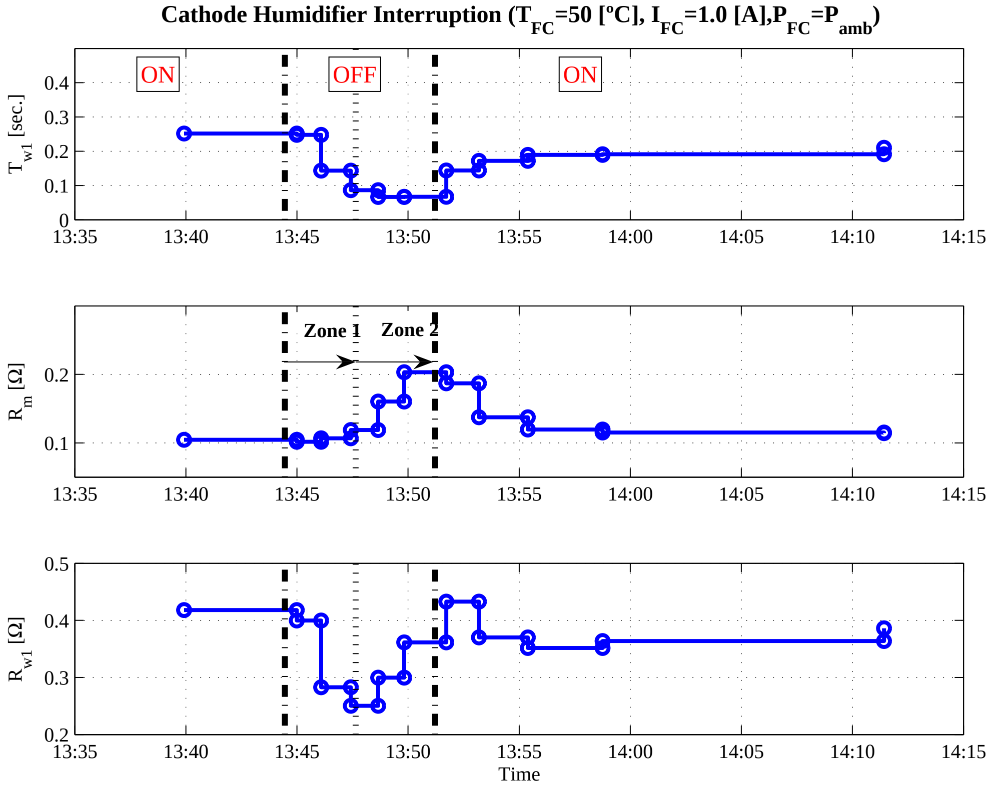

Figure 5.21: Selected equivalent circuit parameters as performance indicators

Analysing in more detail the evolution of these selected parameters in the interval where the humidification is interrupted, two zones can be defined. A physical interpretation of the phenomena occurring in each zone is summarised as:

- **Zone 1: Diffusion improvement**

In this zone the water inside the catalyst layer, the channel and the GDL rapidly disappears leading to an improvement of the effective diffusion coefficient and hence, an increase in the oxygen concentration at the catalyst layer. This interpretation is supported by the evolution of selected *performance indicators*: R_m starts to grow, at a low rate, the R_W and the τ_W decrease their values, due to a better effective diffusion process.

- **Zone 2: reaction sites losses**

In this zone, the diffusion coefficient reaches its limit; the membrane water content starts to reduce at a fast rate and also the reaction sites are lost due to the proton water path losses.

This interpretation is supported by the evolution of the selected *performance indicators*: R_m grows rapidly indicating water content reduction, R_W increases its value again, showing the loss of the reaction sites and the time constant τ_W arrives to stable values indicating the stabilization of the diffusion process.

- **Humidification reconnection**

From the evolution of the equivalent circuit parameters at the reconnection of cathode humidification system, it can be observed that there are no maximums and minimums in none of them. Therefore a separation in two zones is not seen, because of the concurrence of the diffusion deterioration and the increment of reaction sites.

5.6.1 Cathode humidification interruption temperature variation

In order to complete the analysis of the effects of the cathode humidification interruption on the performance indicators, their evolution for different operating temperatures is presented in figure 5.22.

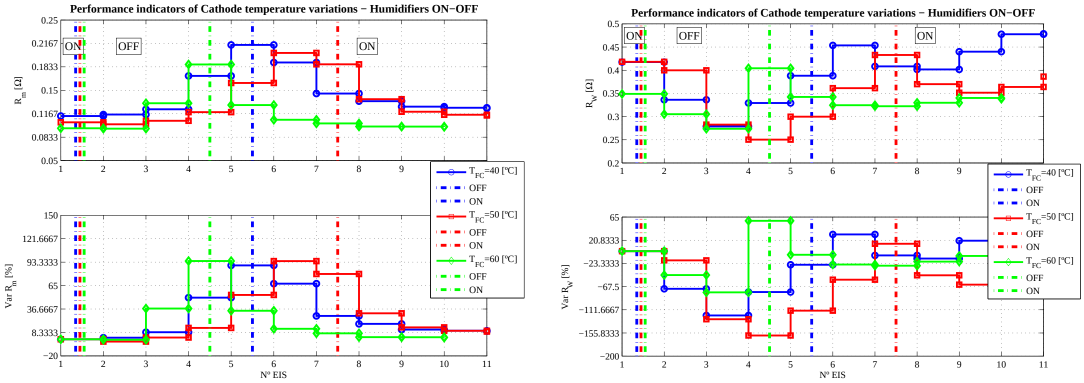

(a) R_m (b) R_W

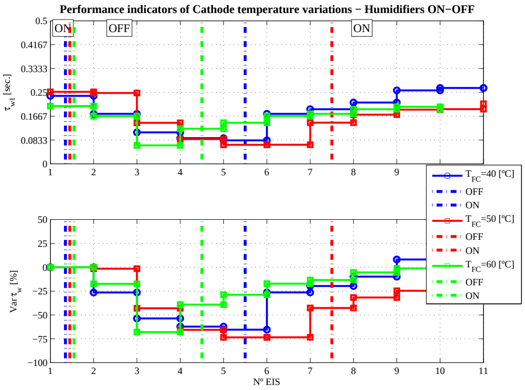

(c) τ_W

Figure 5.22: Performance indicators by EC, cathode temperature variation

The evolution of all the selected performance indicators has the same profile in all cases. Also, using the equation 5.6, the maximum of the effective diffusion coefficients for different temperatures are calculated and presented in table 5.9. In this table, it can be seen that the effective diffusion coefficient improves its maximum value with temperature.

Table 5.9: Maximum effective diffusion coefficients, cathode humidification temperature

T_{FC} $^o[C]$	40	50	60
D_{eff} $[\frac{cm^2}{s}]$	0.0079	0.0097	0.010

This shows that the indicators behave in a repetitive way in front of similar conditions and that they are appropriately chosen.

5.6.2 Anode humidification interruption

The figure 5.23 presents the comparison between the estimated parameters obtained using the two procedures described at the beginning of the section 5.6 for the *Anode humidification Interruption*.

The response to the anode humidification interruption shows that the membrane is continuously drying. When the interruption of the anode humidification occurs, there is no water accumulation and the drying effect appears immediately. On the cathode side, the water accumulated moves towards the anode side due to "back diffusion" (water concentration difference between anode and cathode), but this effect is not reflected as a gas diffusion improvement.

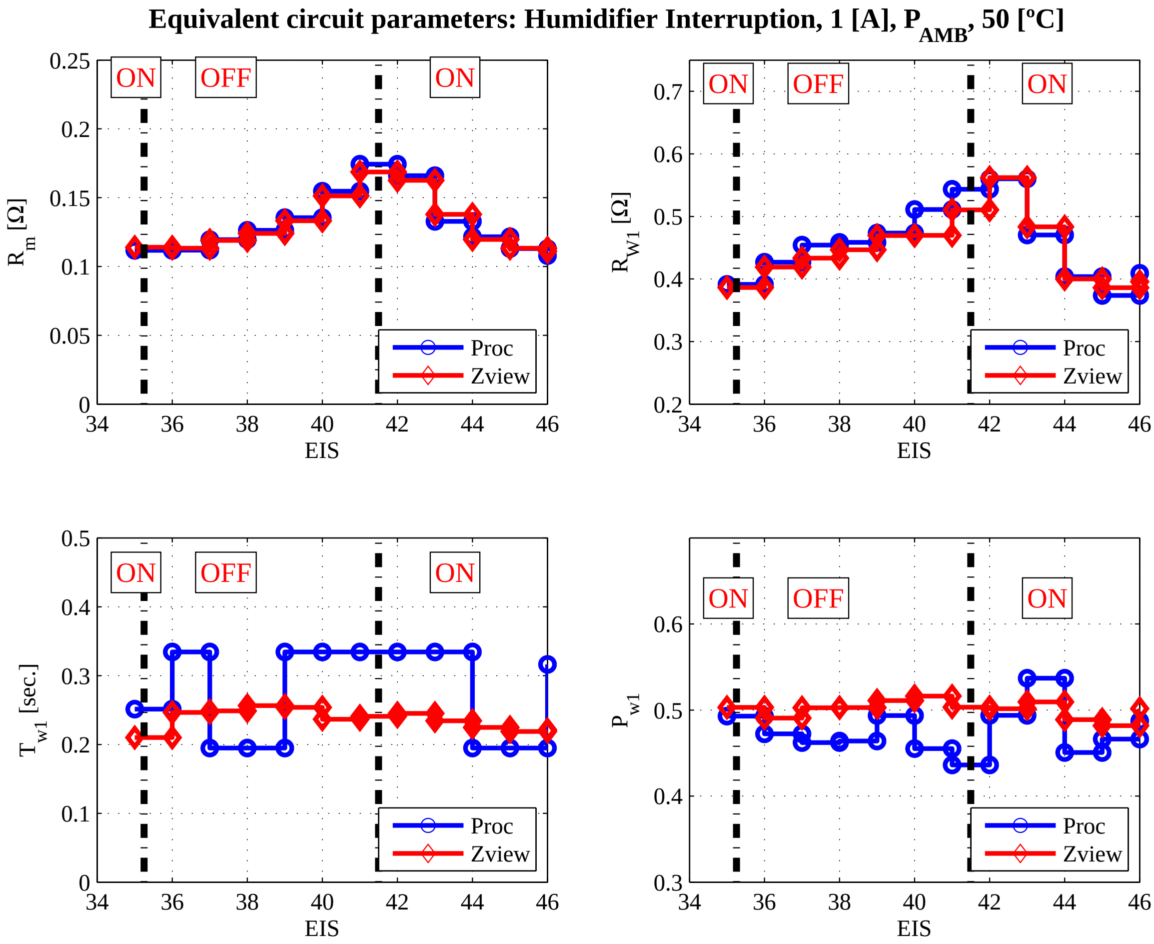

Figure 5.23: Comparison of the equivalent circuit parameters, $I_{FC} = 1[A]$, $T_{FC} = 50$[ºC] and $P_{FC} = P_{amb}$

The evolution of the selected *Performance Indicators* for the anode humidification interruption is showed in figure 5.24.

The maximum effective diffusion coefficient is calculated from the minimum value of τ_W

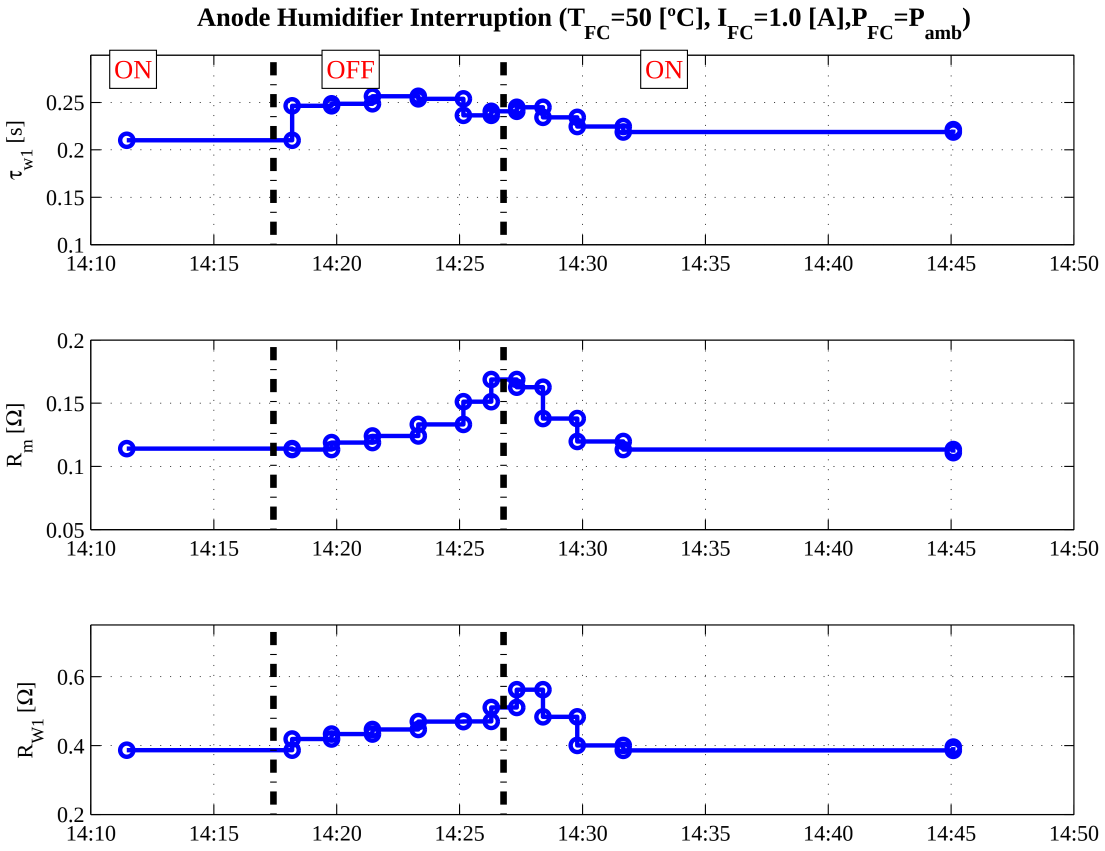

Figure 5.24: Performance indicators from Equivalent Circuit, anode interruption

as follows:

$$D_{eff}|_{max} = 0.0030 \left[\frac{cm^2}{s}\right] \tag{5.7}$$

This value is closer to the initial value of effective diffusion coefficient (D_{eff}=0.0025 [cm^2/seg]).

During the anode humidification interruption, the evolution of R_m and R_W depicts the drying effect over the membrane and the active area reduction of the fuel cell. The anode humidification interruption results in a drying effect and is reflected through a slow increase in the membrane resistance. The increase is not so fast as in the cathode humidification interruption test, because part of the water created in the cathode side is moving to the anode, reducing the rate of the drying effect, but not sufficiently to stop it. At the same time, reaction sites losses occurs at the cathode catalyst layer, due to the loss of water paths for protons to arrive to the reaction sites.

The evolution of τ_W gives support to the idea that the diffusion is not considerably affected by the anode humidification interruption, maintaining its value closer to the initial one. This is an interesting conclusion, supporting the assumption that the cathode side dominates the diffusion process and the low frequency losses.

5.6.3 Anode humidification temperature variation

In order to complete the analysis of the effects of the anode humidification interruption on the performance and on the indicators, the evolution of R_m , R_w and τ_w are presented for different operating temperatures.

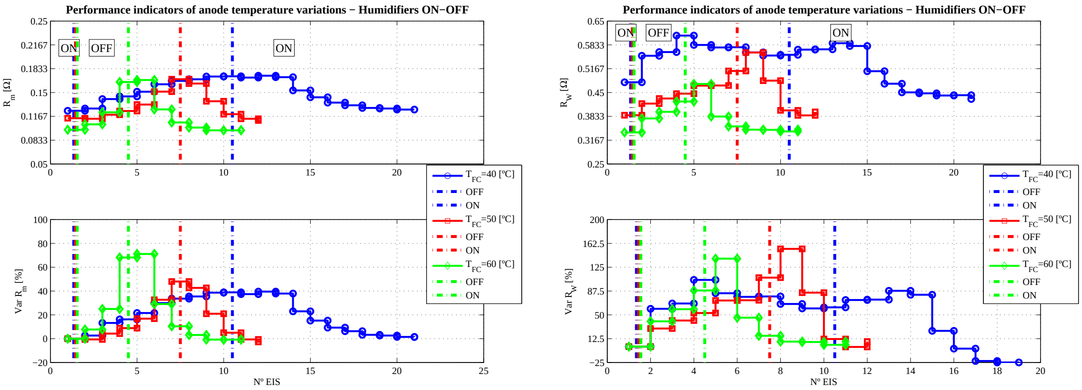

(a) R_m (b) R_w

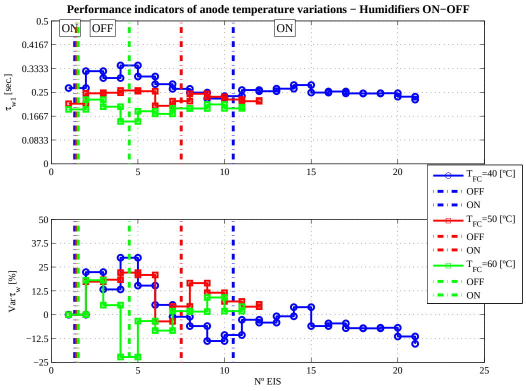

(c) τ_w

Figure 5.25: Performance indicators by EC, anode temperature variation

The evolution of the *selected performance indicators* presents the same global trends for all temperature cases. This supports the precedent conclusions that these indicators are appropriated to describe the interval evolution of the fuel cell.

The maximum of the effective diffusion coefficients for different temperatures when the anode humidification is interrupted are calculated and presented in table 5.10.

In this table, again, it can be seen that the effective diffusion coefficient improves its maximum value with temperature.

Table 5.10: Effective diffusion coefficients, anode humidification temperature

T_{FC} °$[C]$	40	50	60
D_{eff} $[\frac{cm^2}{s}]$	0.0030	0.0031	0.0044

The main difference of the effective diffusion coefficient compared with the cathode humidification interruption calculated ones, is that in this case the values are really closer to the initial ones. This fact confirms that the diffusion process of the anode side has a small influence.

5.6.4 Use of the humidification interruption test with the equivalent circuit parameters as a diagnosis tool

A simple equivalent circuit has been chosen for this diagnosis procedure, see figure 5.18 as well as its most sensitive parameters, which are R_m, τ_W and R_W. Initial values of these parameters are derived from the relevant characteristics as is explained in section 5.6. The procedure consists in monitoring and observing the evolution of these parameters after a humidification interruption. As is described in section 5.5.4 the diagnostic will depend of the existence and size of zone 1.

The importance of using the equivalent circuit parameters is the easy physical interpretation of them. Specifically the three selected parameters are: the membrane resistance R_m, the Warburg time constant τ_W, directly related to the diffusion process time constant, and the Warburg resistance R_W, directly related to the diffusion resistance.

Another important contribution of this diagnosis method is that, from the τ_W, the effective diffusion coefficient D_{eff} of the fuel cell can be obtained. Effectively, from the cathode humidification interruption, this diagnosis method allows the estimation of the effective diffusion coefficient, which has the following advantages:

- The effective diffusion coefficient corresponds to a physical property of the fuel cell
- It is useful for modelling purposes, specially in water transport modelling
- It is possible to find out the effective diffusion coefficient maximum which is a reference value that can be useful for degradation studies

5.7 Model based diagnosis tool

This section is devoted to complete the information of the phenomena occurring in the fuel cell during an humidification interruption. The additional information is obtained from a combination of the polarisation and the EIS curves, both deduced before the humidification test. In the first part of this section, the theoretic model of the polarisation curve is examined as well as the experimental conditions to obtain it experimentally. In the next subsection the relationship between the polarisation curve and the low frequency resistance deduced from EIS is presented. In the following subsection an estimation of the effective active area is proposed and subsequently used as the initial value for the adjustment during the humidification interruption test. Finally a selection of performance indicators is proposed and analysed under different operating conditions.

5.7.1 Polarization curve

In order to complement the performance indicators, the polarization curve (PC) of the fuel cell is very helpful.

The polarization curve of a fuel cell can be obtained from experimental response, under normal operating conditions (with both humidifications connected, ambient pressure and of a fixed fuel cell temperature). For example, the polarization curve obtained for the single fuel cell used in this thesis (described in chapter 2) when O_2/H_2 or Air/H_2 are used as reactants can be seen in figure 5.26.

Using the polarization expression described by Barbir [2005], the fuel cell voltage can be obtained from equation:

$$v_{fc} = E_0 - v_{ohm} - v_{act} - v_{conc} \tag{5.8}$$

Where, v_{fc} is fuel cell voltage, E_0 is the open circuit voltage, v_{ohm} is the ohmic voltage loss, v_{act} is the activation voltage loss and v_{conc} is the concentration voltage loss.

The *Open circuit voltage (E_0)* is the real voltage obtained when no current is applied. As is described in *chapter 2*, the open circuit real voltage, E_0, is lower than the ideal voltage $E_{0,ideal}$ for a fuel cell using hydrogen and oxygen as reactants where $E_{0,ideal}$= 1.229 [V]. E_0 can be calculated with the following expression (see reference Pukrushpan *et al.* [2004a]):

$$E_0 = E_{0,ideal} - K_{temp}(T_{fc} - T_{0,ref}) + K_{press}T_{fc}(log(p_{H_2}) + \frac{1}{2}log(p_{O_2})) \tag{5.9}$$

Where $T_{0,ref}$=298.15 [°K], is the reference temperature and p_{H_2} and p_{O_2} the reactants partial pressure in [atm] and T_{FC} the operating temperature of the fuel cell.

The *Ohmic losses* are caused by the ionic resistance in the membrane and in the electrodes (Larminie & Dicks [2003]), the electronic resistance in the electrodes, in the current collectors, and also the contact resistances. Ohmic losses are proportional to the current density, depending also of the material, the working temperature and the water content in the membrane (Barbir [2005]):

$$v_{ohm} = r_{ohm}i_{fc} \tag{5.10}$$

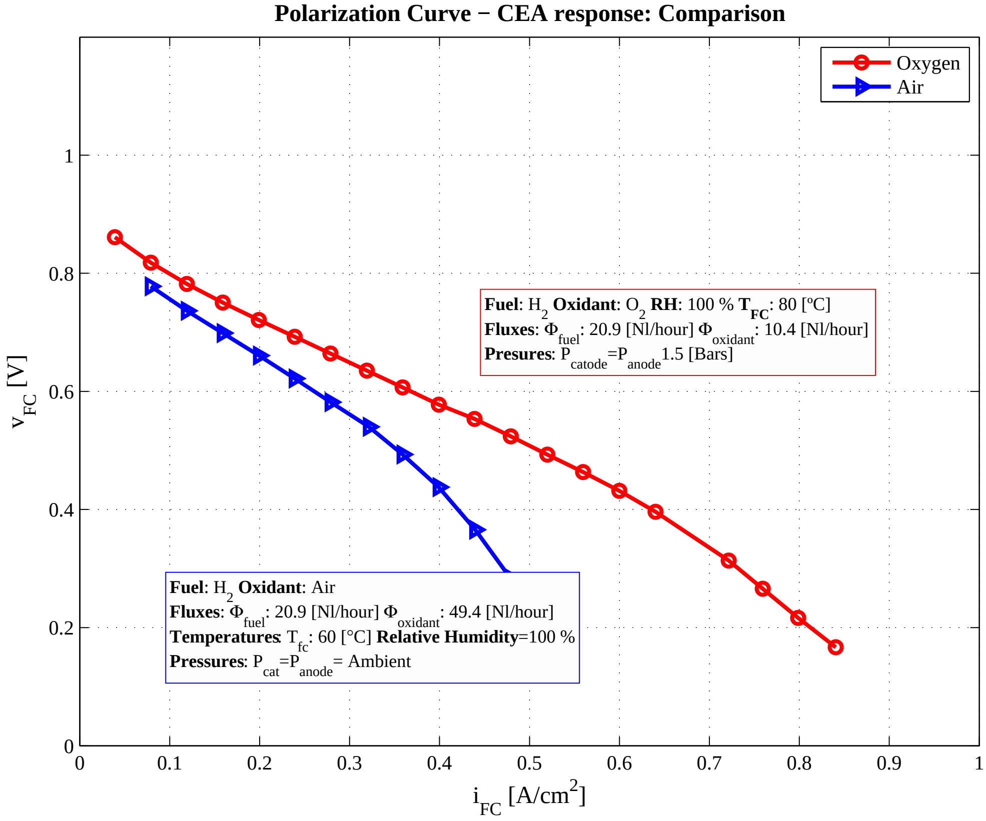

Figure 5.26: Polarization curve with O_2/H_2 and Air/H_2

Where r_{ohm} is the ohmic resistance per area [Ωcm^2] and i_{fc} is the current density [A$/cm^2$].

The *Activation polarisation losses* are due to the energy loss caused by the transfer of the electrical charge. Transfer of electrical charge is the activation energy barrier that the charge must overcome in moving from the electrolyte to the electrode or vice versa (seeBarbir [2005]). At equilibrium there is not charge transfer through the membrane. However, in the anode and in the cathode exists an exchange current density, defined as the inverse of the barrier that the charge has to overcome moving from the electrolyte to the catalyst surface. The exchange current density i_0 is a measure of an electrode's readiness to proceed with the electrochemical reaction. It depends on the concentration of reactants and in the anode it is much larger than in the cathode.

A simplified way to present the activation losses is using the Tafel equation:

$$v_{act} = \frac{RT}{\alpha F} \ln\left(\frac{i}{i_0}\right) \tag{5.11}$$

The *Concentration (mass transport) losses* are resulting of finite mass transport limitations rates of reactants, and depends strongly on the current density, the reactant activity and the electrode structure. One of the most used expressions is (Barbir [2005]):

$$v_{conc} = \frac{RT}{4F} \ln\left(\frac{i_L}{i_L - i}\right) \tag{5.12}$$

Where R is the universal gas constant $[J/(^oKmol)]$, T is fuel cell temperature $[^oK]$, F is the Faraday constant $[C/mol]$, i is the current density $[A/cm^2]$ and i_L is the limit current density $[A/cm^2]$.

The limit current density i_L is the maximum reachable current related with the concentration of oxygen at the channel and is defined as follows:

$$i_L = \frac{nFDc_{O_2,channel}}{\delta_{GDL}} \tag{5.13}$$

Where n is the number of electrons involved in the reaction, D is the effective diffusion coefficient and δ_{GDL} is the gas diffusion layer thickness (in the single fuel cell used in this thesis, $\delta_{GDL} = 0.01905$ [cm], according to Electrochem®data, coincident with toray TGP-H-060 carbon paper cloth data).

Summarizing, the voltage equation to model the fuel cell voltage is then:

$$v_{FC} = E_0 - r_{ohm}i - \frac{RT}{\alpha F}\ln(\frac{i}{i_0}) - \frac{RT}{4F}log(\frac{i_L}{i_L - i}) \tag{5.14}$$

If the parameters of equation 5.14, varies during the fuel cell life, its polarisation curve will also change, as is reflected in figure 5.27.

5.7.2 Calculation of the polarisation curve

The polarisation curve is obtained from the information under stable conditions. In this section, the polarisation curve of PEMFC the same day of the humidification interruption is searched from two experimental points and some modelling and calculations. The calculations are done for the general conditions presented in table 5.11.

Table 5.11: General conditions for polarisation experimental curve estimation

P_{cat} [bar]	P_{anod}[bar]	T_{FC}[°C]	$T_{cat,hum}$[°C]	$T_{anod,hum}$[°C]
1.10	1.07	50.8	49.9	50.5

In order to obtain the fuel cell voltage defined by equation 5.14, additional calculations must be done. Using the ideal gas law, it is possible to obtain the total concentration of all the present gases in the cathode and the anode humidifications:

$$c_{cat,tot,HUM} = \frac{P_{cat}}{RT_{cat,HUM}} \tag{5.15}$$

$$c_{anod,tot,HUM} = \frac{P_{anod}}{RT_{anod,HUM}} \tag{5.16}$$

Again, using the ideal gas law, it is possible to obtain the water vapour concentration at the humidification:

$$c_{H_2O,hum} = \frac{n_{H_2O,hum}}{V_{hum}} = \frac{p_{sat}(T_{hum})}{RT_{hum}} \tag{5.17}$$

where $p_{sat}(T_{hum})$ is the water saturation pressure at the humidifier temperature in the anode and the cathode side.

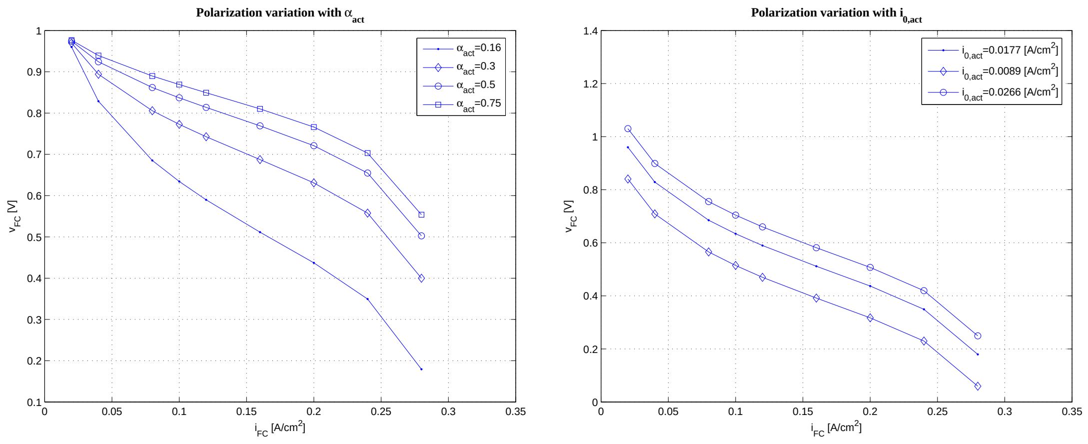

(a) α variation (b) i_0 variation

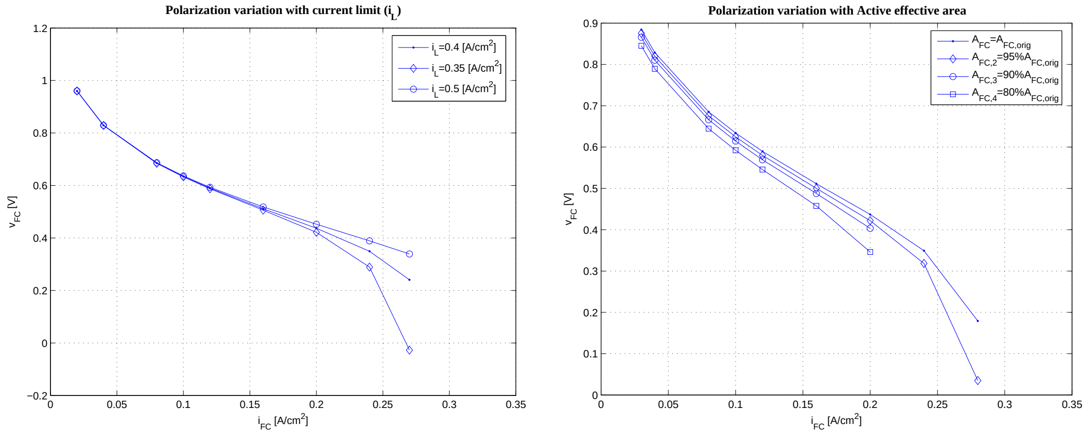

(c) i_L variation (d) A_{FC} variation

Figure 5.27: Polarization curve variations parameters

Using the relationship between nitrogen and oxygen concentration:

$$\frac{c_{O_2}}{c_{N_2}} = \frac{0.21}{0.79} \tag{5.18}$$

The calculation of the oxygen and hydrogen concentration at humidifier are given by:

$$c_{O_2,hum} = \frac{(P_{hum,cat} - p_{sat}(T_{hum,cat}))}{RT_{hum,cat}} \frac{1}{(1 + ({}^{0.79}/_{0.21}))} \tag{5.19}$$

$$c_{H_2,hum} = \frac{(P_{hum,anod} - p_{sat}(T_{hum,anod}))}{RT_{hum,anod}} \tag{5.20}$$

The relationship between $c_{O_2,hum}$ and $c_{cat,tot,hum}$ and between $c_{H_2,hum}$ and $c_{anod,tot,hum}$ can be obtained as:

$$k_{O_2,hum} = \frac{c_{o_2,hum}}{c_{cat,tot,hum}} \tag{5.21}$$

$$k_{H_2,hum} = \frac{c_{H_2,hum}}{c_{anod,tot,hum}} \tag{5.22}$$

The total gas concentration at the fuel cell channels is obtained with ideal gas law as:

$$c_{cat,tot,ch} = \frac{P_{cat}}{RT_{FC}} \tag{5.23}$$

$$c_{anod,tot,ch} = \frac{P_{anod}}{RT_{FC}} \tag{5.24}$$

The Oxygen and Hydrogen concentration at the fuel cell channel are:

$$c_{O_2,ch} = k_{O_2,hum} c_{cat,tot,ch} = 0.76.10^{-5} \left[\frac{cm^3}{mol}\right] \tag{5.25}$$

$$c_{H_2,ch} = k_{H_2,hum} c_{anod,tot,ch} = 0.35^{-4} \left[\frac{cm^3}{mol}\right] \tag{5.26}$$

From these obtained concentration values, the partial pressures are calculated as follows:

$$p_{O_2} = c_{O_2,ch} RT_{FC} = 0.20\,[atm] \tag{5.27}$$

$$p_{H_2} = c_{H_2,ch} RT_{FC} = 0.93\,[atm] \tag{5.28}$$

The rest of variables needed to calculate the fuel cell polarization curve are: the effective diffusion coefficient (D_{eff}) , the limit current density (i_L), the ohmic resistance (R_m) and the activation polarisation parameters (α and i_0).

The effective diffusion coefficient is given by:

$$D_{eff} = \frac{\delta_{GDL}^2}{T_W} = 0.0026 \left[\frac{cm^2}{seg}\right] \tag{5.29}$$

where δ_{GDL}=0.0191 [cm] and T_W=0.25 [s], are obtained from the equivalent circuit parameters.

The limit current density is calculated as follows:

$$i_L = \frac{nFD_{eff} c_{O_2,ch}}{\delta_{GDL}} = 0.39 \left[\frac{A}{cm^2}\right] \tag{5.30}$$

The ohmic resistance (R_m) (and ohmic resistance per area r_{ohm}), is obtained from relevant characteristics as follows:

$$R_m = R_{HF} = 0.103\,[\Omega] \Rightarrow r_o hm = R_{HF}.A_{FC} = 0.515\,[\Omega.cm^2] \tag{5.31}$$

where A_{FC}=5 [cm^2], is the active area (from builder data).

And finally, when all the voltage losses are calculated, the activation voltage is obtained as follows:

$$v_{act} = E_0 - v_{FC,measured} - v_{ohm} - v_{conc} \tag{5.32}$$

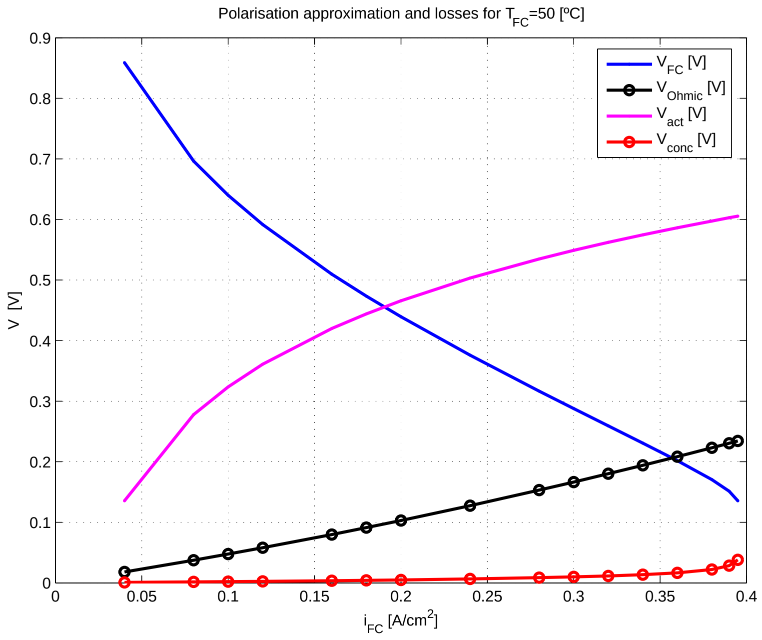

Figure 5.28: Polarization curve (T_{FC}=50 [°C], P_{FC}=P_{amb})

Then, combining the information from the equations 5.32 and 5.11, and two calculated points ($v_{act,1}$, $v_{act,2}$ at density currents i_1=0.1 [A/cm^2] and i_2=0.2 [A/cm^2]) obtained from two experimental points, the rest of parameters are calculated as follows:

$$\alpha_{act} = \frac{R.T_{FC}}{F\left(\frac{v_{act,1}-v_{act,2}}{\ln(i_1)-\ln(i_2)}\right)} = 0.16 \tag{5.33}$$

$$i_0 = e^{-\frac{F\alpha_{act}\left(v_{act,1}-\left(\frac{v_{act,1}-v_{act,2}}{\ln(i_1)-\ln(i_2)}\right)\ln i_1\right)}{RT}} = 0.017\left[\frac{A}{cm^2}\right] \tag{5.34}$$

With all the measured and calculated values, the polarisation curve is presented in figure 5.28.

5.7.3 Relationship between the polarisation curve and EIS results

As is described in references Yuan *et al.* [2007] and Macdonald & Barsoukov [2005], the relationship between the Nyquist plot and polarisation curves is that the low frequency resistance of the cell measured at a certain potential corresponds to the slope of the tangent of the polarisation curve at that potential (see figure 5.29).

Defining the polarization resistance as the slope of the polarisation curve at a given operating point, it can be obtained as:

$$R_{LF} = -\frac{\Delta V_{FC}}{\Delta I_{FC}} \tag{5.35}$$

where, R_{LF} is the low frequency resistance [Ω], V_{FC} is the fuel cell voltage [V], and I_{FC} is the current [A].

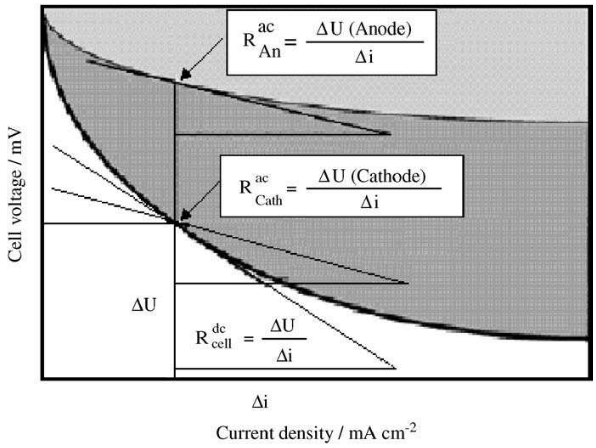

Figure 5.29: Relation between polarization curve and EIS (extracted from Macdonald & Barsoukov [2005])

If the current density i_{FC}, (in $[A/cm^2]$), is used instead of the current I_{FC}, the low frequency resistance per area r_{LF} (in $[\Omega cm^2]$), can be obtained as:

$$r_{LF} = -\frac{\Delta v_{FC}}{\Delta i_{FC}} \approx -\frac{dv_{fc}}{di_{fc}} \tag{5.36}$$

Combining the information from equation 5.36 and the cell voltage from the polarization curve (equation 5.14), the low frequency resistance can be approximated by:

$$r_{LF} \approx -\frac{dv_{fc}}{di_{fc}} = -(\frac{dv_{fc}}{di_{fc}}|_{ohm} + \frac{dv_{fc}}{di_{fc}}|_{act} + \frac{dv_{fc}}{di_{fc}}|_{conc}) \tag{5.37}$$

In this case, a calculation of the contribution of the losses (activation, ohmic and mass transport) to the low frequency resistance per area is described in the following steps.

The ohmic losses contribution is calculated as follows:

$$-\frac{dv_{fc}}{di_{fc}}|_{ohm} = r_{ohm} \approx R_{HF}.A_{FC} \tag{5.38}$$

where r_{ohm} is the ohmic losses per area $[\Omega cm^2]$, R_{HF} is the high frequency resistance (from Relevant Characteristics, $[\Omega]$) and A_{FC} is the active area, in $[cm^2]$.

The activation losses contribution is represented as:

$$-\frac{dv_{fc}}{di_{fc}}|_{act} = r_{act} = \frac{RT}{2\alpha Fi} \tag{5.39}$$

where r_{act} is the activation losses per area $[\Omega cm^2]$, R is the universal gas constant $[J/(^oKmol)]$, T is fuel cell temperature $[^oK]$, F is the Faraday constant $[C/mol]$, i is the current density $[A/cm^2]$ and i_L is the limit current density $[A/cm^2]$.

And finally, the concentration losses contribution is defined as:

$$-\frac{dv_{fc}}{di_{fc}}|_{conc} = r_{conc} = \frac{RT}{4F}\frac{1}{(i_L - i)} \tag{5.40}$$

where r_{conc} is the concentration losses per area $[\Omega cm^2]$, R is the universal gas constant $[J/(^oKmol)]$, T is fuel cell temperature $[^oK]$, F is the Faraday constant $[C/mol]$, i is the current density $[A/cm^2]$ and i_L is the limit current density $[A/cm^2]$.

Finally, the low frequency resistance can be calculated by

$$r_{LF} = r_{ohm} + \frac{RT}{2\alpha F i} + \frac{RT}{4F}\frac{1}{(i_L - i)} \tag{5.41}$$

The response of the low frequency resistance per area, r_{LF}, in $[\Omega.cm^2]$ as function of current density is presented in figure 5.30, considering the active area as the geometrical one, A_{FC}=5 cm^2.

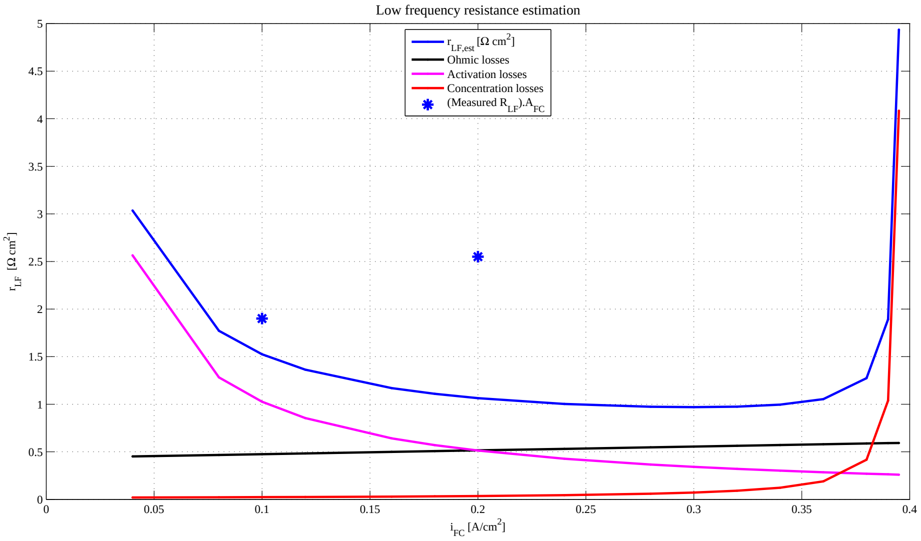

Figure 5.30: Low frequency resistance with current density

The response of the figure 5.30, shows that the calculated low frequency resistance (r_{LF}) is lower than the measured values of the low frequency resistance, multiplied by the geometrical area ($R_{LF} * A_{FC}$). This fact indicates that the effective area is lower than the geometrical area and should be calculated in order to obtain a good fitting between estimated and measured values.

Using the equation 5.14 of the fuel cell voltage jointly with the equations of the individual losses (from equation 5.10 to 5.12) and expressions from limit current density and effective diffusion coefficient (5.30 and 5.29), it is possible to calculate all the individual voltages of the polarisation curve as is shown in figure 5.31. The evolution of the equivalent resistances corresponding to the ohmic, concentration and activation losses are also given in figure 5.32.

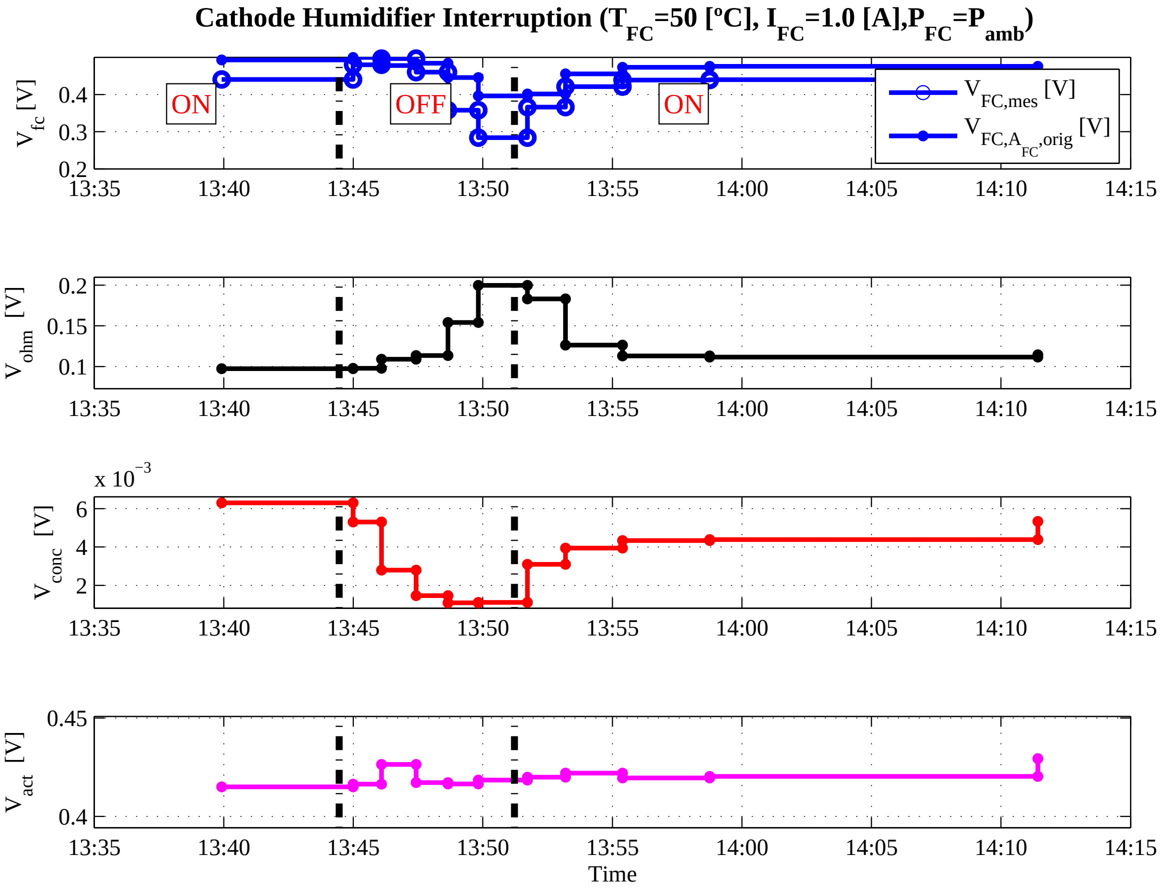

Figure 5.31: Voltages evolution with cathode humidifier interruption

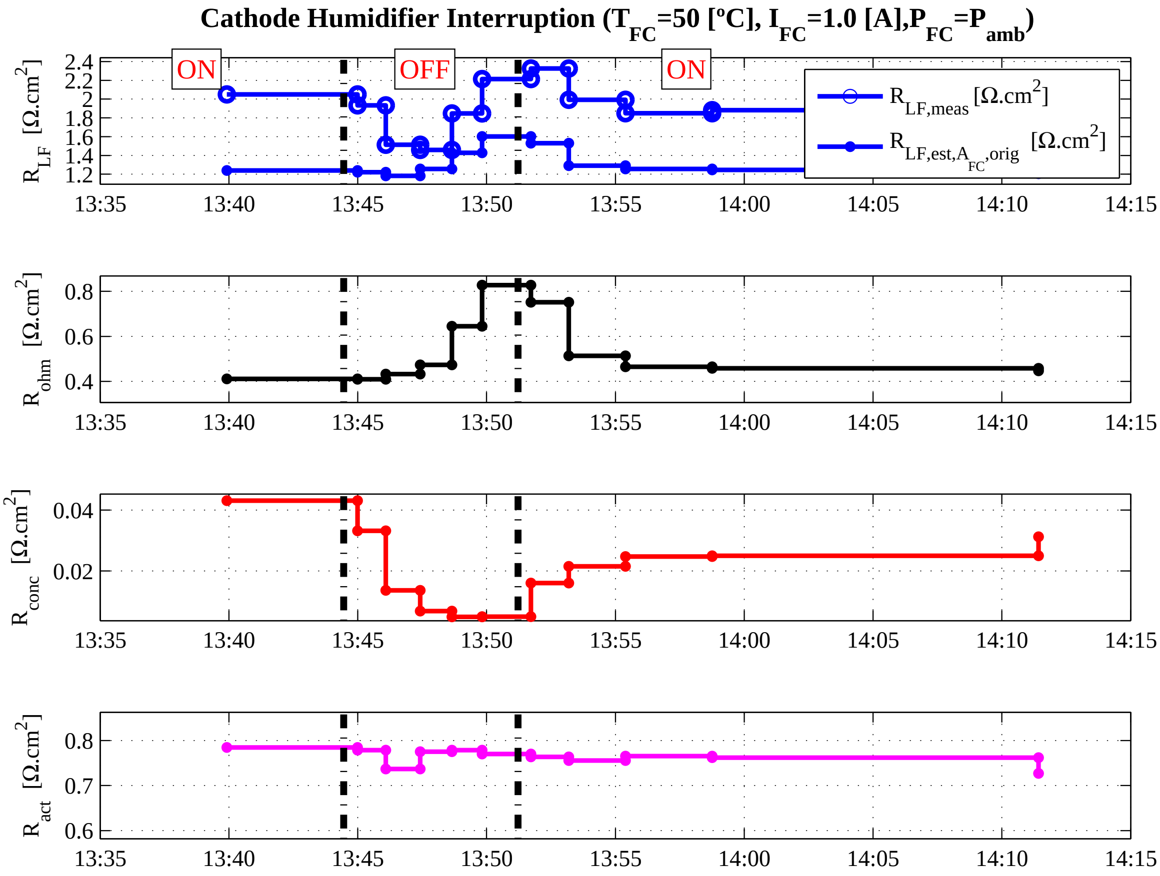

Figure 5.32: LF resistance evolution with cathode humidifier interruption

5.7.4 Effective active area estimation

The objective of this subsection is to study the performance degradation derived from the effective active area estimation (see reference Larminie & Dicks [2003]).

The active area modification in the fuel cell can be interpreted as the cause of the increase/decrease of resistances and voltage losses due to new inaccessible reaction sites.

Observing the evolution of the membrane resistance ($R_m = R_{HF}$) when the cathode humidification interruption is applied and the Warburg resistance (R_W, related with low frequency R_{LF} resistance), it is clear that the membrane holds the internal water until all liquid and water vapour inside the cathode GDL and catalyst layer has moved out to the cathode channel, coincident with diffusion coefficient improvement. Then, the membrane resistance raises at a high rate while the membrane water content starts to reduce.

An estimation of the actual effective active area, $A_{eff,FC}$, can be done from the measured low frequency resistance $R_{LF,meas}$. The applied procedure can be summarized as follow:

- Starting from equation 5.41, the low frequency resistance can be written as:

$$R_{LF}A_{eff,FC} = R_{HF}A_{eff,FC} + \frac{RT_{FC}}{\alpha F \frac{I_{FC}}{A_{eff,FC}}} + \frac{RT_{FC}}{4F\left(i_L - \frac{I_{FC}}{A_{eff,FC}}\right)} \tag{5.42}$$

- Arranging the equation 5.42, the relationship between R_{LF} and $A_{eff,FC}$ is:

$$\begin{array}{l} R_{LF} = R_{HF} + \frac{RT_{FC}}{\alpha F I_{FC}} + \frac{RT_{FC}}{4F\left(A_{eff,FC}i_L - I_{FC}\right)} \\ R_{ohm} = R_{HF};\ R_{act} = \frac{RT_{FC}}{\alpha F I_{FC}};\ R_{conc} = \frac{RT_{FC}}{4F(A_{eff,FC}i_L - I_{FC})}; \end{array} \tag{5.43}$$

- Using this equation as a reference, a relationship between the effective estimated area $A_{eff,FC}$ and α is obtained:

$$\alpha = \frac{4RT_{FC}\left(i_L A_{eff,FC} - I_{FC}\right)}{I_{FC}\left(4F(R_{LF} - R_{HF})\left(i_L A_{eff,FC} - I_{FC}\right) - RT_{FC}\right)} \tag{5.44}$$

- Once measured the values R_{LF} and R_{HF} at the operating current, I_{FC}, the estimated evolution of R_{LF} and of α with $A_{eff,FC}$ is obtained and presented in figure 5.33.

- Selection of the effective area reduction solution: As can be seen there are two possible values of estimated $R_{LF,approx}$ and α (intersection with $R_{LF,meas}$). The most suitable selection of the R_{LF} and α is for the higher value of $A_{eff,FC}$, because there is one special condition that must be fulfilled:

$$\left(i_L A_{eff,FC} - I_{FC}\right) > 0 \Rightarrow \frac{I_{FC}}{A_{eff,FC}} < i_L \tag{5.45}$$

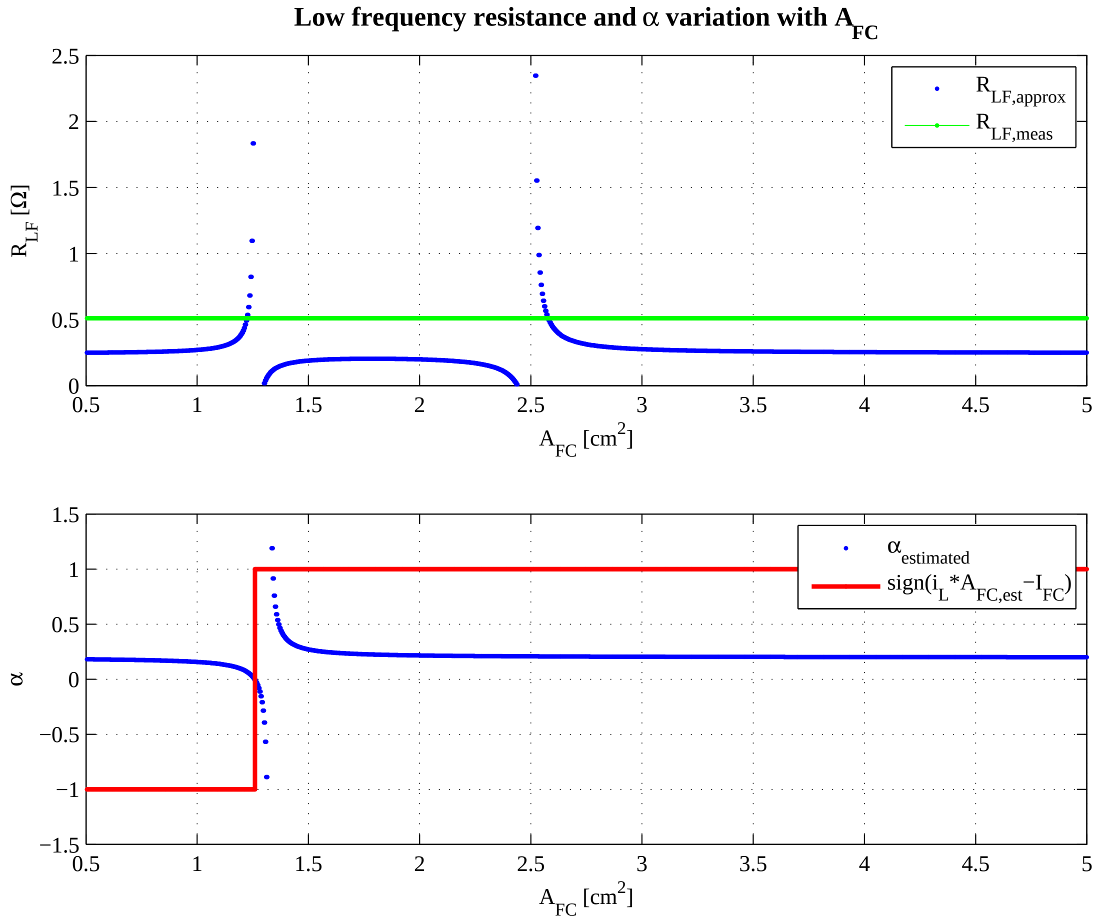

Figure 5.33: R_{LF} and α evolution with $A_{eff,FC}$

This condition is given for the meaning of *limit current density* (i_L), that is the maximum reachable current with the oxygen gas concentration at channel (see equation 5.13). In figure 5.33, the sign of function ($i_L A_{eff,FC} - I_{FC}$) is plotted together with α, giving the support to the $A_{eff,FC}$ selection. With the values obtained by this approximation, the low frequency resistance for the range of currents possible in the fuel cell is presented in figure 5.34, showing a good fit to the measured values and gives one explanation to the reduction of performance of the fuel cell.

- Finally, the only parameter that must also be adjusted in order to get total information about the low frequency resistance and fuel cell voltage is the exchange current density i_0, which can be obtained combining equations 5.14 and 5.41 as follows:

$$i_0 = \frac{I_{FC}}{A_{eff,FC}} e^{\left(\frac{-\alpha F}{RT_{FC}}\left(E_0 - v_{FC,meas} - R_m I_{FC} - \frac{RT_{FC}}{4F}\ln\left(\frac{i_L}{i_L - \frac{I_{FC}}{A_{eff,FC}}}\right)\right)\right)} \tag{5.46}$$

The estimated values of *effective active area* "$A_{eff,FC}$", *transfer coefficient* "α" and *exchange current density* "i_0" for fuel cell working at $T_{FC} = 50$ [°C], $P_{FC} = P_{amb}$, RH_{FC}=100

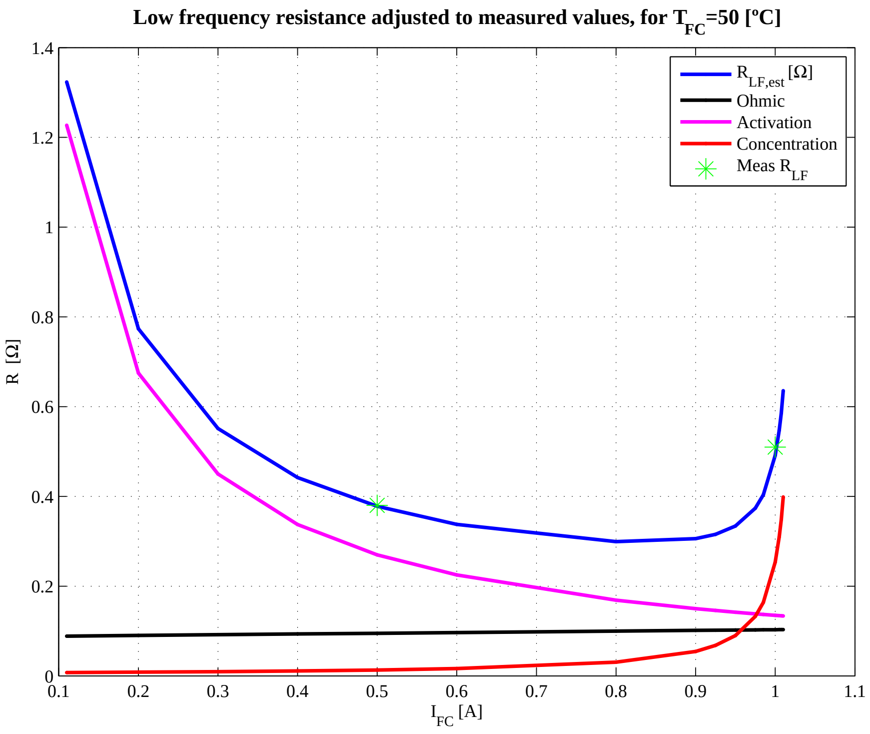

Figure 5.34: Low frequency resistance R_{LF} estimated

[%] and are detailed in table 5.12:

Table 5.12: Estimated values with $R_{LF,approx}$, T_{FC}=50 [°C], P_{amb} and RH_{FC}=100 [%]

$A_{eff,FC}$ $[cm^2]$	α	i_0 $[A/cm^2]$
2.59	0.206	0.016

The estimated value of transfer coefficient α is closer to those presented in literature, for example in the Barbir [2005], where the value of α is in the range $\alpha = 0.1 -> 0.5$. The effective active area is about the half of geometrical active area according to the cell builder, $A_{FC} = 5[cm^2]$, denoting the performance degradation of a hundred hours of testing and flooding/drying effects. The estimated values presented in table 5.12 are used to calculate the evolution of the low frequency resistance.

5.7.4.1 Effective active area estimation with the cathode humidifier interruption

In this section, an effective area estimation procedure applied during the cathode humidifier interruption is presented. The used model is represented by the equation 5.43, for the low frequency resistance and the equation 5.14, for the fuel cell voltage.

From the operating conditions measurements (I_{FC}, T_{FC}, $T_{HUM,CA}$, etc.), the reactants concentration and partial pressure are calculated at every time using the equations 5.15 to 5.28. The *relevant characteristics* and *equivalent circuit parameters* useful for the model are used at the corresponding EIS time (see tables 5.1 and 5.8) for the model actualisation. The effective diffusion coefficient is calculated using the equation 5.29 and combined with the other measured and calculated values, the limit current is calculated using the expression 5.30.

Three different options of the $A_{eff,FC}$ and i_0 application of the model are shown:

- **$A_{eff,FC}$ and i_0 constants**: Using the estimated values presented in table 5.12 as the reference values, $A_{eff,FC}$ and i_0 are keeped constant, observing the evolution of the model graphed in *red line*, showing the necessity of more adjustment of the response

- **$A_{eff,FC}$ variation and i_0 constant**: The variation of effective active area $A_{eff,FC}$ is done to minimize the SSE (equation 5.47) between measured $R_{LF,meas}$ and estimated $R_{LF,est}$ low frequency resistance.

  $$|R_{LF,meas} - R_{LF,A_{FC},est}| < \delta \tag{5.47}$$

  where δ is less than 1 %. The effective active area is estimated and the result is graphed in *black line*, in this case. The evolution of low frequency resistance is well adjusted (see figure 5.35(b)), but the fuel cell voltage 5.35(a) still is not well adjusted.

- **$A_{eff,FC}$ and i_0 variation**: Using the relationship between the "effective active area" and the "exchange current density" presented in equation 5.46, the results of the model adjustment is presented in *green line*. In this case, the voltage evolution 5.35(a) is also adjusted. This fact achieve the objective of get a physical interpretation of humidifier interruption effects.

The results are presented in figure 5.35, where the measured values of the fuel cell voltage 5.35(a) and low frequency resistance 5.35(b) are graphed with *blue line*. The results of the model when the *first option* ($A_{eff,FC}$ and i_0 constants) is used, are graphed with *red line*. The results of model when the *second option* ($A_{eff,FC}$ variable and i_0 constant) is applied, are graphed with *black line*. Finally, the results of the model when the *third option* ($A_{eff,FC}$ and i_0 variables) is applied, are graphed with *green line*.

It is important to note that the estimated value of active area (see figure 5.35(c)) is presented referenced to the estimated value showed in table 5.12 in order to get the evolution in percent.

In figure 5.36 the evolution of the estimated current density and the voltage activation losses are showed. Graphed in *red line* is the estimated value of i_0 (see table 5.12). In *black line* is plotted the variation of activation losses due the "effective active area" adjustment in order to catch the low frequency resistance evolution, and shows the increasing activation losses due to the active area reduction.

When the exchange current density is estimated trough the equation 5.46 and using the variation of the effective active area, the result is the *green line*. In this case, a first zone exists where the oxygen concentration is higher and hence the activation losses are reduced. After this diffusion improvement, the effective active area reduction due to membrane drying zone becomes the most important effect and the activation losses increases. At the same time, the exchange current density reduces its value, coincident with this membrane drying effect.

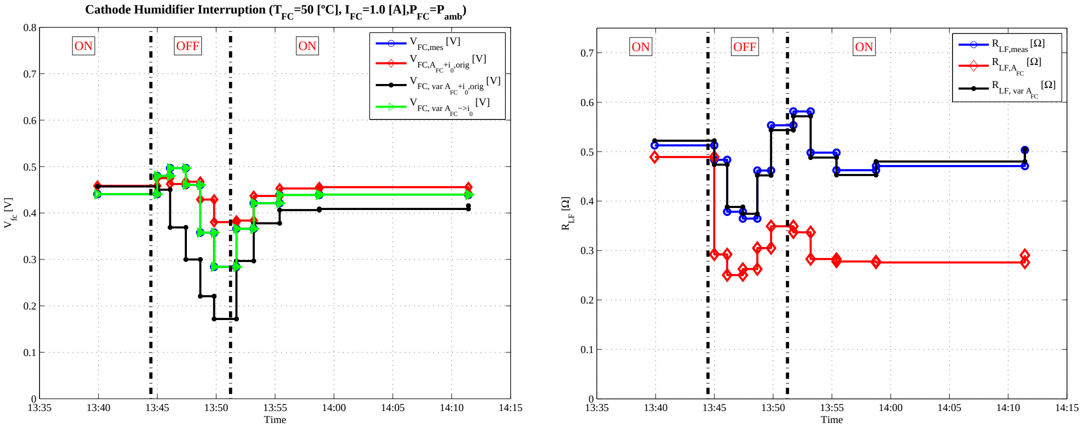

(a) Voltage (b) R_{LF}

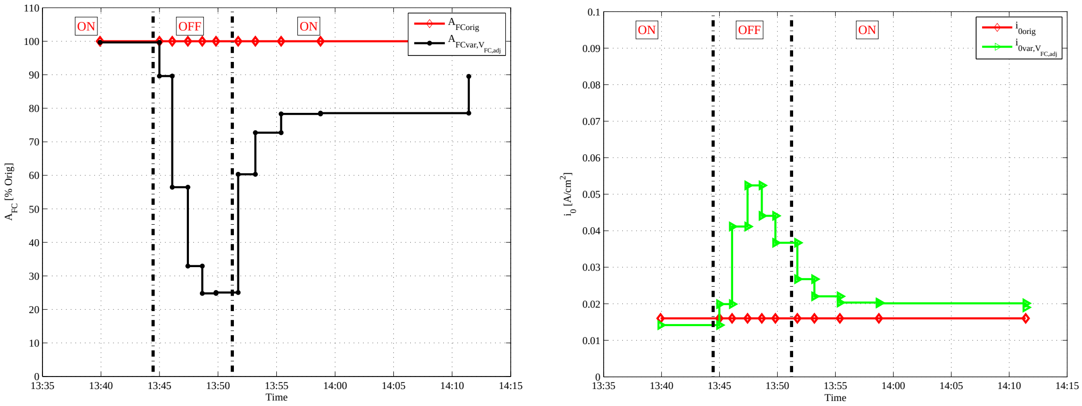

(c) A_{FC} (d) i_0

Figure 5.35: Model results of cathode humidification interruption

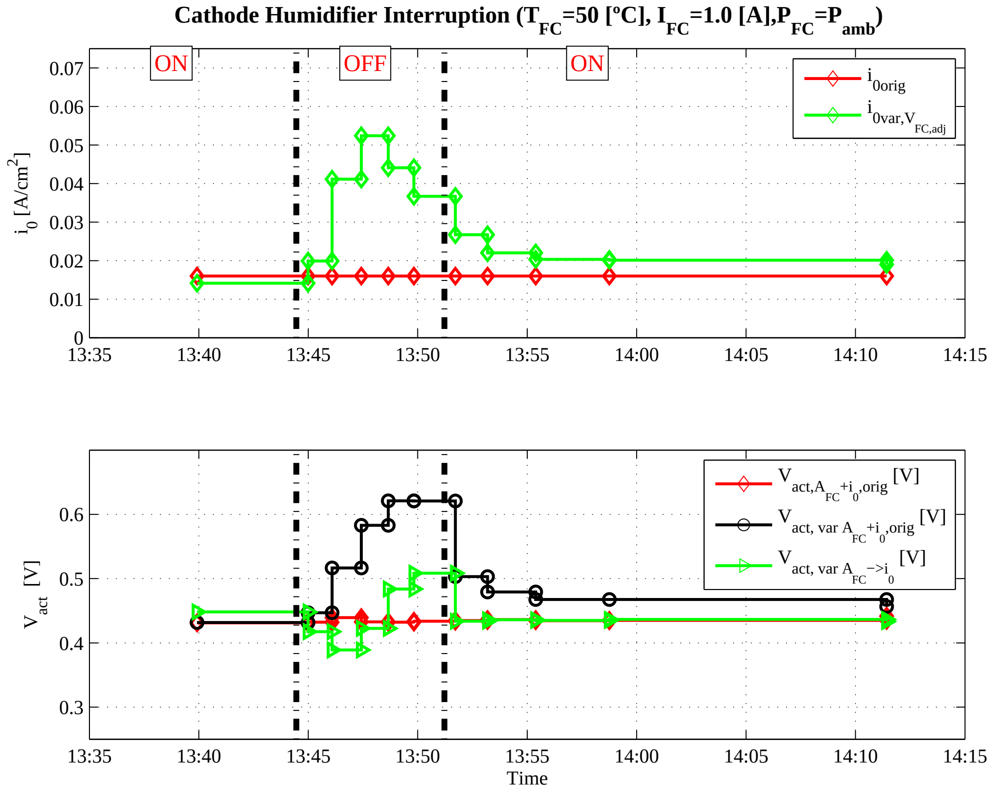

Figure 5.36: Evolution of exchange current density and activation losses

5.7.4.2 Effective active area estimation applied to the anode humidification interruption

Using the same procedure described in the cathode humidification interruption for the effective active area adjustment in the three cases: $A_{eff,FC}$ **and** i_0 **constants** graphed with *red line*, $A_{eff,FC}$ **variation and** i_0 **constant** plotted in *black line* and $A_{eff,FC}$ **and** i_0 **variation** depicted in *green line*, is presented in figure 5.37. The measured v_{FC} and R_{LF} are graphed with *blue line*.

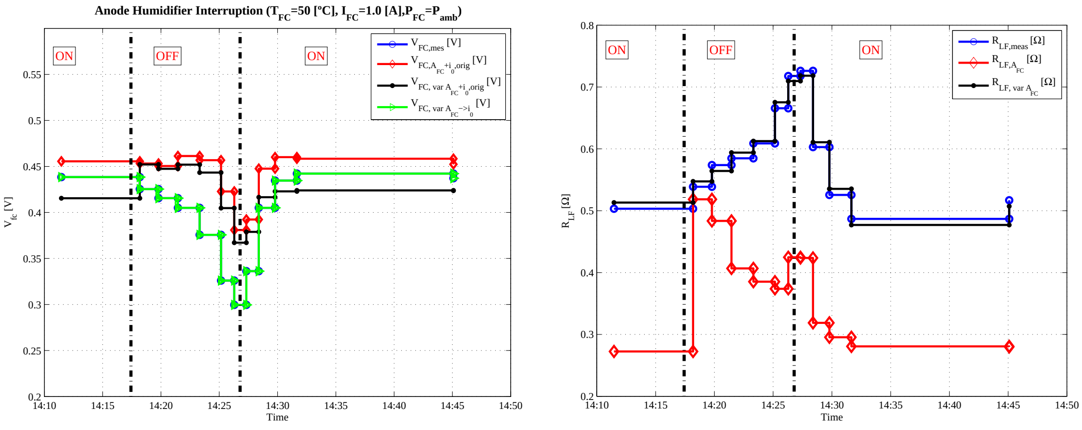

(a) Voltage

(b) R_{LF}

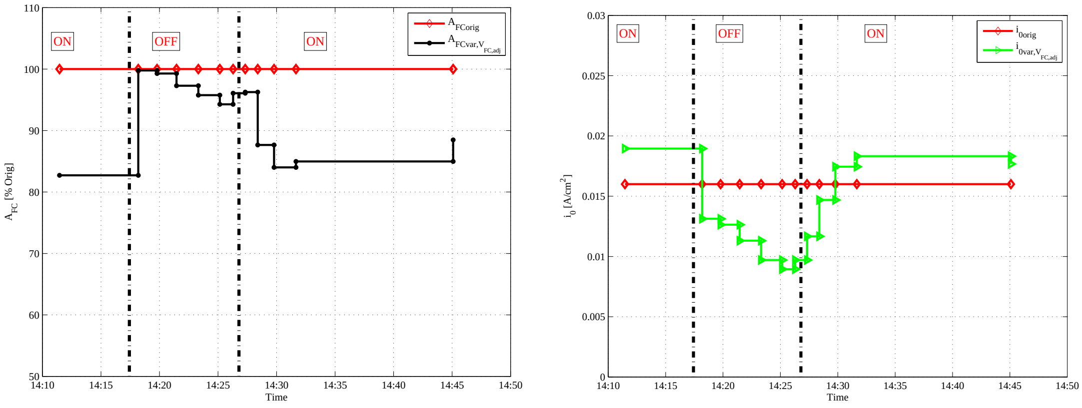

(c) A_{FC}

(d) i_0

Figure 5.37: Model results of anode humidification interruption

The results show that the variation of *effective active area* and its influence over the *exchange current density*, has to be accounted in all the cases. Observing the final adjustment evolution, after the anode humidifier interruption, the effective active area suddenly increases, due to hydrogen concentration increment at channel. Then, the effective area reduces due to a membrane drying effect and active reaction sites loss.

To complete the study, in figure 5.38 the evolution of exchange current density and the activation losses are presented. In this case, the evolution of exchange current density reduces after the anode humidification interruption, increasing the activation losses.

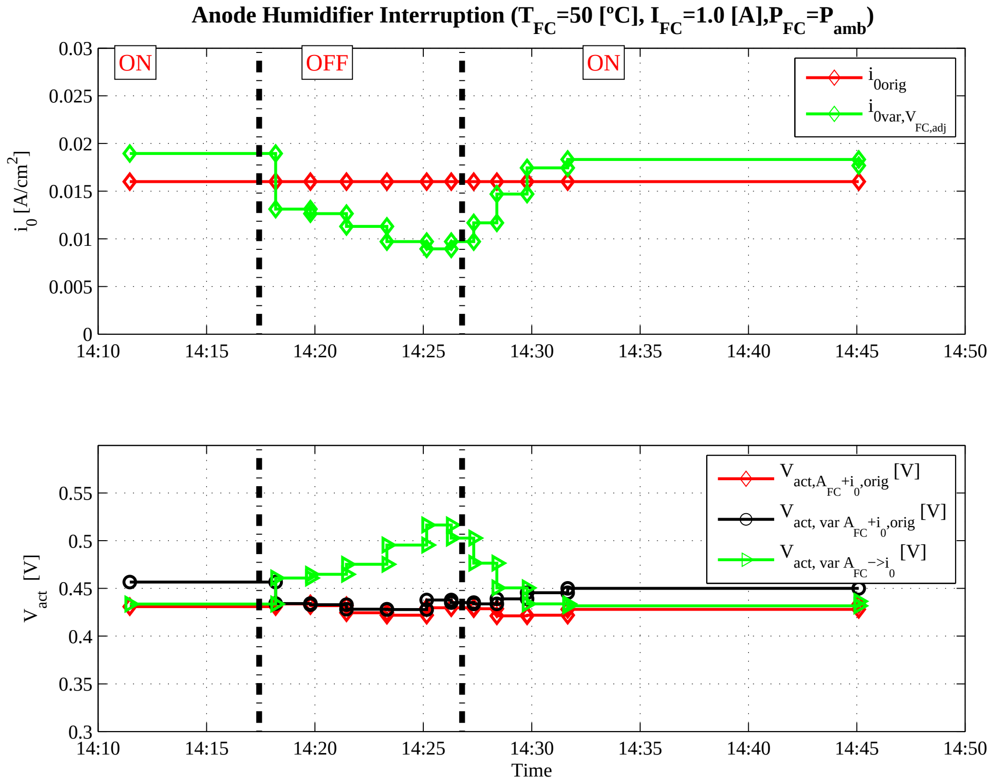

Figure 5.38: Evolution of exchange current density

5.7.5 Performance indicators from modelling issues

From the experimental response and the model presented in the precedent sections, the selected performance indicators are:

- **Membrane resistance**, R_m
- **Effective diffusion coefficient**, D_{eff}
- **Effective active area**, $A_{eff,FC}$

What is the reason for that performance indicators selection?

"R_m" models the membrane resistance, which indicates the hydration state of the membrane. It is an important parameter to know the most important degradation point: the drying effect of the membrane, causing water paths loss for hydrogen protons to reaction sites. This indicator is directly related to the ohmic losses.

"D_{eff}" is the effective diffusion of the overall fuel cell. Specially at cathode side where this effect is predominant and is indicating if water is blocking the pass of oxygen to the reaction sites. For example, when the cathode humidifier is by-passed, the effective diffusion coefficient increases its value denoting the better distribution of water allowing oxygen to access to the reaction sites. It is a good indicator of mass transport losses.

"$A_{eff,FC}$" is the effective active area, this indicator is related to the reaction sites losses due to drying effect in the fuel cell, specially in the catalyst layer interface due to the breaking of water paths necessary for protons. This indicator is related with the activation losses.

Figure 5.39 shows the evolution of the selected parameters during the cathode humidifier interruption.

In this figure are marked the two zones of evolution during the humidification interruption. In the first zone occurs the *diffusion and improvement*, where the effective diffusion coefficient increases its value and the effective active area starts a decreasing trend (because the drying effect is concurrent with diffusion improvement) and the membrane resistance starts to grow, but at a slow rate. In the second zone, *membrane drying zone*, the diffusion coefficient arrives to a maximum stable value and the membrane resistance increases strongly, while the area reduction decreases to a minimum value, confirming the drying effect over the ohmic and the activation losses at the same time.

Figure 5.40 presents the evolution of the selected parameters during the anode humidification interruption. In this case, there is the only the *membrane drying effect*, where the diffusion coefficient has a small initial variation due to the increase of the hydrogen concentration and the membrane resistance grows at a slower rate than in the cathode humidification interruption case. The effective active area increases in the first part (due to improvement of hydrogen concentration) but after that, starts to reduce its value showing the effect of slow membrane drying.

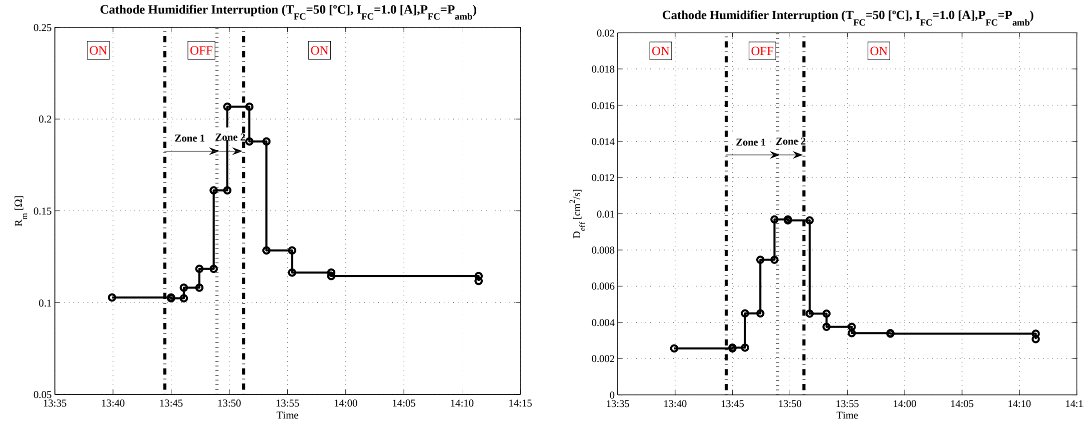

(a) R_m

(b) D_{eff}

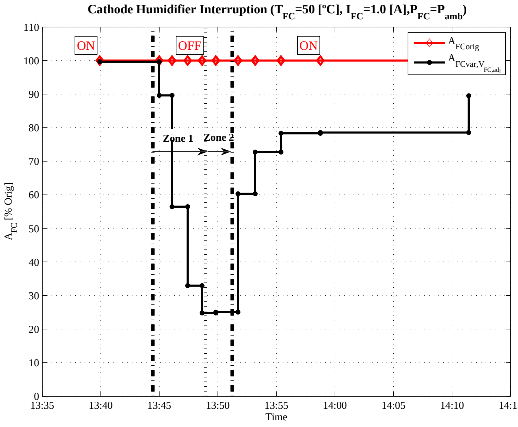

(c) $A_{FC,red}$

Figure 5.39: Performance indicators from model based diagnosis, cathode humidification interruption

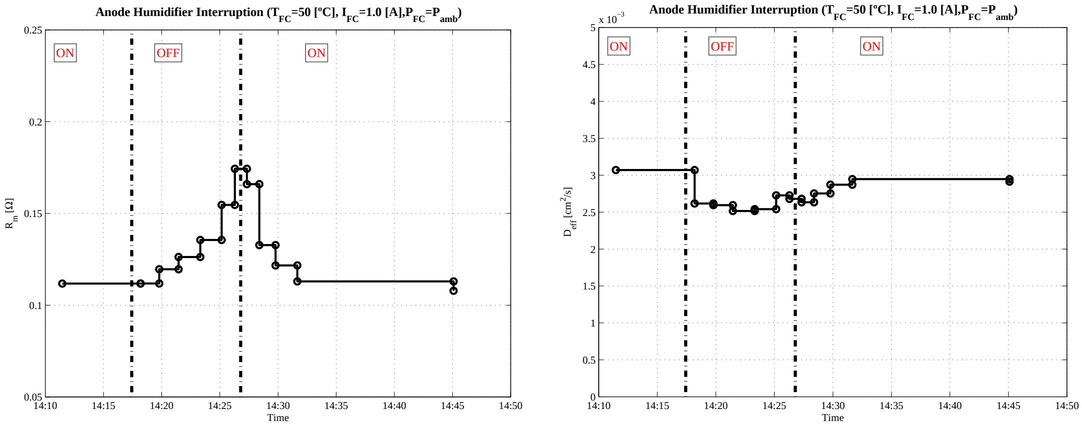

(a) R_m (b) D_{eff}

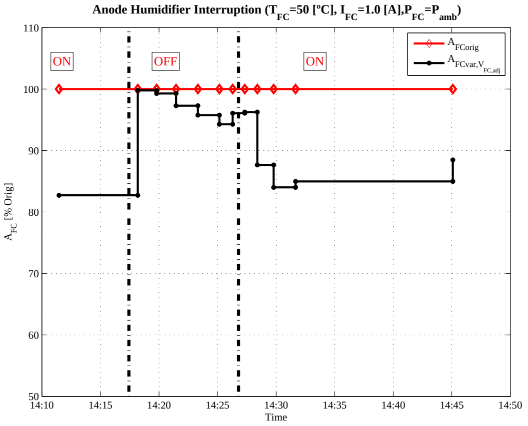

(c) $A_{eff,FC}$

Figure 5.40: Performance indicators from model based diagnosis, anode interruption

5.7.6 Temperature variations of performance indicators from model based diagnosis

The estimated values before a humidification interruption of the *effective active area* "$A_{eff,FC}$", *effective diffusion coefficient* "D_{eff}" and *membrane resistance* "R_m", for the fuel cell working at different temperatures and $P_{FC} = P_{amb}$, are detailed in table 5.13.

Table 5.13: Initial performance indicators, temperature variation

T_{FC} [°C]	$A_{eff,FC}$ [cm^2]	R_m [Ω]	D_{eff} [cm^2/s]
40.0	2.30	0.111	0.0026
50.0	2.59	0.103	0.0027
60.0	2.35	0.095	0.0032

From these initial values of the performance indicators, a simple comparison of the values of R_m and D_{eff}, is a good representation of its evolution with temperature (see chapter 3). Membrane resistance and effective diffusion coefficients improve with temperature. On the other hand, the effective active area estimation shows a different trend, improving the value from 40 [°C] to 50 [°C], where the values and the variation rates are slower. But, at 60 [°C], there is needed more energy to drive the system.

The evolution of the performance indicators during a cathode humidification interruption at different temperatures is presented in figure 5.41.

The response of cathode humidification interruption denotes the same evolution for all selected performance indicators, but at different rates. It is very interesting that the initial values of R_m, follows the fact that at higher temperatures, the lower the resistance (see reference Barbir [2005]), but the evolution from there shows that the degradation is faster at T_{FC}=60 [°C] than T_{FC}=40 [°C] and T_{FC}=50 [°C] (better working conditions). This faster degradation can be explained by the hihgher drying effect at 60 [°C]

At the same time, the effective diffusion coefficient D_{eff} moves faster to a higher values when the temperatures are higher, due to high energy available. Water is evaporated at faster rate, arriving earlier to better conditions of mass transport losses.

Finally, the effective area estimation ($A_{eff,FC}$) is compared, and the faster response is also for T_{FC}=60 [°C], where the effect of higher energy makes the membrane drying stronger and faster. Observing the response, the better working temperature for a slow reduction rate is T_{FC}=50 [°C].

The variation of the performance indicators with the fuel cell temperature during an anode humidification interruption is studied in figure 5.42.

The response to the anode humidification interruption denotes the same evolution for all selected performance indicators but, as for the cathode humidification, at different rates. Again the initial values of R_m, also follows the fact that the higher temperatures the lower is the resistance (see a reference Barbir [2005]). Degradation is also faster at T_{FC}=60 [°C] than T_{FC}=40 [°C] and T_{FC}=50 [°C] for the same reasons than in the cathode case. On the other hand, the effective diffusion coefficient (D_{eff}) evolution is very different, the effect of anode interruption is not so strong in temperature variation, keeping D_{eff} at closer values compared with the initial ones during all the interruption.

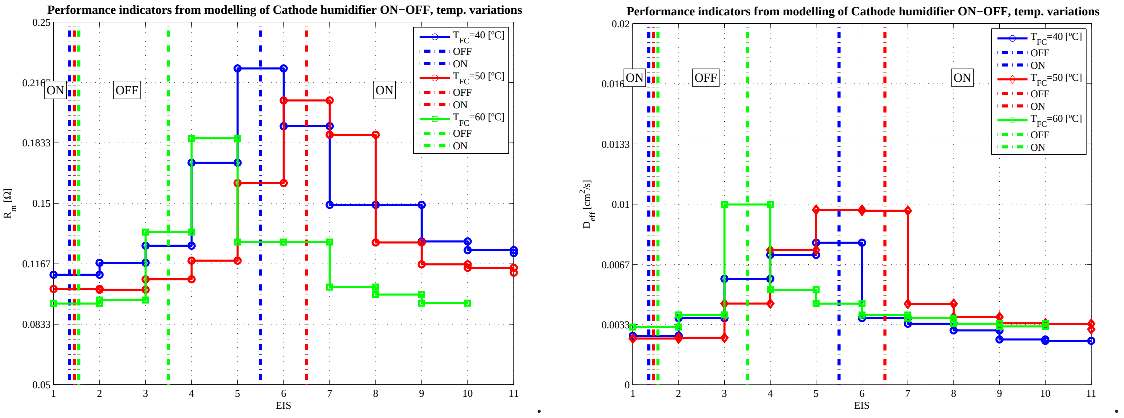

(a) R_m (b) D_{eff}

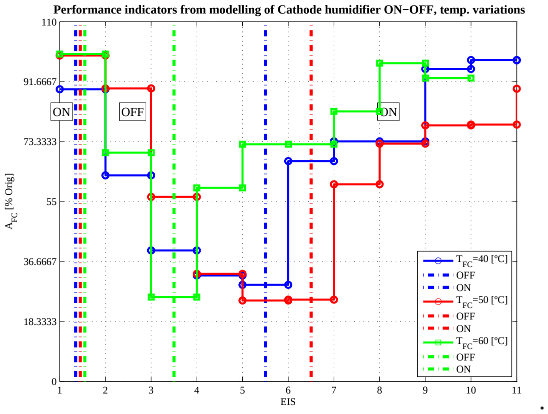

(c) $A_{eff,FC}$

Figure 5.41: Performance indicators, cathode humidifier temperature variation

.

Finally, the estimated effective active area ($A_{eff,FC}$), is compared for different temperatures. In all cases it has the same evolution.

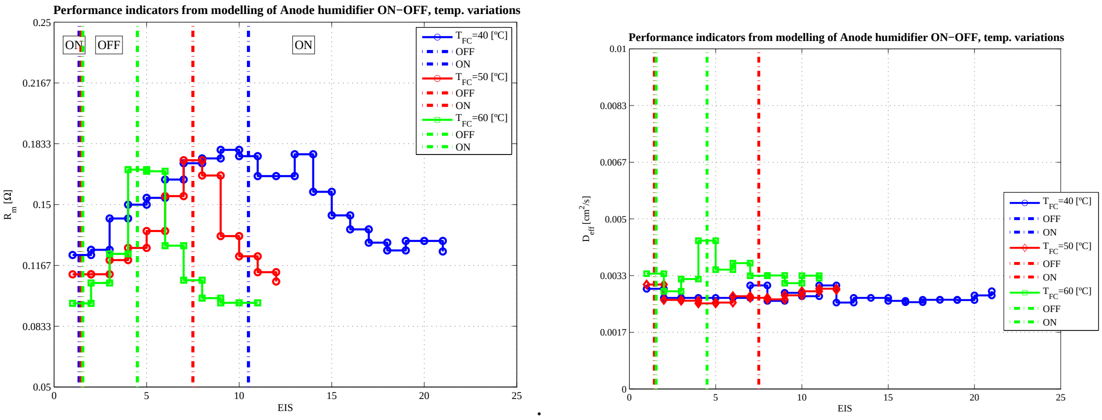

(a) R_m (b) D_{eff}

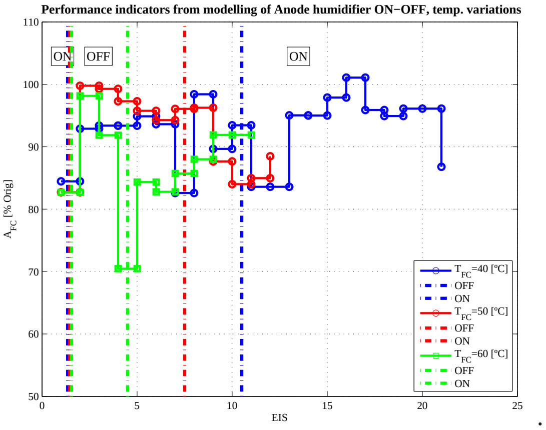

(c) $A_{eff,FC}$

Figure 5.42: Performance indicators anode humidifier, temperature variation

.

5.7.7 Use of the humidification interruption test with model based diagnosis tool

Based on physical phenomena, three parameters have been chosen for this diagnosis procedure. These parameters are R_m, D_{eff} and $A_{eff,FC}$. The procedure consists in monitoring and observing the evolution of R_m and D_{eff} during the humidification interruption, and as is described in section 5.5.4, the diagnostic will depend of the existence and size of zone 1, that, in this case, is defined by the time interval needed for D_{eff} to reach stationary state and for R_m to abruptly change its slope.

The third parameter, $A_{eff,FC}$, involved in this diagnosis procedure can be calculated independently of the humidification test and gives the effective active area in that operating point. This new indicator is useful to relate the availability of the reaction sites with the humidification. It can also be helpful when comparing different operating conditions, for example, to select the most suitable temperature as is shown on table 5.13.

5.8 Conclusions

In this section the main conclusions of this chapter are presented. They refer to the advantages of the diagnostic tools proposed in this chapter.

5.8.1 Conclusions of the *Relevant Characteristics* as a diagnostic tool

The main advantage of using the EIS **relevant characteristics** is the easy and fast deduction of these performance indicators from the EIS response of fuel cell system. This fact also indicates the possibility to use these indicators as *in-situ experimental diagnosis technique*, observing their deviation during the humidification interruption from the values obtained at nominal conditions.

Both for the cathode or anode humidification interruption, the evolution of each relevant characteristic, R_{LF}, R_{HF} and $f_{\phi,max,LF}$, at different temperatures presents the same profile, showing the robustness and repeatability of these performance indicators.

This test can be used as diagnosis tool for the determination of the state of the fuel cell humidification, through the discrimination of the different *zones* of the evolution of the performance indicators during the test.

One of the disadvantages of these relevant characteristics when are used for diagnosis, is the indirect link with the internal phenomena occurring inside the fuel cell. The physical interpretation will be easier with the use of simple equivalent circuits as is done in the equivalent circuit study as performance indicators.

5.8.2 Conclusions of the *equivalent circuit indicators* as a diagnosis tool

The main advantage of using the **equivalent circuit indicators as diagnosis tool** is the relationship between the equivalent circuit parameters with the internal physical properties of the fuel cell system. Again these indicators present the same evolution profile in all the studied cases of cathode and anode humidification interruptions.

During the cathode humidification interruption, the evolution of the equivalent circuit parameters presents two different zones. A physical interpretation of the phenomena occurring during these *zones* is summarised as follows:

- **Zone 1: Diffusion improvement:** When the humidification is stopped, the vapour/liquid water contained in the cathode catalyst-GDL-channel is progressively removed and dry air takes its place. As a consequence, the air diffusion improves and the oxygen concentration increases. This interpretation is supported with the evolution of the selected *performance indicators*: the Warburg resistance (R_w) and the time constant (τ_W) decrease their values, and due to an improvement of the diffusion and the membrane resistance, (R_m) starts to grow with a slow rate.

- **Zone 2: reduction of active reactions sites:** When the diffusion is reaching its limit, the water content in the membrane starts to decrease at a fast rate and the reaction sites start to reduce due to the protons water path loss. The air diffusion attains its maximum when all the water is removed from the GDL. This interpretation is supported with the evolution of the selected *performance indicators*: the membrane resistance grows quickly indicating a membrane water content reduction; the Warburg resistance increases, showing the effect of the reaction sites loss; while the Warburg time constant it maintained at a fixed value, showing the stabilization of the diffusion.

- **Humidification reconnection:** From the evolution of the selected performance at the reconnection of cathode humidification system, it can be observed that there are no maximums and minimums in none of them. Therefore a separation in two zones is not seen, because of the concurrence of the diffusion deterioration and the increment of reaction sites.

During the anode humidification interruption test, the trends of the R_m and R_W depict the same drying effect over the membrane and the active area as in the cathode side *zone 2*. However, the magnitudes of the changes are smaller. The evolution of the Warburg time constant confirms that the diffusion is not considerably affected by the anode humidification interruption, maintaining values close to the initial ones. Then, the cathode side dominates the diffusion process.

The *performance indicators* derived from the equivalent circuits give an interpretation of the internal phenomena. Note, however, that is possible to find more than one equivalent circuit that fits the EIS response. Then, a selection of the equivalent circuit must be done combining knowledge from experience and references from the literature.

This diagnosis tool is possible to be used as an *in-situ experimental diagnosis technique*, saving the stable values (extracted from long EIS response at nominal conditions) and observing the deviation from those values when the humidification interruption is done. One disadvantage is that the fitting procedure using the Zview®software is not automatic and must be replaced with a specific fitting algorithm designed for this objective.

5.8.3 Conclusions of model based diagnosis

The phenomena affected by the water changes observed in the previous sections are modelled. This includes the diffusion, the membrane resistance and the reduction of active sites. The selected performance indicators related with these phenomena are the *effective coefficient diffusion*, D_{eff}, the *membrane resistance*, R_m and the *effective active area*, $A_{eff,FC}$.

The monitorisation of D_{eff} and R_m during humidification interruption tests can be used to diagnose the water state of the fuel cell through a procedure similar to the one explained in the previous section. Both parameters are directly related to physical proprieties of the system and it is important to note that D_{eff} is only dependent on the water influence on the diffusion and R_m is only dependent on the membrane water content.

The modelling work gives the possibility to quantify the *effective active area*. This performance indicator completes the information of the other indexes. Also, this indicator can be detached from the humidification interruption test and can be used in every moment to estimate the effective active area. Specifically, it can be helpful to compare the performance between different operating conditions or even to close a control loop.

Chapter 6

Conclusions and Future Work

In the first part of this chapter, the general conclusions and main contributions of the thesis are presented. In the second part, recommendations for future work are proposed. The specific conclusions of each subject are already presented at the end of the corresponding chapters.

6.1 General Conclusions and contributions

This thesis studies, proposes and compares different experimental characterisation methods aimed to provide performance indicators related with the water presence into the PEMFC. Based on these indicators, different diagnosis procedures are described which permit to diagnose the internal state of the fuel cell in terms of water through qualitative and quantitative rules. Modelling has been a key element in the diagnosis procedures. Experimental and physical laws based models have been taken into account. The thesis work has a strong experimental orientation.

In *chapter 3*, a systematic use of the **EIS** characterization technique to analyse the influence of different operating conditions over the fuel cell response is performed. The operating variables studied include, among others: the load current, the fuel cell pressure, the fuel cell temperature and the cathode relative humidity. Detailed conclusions are given for each operating variable analysis. Two important conclusions are

- When H_2/O_2 are used as inlet gases, the EIS shows two impedance arcs. On the other hand, when the H_2/Air are the feeding gases there is only one single predominant arc
- If the fuel cell relative humidity is augmented, the EIS response is better (reducing impedance values) until the arrives at higher humidity ratios, where the excess of water presence blocks the oxygen arrival to platinum sites

Seven **relevant characteristics** from the EIS response are identified. The variation of these relevant characteristics with the operating conditions is analysed. Two of these characteristics are the more significant ones: the high, R_{HF}, and the low, R_{LF}, frequency resistances. R_{LF} is the most sensitive relevant characteristic.

In order get closer to find some physical interpretation, an analogy is made between the PEMFC system response and several equivalent circuits. After being analysed, those that have the best fitting with the experimental EIS data are selected. When *Air* is used as oxidant a simple equivalent circuit is selected. When *Oxygen* is used, a more complex equivalent circuit is proposed. Some of the EIS relevant characteristics are related to the parameter of the equivalent circuits, and a complete procedure for the fine tuning of these parameters is presented. Good fittings of the response are always obtained.

A detailed sensitivity analysis is performed indicating those parameters that best capture the influence of the operating conditions. For instance, R_m is not affected by pressure changes and P_W is not affected by most of the studied operating variables.

An **effective area coefficient** relating the geometrical and the effective active area is proposed and the procedure to obtain this coefficient is detailed. The effective area represents the reaction sites that are available for the protons.

In *chapter 4*, a new experimental characterisation technique, based on the **inlet gases humidification interruption** is proposed. This dynamic technique combines the information extracted from the standard characterisation technique (EIS) and the temporal response in order to study the water transport and storage effects in the fuel cell. Two advantages of this proposed technique are the simple hardware configuration and the relative low impact on the fuel cell response, making attractive the **humidification interruption test** to be used as in-situ technique.

The cathode humidification plays an important role in the cell behaviour. Time and frequency responses of the **cathode humidification interruption** show two zones of evolution that reflect in the values of the cell voltage, R_{LF} and R_{HF}. In the first zone, an improvement of the response is due to a better diffusion and to the increase of the concentration of oxygen. The cell voltage and R_{LF} are good indicators of this improvement. At the same time the membrane starts to dry, what reflects through a slow increase of the R_{HF}.

In the second zone the membrane dries at a faster rate, because the water in the GDL and the cathode catalyst layer has already moved out and the membrane water content starts to decrease. Hence, R_{HF} grows rapidly. Also as a consequence of this lack of water inside the membrane, the reaction sites are more difficult to reach for the protons and a reduction of the active area occurs. The humidification must be restablished in order to avoid unacceptable voltage losses.

The **anode humidification interruption** response presents much more softer and limited variations compared with the cathode side humidification interruption response. When the anode humidification is interrupted, R_{LF} and R_{HF} increase their values slowly and tend to new stationary ones. This new operation state allows the system continuing working without restablishing the humidification although with a deteriorated performance.

Due to the relative low impact of the test over the fuel cell state, a diagnosis procedure can be applied whenever it is required. As the cathode test gives more useful information about the humidification conditions, the proposed diagnosis process is based on the cathode humidification interruption. The diagnosis procedure will be useful to determine if the cell with the current operating conditions is over- or under-humidified.

During the **cathode humidification interruption**, the evolution of the response presents two different zones as is explained before.

Three different set of **performance indicators** are proposed as diagnosis tools: *relevant characteristics*, *equivalent circuit parameters* and *model based indicators*.

A set of **relevant characteristics**, based on the EIS response are selected as performance indicators which, if properly monitored can give a diagnostic of the internal state of the fuel cell. Some advantages of using the *relevant characteristics* are their easy and fast obtention and repeatability. The characteristics chosen as performance indicators are: R_{LF}, R_{HF} and $f_{\phi,max,LF}$. The proposed diagnosis procedure based on relevant characteristics and on the cathode humidification interruption is useful to determine if the cell with the current operating conditions is over- or under-humidified:

- If the evolution of the relevant characteristics after the interruption shows a large zone 1 (which is defined as the zone where R_{LF} decreases, R_{HF} increases slightly and $f_{\phi,max,LF}$ increases), the cathode is over-humidified
- If the evolution of the relevant characteristics after the interruption shows a very reduced zone 1, the cathode is optimally humidified
- If the evolution of the relevant characteristics after the interruption shows an inexisting zone 1, the cathode is under-humidified

One of the disadvantages of these *relevant characteristics* when are used as a diagnosis tool, is the indirect link with the internal phenomena occurring inside the fuel cell.

In order to give to the performance indicators a physical interpretation, a simple equivalent circuit is selected. Then, using its most sensitive parameters, which are R_m, τ_W and R_W, these three parameters, defined as **equivalent circuit performance indicators**, can be related to the membrane resistance, the diffusion time constant and to the diffusion resistance. As is described in the relevant characteristics diagnosis tool, the state of humidification of the fuel cell depends on the existence and size of *zone 1*, described, in this case by the decreasing evolution of the Warburg resistance (R_w) and time constant (T_W), due to an improvement of the diffusion and to the slow increasing rate of the membrane resistance (R_m). In *zone 2*, the membrane resistance grows quickly indicating a membrane water content reduction; the Warburg resistance increases, showing the effect of the reaction sites loss; while the Warburg time constant it maintained at a fixed value, showing the stabilization of the diffusion. An important contribution of this diagnosis method is that, from the T_W, the effective diffusion coefficient D_{eff} of the fuel cell can be obtained with the following advantages:

- The effective diffusion coefficient corresponds to a physical property of the fuel cell
- It is possible to find out the effective diffusion coefficient maximum which is a reference value that can be useful for degradation studies

The performance indicators derived from the *equivalent circuit parameters* facilitate an interpretation of the internal phenomena. Note, however, that is possible to find more than one equivalent circuit that fits the EIS response. Then, selection of the equivalent circuit must be done combining knowledge from experience and references from the literature.

Completing the physical phenomena interpretation, a new set of **model based performance indicators** are proposed, with the following physical related parameters: membrane resistance, R_m, effective diffusion coefficient D_{eff} and effective active area, $A_{eff,FC}$. The diagnostic of the fuel cell humidification state depends on the existence and size of *zone 1*, which in this case is defined for the time interval needed for D_{eff} to reach stationary state and for R_m to abruptly change its slope. The third parameter, $A_{eff,FC}$, involved in this diagnosis procedure can be calculated independently of the humidification test and gives the effective active area in that operating point. This new indicator is useful to relate the availability of the reaction sites with the fuel cell humidification state. This indicator can be detached from the humidification interruption test and can be used in every moment to estimate the *effective active area*. Specifically, parameters $A_{eff,FC}$ and D_{eff}, can be helpful to compare the performance between different operating conditions, the analysis of the material degradation and even to close a control loop.

6.2 Future work

In the course of this thesis, a wide experimental study of the PEMFC response has been done. Also, new characterisation techniques and its use as diagnosis tools are presented. However, there are several issues to be further developed:

Experimental characterisation techniques

In **chapter 3**, a set of experimental results of the application of the standard experimental characterisation techniques (EIS) is obtained. This EIS technique consists of the frequency response of the system, obtained using a special equipment (frequency response analyser) and it is difficult to be used as on-line technique. One interesting point that could be studied in the future, is the design and development of experimental techniques that give an information equivalent to the EIS, but with a lower cost and suitable to be used on line, for example, using a Pseudo Random Binary Signal excitation.

Humidification interruption test

The humidification interruption test is presented in **chapter 4** as a new low impact experimental characterisation technique. It has proven to be useful to determine and analyse the water presence and its influence in the system. In order to compare the results for different fuel cells, some items should be solved: automatisation of the humidification interruption sequence, equally time spaced EIS performance, on-line calculation of the relevant characteristics and the application of this technique with H_2/O_2 as reactants. Another interesting subject could be the analysis of the new stable operating point obtained when the anode humidification interruption is applied.

Performance indicators and diagnosis tools of the PEMFC response

The *performance indicators* and their use as *diagnosis tools* are detailed in **chapter 5**. An improvement of these indicators could be achieved incorporating the mass and energy balance to the model based diagnosis tool. Finally, an interesting issue is to study the connection of the diagnosis tools with a supervisory and control system, in order to find an optimal humidification operating point.

Appendix A

Electrochem single fuel cell manual

Information sended by manufacter about single fuel cell used in this thesis A.1.

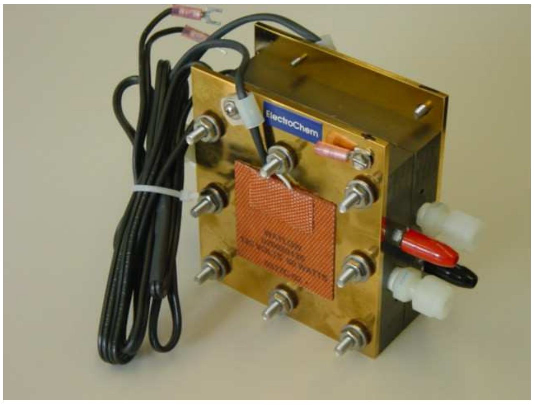

Figure A.1: Single fuel cell

The single fuel cell used for experimental characterization has the following characteristics:

- **Builder:** Electrochem, Inc.
- **Name:** EFC05-01SP®.
- **Type:** Single fuel cell.
- **Serial Number:** E3408
- **Active Area:** 5 [cm^2].
- **Membrane Assembly:** Nafion™ 115 and 1 [$mgPt/cm^2$] (platinum load at both sides) and Toray® carbon fiber paper ”TGP-H-060” with 0.19 [mm] thickness as GDL.
- **Flow path:** 3 pass serpentine flow pattern 0.1524 x 0.1524 x 0.0764(depth) [cm].

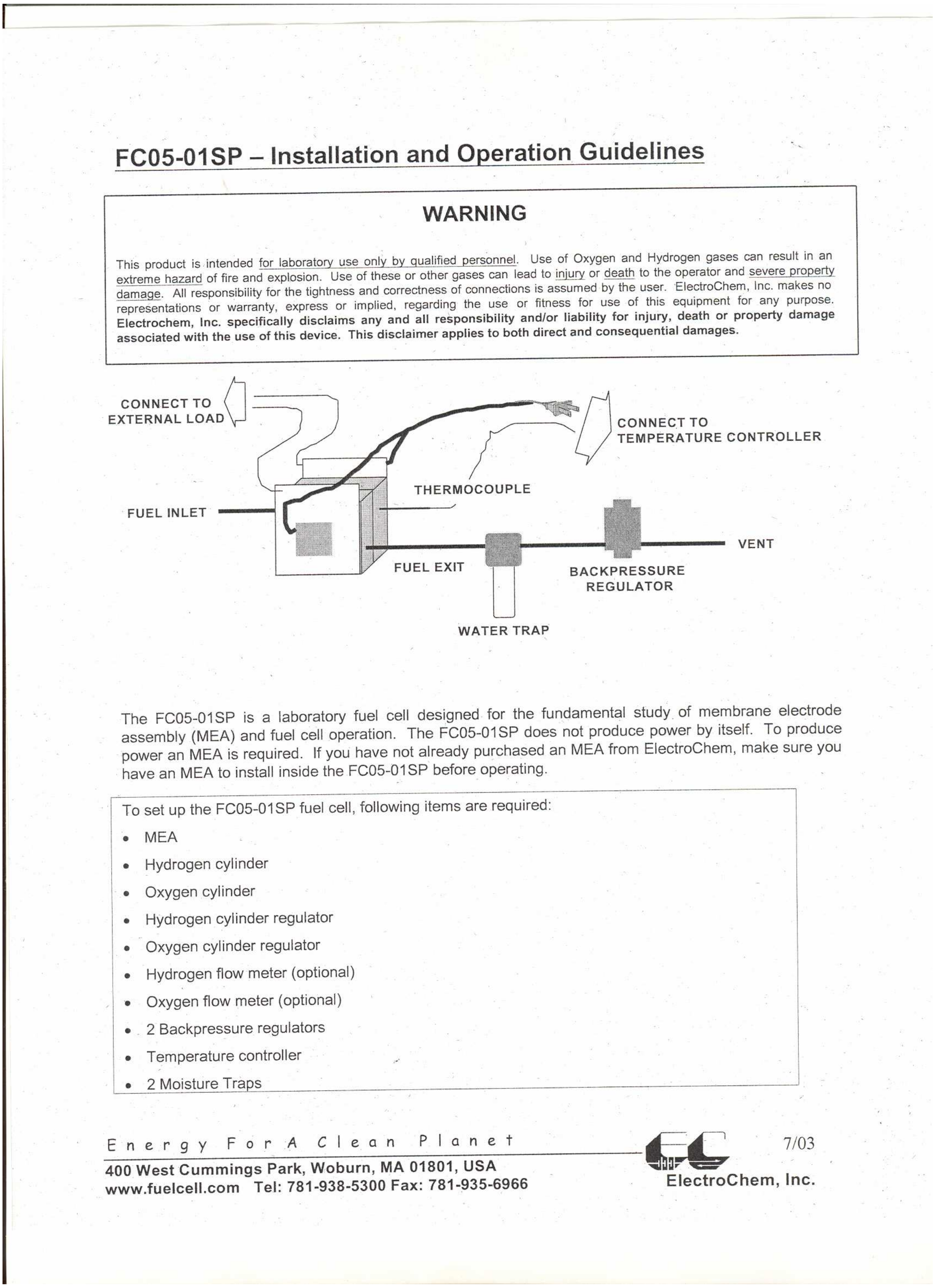

FC05-01SP – Installation and Operation Guidelines

WARNING

This product is intended for laboratory use only by qualified personnel. Use of Oxygen and Hydrogen gases can result in an extreme hazard of fire and explosion. Use of these or other gases can lead to injury or death to the operator and severe property damage. All responsibility for the tightness and correctness of connections is assumed by the user. ElectroChem, Inc. makes no representations or warranty, express or implied, regarding the use or fitness for use of this equipment for any purpose. **Electrochem, Inc. specifically disclaims any and all responsibility and/or liability for injury, death or property damage associated with the use of this device. This disclaimer applies to both direct and consequential damages.**

The FC05-01SP is a laboratory fuel cell designed for the fundamental study of membrane electrode assembly (MEA) and fuel cell operation. The FC05-01SP does not produce power by itself. To produce power an MEA is required. If you have not already purchased an MEA from ElectroChem, make sure you have an MEA to install inside the FC05-01SP before operating.

To set up the FC05-01SP fuel cell, following items are required:

- MEA
- Hydrogen cylinder
- Oxygen cylinder
- Hydrogen cylinder regulator
- Oxygen cylinder regulator
- Hydrogen flow meter (optional)
- Oxygen flow meter (optional)
- 2 Backpressure regulators
- Temperature controller
- 2 Moisture Traps

Energy For A Clean Planet

7/03

400 West Cummings Park, Woburn, MA 01801, USA
www.fuelcell.com Tel: 781-938-5300 Fax: 781-935-6966

ElectroChem, Inc.

Figure A.2: Manual for single fuel cell - Page 1/4

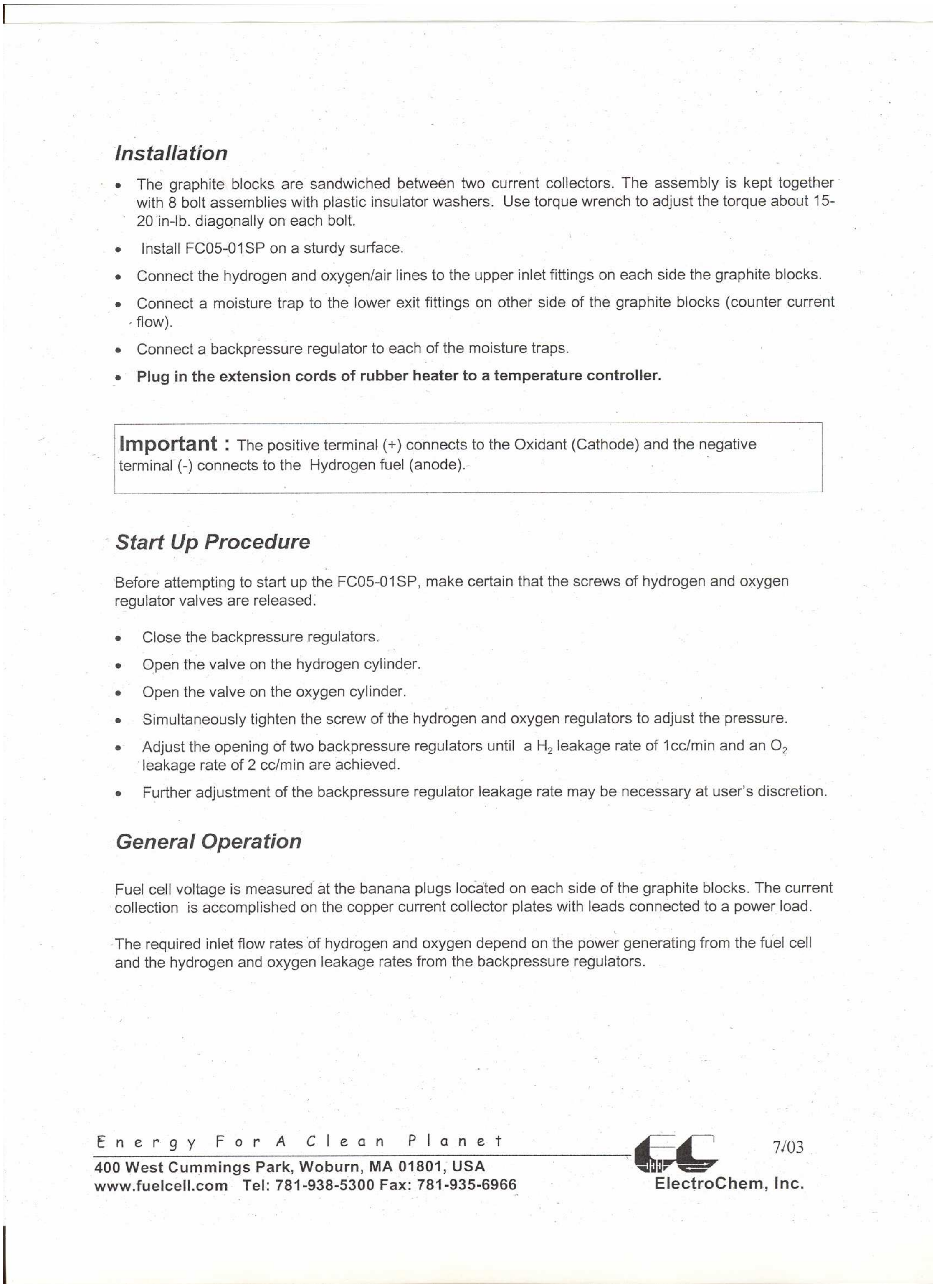

Installation

- The graphite blocks are sandwiched between two current collectors. The assembly is kept together with 8 bolt assemblies with plastic insulator washers. Use torque wrench to adjust the torque about 15-20 in-lb. diagonally on each bolt.
- Install FC05-01SP on a sturdy surface.
- Connect the hydrogen and oxygen/air lines to the upper inlet fittings on each side the graphite blocks.
- Connect a moisture trap to the lower exit fittings on other side of the graphite blocks (counter current flow).
- Connect a backpressure regulator to each of the moisture traps.
- **Plug in the extension cords of rubber heater to a temperature controller.**

Important : The positive terminal (+) connects to the Oxidant (Cathode) and the negative terminal (-) connects to the Hydrogen fuel (anode).

Start Up Procedure

Before attempting to start up the FC05-01SP, make certain that the screws of hydrogen and oxygen regulator valves are released.

- Close the backpressure regulators.
- Open the valve on the hydrogen cylinder.
- Open the valve on the oxygen cylinder.
- Simultaneously tighten the screw of the hydrogen and oxygen regulators to adjust the pressure.
- Adjust the opening of two backpressure regulators until a H_2 leakage rate of 1cc/min and an O_2 leakage rate of 2 cc/min are achieved.
- Further adjustment of the backpressure regulator leakage rate may be necessary at user's discretion.

General Operation

Fuel cell voltage is measured at the banana plugs located on each side of the graphite blocks. The current collection is accomplished on the copper current collector plates with leads connected to a power load.

The required inlet flow rates of hydrogen and oxygen depend on the power generating from the fuel cell and the hydrogen and oxygen leakage rates from the backpressure regulators.

Energy For A Clean Planet

400 West Cummings Park, Woburn, MA 01801, USA
www.fuelcell.com Tel: 781-938-5300 Fax: 781-935-6966

7/03

ElectroChem, Inc.

Figure A.3: Manual for single fuel cell - Page 2/4

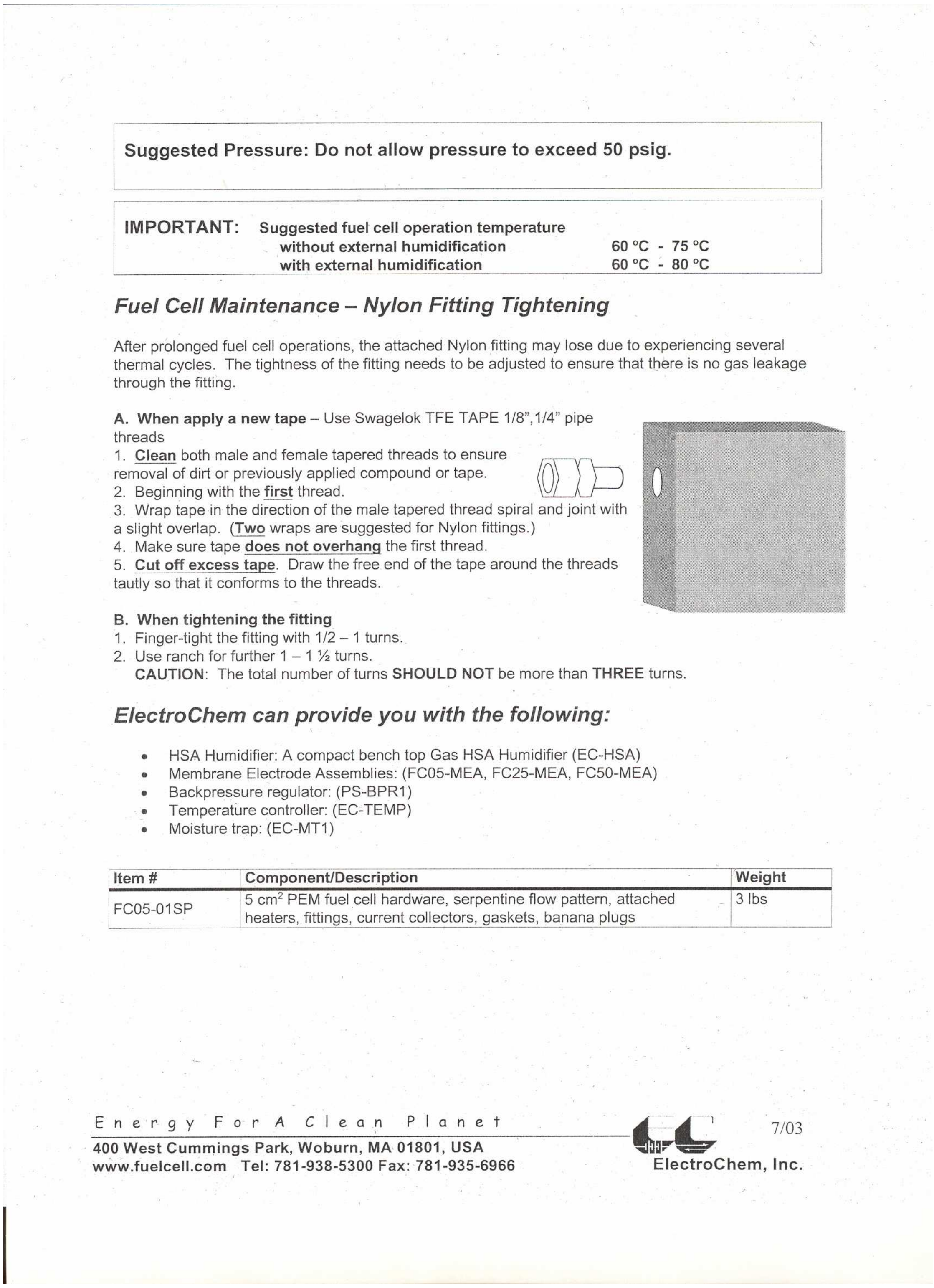

Suggested Pressure: Do not allow pressure to exceed 50 psig.

IMPORTANT: **Suggested fuel cell operation temperature**
without external humidification **60 °C - 75 °C**
with external humidification **60 °C - 80 °C**

Fuel Cell Maintenance – Nylon Fitting Tightening

After prolonged fuel cell operations, the attached Nylon fitting may lose due to experiencing several thermal cycles. The tightness of the fitting needs to be adjusted to ensure that there is no gas leakage through the fitting.

A. When apply a new tape – Use Swagelok TFE TAPE 1/8",1/4" pipe threads
1. **Clean** both male and female tapered threads to ensure removal of dirt or previously applied compound or tape.
2. Beginning with the **first** thread.
3. Wrap tape in the direction of the male tapered thread spiral and joint with a slight overlap. (**Two** wraps are suggested for Nylon fittings.)
4. Make sure tape **does not overhang** the first thread.
5. **Cut off excess tape**. Draw the free end of the tape around the threads tautly so that it conforms to the threads.

B. When tightening the fitting
1. Finger-tight the fitting with 1/2 – 1 turns.
2. Use ranch for further 1 – 1 ½ turns.
CAUTION: The total number of turns **SHOULD NOT** be more than **THREE** turns.

ElectroChem can provide you with the following:

- HSA Humidifier: A compact bench top Gas HSA Humidifier (EC-HSA)
- Membrane Electrode Assemblies: (FC05-MEA, FC25-MEA, FC50-MEA)
- Backpressure regulator: (PS-BPR1)
- Temperature controller: (EC-TEMP)
- Moisture trap: (EC-MT1)

Item #	**Component/Description**	**Weight**
FC05-01SP	5 cm^2 PEM fuel cell hardware, serpentine flow pattern, attached heaters, fittings, current collectors, gaskets, banana plugs	3 lbs

Energy For A Clean Planet
400 West Cummings Park, Woburn, MA 01801, USA
www.fuelcell.com Tel: 781-938-5300 Fax: 781-935-6966

7/03
ElectroChem, Inc.

Figure A.4: Manual for single fuel cell - Page 3/4

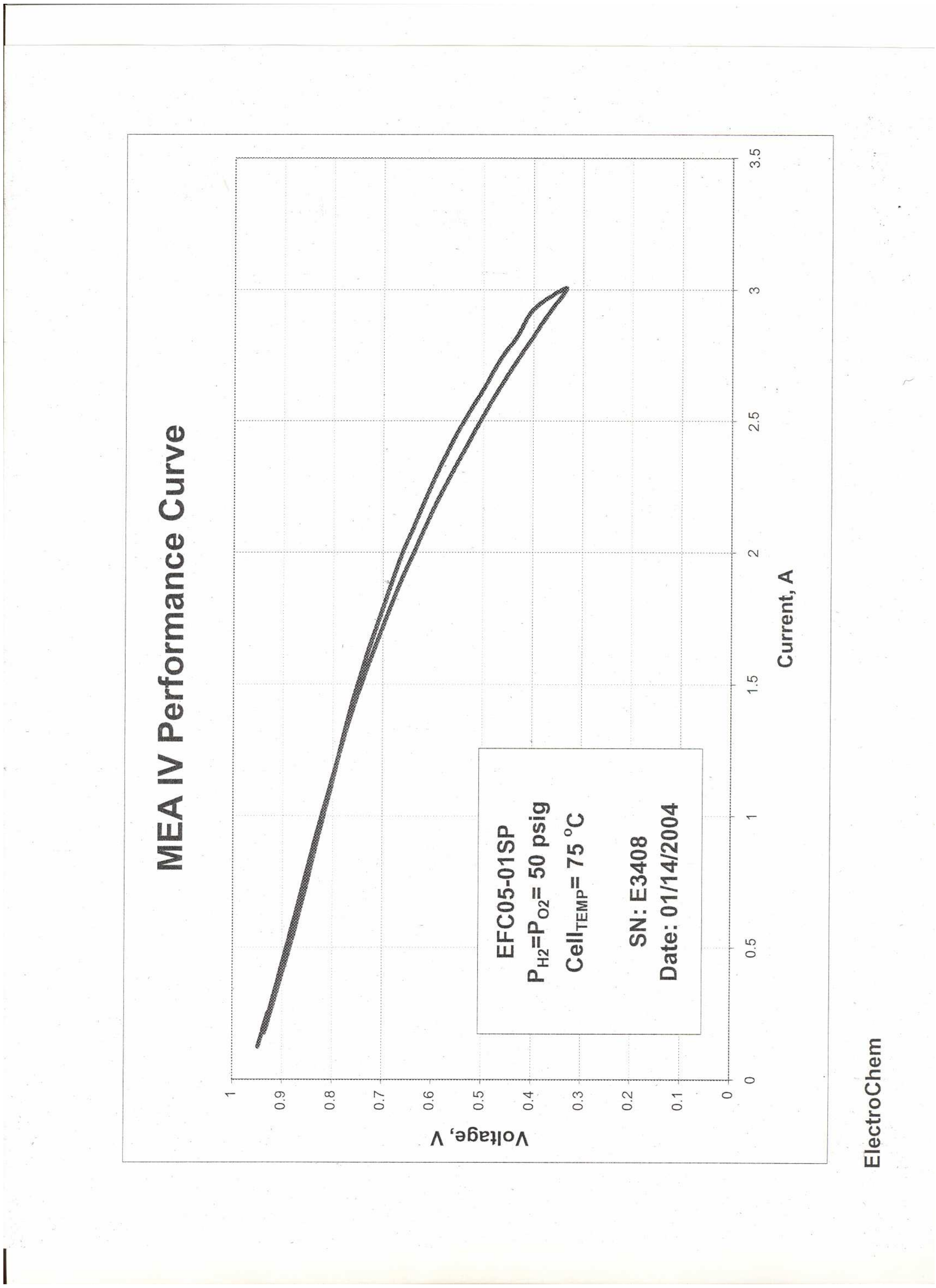

Figure A.5: Manual for single fuel cell - Page 4/4

Appendix B

Humidification interruption results

In this section,all experimental results of humidification interruption are showed.

B.1 Frequency points of EIS

Before humidification interruption is applied, a “Long” EIS is applied, where the specifications of the applied frequencies to the system are showed in table B.1 and mean duration of this test is 12 minutes.

Point	Frec [Hz]	Point	Frec [Hz]	Point	Frec [Hz]
1	0.10	21	10.00	41	1000.01
2	0.13	22	12.59	42	1258.9
3	0.16	23	15.85	43	1584.91
4	0.20	24	19.95	44	1995.28
5	0.25	25	25.12	45	2511.91
6	0.32	26	31.62	46	3162.31
7	0.40	27	39.81	47	3981.11
8	0.50	28	50.12	48	5011.92
9	0.63	29	63.10	49	6309.63
10	0.79	30	79.43	50	7943.36
11	1.00	31	100.00	51	10000.1
12	1.26	32	125.89		
13	1.58	33	158.49		
14	2.00	34	199.53		
15	2.51	35	251.19		
16	3.16	36	316.23		
17	3.98	37	398.11		
18	5.01	38	501.19		
19	6.31	39	630.96		
20	7.94	40	794.33		

Table B.1: Long EIS frequency points

Also, when humidifier interruption is applied, a “Short” EIS are done and the frequency specifications detailed in table B.2. In this case, estimated duration is about 12 seconds.

Point	**Frec [Hz]**
1	0.20
2	0.34
3	0.59
4	1.01
5	1.74
6	2.99
7	5.14
8	8.82
9	15.16
10	26.04
11	44.72
12	76.82
13	131.95
14	226.66
15	389.33
16	668.75
17	1148.72
18	1973.16
19	3389.31
20	5821.83
21	10000.20

Table B.2: Short EIS frequency points

B.2 Day: 01/10/2007

Operating conditions of this day is showed on table B.3:

	$\mathbf{T}_{ca,hum}[^{o}\mathbf{C}]$	$\mathbf{T}_{ca,LH}[^{o}\mathbf{C}]$	$\mathbf{P}_{ca}[\mathbf{bar}_a]$	$\Phi_{cath}[\mathbf{slpm}]$
Cath. (Air)	39.5	50	1	0.824
	$\mathbf{T}_{An,hum}[^{o}\mathbf{C}]$	$\mathbf{T}_{An,LH}[^{o}\mathbf{C}]$	$\mathbf{P}_{An}[\mathbf{bar}_a]$	$\Phi_{an}[\mathbf{slpm}]$
Anode (H_2)	39.5	50	1	0.324
	$\mathbf{T}_{FC}[^{o}\mathbf{C}]$			
Cell	41.5			
Comments: System and humidifiers bypass test EIS				

Table B.3: Operating conditions of 01/10/2007

B.2.1 Day graph response

On this day test on the fuel cell system were done to make the last hour tests before open the cell. First part of the day, we make some test and EIS some verifications, see figures: B.1, B.2 and B.3.

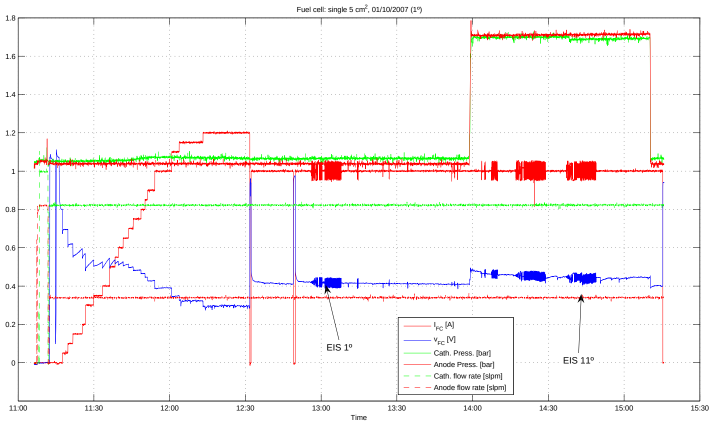

Figure B.1: EIS test part, 1º graph

On second part of day, we make a cathode and anode bypass to see short EIS evolution, see more details on sections *Cathode humidifier by pass* and *Anode humidifier by pass*. General response of these part of day are showed on figures B.4, B.5 and B.6

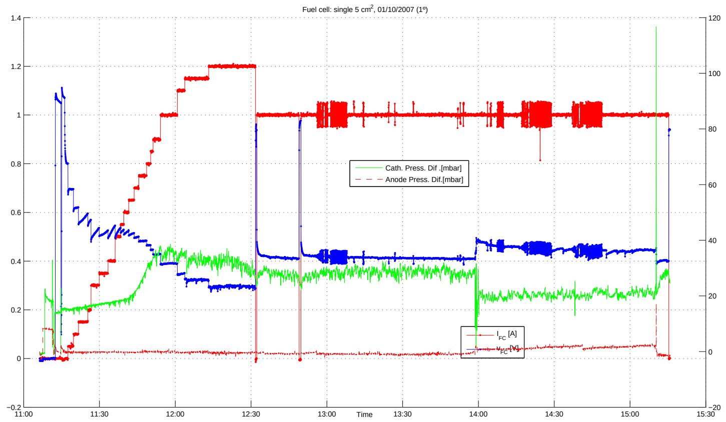

Figure B.2: EIS test part, 2º graph

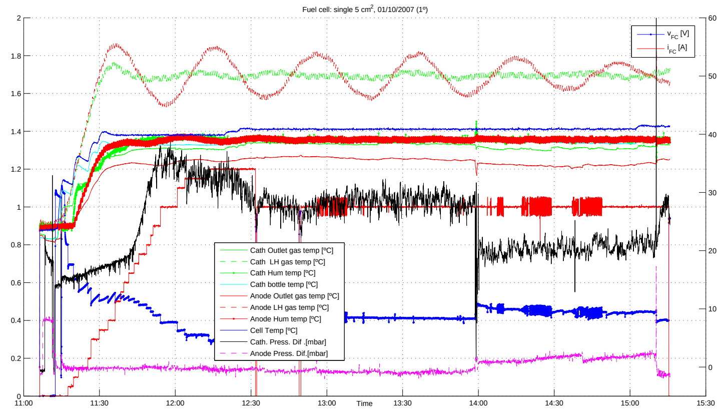

Figure B.3: EIS test part, 3º graph

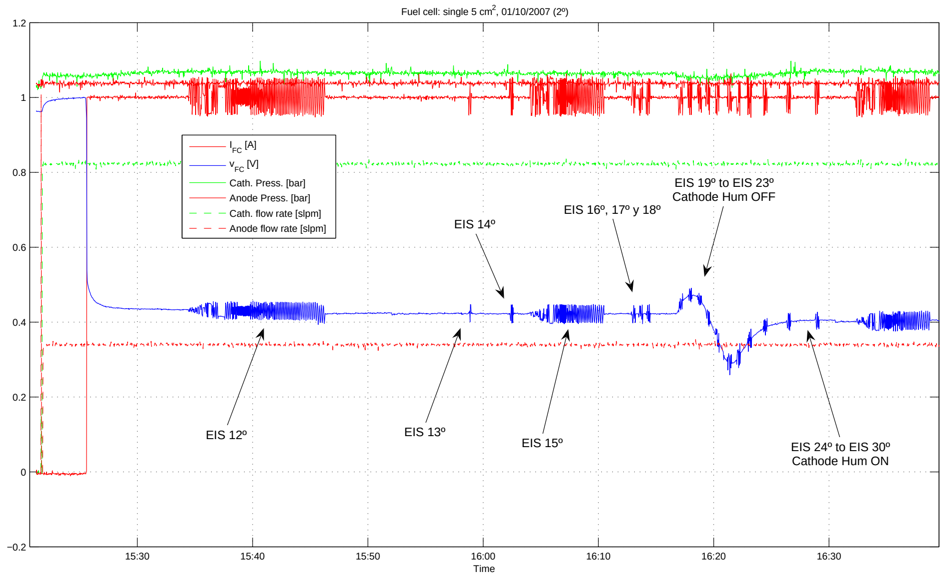

Figure B.4: Anode and cathode humidifier bypass, 1º graph

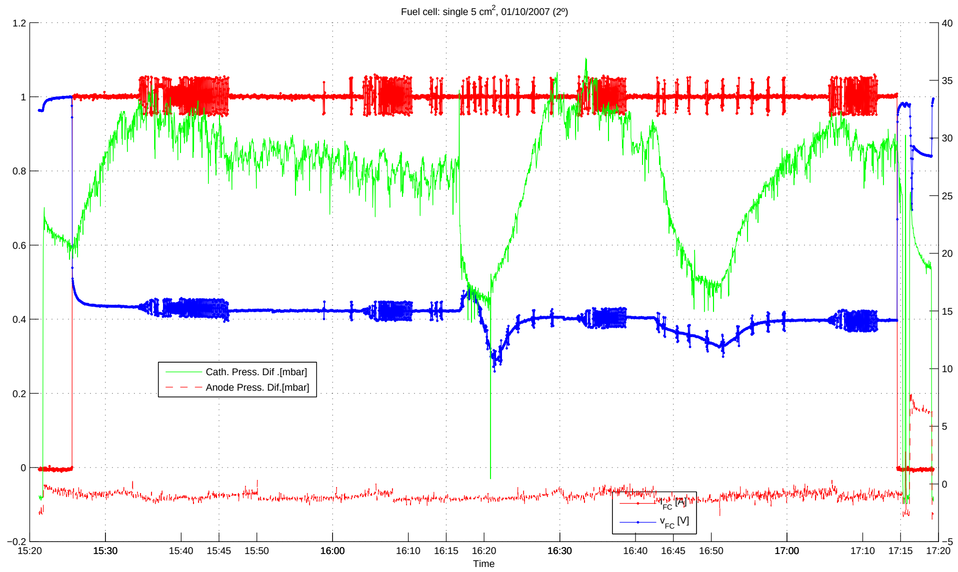

Figure B.5: Anode and cathode humidifier bypass, 2º graph

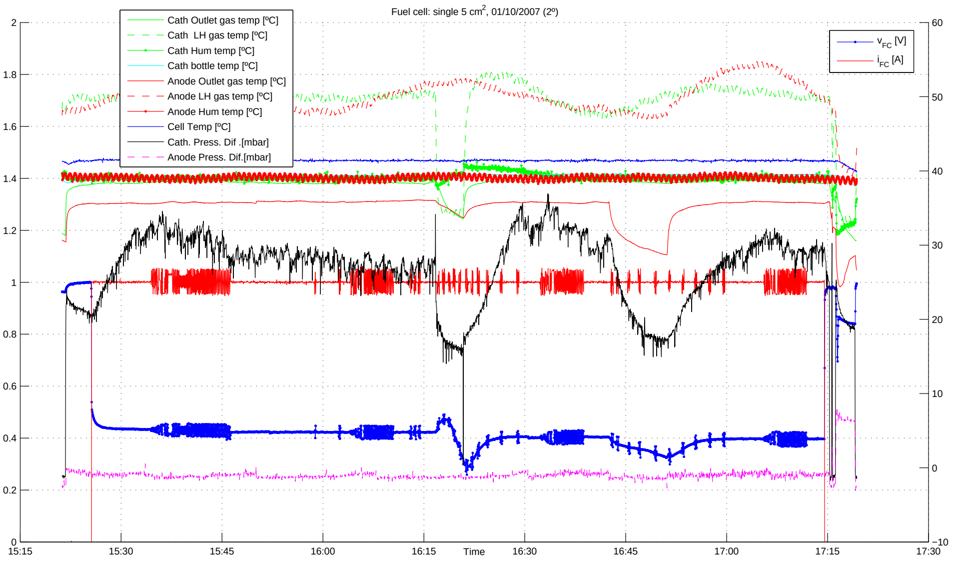

Figure B.6: Anode and cathode humidifier bypass, 3° graph

B.2.2 Impedance Spectroscopy responses

Impedance spectroscopy details of EIS responses of this day were done on table B.4

EIS	**Points**	**I$_{FC}$ [A]**	P$_{FC}$	**Comments**
1	51	1.0	P$_{amb}$	Long EIS test
2	51	1.0	P$_{amb}$	Long EIS test
3	51	1.0	P$_{amb}$	Long EIS test
4	51	1.0	P$_{amb}$	Long EIS test
5	51	1.0	P$_{amb}$	Long EIS test
6	21	1.0	P$_{amb}$	Short EIS test
7	21	1.0	P$_{amb}$	Short EIS test
8	21	1.0	1.7 [Bar]	Short EIS test
9	51	1.0	1.7 [Bar]	Long EIS test
10	51	1.0	1.7 [Bar]	Long EIS test
11	51	1.0	1.7 [Bar]	Long EIS test
12	51	1.0	P$_{amb}$	Long EIS test
13	21	1.0	P$_{amb}$	Short EIS test
14	11	1.0	P$_{amb}$	Short EIS test
15	51	1.0	P$_{amb}$	Long EIS test
16	11	1.0	P$_{amb}$	Short EIS test
17	11	1.0	P$_{amb}$	Short EIS test
18	11	1.0	P$_{amb}$	Short EIS test
19	21	1.0	P$_{amb}$	Cat. by Pass ON
20	21	1.0	P$_{amb}$	Cat. by Pass ON
21	21	1.0	P$_{amb}$	Cat. by Pass ON
22	21	1.0	P$_{amb}$	Cat. by Pass ON
23	21	1.0	P$_{amb}$	Cat. by Pass ON
24	21	1.0	P$_{amb}$	Cat. by Pass OFF
25	21	1.0	P$_{amb}$	Cat. by Pass OFF
26	21	1.0	P$_{amb}$	Cat. by Pass OFF
27	21	1.0	P$_{amb}$	Cat. by Pass OFF
28	21	1.0	P$_{amb}$	Cat. by Pass OFF
29	21	1.0	P$_{amb}$	Cat. by Pass OFF
30	51	1.0	P$_{amb}$	Long EIS
31	21	1.0	P$_{amb}$	Anode by Pass ON
32	21	1.0	P$_{amb}$	Anode by Pass ON
33	21	1.0	P$_{amb}$	Anode by Pass ON
34	21	1.0	P$_{amb}$	Anode by Pass ON
35	21	1.0	P$_{amb}$	Anode by Pass ON
36	21	1.0	P$_{amb}$	Anode by Pass OFF
37	21	1.0	P$_{amb}$	Anode by Pass OFF
38	21	1.0	P$_{amb}$	Anode by Pass OFF
39	21	1.0	P$_{amb}$	Anode by Pass OFF
40	21	1.0	P$_{amb}$	Anode by Pass OFF
41	51	1.0	P$_{amb}$	Long EIS

Table B.4: EIS details of day 01/10/2007, T$_{FC}$=40 [^{o}C]

In this part of day, we make different spectroscopies test in order to get the maximum amount of information about cell response with minimum number of points. Bode response on figure B.7 and Nyquist response on figure B.8. These tests are useful to obtain different conditions to observe humidifier by pass evolution.

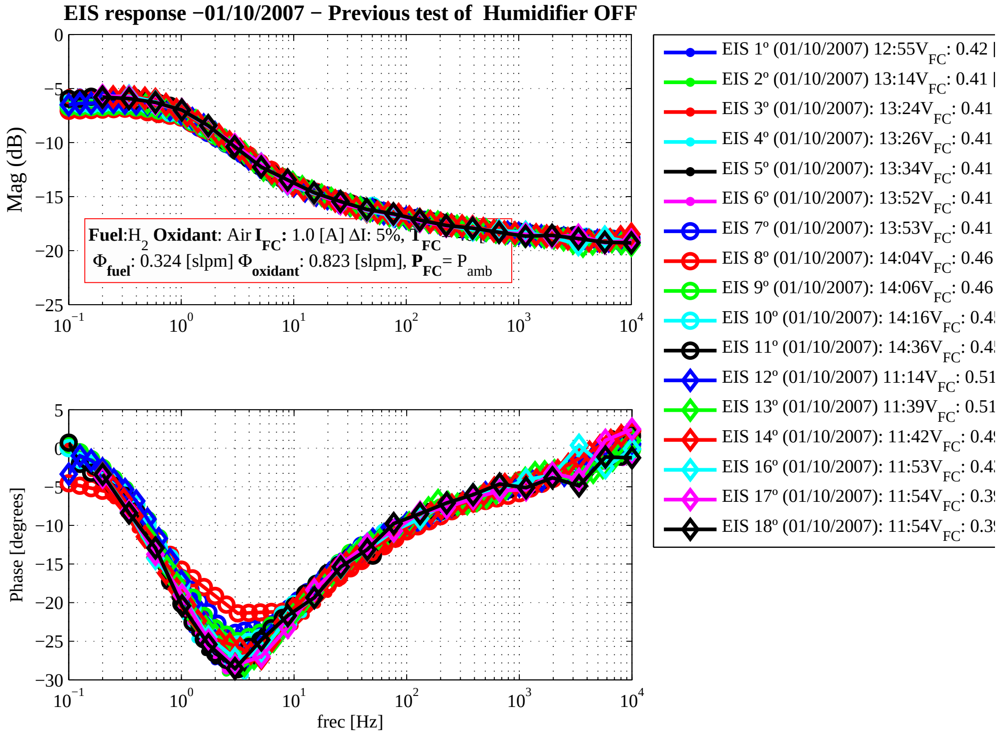

Figure B.7: Bode response of EIS test part

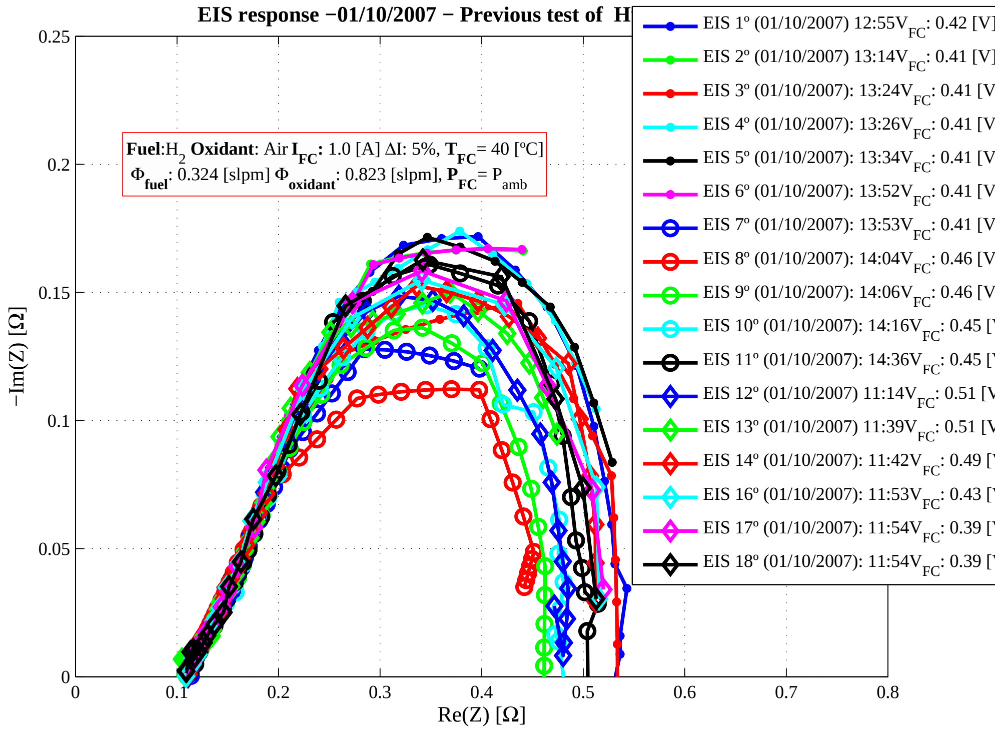

Figure B.8: Nyquist response of EIS test part

B.2.3 Cathode Humidifier ON-OFF (EIS 15 to 30)

Here, we present the time response and EIS results (Nyquist and Bode) on cathode humidifier interruption OFF and ON, with: $I_{FC} = 1.0[A]$ and $P_{FC} = P_{amb}$ at $T_{FC} = 40$ [°C].

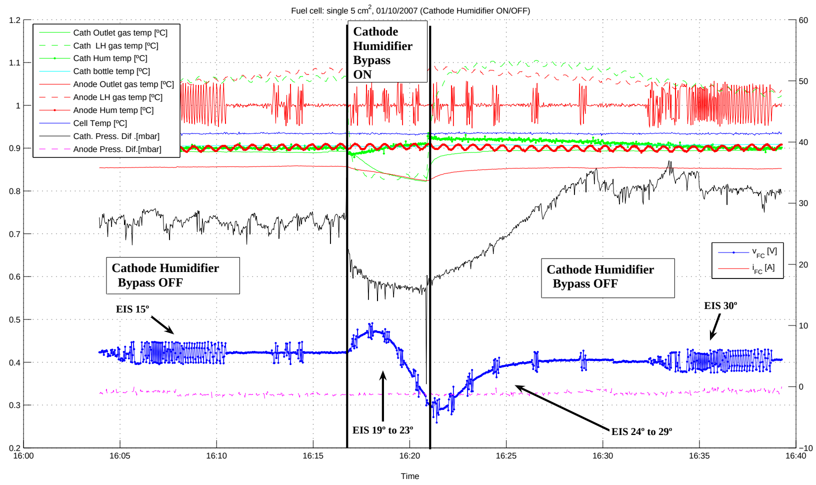

(a) Time evolution

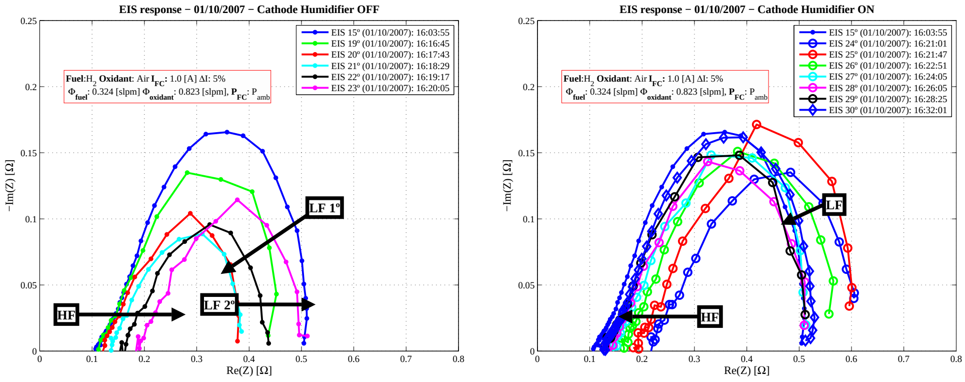

(b) Nyquist (Hum. OFF)

(c) Nyquist (Hum. ON)

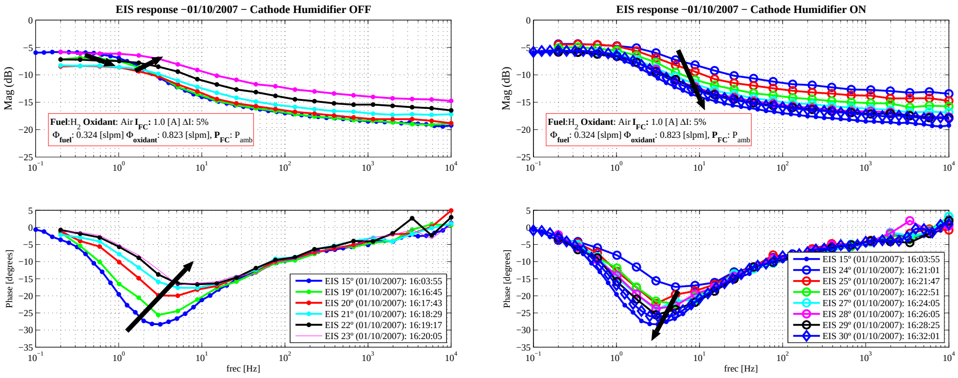

(d) Bode (Hum. OFF)

(e) Bode (Hum. ON)

Figure B.9: Cathode humidifier OFF: T_{FC}= 40 °C, I_{FC}= 1.0, P_{FC}= P_{amb}

B.2.4 Anode Humidifier ON-OFF (EIS 30 to 41)

Here, we present the time response and EIS results (Nyquist and Bode) with anode humidifier interruption OFF and ON, with: $I_{FC} = 1.0[A]$ and $P_{FC} = P_{amb}$ at $T_{FC} = 40$ [°C].

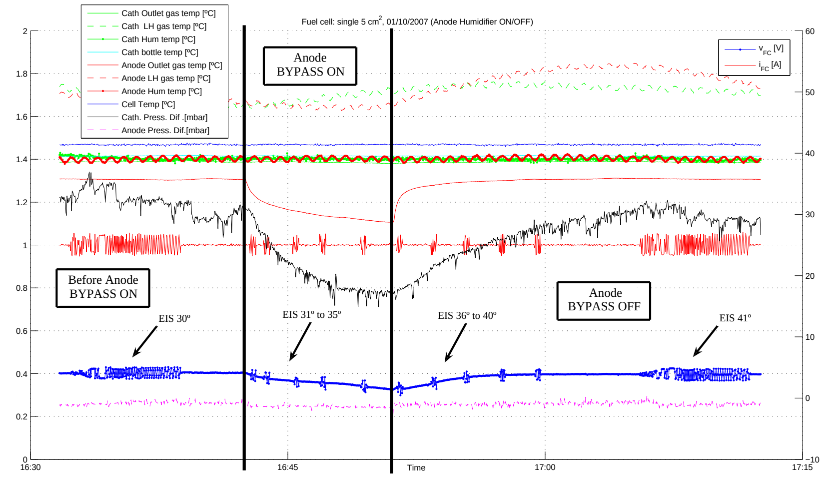

(a) Time evolution

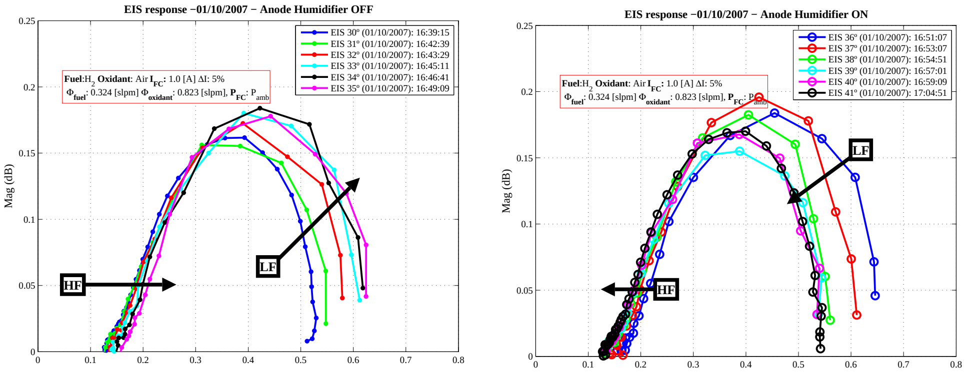

(b) Nyquist (Hum. OFF) (c) Nyquist (Hum. ON)

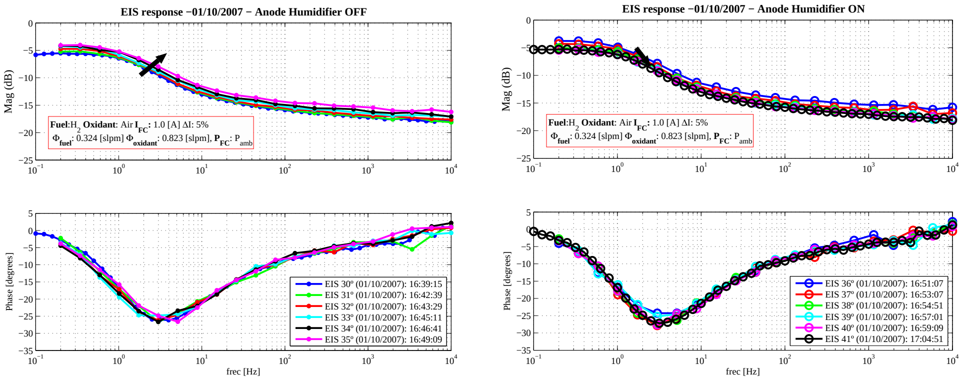

(d) Bode (Hum. OFF) (e) Bode (Hum. ON)

Figure B.10: Anode humidifier OFF: T_{FC}= 40 °C, I_{FC}= 1.0 A, P_{FC}= P_{amb}

B.3 Day: 02/10/2007

Operating conditions of this day is showed on table B.5:

	$\mathbf{T}_{ca,hum}$[^{o}C]	$\mathbf{T}_{ca,LH}$[^{o}C]	$\mathbf{P}_{ca}$[bar$_a$]	Φ_{cath}[slpm]
Cath. (Air)	39.5	50	1	0.824
	$\mathbf{T}_{An,hum}$[^{o}C]	$\mathbf{T}_{An,LH}$[^{o}C]	$\mathbf{P}_{An}$[bar$_a$]	Φ_{an}[slpm]
Anode (H_2)	39.5	50	1	0.324
	$\mathbf{T}_{FC}$[^{o}C]			
Cell	41.5			
Comments: Humidifiers bypass test EIS with 40 [°C] and pressure change to 10 [PSIg]				

Table B.5: Operating conditions of 02/10/2007

B.3.1 Day graph response

General evolution of this day can be seen on figures: B.11, B.12 and B.13.

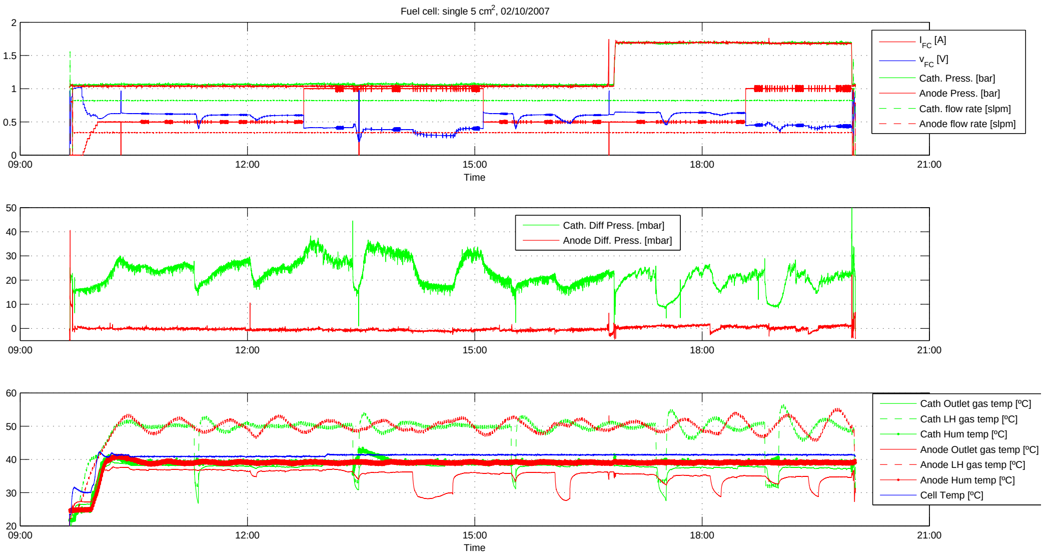

Figure B.11: Day evolution, first graph

Figure B.12: Day evolution, second graph

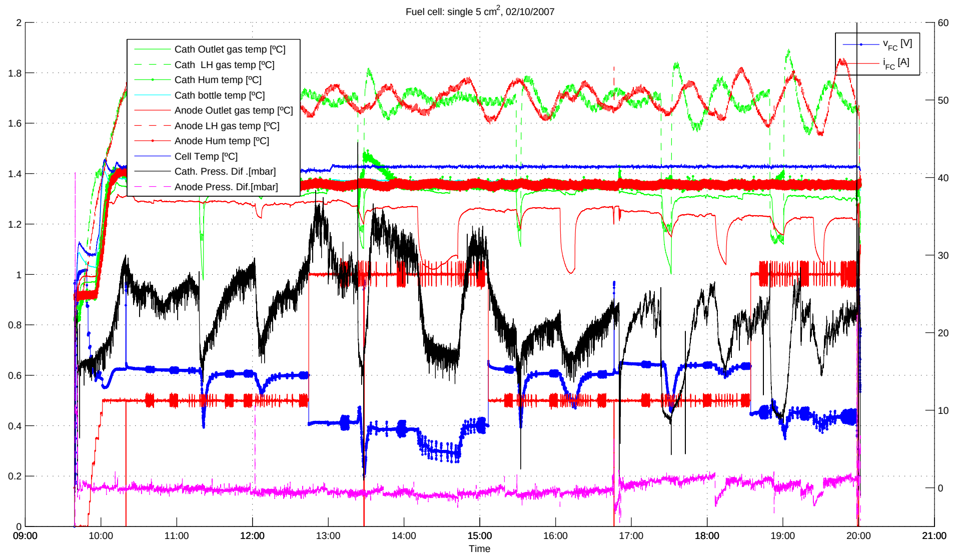

Figure B.13: Day evolution, third graph

On table B.6, we give the general view of different spectroscopies of day 02/10/2007.

EIS	**Points**	**I$_{FC}$ [A]**	**P$_{FC}$ [Bar]**	**Comments**
1	51	0.5	P_{amb}	Long EIS
2	51	0.5	P_{amb}	Long EIS
3	21	0.5	P_{amb}	short EIS, probe
4	11	0.5	P_{amb}	short EIS, probe
5	21	0.5	P_{amb}	short EIS, probe
6→8	21	0.5	P_{amb}	Cathode humidifier OFF (1°), short EIS
9→14	21	0.5	P_{amb}	Cathode humidifier ON (1°), short EIS
15	51	0.5	P_{amb}	Long EIS
16	51	0.5	P_{amb}	Long EIS
17→19	21	0.5	P_{amb}	Anode humidifier OFF (1°), short EIS
20→28	21	0.5	P_{amb}	Anode humidifier ON (1°), short EIS
29	51	0.5	P_{amb}	Long EIS
30	51	1	P_{amb}	Long EIS
31→34	21	1	P_{amb}	Cathode humidifier OFF, short EIS
35→39	21	1	P_{amb}	Cathode humidifier ON, short EIS
40	51	1	P_{amb}	Long EIS
41→51	21	1	P_{amb}	Anode humidifier OFF, short EIS
52→59	21	1	P_{amb}	Anode humidifier ON, short EIS
60	51	1	P_{amb}	Long EIS
61	51	0.5	P_{amb}	Long EIS
62→64	21	0.5	P_{amb}	Cathode humidifier OFF (2°), short EIS
65→70	21	0.5	P_{amb}	Cathode humidifier ON (2°), short EIS
71	51	0.5	P_{amb}	Long EIS
72→78	21	0.5	P_{amb}	Anode humidifier OFF (2°), short EIS
79→86	21	0.5	P_{amb}	Anode humidifier ON (2°), short EIS
87	51	0.5	P_{amb}	Long EIS
88	51	0.5	$P_{amb} + 10[PSI]$	Long EIS
89→94	21	0.5	$P_{amb} + 10[PSI]$	Cathode humidifier OFF, short EIS
95→102	21	0.5	$P_{amb} + 10[PSI]$	Cathode humidifier ON, short EIS
103	51	0.5	$P_{amb} + 10[PSI]$	Long EIS
104→107	21	0.5	$P_{amb} + 10[PSI]$	Anode humidifier OFF, short EIS
108→111	21	0.5	$P_{amb} + 10[PSI]$	Anode humidifier ON, short EIS
112	51	0.5	$P_{amb} + 10[PSI]$	Long EIS
113	51	1	$P_{amb} + 10[PSI]$	Long EIS
114→119	21	1	$P_{amb} + 10[PSI]$	Cathode humidifier OFF, short EIS
120→124	21	1	$P_{amb} + 10[PSI]$	Cathode humidifier ON, short EIS
125	51	1	$P_{amb} + 10[PSI]$	Long EIS
126→129	21	1	$P_{amb} + 10[PSI]$	Anode humidifier OFF, short EIS
130→133	21	1	$P_{amb} + 10[PSI]$	Anode humidifier ON, short EIS
134	51	1	$P_{amb} + 10[PSI]$	Long EIS

Table B.6: EIS details with T$_{FC}$=40 [^{o}C],02/10/2007

Like you will see, on these day, we make current variation from 0.5 [A] to 1.0 [A] and then returning to 0.5 [A], then we increase the pressure up to 10 [PSIg] and we make current variation.

B.3.2 Cathode Humidifier ON-OFF (EIS 1 to 15)

Here, we present the time response and EIS results (Nyquist and Bode) on cathode humidifier interruption OFF and ON, with: $I_{FC} = 0.5[A]$ and $P_{FC} = P_{amb}$ at $T_{FC} = 40$ [°C] (1° set).

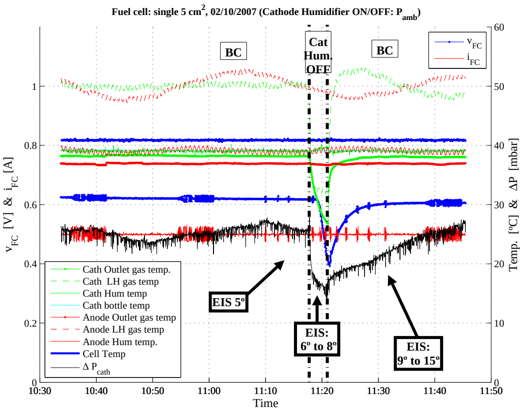

(a) Time evolution

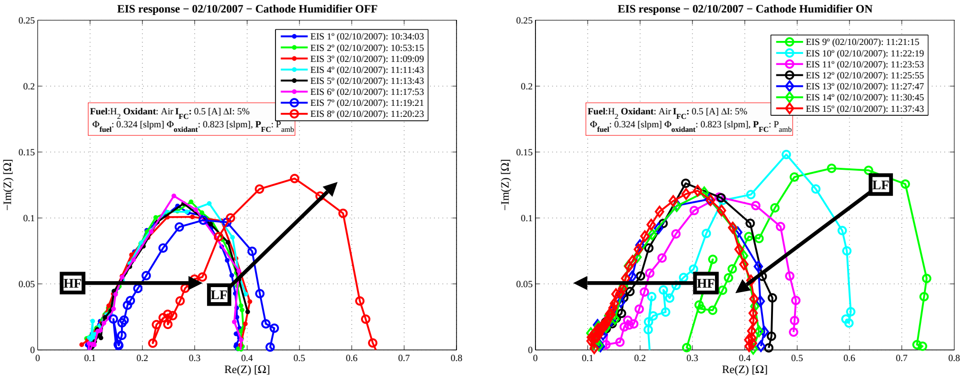

(b) Nyquist (Hum. OFF)

(c) Nyquist (Hum. ON)

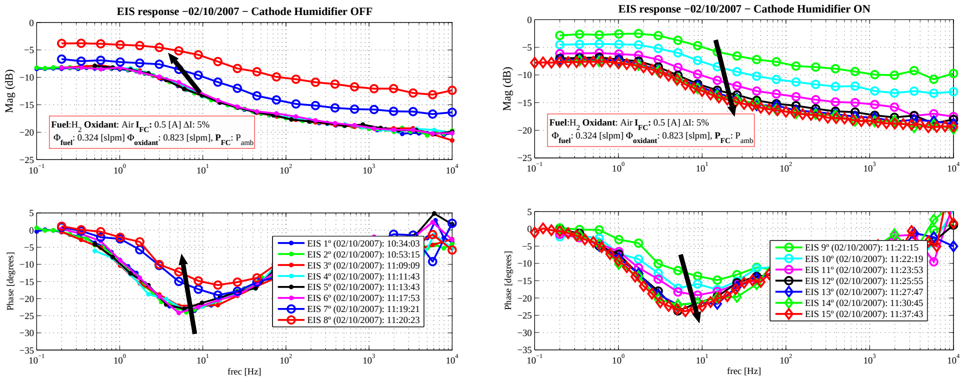

(d) Bode (Hum. OFF)

(e) Bode (Hum. ON)

Figure B.14: Cathode humidifier OFF: T_{FC}= 40 °C, I_{FC}= 0.5 A, P_{FC}= P_{amb} (1°)

B.3.3 Anode Humidifier ON-OFF (EIS 16 to 29)

Here, we present the time response and EIS results (Nyquist and Bode) with anode humidifier interruption OFF and ON, with: $I_{FC} = 0.5[A]$ and $P_{FC} = P_{amb}$ at $T_{FC} = 40$ [°C] (1° set).

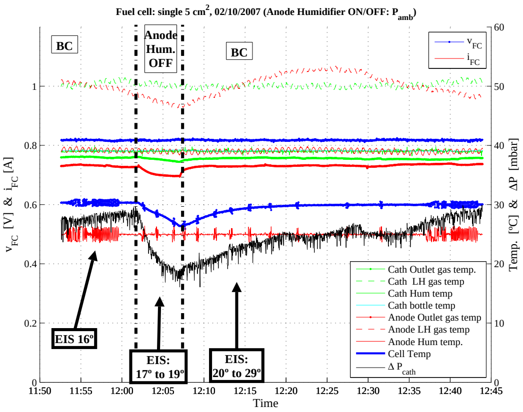

(a) Time evolution

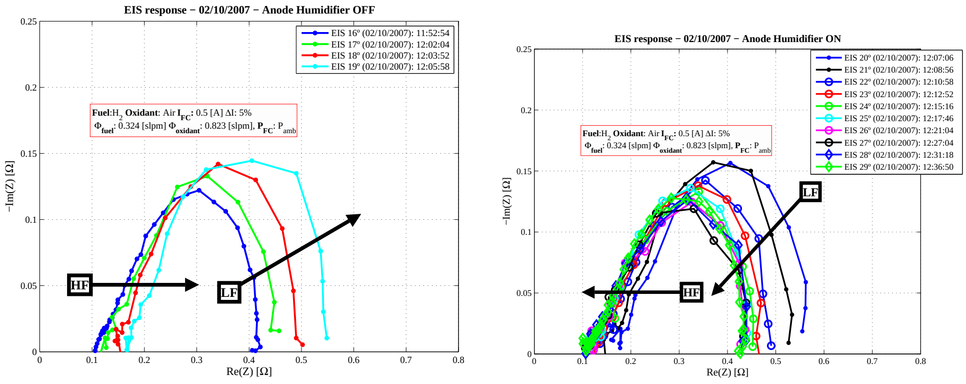

(b) Nyquist (Hum. OFF)

(c) Nyquist (Hum. ON)

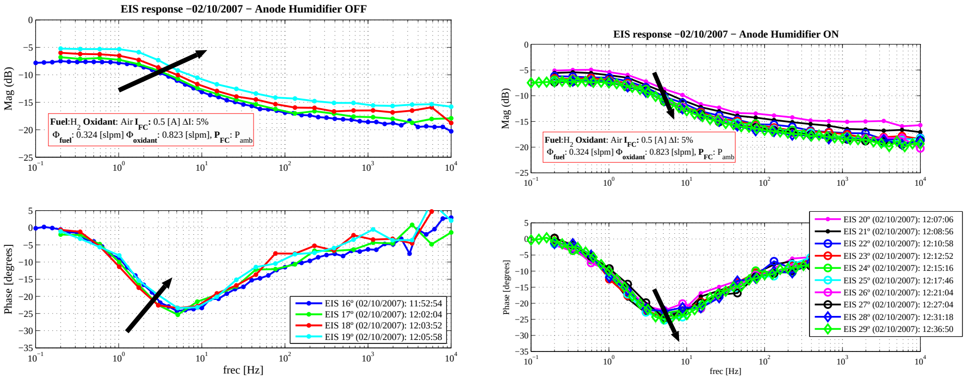

(d) Bode (Hum. OFF)

(e) Bode (Hum. ON)

Figure B.15: Anode humidifier OFF: T_{FC}= 40 °C, I_{FC}= 0.5 A, P_{FC}= P_{amb} (1°)

B.3.4 Cathode Humidifier ON-OFF (EIS 30 to 40)

Here, we present the time response and EIS results (Nyquist and Bode) on cathode humidifier interruption OFF and ON, with: $I_{FC} = 1.0[A]$ and $P_{FC} = P_{amb}$ at $T_{FC} = 40$ [°C] (1° set).

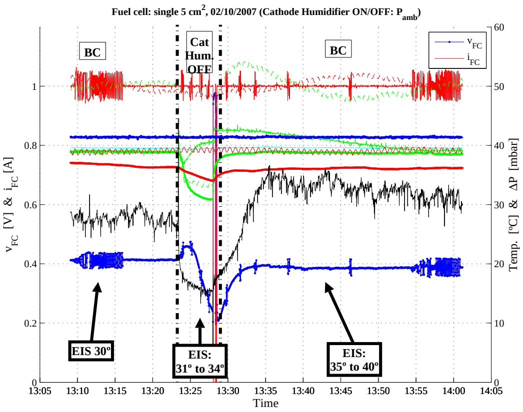

(a) Time evolution

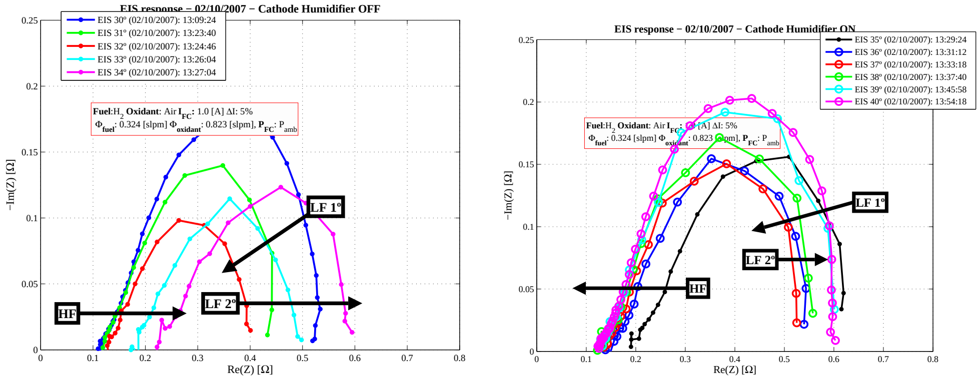

(b) Nyquist (Hum. OFF) (c) Nyquist (Hum. ON)

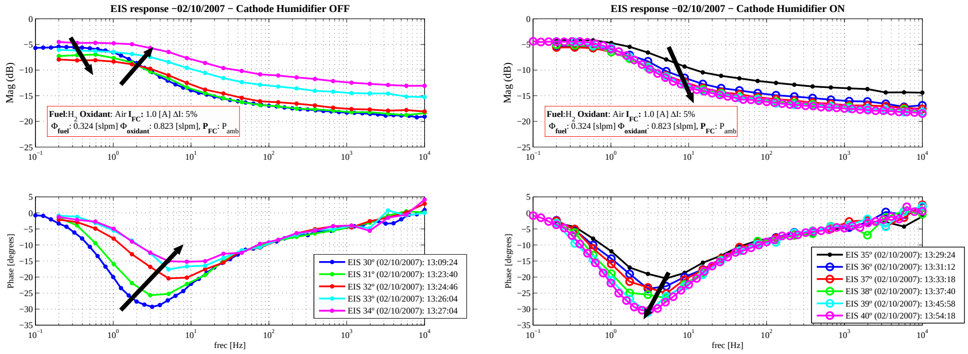

(d) Bode (Hum. OFF) (e) Bode (Hum. ON)

Figure B.16: Cathode humidifier OFF: T_{FC}= 40 °C, I_{FC}= 1.0 A, P_{FC}= P_{amb} (1°)

B.3.5 Anode Humidifier ON-OFF (EIS 40 to 60)

Here, we present the time response and EIS results (Nyquist and Bode) with anode humidifier interruption OFF and ON, with: $I_{FC} = 1.0[A]$ and $P_{FC} = P_{amb}$ at $T_{FC} = 40$ [°C].

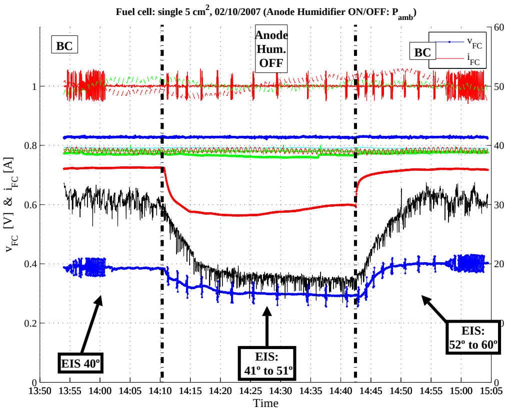

(a) Time evolution

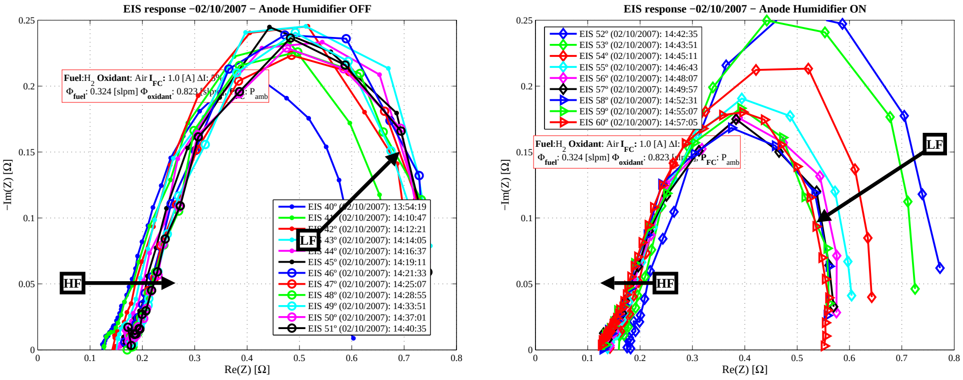

(b) Nyquist (Hum. OFF)   (c) Nyquist (Hum. ON)

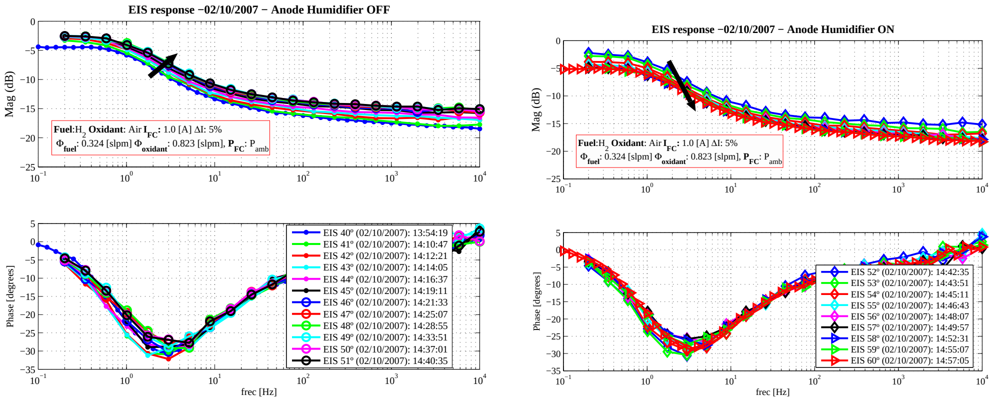

(d) Bode (Hum. OFF)   (e) Bode (Hum. ON)

Figure B.17: Anode humidifier OFF: T_{FC}= 40 °C, I_{FC}= 1.0 A, P_{FC}= P_{amb}

B.3.6 Cathode Humidifier ON-OFF (EIS 61 to 71)

Here, we present the time response and EIS results (Nyquist and Bode) on cathode humidifier interruption OFF and ON, with: $I_{FC} = 0.5[A]$ and $P_{FC} = P_{amb}$ at $T_{FC} = 40$ [°C] (2° set).

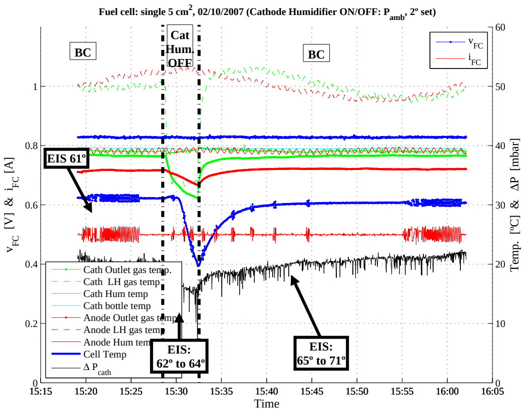

(a) Time evolution

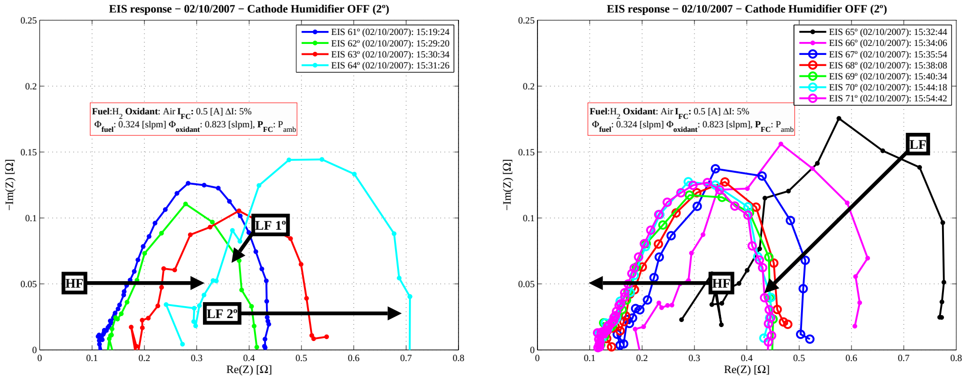

(b) Nyquist (Hum. OFF) (c) Nyquist (Hum. ON)

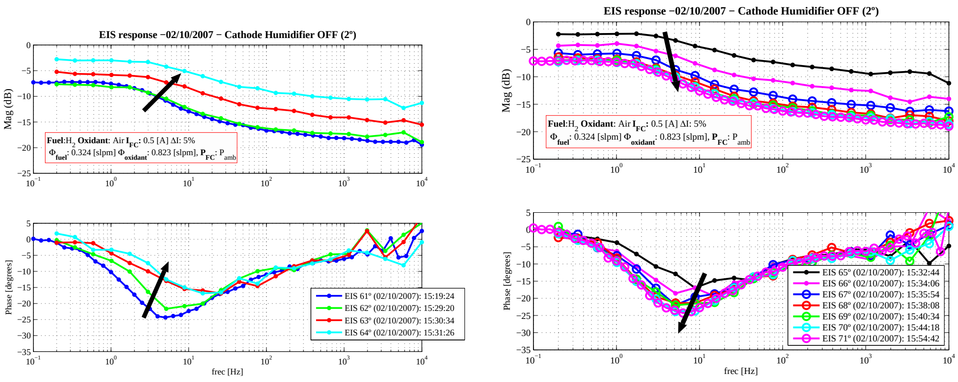

(d) Bode (Hum. OFF) (e) Bode (Hum. ON)

Figure B.18: Cathode humidifier OFF: T_{FC}= 40 °C, I_{FC}= 0.5 A, P_{FC}= P_{amb} (2°)

B.3.7 Anode Humidifier ON-OFF (EIS 71 to 87)

Here, we present the time response and EIS results (Nyquist and Bode) on anode humidifier interruption OFF and ON, with: $I_{FC} = 0.5[A]$ and $P_{FC} = P_{amb}$ at $T_{FC} = 40$ [°C] (2° set).

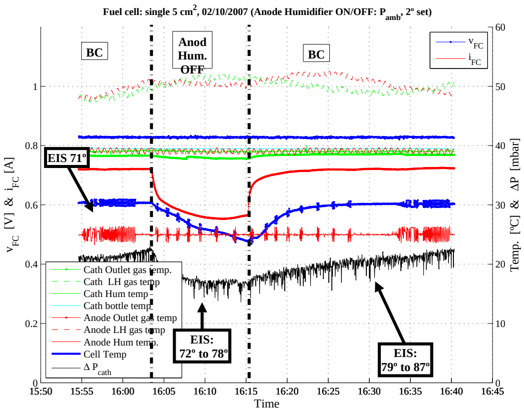

(a) Time evolution

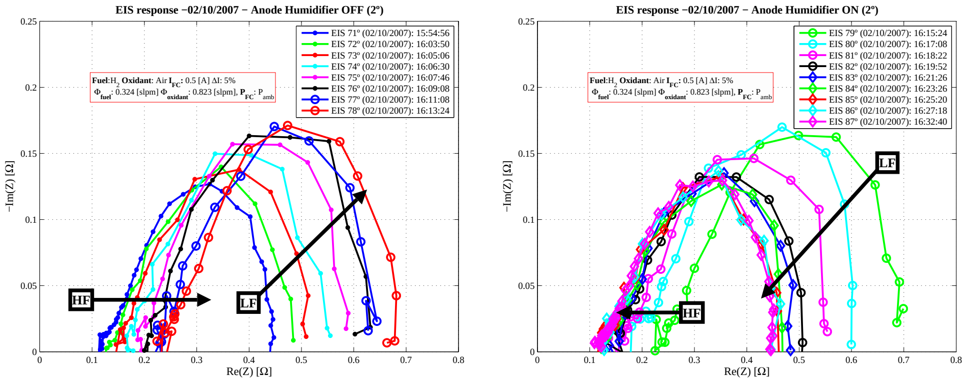

(b) Nyquist (Hum. OFF) (c) Nyquist (Hum. ON)

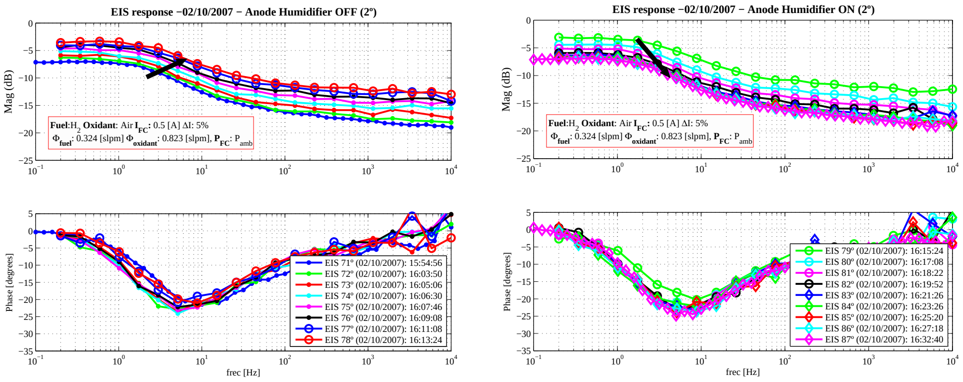

(d) Bode (Hum. OFF) (e) Bode (Hum. ON)

Figure B.19: Anode humidifier OFF: T_{FC}= 40 °C, I_{FC}= 0.5 A, P_{FC}= P_{amb} (2°)

B.3.8 Cathode Humidifier ON-OFF (EIS 88 to 103)

Here, we present the time response and EIS results (Nyquist and Bode) on cathode humidifier interruption OFF and ON, with: $I_{FC} = 0.5[A]$ and $P_{FC} = P_{amb} + 10PSI$ at $T_{FC} = 40$ [°C].

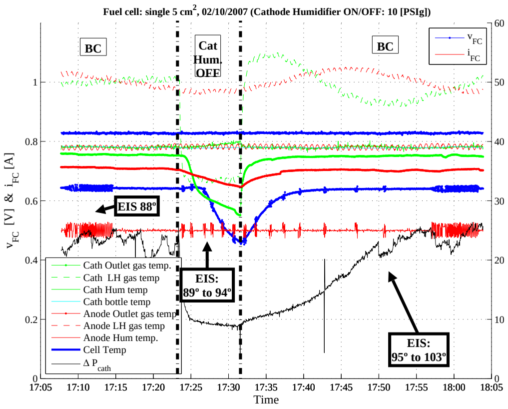

(a) Time evolution

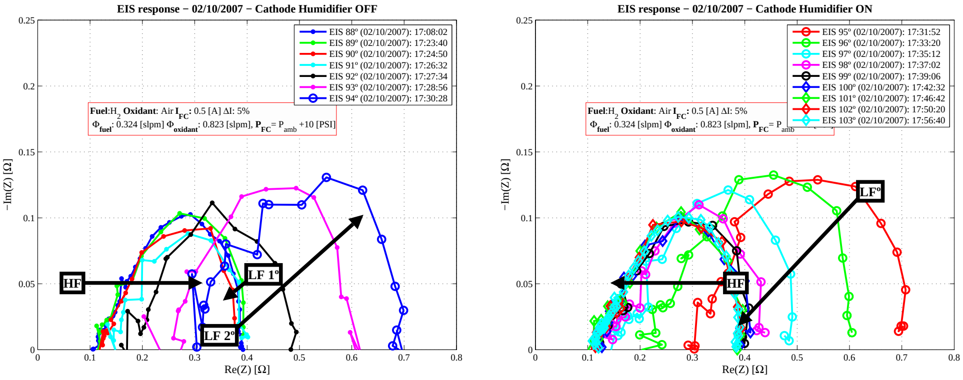

(b) Nyquist (Hum. OFF)

(c) Nyquist (Hum. ON)

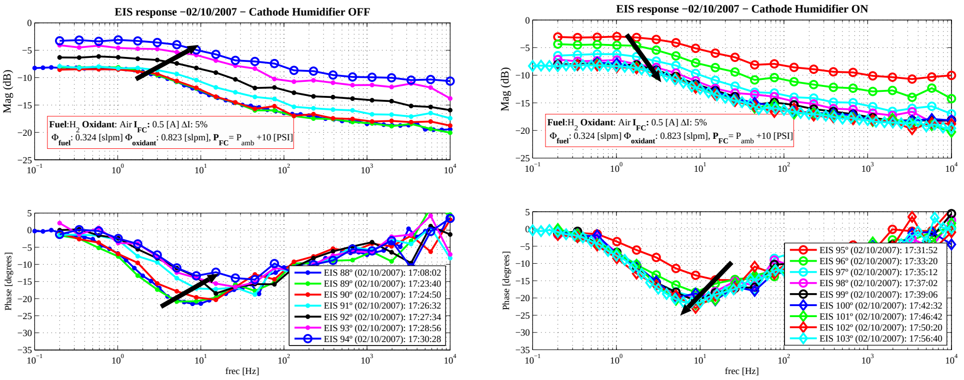

(d) Bode (Hum. OFF)

(e) Bode (Hum. ON)

Figure B.20: Cathode humidifier OFF: T_{FC}= 40 °C, I_{FC}= 0.5 A, P_{FC}= $P_{amb} + 10PSI$

B.3.9 Anode Humidifier ON-OFF (EIS 103 to 112)

Here, we present the time response and EIS results (Nyquist and Bode) on anode humidifier interruption OFF and ON, with: $I_{FC} = 0.5[A]$ and $P_{FC} = P_{amb} + 10PSI$ at $T_{FC} = 40$ [°C].

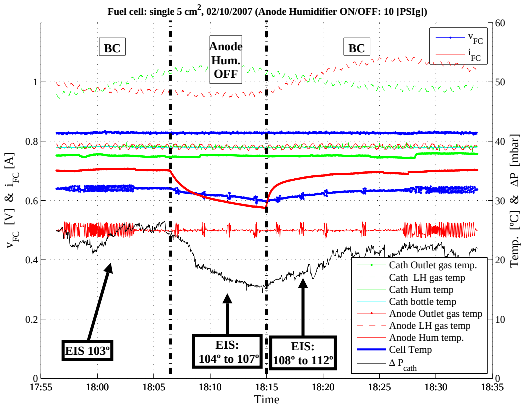

(a) Time evolution

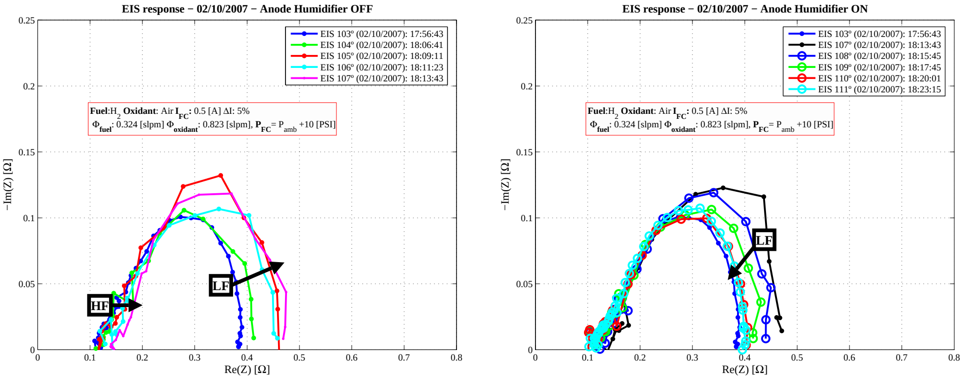

(b) Nyquist (Hum. OFF) (c) Nyquist (Hum. ON)

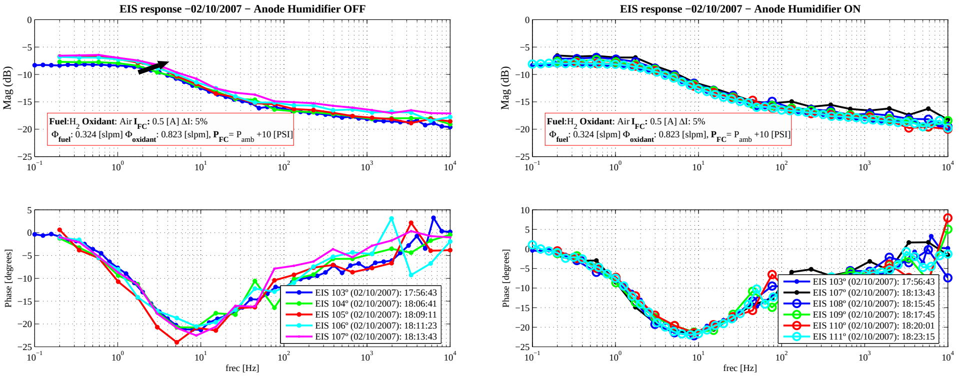

(d) Bode (Hum. OFF) (e) Bode (Hum. ON)

Figure B.21: Anode humidifier OFF: T_{FC}= 40 °C, I_{FC}= 0.5 A, P_{FC}= $P_{amb} + 10PSI$

B.3.10 Cathode Humidifier ON-OFF (EIS 113 to 125)

Here, we present the time response and EIS results (Nyquist and Bode) on cathode humidifier interruption OFF and ON, with: $I_{FC} = 1.0[A]$ and $P_{FC} = P_{amb} + 10PSI$ at $T_{FC} = 40$ [°C].

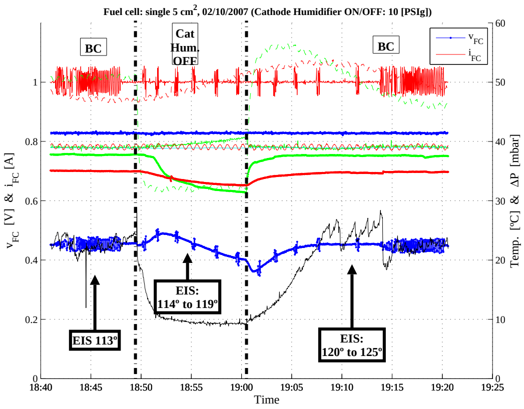

(a) Time evolution

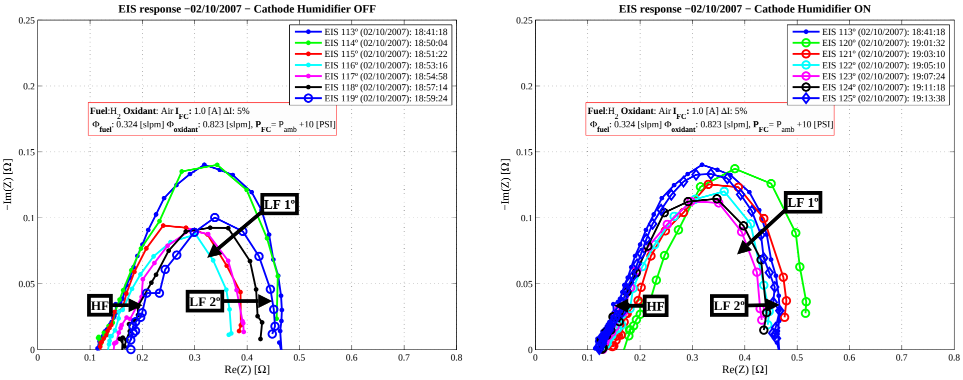

(b) Nyquist (Hum. OFF)

(c) Nyquist (Hum. ON)

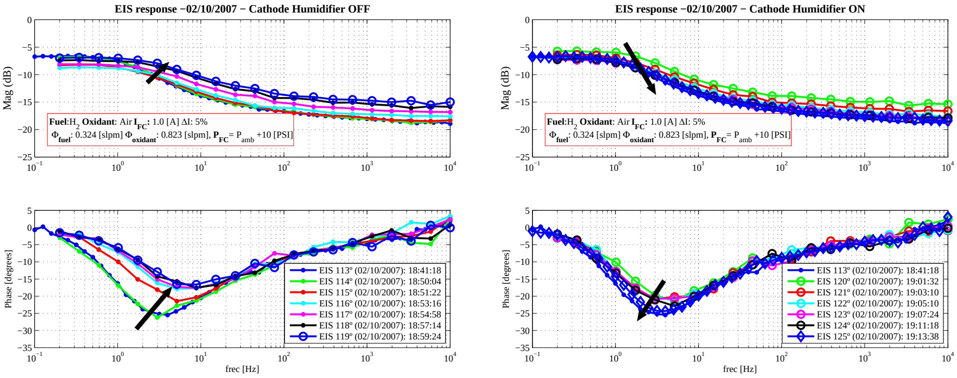

(d) Bode (Hum. OFF)

(e) Bode (Hum. ON)

Figure B.22: Cathode humidifier OFF: T_{FC}= 40 °C, I_{FC}= 1.0 A, P_{FC}= $P_{amb} + 10PSI$

B.3.11 Anode Humidifier ON-OFF (EIS 125 to 134)

Here, we present the time response and EIS results (Nyquist and Bode) on anode humidifier interruption OFF and ON, with: $I_{FC} = 1.0[A]$ and $P_{FC} = P_{amb} + 10PSI$ at $T_{FC} = 40$ [°C].

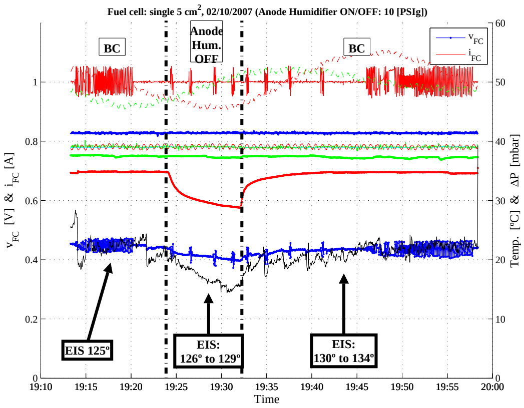

(a) Time evolution

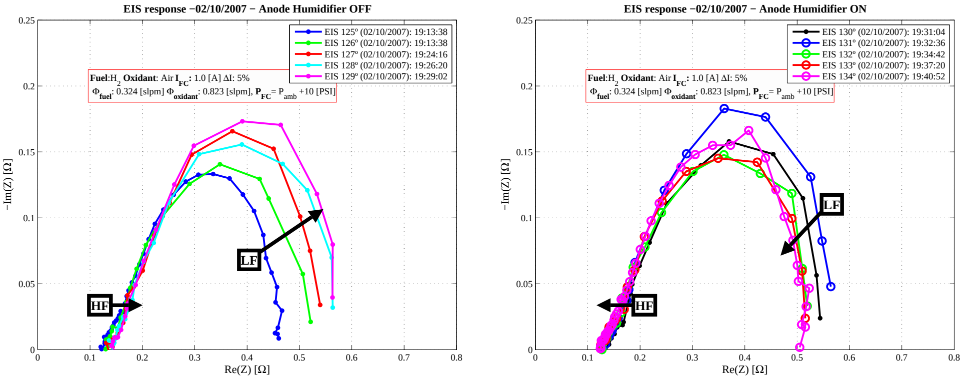

(b) Nyquist (Hum. OFF)

(c) Nyquist (Hum. ON)

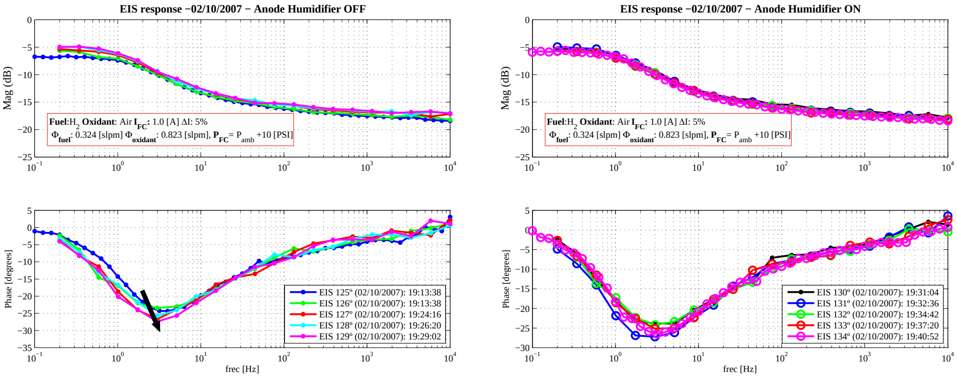

(d) Bode (Hum. OFF)

(e) Bode (Hum. ON)

Figure B.23: Anode humidifier OFF: T_{FC}= 40 °C, I_{FC}= 1.0 A, $P_{FC}= P_{amb} + 10PSI$

B.4 Day: 03/10/2007

Operating conditions of this day is showed on table B.7:

	$\mathbf{T}_{ca,hum}$[^{o}C]	$\mathbf{T}_{ca,LH}$[^{o}C]	$\mathbf{P}_{ca}$[bar$_a$]	Φ_{cath}[slpm]
Cath. (Air)	50.1	57.8	1	0.824
	$\mathbf{T}_{An,hum}$[^{o}C]	$\mathbf{T}_{An,LH}$[^{o}C]	$\mathbf{P}_{An}$[bar$_a$]	Φ_{an}[slpm]
Anode (H_2)	50.0	60	1	0.324
	$\mathbf{T}_{FC}$[^{o}C]			
Cell	48.5			
Comments: Humidifiers bypass test EIS with 50 [°C] and pressure change to 10 [PSIg]				

Table B.7: Operating conditions of 03/10/2007

B.4.1 Day graph response

General evolution of this day can be seen on figures: B.24, B.25 and B.26.

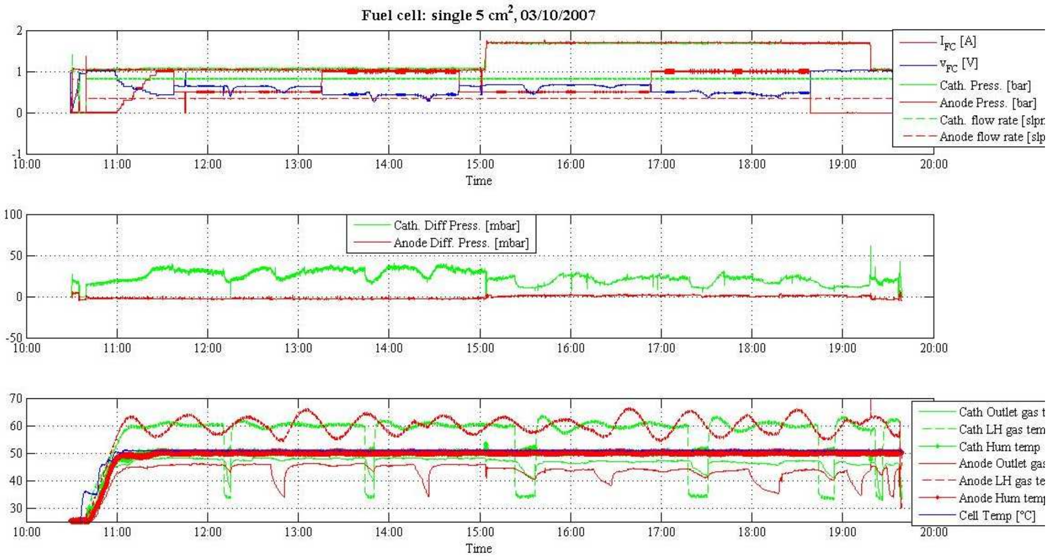

Figure B.24: Day evolution, first graph

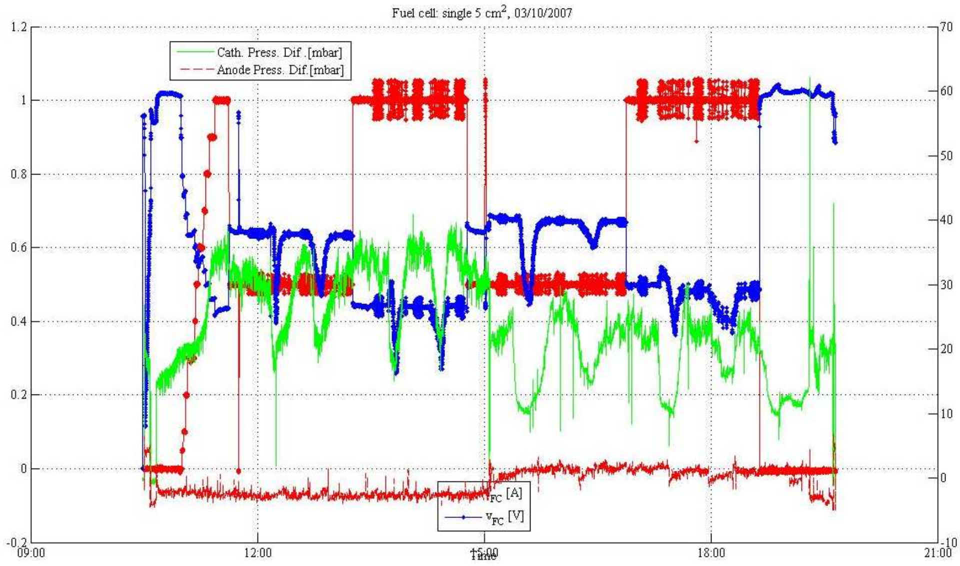

Figure B.25: Day evolution, second graph

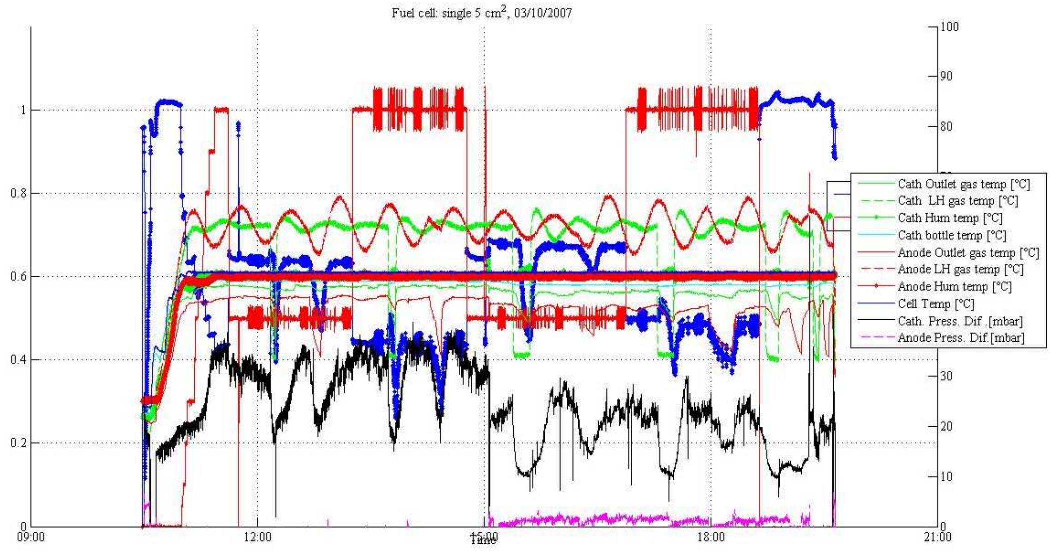

Figure B.26: Day evolution, third graph

On table B.8, we give the general view of different spectroscopies

EIS	**Points**	**I$_{FC}$ [A]**	**P$_{FC}$ [Bar]**	**Comments**
1	51	0.5	P$_{amb}$	Long EIS
2→6	21	0.5	P$_{amb}$	Cathode humidifier OFF, short EIS
7→11	21	0.5	P$_{amb}$	Cathode humidifier ON, short EIS
12	51	0.5	P$_{amb}$	Long EIS
13→17	21	0.5	P$_{amb}$	Anode humidifier OFF, short EIS
18→23	21	0.5	P$_{amb}$	Anode humidifier ON, short EIS
24	51	0.5	P$_{amb}$	Long EIS
25	51	1	P$_{amb}$	Long EIS
26→30	21	1	P$_{amb}$	Cathode humidifier OFF, short EIS
31→34	21	1	P$_{amb}$	Cathode humidifier ON, short EIS
35	51	1	P$_{amb}$	Long EIS
36→41	21	1	P$_{amb}$	Anode humidifier OFF, short EIS
42→45	21	1	P$_{amb}$	Anode humidifier ON, short EIS
46	51	1	P$_{amb}$	Long EIS
47	51	0.5	P$_{amb} + 10[PSI]$	Long EIS
48→54	21	0.5	P$_{amb} + 10[PSI]$	Cathode humidifier OFF, short EIS
55→62	21	0.5	P$_{amb} + 10[PSI]$	Cathode humidifier ON, short EIS
63	51	0.5	P$_{amb} + 10[PSI]$	Long EIS
64→69	21	0.5	P$_{amb} + 10[PSI]$	Anode humidifier OFF, short EIS
70→74	21	0.5	P$_{amb} + 10[PSI]$	Anode humidifier ON, short EIS
75	51	0.5	P$_{amb} + 10[PSI]$	Long EIS
76	51	1	P$_{amb} + 10[PSI]$	Long EIS
77→83	21	1	P$_{amb} + 10[PSI]$	Cathode humidifier OFF, short EIS
84→88	21	1	P$_{amb} + 10[PSI]$	Cathode humidifier ON, short EIS
89	51	1	P$_{amb} + 10[PSI]$	Long EIS
90→96	21	1	P$_{amb} + 10[PSI]$	Anode humidifier OFF, short EIS
97→101	21	1	P$_{amb} + 10[PSI]$	Anode humidifier ON, short EIS
102	51	1	P$_{amb} + 10[PSI]$	Long EIS

Table B.8: EIS conditions with T$_{FC}$=50 [^{o}C], 03/10/2007

Like you will see, on these day, we make current variation from 0.5 [A] to 1.0 [A] and then returning to 0.5 [A], then we increase the pressure up to 10 [PSIg] and we make current variation.

B.4.2 Cathode Humidifier ON-OFF (EIS 1 to 12)

Here, we present the time response and EIS results (Nyquist and Bode) on cathode humidifier interruption OFF and ON, with: $I_{FC} = 0.5[A]$ and $P_{FC} = P_{amb}$ at $T_{FC} = 50$ [°C].

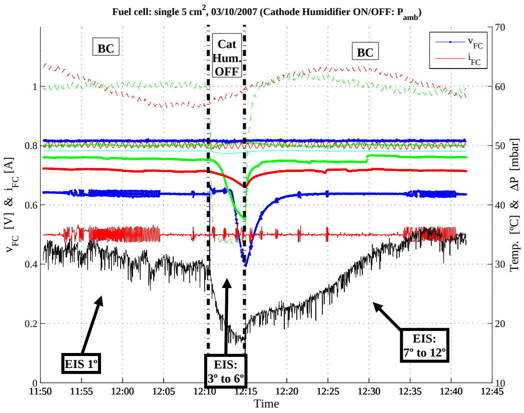

(a) Time evolution

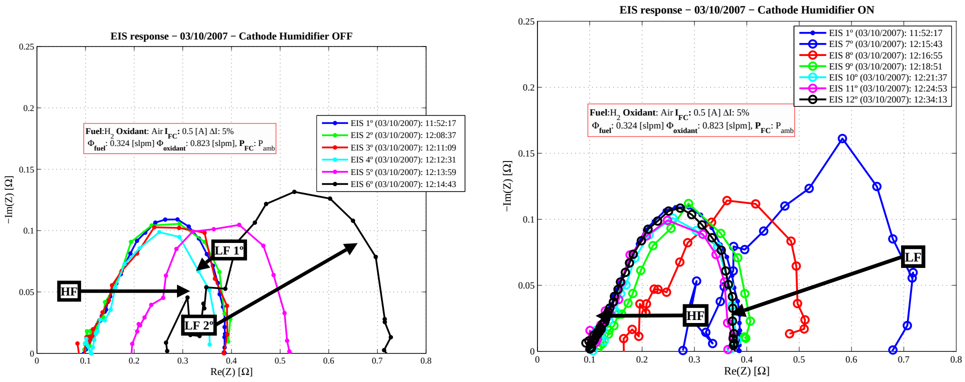

(b) Nyquist (Hum. OFF)

(c) Nyquist (Hum. ON)

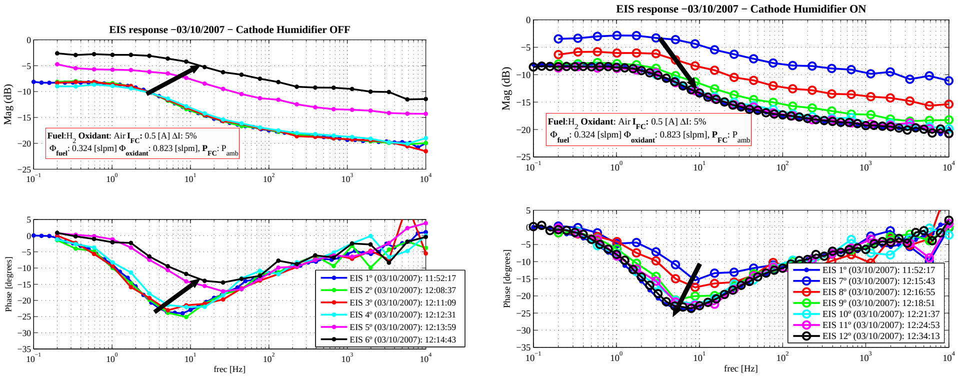

(d) Bode (Hum. OFF)

(e) Bode (Hum. ON)

Figure B.27: Cathode humidifier OFF: T_{FC}= 50 °C, I_{FC}= 0.5 A, P_{FC}= P_{amb}

B.4.3 Anode Humidifier ON-OFF (EIS 12 to 24)

Here, we present the time response and EIS results (Nyquist and Bode) on anode humidifier interruption OFF and ON, with: $I_{FC} = 0.5[A]$ and $P_{FC} = P_{amb}$ at $T_{FC} = 50$ [°C].

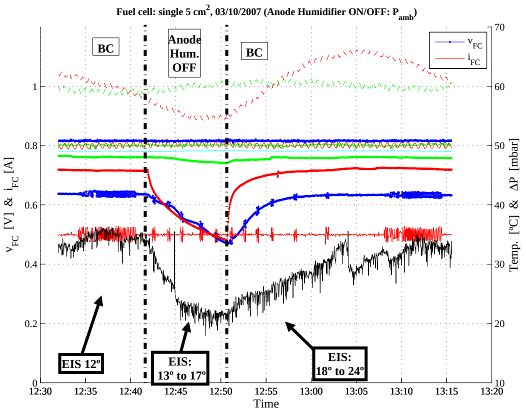

(a) Time evolution

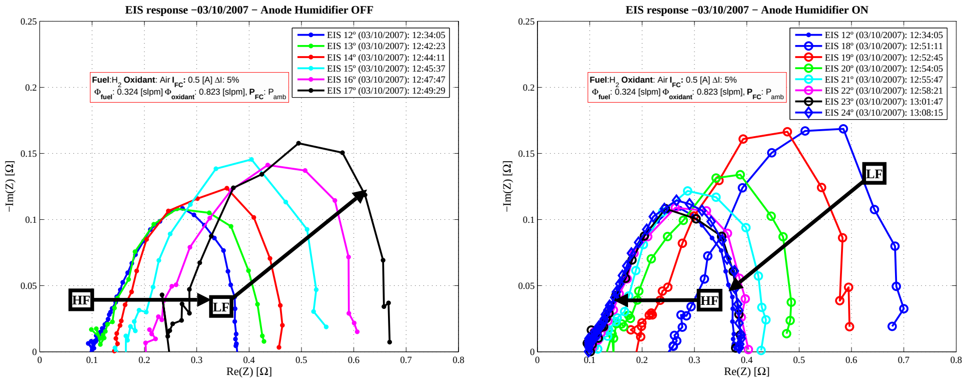

(b) Nyquist (Hum. OFF)

(c) Nyquist (Hum. ON)

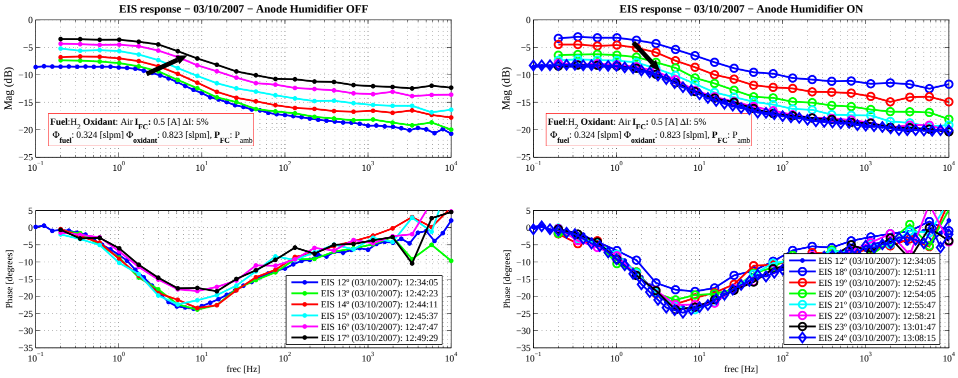

(d) Bode (Hum. OFF)

(e) Bode (Hum. ON)

Figure B.28: Anode humidifier OFF: T_{FC}= 50 °C, I_{FC}= 0.5 A, P_{FC}= P_{amb}

B.4.4 Cathode Humidifier ON-OFF (EIS 25 to 35)

Here, we present the time response and EIS results (Nyquist and Bode) on cathode humidifier interruption OFF and ON, with: $I_{FC} = 1.0[A]$ and $P_{FC} = P_{amb}$ at $T_{FC} = 50$ [°C].

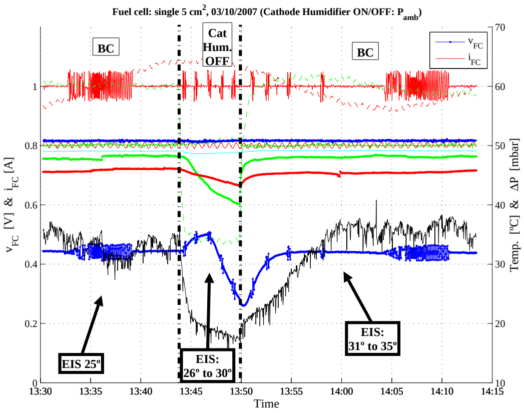

(a) Time evolution

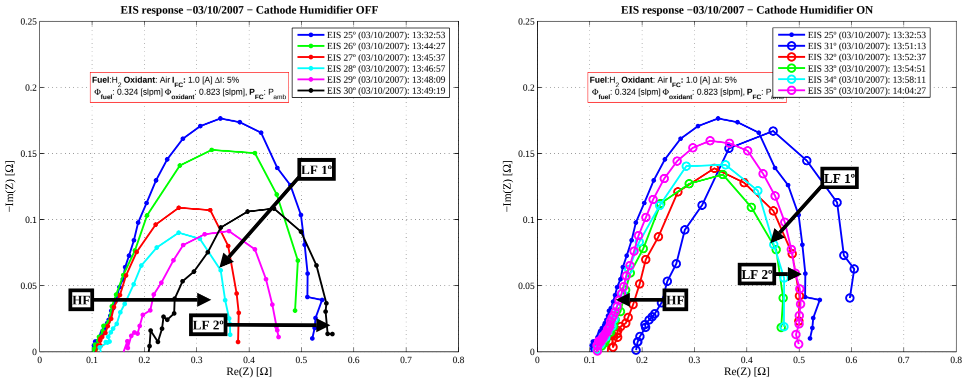

(b) Nyquist (Hum. OFF) (c) Nyquist (Hum. ON)

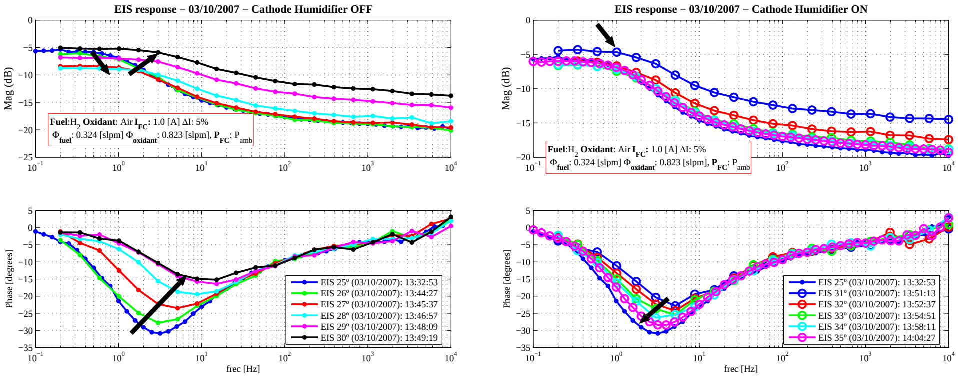

(d) Bode (Hum. OFF) (e) Bode (Hum. ON)

Figure B.29: Cathode humidifier OFF: T_{FC}= 50 °C, I_{FC}= 1.0 A, P_{FC}= P_{amb}

B.4.5 Anode Humidifier ON-OFF (EIS 35 to 46)

Here, we present the time response and EIS results (Nyquist and Bode) on anode humidifier interruption OFF and ON, with: $I_{FC} = 1.0[A]$ and $P_{FC} = P_{amb}$ at $T_{FC} = 50$ [°C].

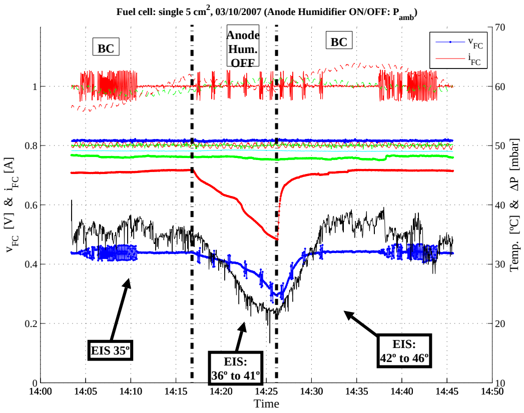

(a) Time evolution

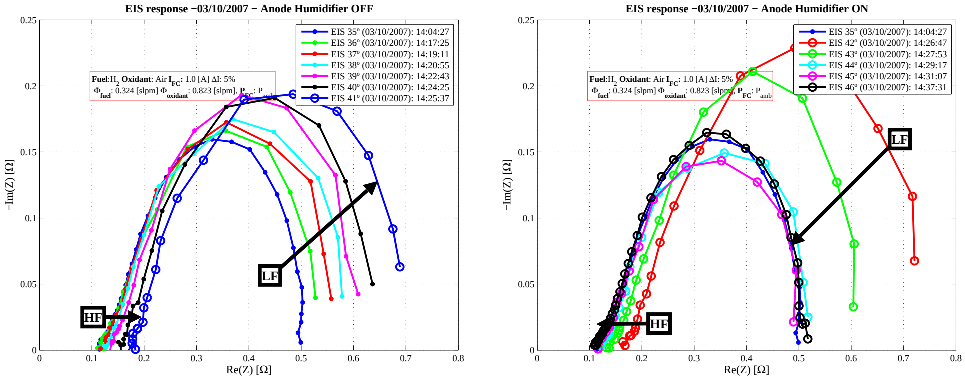

(b) Nyquist (Hum. OFF) (c) Nyquist (Hum. ON)

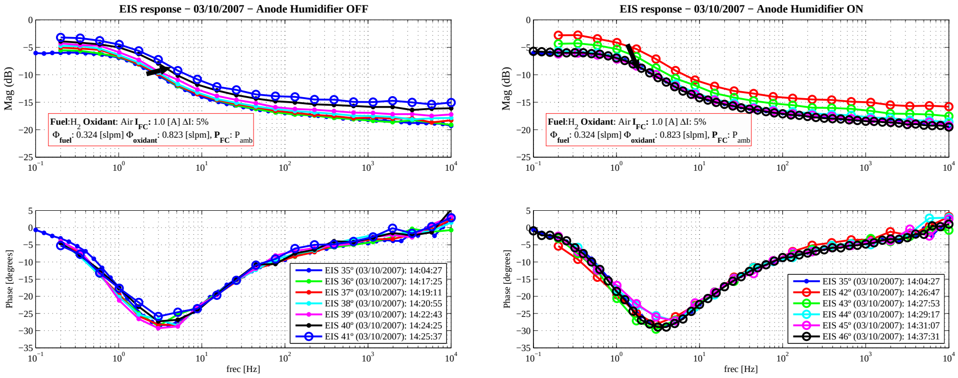

(d) Bode (Hum. OFF) (e) Bode (Hum. ON)

Figure B.30: Anode humidifier OFF: T_{FC}= 50 °C, I_{FC}= 1.0 A, P_{FC}= P_{amb}

B.4.6 Cathode Humidifier ON-OFF (EIS 47 to 63)

Here, we present the time response and EIS results (Nyquist and Bode) on cathode humidifier interruption OFF and ON, with: $I_{FC} = 0.5[A]$ and $P_{FC} = P_{amb} + 10PSI$ at $T_{FC} = 50$ [°C].

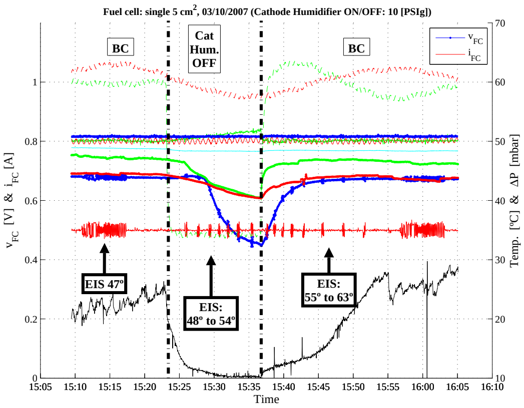

(a) Time evolution

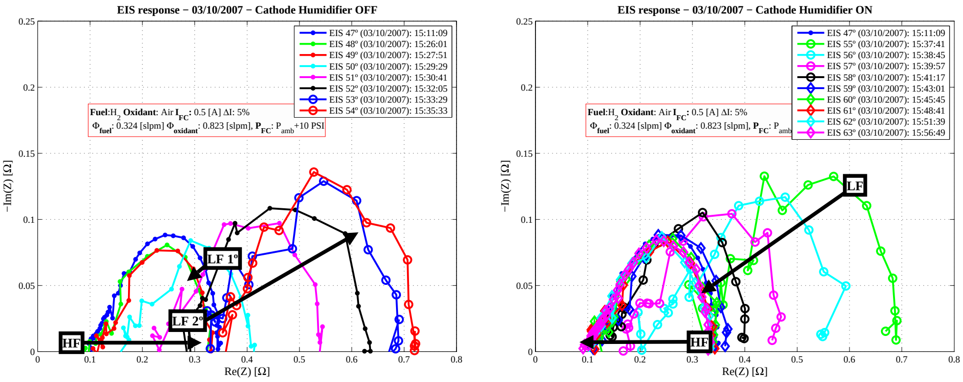

(b) Nyquist (Hum. OFF) (c) Nyquist (Hum. ON)

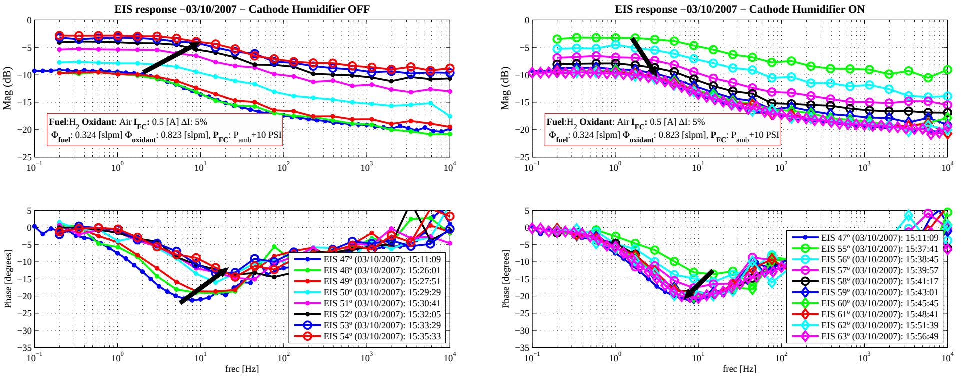

(d) Bode (Hum. OFF) (e) Bode (Hum. ON)

Figure B.31: Cathode humidifier OFF: T_{FC}= 50 °C, I_{FC}= 0.5 A, P_{FC}= $P_{amb} + 10PSI$

B.4.7 Anode Humidifier ON-OFF (EIS 63 to 75)

Here, we present the time response and EIS results (Nyquist and Bode) on anode humidifier interruption OFF and ON, with: $I_{FC} = 0.5[A]$ and $P_{FC} = P_{amb} + 10PSI$ at $T_{FC} = 50$ [°C].

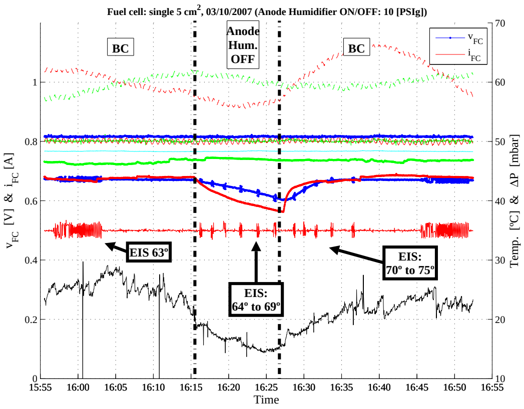

(a) Time evolution

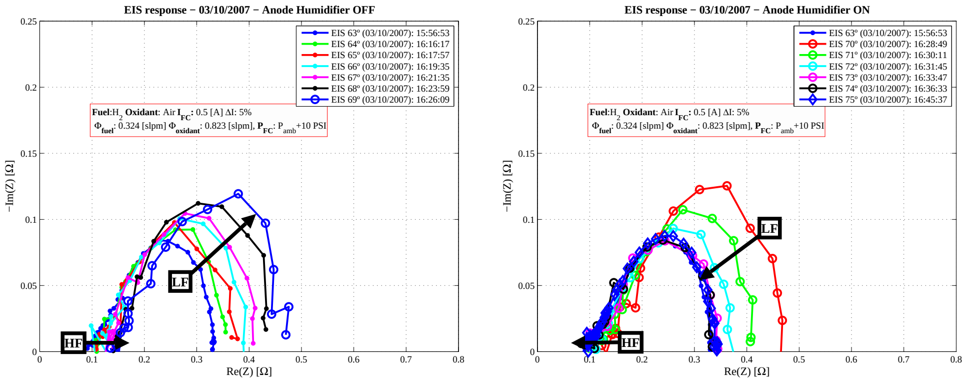

(b) Nyquist (Hum. OFF) (c) Nyquist (Hum. ON)

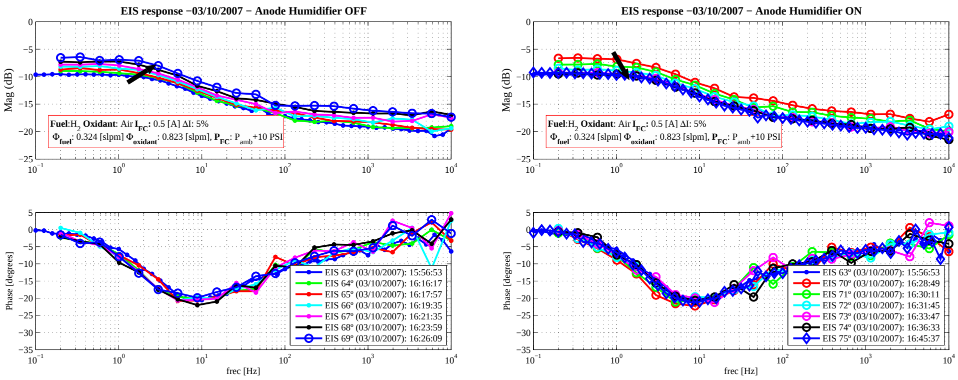

(d) Bode (Hum. OFF) (e) Bode (Hum. ON)

Figure B.32: Anode humidifier OFF: T_{FC}= 50 °C, I_{FC}= 0.5 A, P_{FC}= $P_{amb} + 10PSI$

B.4.8 Cathode Humidifier ON-OFF (EIS 76 to 89)

Here, we present the time response and EIS results (Nyquist and Bode) on cathode humidifier interruption OFF and ON, with: $I_{FC} = 1.0[A]$ and $P_{FC} = P_{amb} + 10PSI$ at $T_{FC} = 50$ [°C].

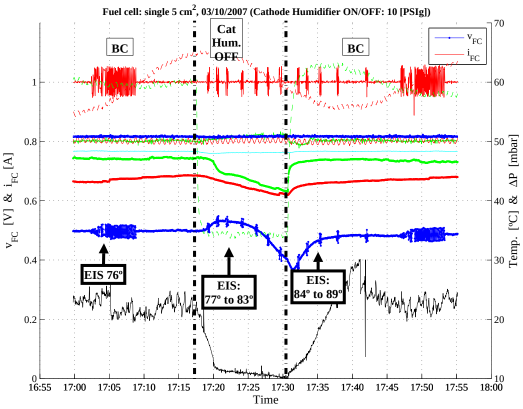

(a) Time evolution

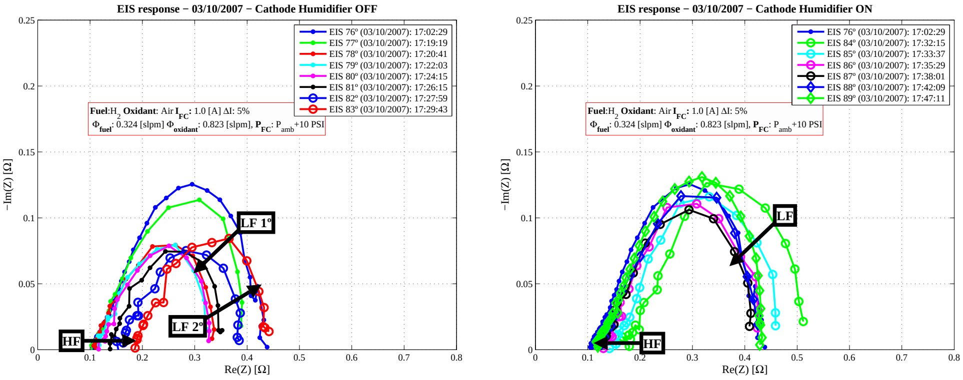

(b) Nyquist (Hum. OFF) (c) Nyquist (Hum. ON)

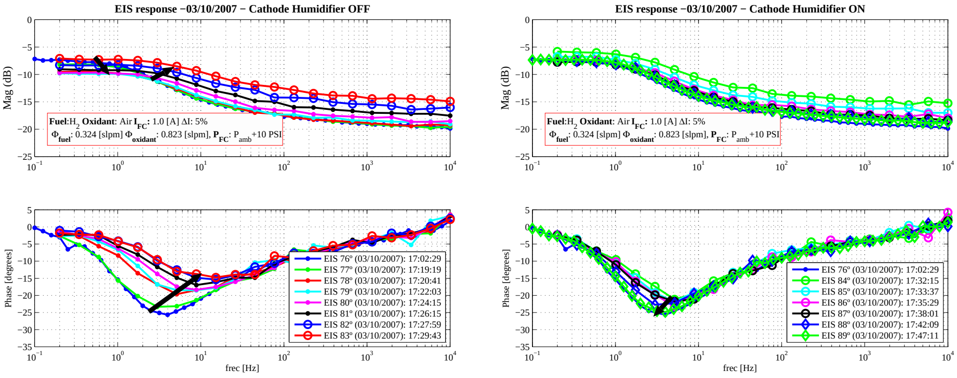

(d) Bode (Hum. OFF) (e) Bode (Hum. ON)

Figure B.33: Cathode humidifier OFF: T_{FC}= 50 °C, I_{FC}= 0.5 A, P_{FC}= $P_{amb} + 10PSI$

B.4.9 Anode Humidifier ON-OFF (EIS 89 to 102)

Here, we present the time response and EIS results (Nyquist and Bode) on anode humidifier interruption OFF and ON, with: $I_{FC} = 1.0[A]$ and $P_{FC} = P_{amb} + 10PSI$ at $T_{FC} = 50$ [°C].

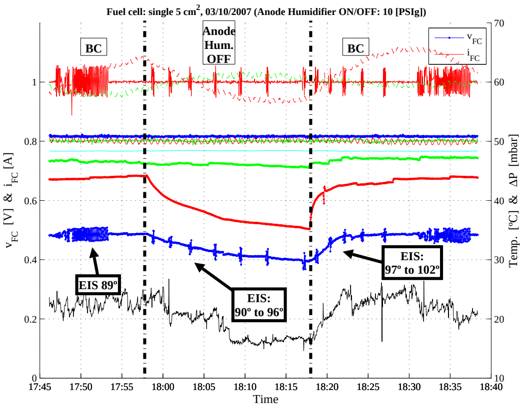

(a) Time evolution

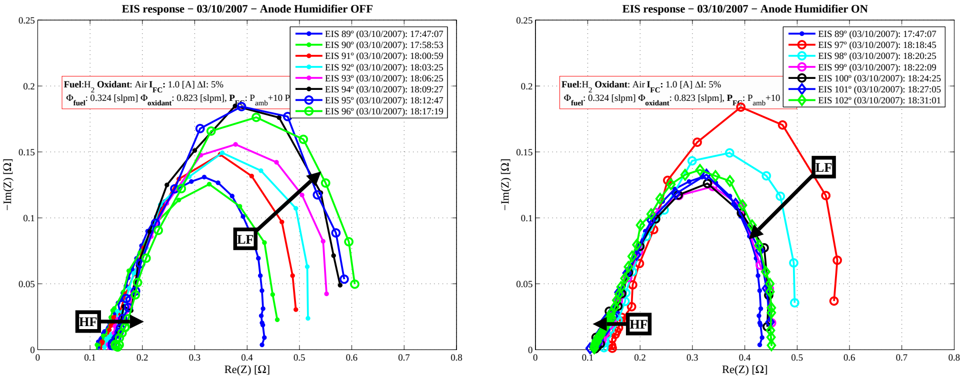

(b) Nyquist (Hum. OFF) (c) Nyquist (Hum. ON)

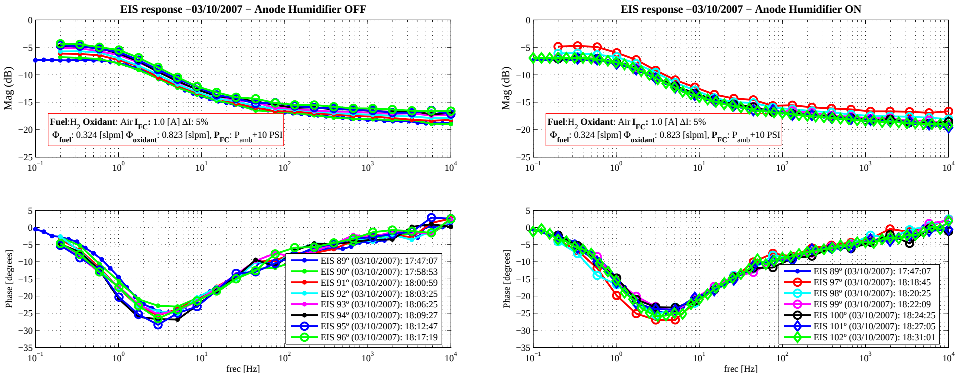

(d) Bode (Hum. OFF) (e) Bode (Hum. ON)

Figure B.34: Anode humidifier OFF: T_{FC}= 50 °C, I_{FC}= 0.5 A, P_{FC}= $P_{amb} + 10PSI$

B.4.10 Day: 04/10/2007

Operating conditions of this day is showed on table B.9:

	$\mathbf{T}_{ca,hum}[^{o}\mathbf{C}]$	$\mathbf{T}_{ca,LH}[^{o}\mathbf{C}]$	$\mathbf{P}_{ca}[\mathbf{bar}_a]$	$\Phi_{cath}[\mathbf{slpm}]$
Cath. (Air)	60.0	67.2	1	0.824
	$\mathbf{T}_{An,hum}[^{o}\mathbf{C}]$	$\mathbf{T}_{An,LH}[^{o}\mathbf{C}]$	$\mathbf{P}_{An}[\mathbf{bar}_a]$	$\Phi_{an}[\mathbf{slpm}]$
Anode ($\mathbf{H_2}$)	59.8	69.7	1	0.324
	$\mathbf{T}_{FC}[^{o}\mathbf{C}]$			
Cell	58.9			
Comments:				
Humidifiers bypass test EIS with 60 [°C] and pressure increment to 10 [PSIg]				

Table B.9: Operating conditions of 04/10/2007

Day graph response

General evolution of this day can be seen on figures: B.35, B.36 and B.37.

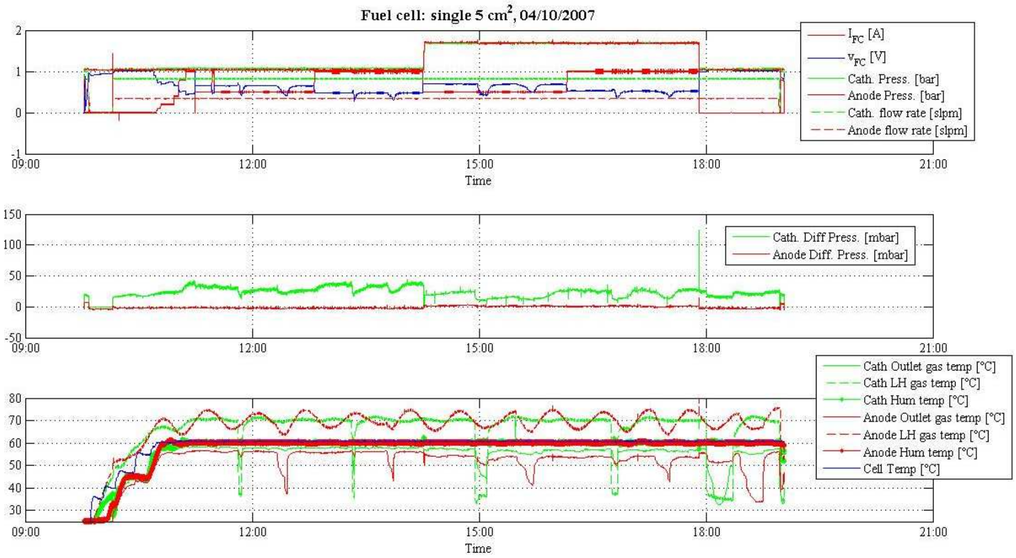

Figure B.35: Day evolution, first graph

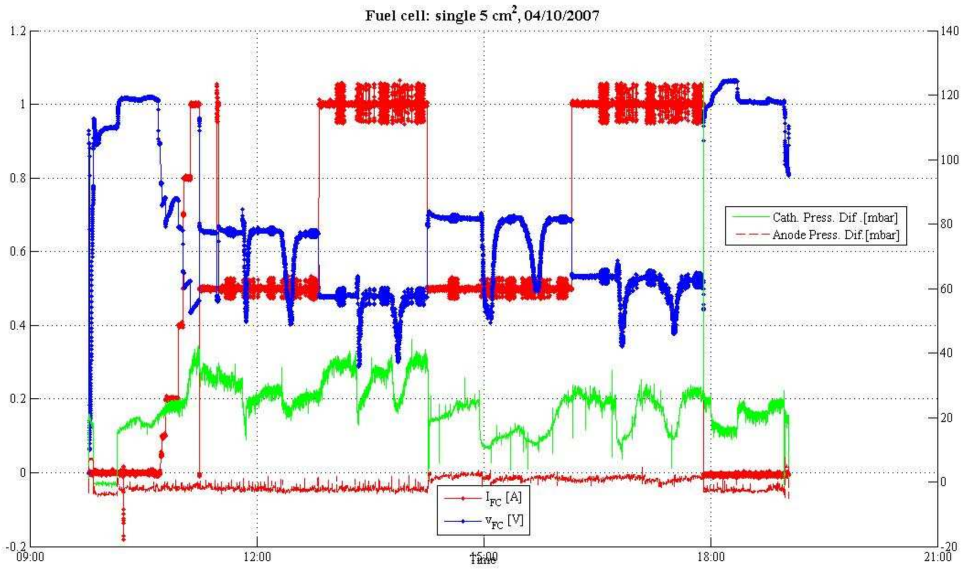

Figure B.36: Day evolution, second graph

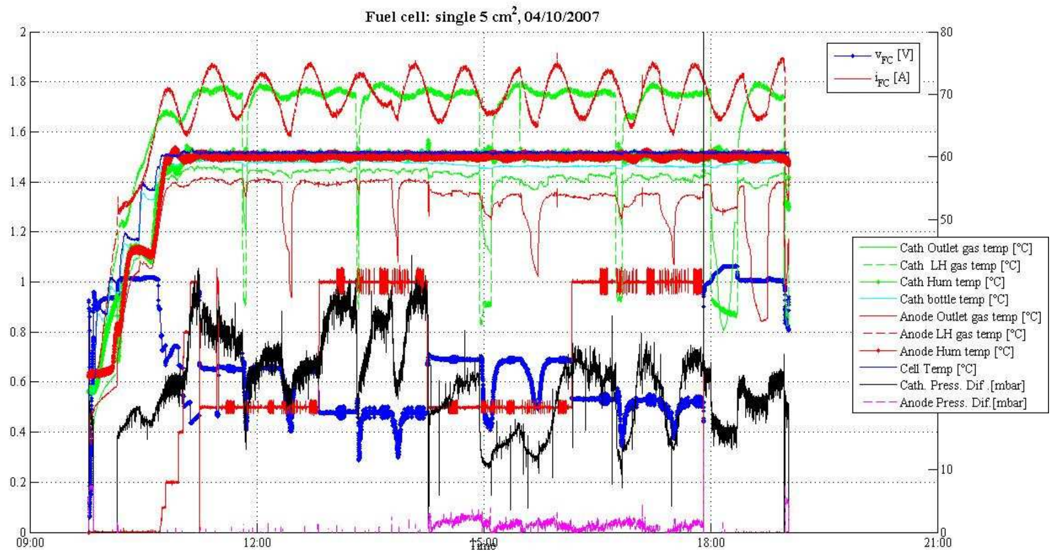

Figure B.37: Day evolution, third graph

Impedance Spectroscopies of day

On table B.10, we give the general view of different spectroscopies

EIS	**Points**	**I_{FC} [A]**	**P_{FC} [Bar]**	**Comments**
1	51	0.5	P_{amb}	Long EIS
2→4	21	0.5	P_{amb}	Cathode humidifier OFF, short EIS
5→9	21	0.5	P_{amb}	Cathode humidifier ON, short EIS
10	51	0.5	P_{amb}	Long EIS
11→16	21	0.5	P_{amb}	Anode humidifier OFF, short EIS
17→22	21	0.5	P_{amb}	Anode humidifier ON, short EIS
23	51	0.5	P_{amb}	Long EIS
24	51	1	P_{amb}	Long EIS
25→26	21	1	P_{amb}	Cathode humidifier OFF, short EIS
27→32	21	1	P_{amb}	Cathode humidifier ON, short EIS
33	51	1	P_{amb}	Long EIS
34→36	21	1	P_{amb}	Anode humidifier OFF, short EIS
37→42	21	1	P_{amb}	Anode humidifier ON, short EIS
43	51	1	P_{amb}	Long EIS
44	51	0.5	$P_{amb} + 10[PSI]$	Long EIS
45→50	21	0.5	$P_{amb} + 10[PSI]$	Cathode humidifier OFF, short EIS
51→56	21	0.5	$P_{amb} + 10[PSI]$	Cathode humidifier ON, short EIS
57	51	0.5	$P_{amb} + 10[PSI]$	Long EIS
58→64	21	0.5	$P_{amb} + 10[PSI]$	Anode humidifier OFF, short EIS
65→70	21	0.5	$P_{amb} + 10[PSI]$	Anode humidifier ON, short EIS
71	51	0.5	$P_{amb} + 10[PSI]$	Long EIS
72	51	1	$P_{amb} + 10[PSI]$	Long EIS
73→77	21	1	$P_{amb} + 10[PSI]$	Cathode humidifier OFF, short EIS
78→83	21	1	$P_{amb} + 10[PSI]$	Cathode humidifier ON, short EIS
84	51	1	$P_{amb} + 10[PSI]$	Long EIS
85→90	21	1	$P_{amb} + 10[PSI]$	Anode humidifier OFF, short EIS
91→96	21	1	$P_{amb} + 10[PSI]$	Anode humidifier ON, short EIS
97	51	1	$P_{amb} + 10[PSI]$	Long EIS

Table B.10: EIS conditions with T_{FC}=50 [^oC],04/10/2007

Like you will see, on these day, we make current variation from 0.5 [A] to 1.0 [A], then we increase the pressure up to 10 [PSIg] and we make the current variation again.

B.4.11 Cathode Humidifier ON-OFF (EIS 1 to 10)

Here, we present the time response and EIS results (Nyquist and Bode) on cathode humidifier interruption OFF and ON, with: $I_{FC} = 0.5[A]$ and $P_{FC} = P_{amb}$ at $T_{FC} = 60$ [°C].

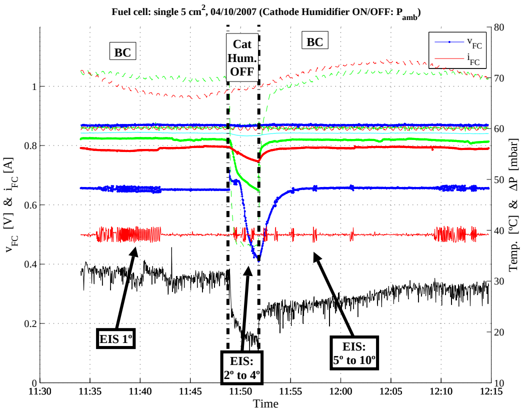

(a) Time evolution

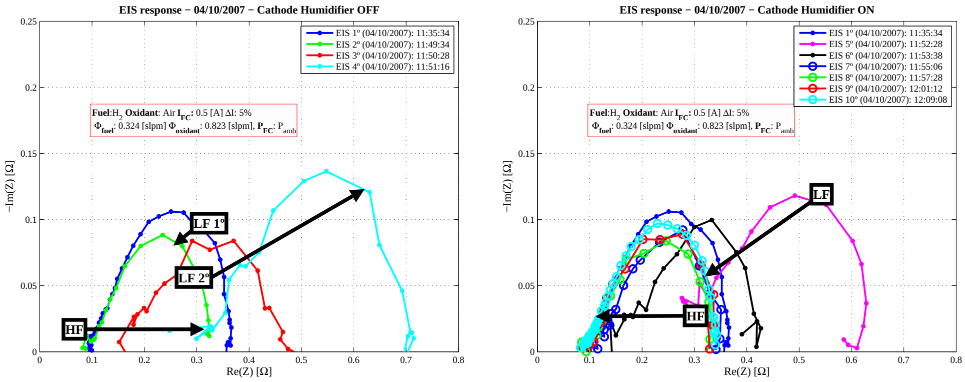

(b) Nyquist (Hum. OFF)

(c) Nyquist (Hum. ON)

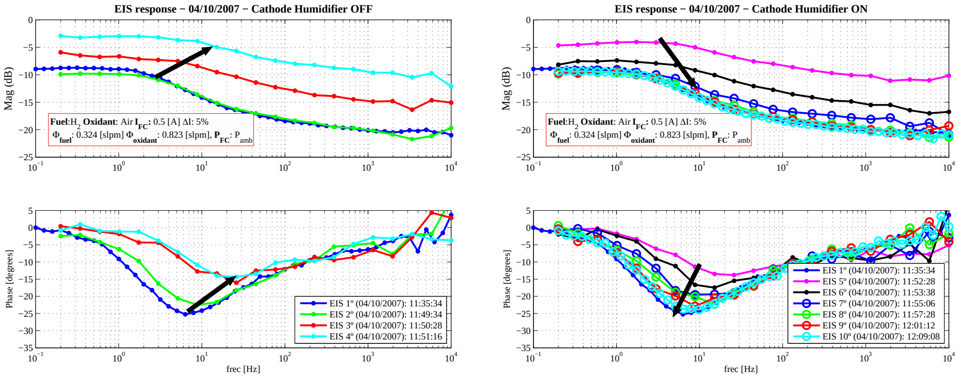

(d) Bode (Hum. OFF)

(e) Bode (Hum. ON)

Figure B.38: Cathode humidifier OFF: T_{FC}= 60 °C, I_{FC}= 0.5 A, P_{FC}= P_{amb}

B.4.12 Anode Humidifier ON-OFF (EIS 10 to 23)

Here, we present the time response and EIS results (Nyquist and Bode) on anode humidifier interruption OFF and ON, with: $I_{FC} = 0.5[A]$ and $P_{FC} = P_{amb}$ at $T_{FC} = 60$ [°C].

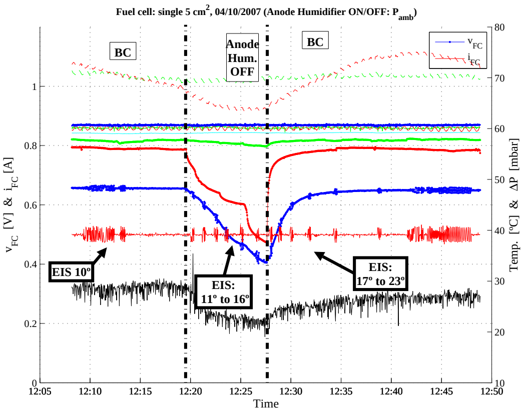

(a) Time evolution

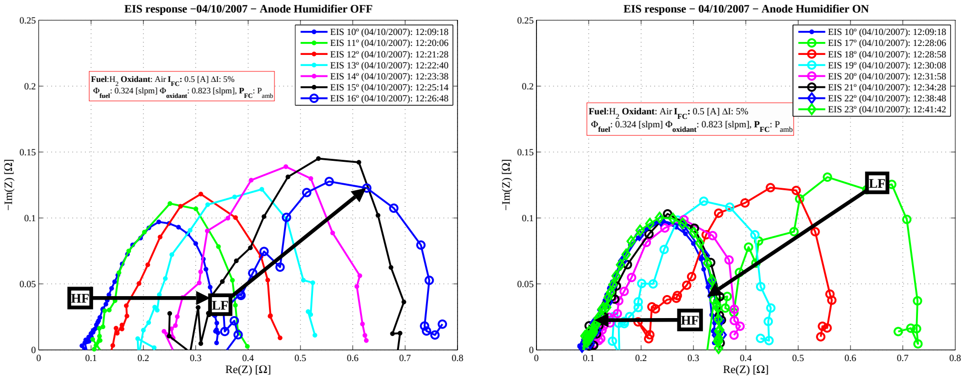

(b) Nyquist (Hum. OFF)

(c) Nyquist (Hum. ON)

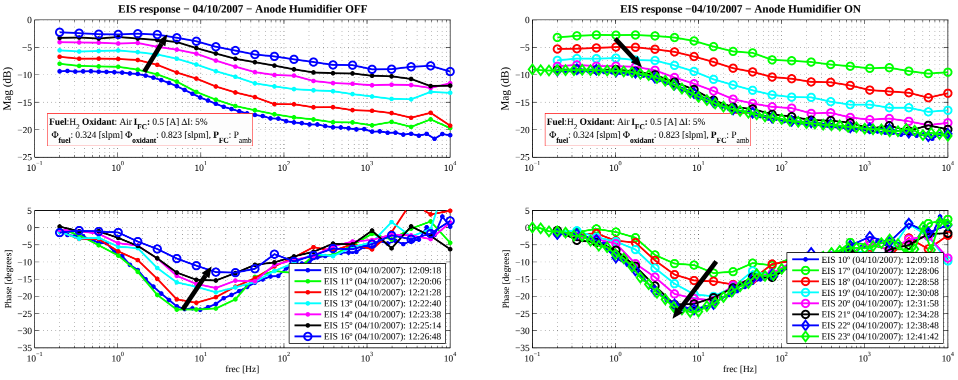

(d) Bode (Hum. OFF)

(e) Bode (Hum. ON)

Figure B.39: Anode humidifier OFF: T_{FC}= 60 °C, I_{FC}= 0.5 A, P_{FC}= P_{amb}

B.4.13 Cathode Humidifier ON-OFF (EIS 24 to 33)

Here, we present the time response and EIS results (Nyquist and Bode) on cathode humidifier interruption OFF and ON, with: $I_{FC} = 1.0[A]$ and $P_{FC} = P_{amb}$ at $T_{FC} = 60$ [°C].

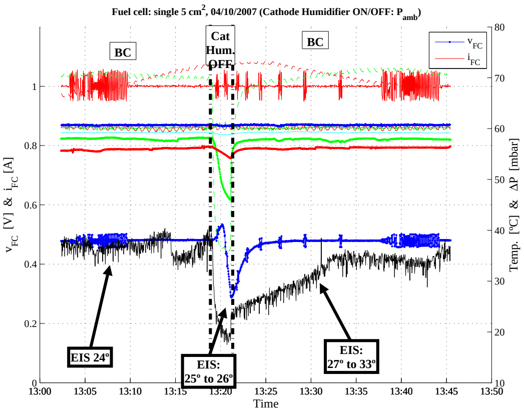

(a) Time evolution

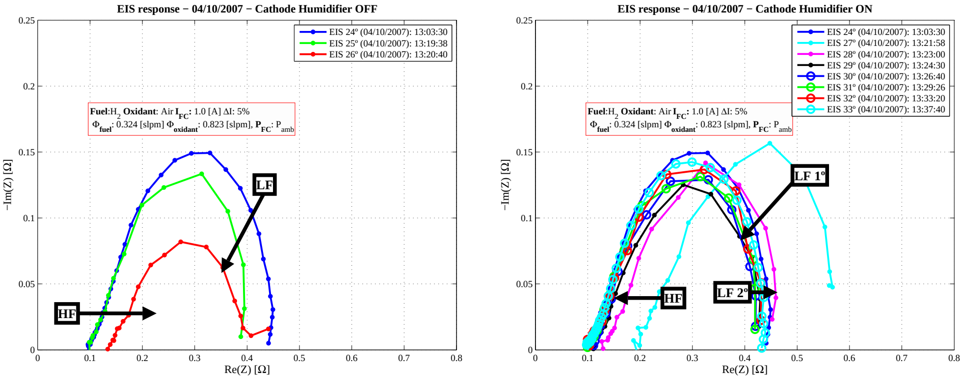

(b) Nyquist (Hum. OFF)

(c) Nyquist (Hum. ON)

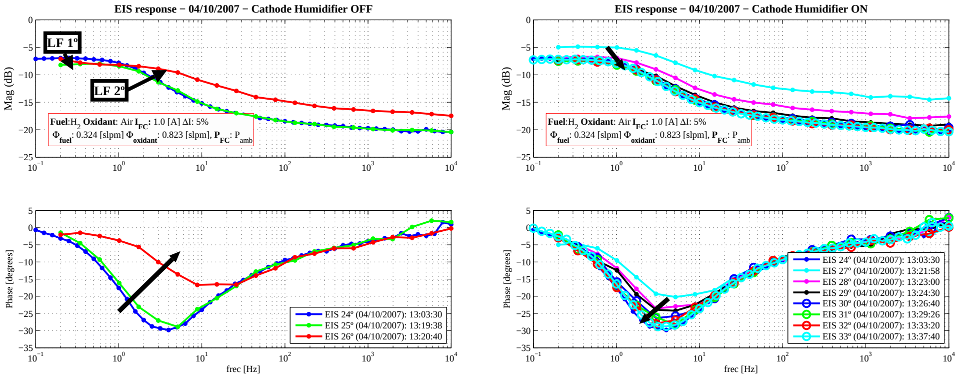

(d) Bode (Hum. OFF)

(e) Bode (Hum. ON)

Figure B.40: Cathode humidifier OFF: T_{FC}= 60 °C, I_{FC}= 1.0 A, P_{FC}= P_{amb}

B.4.14 Anode Humidifier ON-OFF (EIS 33 to 43)

Here, we present the time response and EIS results (Nyquist and Bode) on anode humidifier interruption OFF and ON, with: $I_{FC} = 1.0[A]$ and $P_{FC} = P_{amb}$ at $T_{FC} = 60$ [°C].

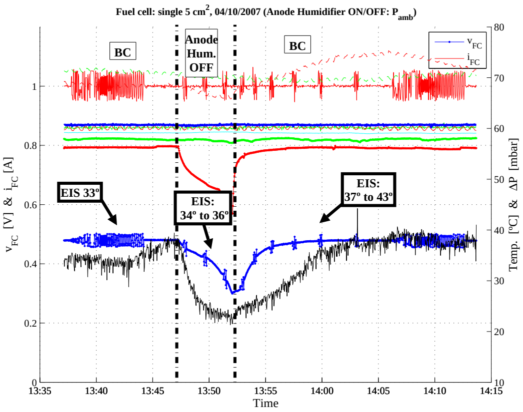

(a) Time evolution

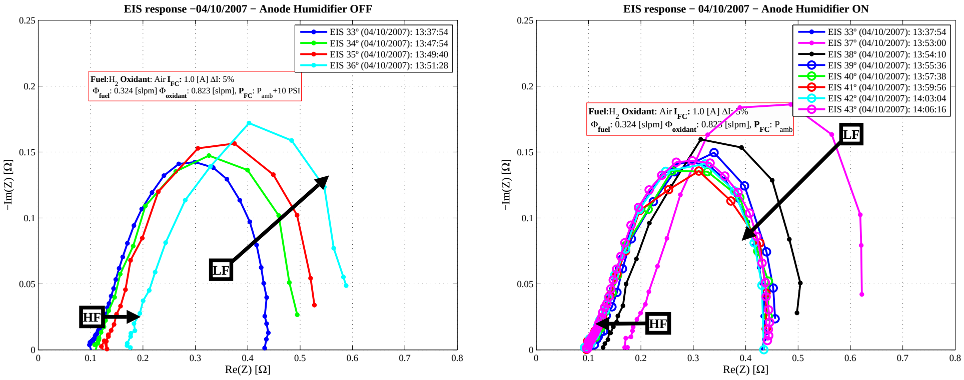

(b) Nyquist (Hum. OFF)

(c) Nyquist (Hum. ON)

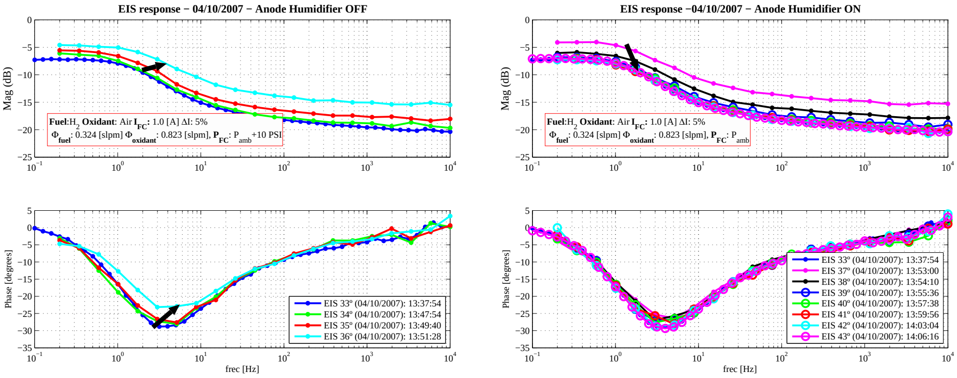

(d) Bode (Hum. OFF)

(e) Bode (Hum. ON)

Figure B.41: Anode humidifier OFF: T_{FC}= 60 °C, I_{FC}= 1.0 A, P_{FC}= P_{amb}

B.4.15 Cathode Humidifier ON-OFF (EIS 44 to 57)

Here, we present the time response and EIS results (Nyquist and Bode) on cathode humidifier interruption OFF and ON, with: $I_{FC} = 0.5[A]$ and $P_{FC} = P_{amb} + 10[PSI]$ at $T_{FC} = 60$ [°C].

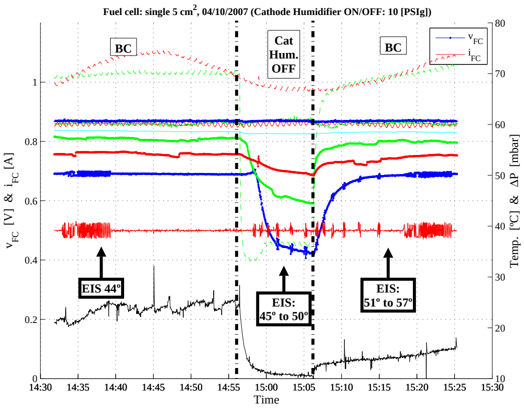

(a) Time evolution

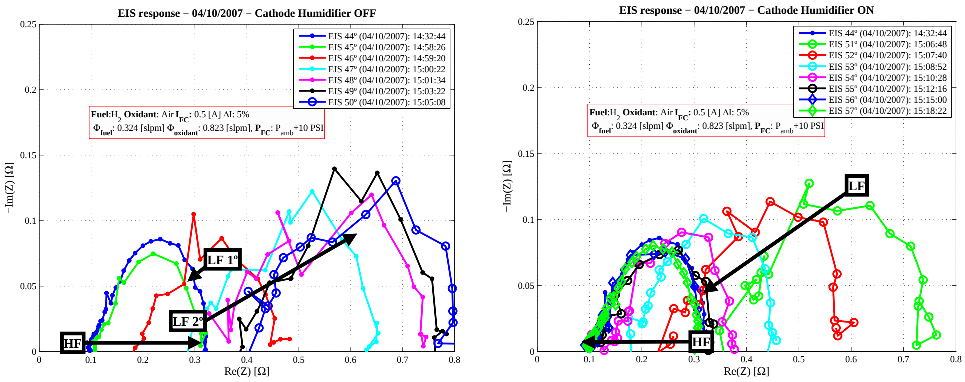

(b) Nyquist (Hum. OFF)
(c) Nyquist (Hum. ON)

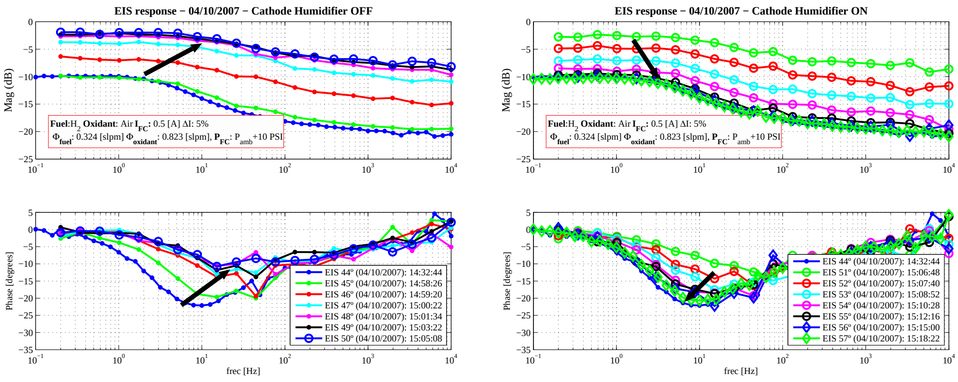

(d) Bode (Hum. OFF)
(e) Bode (Hum. ON)

Figure B.42: Cathode humidifier OFF: T_{FC}= 60 °C, I_{FC}= 0.5 A, P_{FC}= $P_{amb} + 10PSI$

B.4.16 Anode Humidifier ON-OFF (EIS 57 to 71)

Here, we present the time response and EIS results (Nyquist and Bode) on anode humidifier interruption OFF and ON, with: $I_{FC} = 0.5[A]$ and $P_{FC} = P_{amb} + 10PSI$ at $T_{FC} = 60$ [°C].

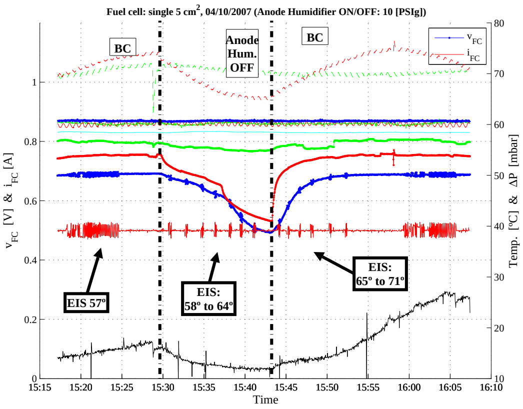

(a) Time evolution

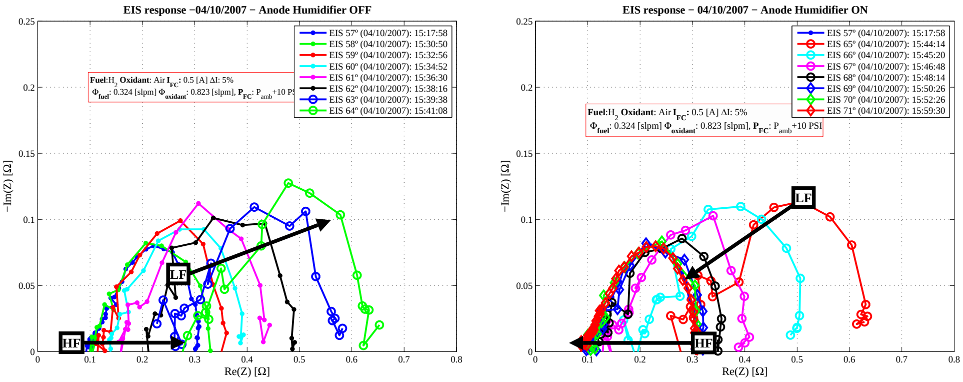

(b) Nyquist (Hum. OFF)

(c) Nyquist (Hum. ON)

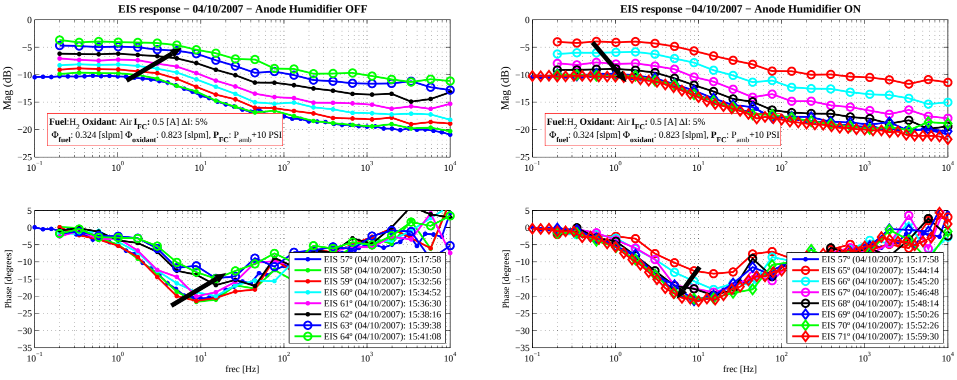

(d) Bode (Hum. OFF)

(e) Bode (Hum. ON)

Figure B.43: Anode humidifier OFF: T_{FC}= 60 °C, I_{FC}= 0.5 A, P_{FC}= $P_{amb} + 10PSI$

B.4.17 Cathode Humidifier ON-OFF (EIS 72 to 84)

Here, we present the time response and EIS results (Nyquist and Bode) on cathode humidifier interruption OFF and ON, with: $I_{FC} = 1.0[A]$ and $P_{FC} = P_{amb} + 10[PSI]$ at $T_{FC} = 60$ [°C].

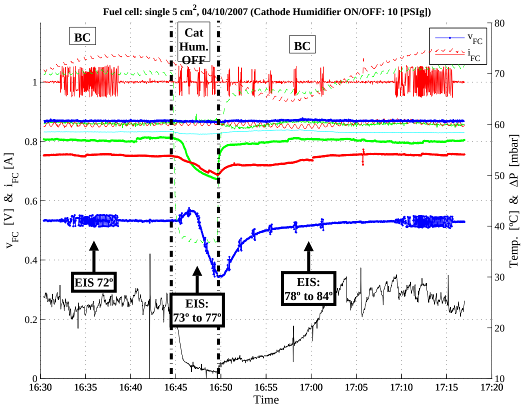

(a) Time evolution

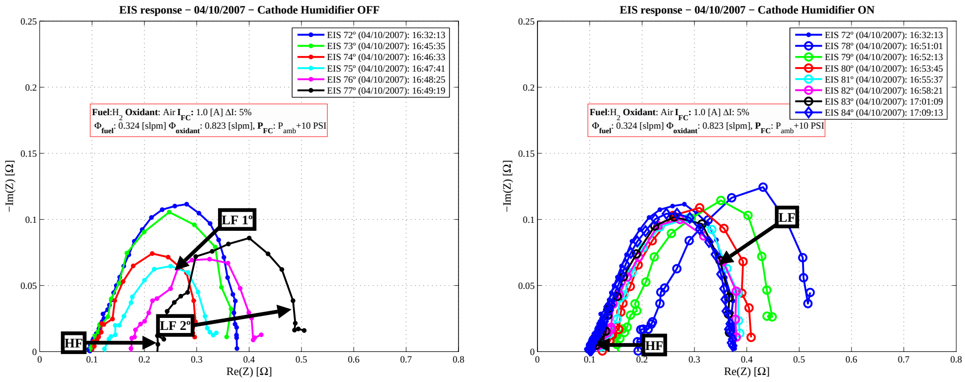

(b) Nyquist (Hum. OFF)

(c) Nyquist (Hum. ON)

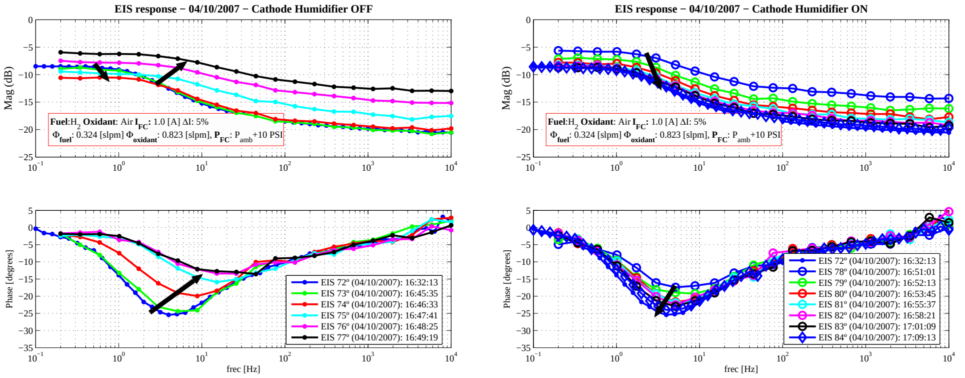

(d) Bode (Hum. OFF)

(e) Bode (Hum. ON)

Figure B.44: Cathode humidifier OFF: T_{FC}= 60 °C, I_{FC}= 1.0 A, P_{FC}= $P_{amb} + 10PSI$

B.4.18 Anode Humidifier ON-OFF (EIS 84 to 97)

Here, we present the time response and EIS results (Nyquist and Bode) on anode humidifier interruption OFF and ON, with: $I_{FC} = 1.0[A]$ and $P_{FC} = P_{amb} + 10PSI$ at $T_{FC} = 60$ [°C].

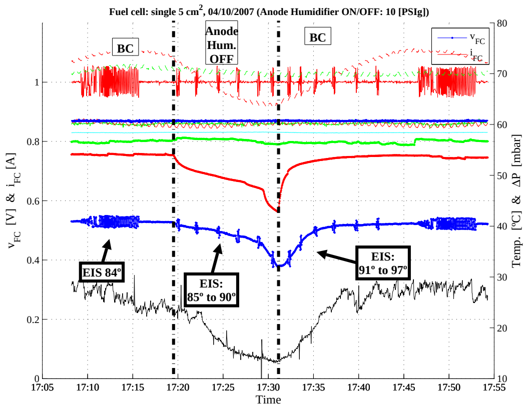

(a) Time evolution

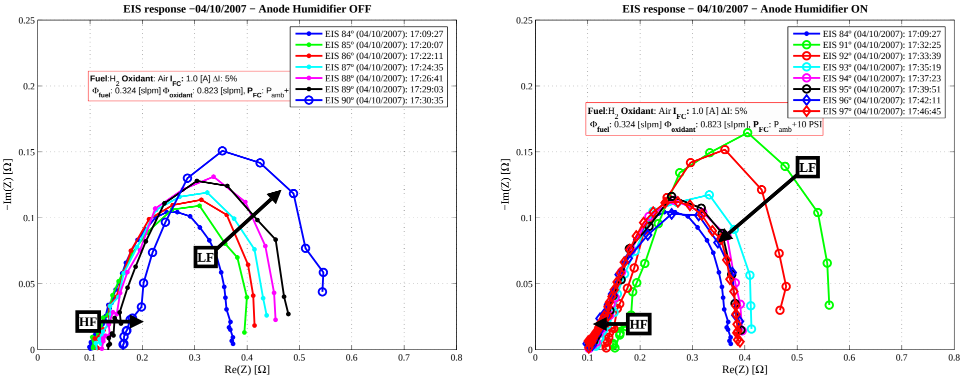

(b) Nyquist (Hum. OFF) (c) Nyquist (Hum. ON)

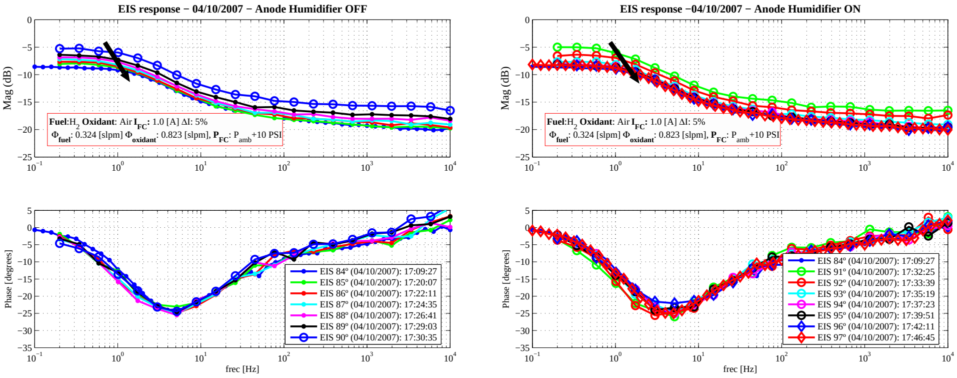

(d) Bode (Hum. OFF) (e) Bode (Hum. ON)

Figure B.45: Anode humidifier OFF: T_{FC}= 60 °C, I_{FC}= 1.0 A, P_{FC}= $P_{amb} + 10PSI$

Appendix C

Humidification interruption: relevant characteristics

In this appendix, the tables and individual graphs of the obtained relevant characteristics for the humidifier interruption cases presented in chapter 4: **Design of experimental techniques for PEMFC characterisation**, are presented. The different experimental test resumed for the humidifiers (cathode vs. anode, current, pressure and temperature) interruptions are done. All those experimental tests are done with Air and H_2 as reactants and the main operating conditions are summarised on table C.1.

Day	T_{FC} **[°C]**	**EIS**	**Conditions**
01/10/2007	40	40	Testing humidifier interrupt at I_{FC}=1[A]
02/10/2007	40	134	I_{FC}=0.5[A] and 1[A], $P_{FC}=P_{amb}$ and 10 [PSIg]
03/10/2007	50	102	I_{FC}=0.5[A] and 1[A], $P_{FC}=P_{amb}$ and 10 [PSIg]
04/10/2007	60	97	I_{FC}=0.5[A] and 1[A], $P_{FC}=P_{amb}$ and 10 [PSIg]

Table C.1: Operating conditions of the humidifier interruptions

Remembering that all the time and frequency response are resumed in appendix 3: “Humidifier Interruption Tests”, in this section the relevant characteristics are resumed using tables and graphical evolutions. In this section, the responses of the humidifiers interruption are represented with the following comparisons:

- Anode vs. Cathode response.
- Current variation (anode and cathode, I_{FC}=0.5 A and 1.0 A).
- Pressure variation (anode and cathode, $P_{FC}=P_{amb}$ and P_{amb}+10 PSI).
- Temperature variation (anode and cathode, T_{FC}=40 °C, 50 °C and 60 °C).

C.1 Anode vs. Cathode humidifier interruption response

In this subsection, relevant characteristics of the anode and the cathode responses for the same operating condition of temperature, pressure and current are presented.

The response of the anode humidifier interruption at the operating conditions: current is $I_{FC} = 1$ [A], fuel cell pressure is $P_{FC} = P_{amb}$, fuel cell temperature is $T_{FC} = 40$ [°C] and 100 [%] of relative humidity of the inlet gases (H_2/Air), is presented in the figure C.1 and in the table C.2.

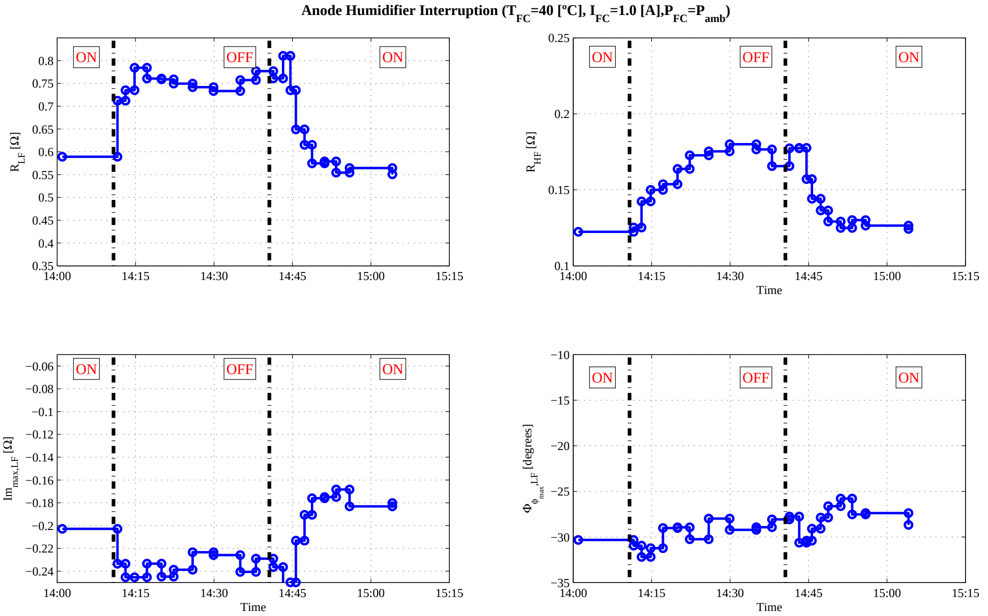

Figure C.1: Relevant characteristics of Anode humidifier ON-OFF

The response of the cathode humidifier interruption at the operating conditions: current is $I_{FC} = 1$ [A], fuel cell pressure is $P_{FC} = P_{amb}$, fuel cell temperature is $T_{FC} = 40$ [°C] and 100 [%] of relative humidity of the inlet gases (H_2/Air), is presented in the figure C.2 and in the table C.3.

Table C.2: Relevant characteristics, Anode humidifier interruption

EIS	**Hour**	V_{FC}[V]	R_{LF}[Ω]	$f_{Imax,LF}$[Hz]	$Im_{Imax,LF}$ [Ω]	$\phi_{\phi max,LF}$ [°]	$f_{\phi_{max,LF}}$[Hz]	R_{HF}[Ω]
40	13:54	0.388	0.589	1.25	-0.20	-30.32	2.51	0.122
41	14:10	0.353	0.712	1.01	-0.23	-30.94	2.99	0.125
42	14:12	0.340	0.735	1.01	-0.24	-32.17	2.99	0.142
43	14:14	0.321	0.784	1.01	-0.24	-31.22	1.74	0.150
44	14:16	0.325	0.761	1.01	-0.23	-29.01	2.99	0.154
45	14:19	0.306	0.759	1.74	-0.24	-28.93	1.74	0.164
46	14:21	0.301	0.749	1.74	-0.24	-30.25	2.99	0.173
47	14:25	0.301	0.742	1.74	-0.22	-27.97	2.99	0.175
48	14:28	0.298	0.733	1.74	-0.22	-29.22	2.99	0.180
49	14:33	0.297	0.757	1.74	-0.24	-28.93	2.99	0.177
50	14:37	0.292	0.777	1.74	-0.23	-28.07	5.13	0.166
51	14:40	0.293	0.761	1.74	-0.24	-27.75	5.13	0.177
52	14:42	0.290	0.810	1.74	-0.26	-30.62	2.99	0.178
53	14:43	0.328	0.735	1.74	-0.25	-30.40	2.99	0.157
54	14:45	0.358	0.649	1.01	-0.21	-29.08	2.99	0.144
55	14:46	0.381	0.615	1.74	-0.19	-27.86	2.99	0.136
56	14:48	0.392	0.575	1.74	-0.18	-26.61	5.13	0.129
57	14:49	0.399	0.579	1.74	-0.17	-25.78	2.99	0.125
58	14:52	0.401	0.554	1.74	-0.17	-27.52	5.13	0.130
59	14:55	0.401	0.564	1.74	-0.18	-27.37	2.99	0.126
60	14:57	0.401	0.551	1.58	-0.18	-28.67	3.16	0.124

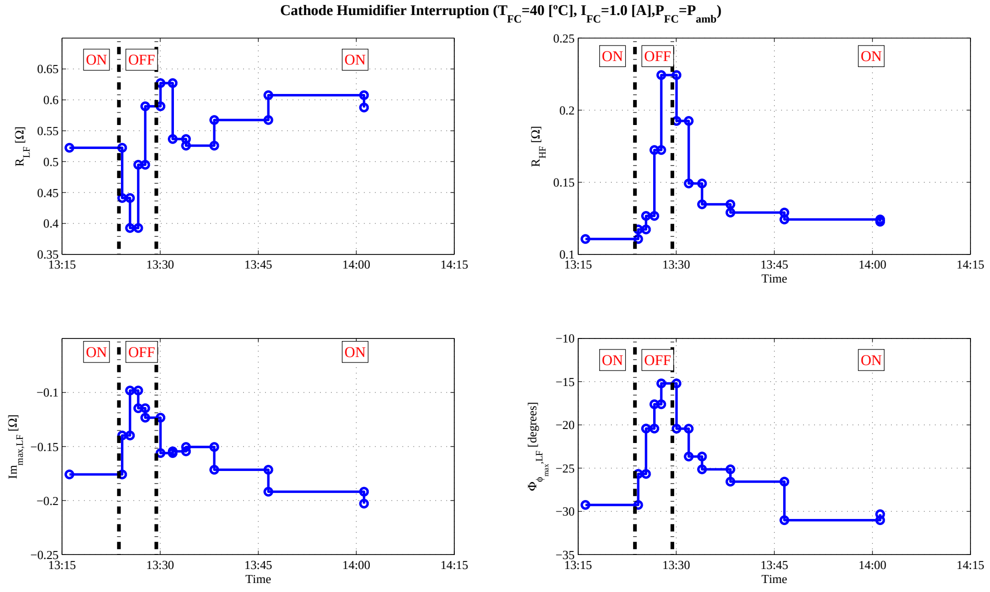
Cathode Humidifier Interruption (T_{FC}=40 [°C], I_{FC}=1.0 [A],P_{FC}=P_{amb})

Figure C.2: Relevant characteristics of Cathode humidifier ON-OFF

Table C.3: Relevant characteristics, Cathode humidifier interruption

EIS	**Hour**	V_{FC}[V]	R_{LF}[Ω]	$f_{Imax,LF}$[Hz]	$Im_{Imax,LF}$ [Ω]	$\phi_{\phi max,LF}$ [^{o}]	$f_{phi_{max,LF}}$[Hz]	R_{HF}[Ω]
30	13:09	0.413	0.522	1.58	-0.18	-29.26	3.16	0.111
31	13:23	0.456	0.441	1.74	-0.14	-25.67	2.99	0.117
32	13:24	0.447	0.393	5.14	-0.10	-20.42	5.14	0.127
33	13:26	0.339	0.495	5.14	-0.11	-17.61	5.14	0.172
34	13:27	0.257	0.590	5.14	-0.12	-15.21	8.82	0.224
35	13:29	0.310	0.627	1.74	-0.16	-20.44	5.14	0.193
36	13:31	0.377	0.537	2.99	-0.15	-23.66	2.99	0.149
37	13:33	0.392	0.526	1.74	-0.15	-25.13	5.14	0.135
38	13:37	0.387	0.567	1.74	-0.17	-26.56	5.14	0.129
39	13:45	0.384	0.608	1.74	-0.19	-31.02	2.99	0.124
40	13:54	0.388	0.589	1.26	-0.20	-30.32	2.51	0.122

C.1.1 Current variation: cathode humidifier interruption

In this subsection, relevant characteristics of the cathode humidifier interruption responses for the nominal current variations ($I_{FC} = 0.5[A]$ and $I_{FC} = 1.0[A]$).

The response of the cathode humidifier interruption at the operating conditions: current is $I_{FC} = 0.5$ [A], fuel cell pressure is $P_{FC} = P_{amb}$, fuel cell temperature is $T_{FC} = 50$ [°C] and 100 [%] of relative humidity of the inlet gases (H_2/Air), is presented in the figure C.3 and in the table C.4.

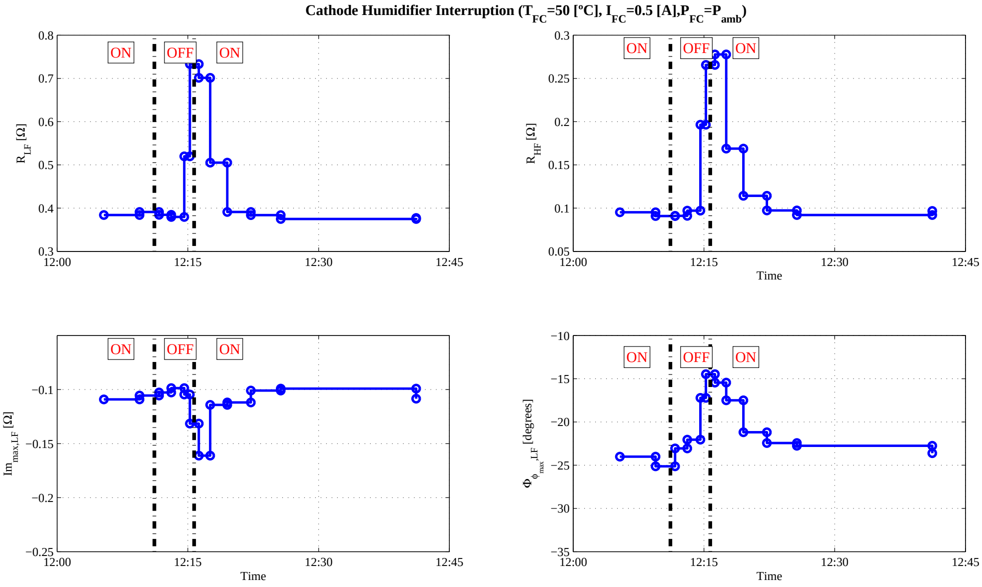

Figure C.3: Relevant characteristics, cathode humidifier ON-OFF, I_{FC}=0.5 [A]

Table C.4: Relevant characteristics, cathode humidifier, I_{FC}=0.5 [A]

EIS	**Hour**	V_{FC}[V]	R_{LF}[Ω]	$f_{Imax,LF}$[Hz]	$Im_{Imax,LF}$[Ω]	$\phi_{\phi max,LF}$ [°]	$f_{\phi_{max},LF}$[Hz]	R_{HF}[Ω]
1	11:52	0.638	0.38	3.16	-0.11	-24.01	7.94	0.095
2	12:08	0.636	0.39	2.99	-0.11	-25.13	8.82	0.091
3	12:11	0.646	0.38	5.14	-0.10	-23.06	5.14	0.091
4	12:12	0.650	0.38	5.14	-0.10	-22.05	8.82	0.097
5	12:13	0.423	0.52	8.82	-0.10	-17.21	26.04	0.196
6	12:14	0.417	0.73	15.16	-0.13	-14.48	26.04	0.266
7	12:15	0.524	0.70	8.82	-0.16	-15.46	8.82	0.278
8	12:16	0.590	0.51	8.82	-0.11	-17.50	8.82	0.169
9	12:18	0.624	0.39	5.14	-0.11	-21.19	5.14	0.114
10	12:21	0.634	0.38	5.14	-0.10	-22.43	8.82	0.097
11	12:24	0.637	0.37	5.14	-0.10	-22.75	8.82	0.092
12	12:34	0.636	0.38	3.98	-0.11	-23.62	7.94	0.097

The response of the cathode humidifier interruption at the current ($I_{FC} = 1.0$ [A]), is presented in the figure C.4 and in the table C.5.

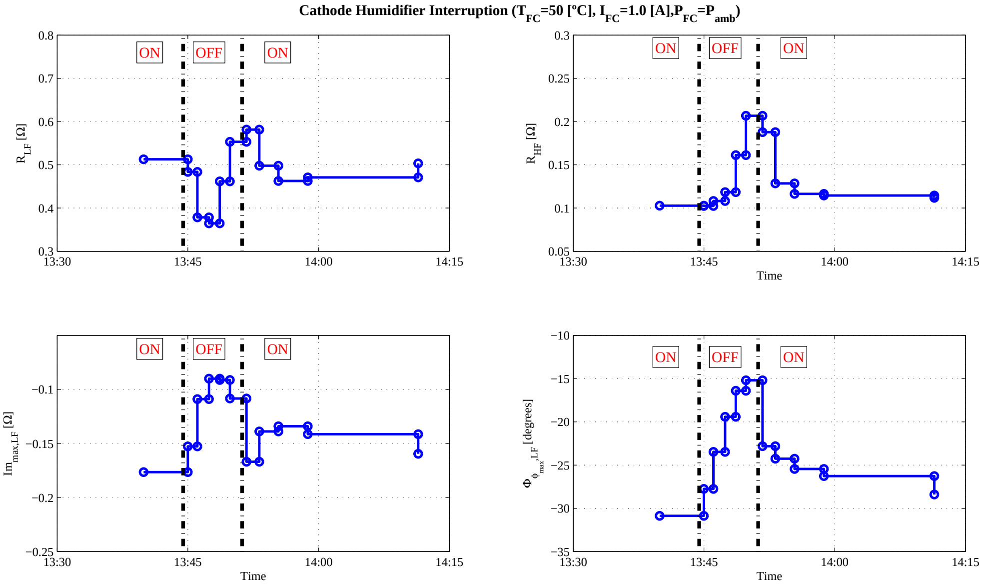

Figure C.4: Relevant characteristics, cathode humidifier, I_{FC}=1.0[A]

Table C.5: Relevant characteristics, cathode humidifier, I_{FC}=1.0 [A]

EIS	**Hour**	V_{FC}[V]	$R_{LF}[\Omega]$	$f_{Imax,LF}$[Hz]	$Im_{Imax,LF}[\Omega]$	$\phi_{\phi max,LF}[^o]$	$f_{\phi_{max},LF}$[Hz]	$R_{HF}[\Omega]$
25	13:32	0.441	0.51	1.58	-0.18	-30.86	3.16	0.103
26	13:44	0.480	0.48	1.74	-0.15	-27.75	2.99	0.102
27	13:45	0.497	0.38	2.99	-0.11	-23.47	5.14	0.108
28	13:46	0.460	0.36	5.14	-0.09	-19.42	8.82	0.118
29	13:48	0.358	0.46	5.14	-0.09	-16.40	15.16	0.161
30	13:49	0.284	0.55	5.14	-0.11	-15.19	15.16	0.207
31	13:51	0.366	0.58	2.99	-0.17	-22.81	5.14	0.188
32	13:52	0.421	0.50	2.99	-0.14	-24.26	5.14	0.128
33	13:54	0.439	0.46	1.74	-0.13	-25.45	5.14	0.116
34	13:58	0.440	0.47	1.74	-0.14	-26.27	2.99	0.114
35	14:04	0.439	0.50	2.00	-0.16	-28.39	3.98	0.112

C.1.2 Current variation: Anode humidifier interruption

In this subsection, relevant characteristics of the anode humidifier interruption responses for the nominal current variations ($I_{FC} = 0.5[A]$ and $I_{FC} = 1.0[A]$).

The response of the anode humidifier interruption at the operating conditions: current is $I_{FC} = 0.5$ [A], fuel cell pressure is $P_{FC} = P_{amb}$, fuel cell temperature is $T_{FC} = 60$ [°C] and 100 [%] of relative humidity of the inlet gases (H_2/Air), is presented in the figure C.5 and in the table C.6

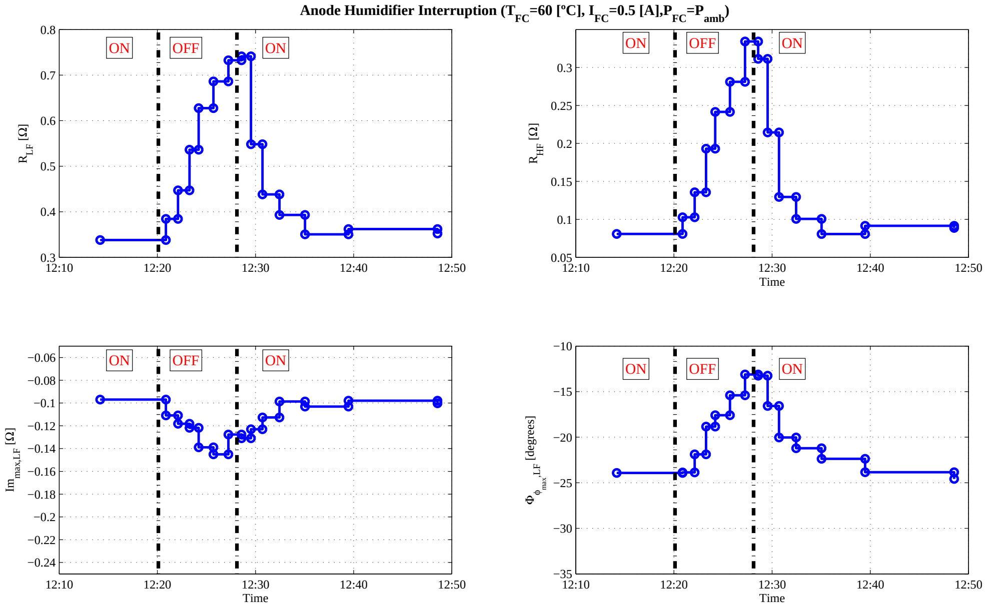

Figure C.5: Relevant characteristics, anode humidifier ON-OFF, I_{FC}=0.5 [A]

Table C.6: Relevant characteristics, anode humidifier interruption, I_{FC}=0.5 [A]

EIS	**Hour**	V_{FC}[V]	R_{LF}[Ω]	$f_{Imax,LF}$[Hz]	$Im_{Imax,LF}$[Ω]	$\phi_{\phi max,LF}[^o]$	$f_{\phi_{max,LF}}$[Hz]	R_{HF}[Ω]
10	12:09	0.66	0.338	5.14	-0.10	-23.92	9.83	0.081
11	12:20	0.62	0.384	5.14	-0.11	-23.86	5.14	0.103
12	12:21	0.58	0.447	5.14	-0.12	-21.88	8.82	0.136
13	12:22	0.52	0.536	5.14	-0.12	-18.83	15.16	0.193
14	12:23	0.48	0.627	8.82	-0.14	-17.59	15.16	0.242
15	12:25	0.45	0.686	8.82	-0.15	-15.40	15.16	0.281
16	12:26	0.41	0.733	15.16	-0.13	-13.11	26.04	0.334
17	12:28	0.50	0.741	15.16	-0.13	-13.25	15.16	0.311
18	12:28	0.57	0.548	8.82	-0.12	-16.57	26.04	0.215
19	12:30	0.61	0.438	8.82	-0.11	-20.03	15.16	0.130
20	12:31	0.63	0.393	5.14	-0.10	-21.21	15.16	0.101
21	12:34	0.64	0.350	5.14	-0.10	-22.37	5.14	0.081

The response of the anode humidifier interruption at the current ($I_{FC} = 1.0$ [A]), is presented in the figure C.6 and in the table C.7.

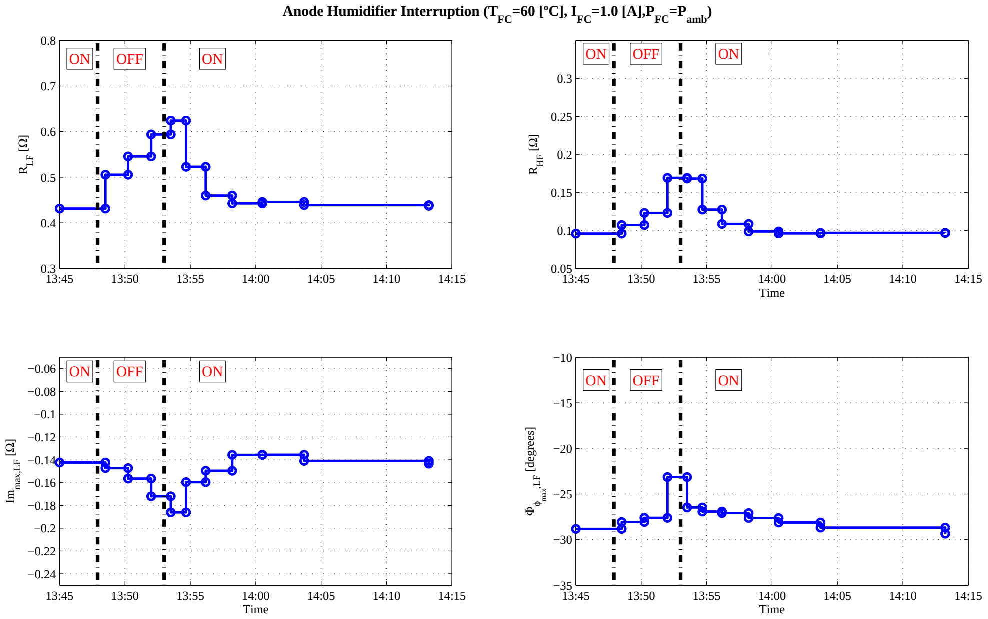

Figure C.6: Relevant characteristics, anode humidifier, I_{FC}=1.0[A]

Table C.7: Relevant characteristics, anode humidifier, I_{FC}=1.0 [A]

EIS	**Hour**	V_{FC}[V]	R_{LF}[Ω]	$f_{Imax,LF}$[Hz]	$Im_{Imax,LF}$[Ω]	$\phi_{\phi max,LF}[^o]$	$f_{\phi_{max,LF}}$[Hz]	R_{HF}[Ω]
33	13:37	0.48	0.431	2.00	-0.14	-28.82	3.16	0.096
34	13:47	0.44	0.506	1.74	-0.15	-28.08	5.14	0.107
35	13:49	0.41	0.546	1.74	-0.16	-27.61	5.14	0.123
36	13:51	0.30	0.594	2.99	-0.17	-23.14	2.99	0.169
37	13:53	0.38	0.624	1.74	-0.19	-26.47	5.14	0.168
38	13:54	0.44	0.523	2.99	-0.16	-26.92	2.99	0.127
39	13:55	0.46	0.460	1.74	-0.15	-27.09	2.99	0.109
40	13:57	0.47	0.443	2.99	-0.14	-27.63	2.99	0.099
41	13:59	0.48	0.446	1.74	-0.14	-28.13	5.14	0.096
42	14:03	0.48	0.439	1.74	-0.14	-28.69	2.99	0.097
43	14:06	0.48	0.437	2.00	-0.14	-29.35	3.98	0.097

C.1.3 Pressure variation: cathode humidifier interruption

In this subsection, the relevant characteristics of the cathode humidifier interruption at different nominal operating pressures ($P_{FC}{=}P_{amb}$ and $P_{FC}{=}P_{amb} + 10[PSIg] \approx 1.68$ [Bar]) are compared.

The response of the cathode humidifier interruption at the operating conditions: current is $I_{FC} = 1.0$ [A], fuel cell pressure is $P_{FC} = P_{amb} + 10[PSIg] \approx 1.68$ [bar], fuel cell temperature is $T_{FC} = 40$ [°C] and 100 [%] of relative humidity of the inlet gases (H_2/Air), is presented in the figure C.7 and in the table C.8.

Remembering that relevant characteristics of the selected responses, for $P_{FC}{=}P_{amb}$, the results are already presented in the figure C.2 and in the table C.3.

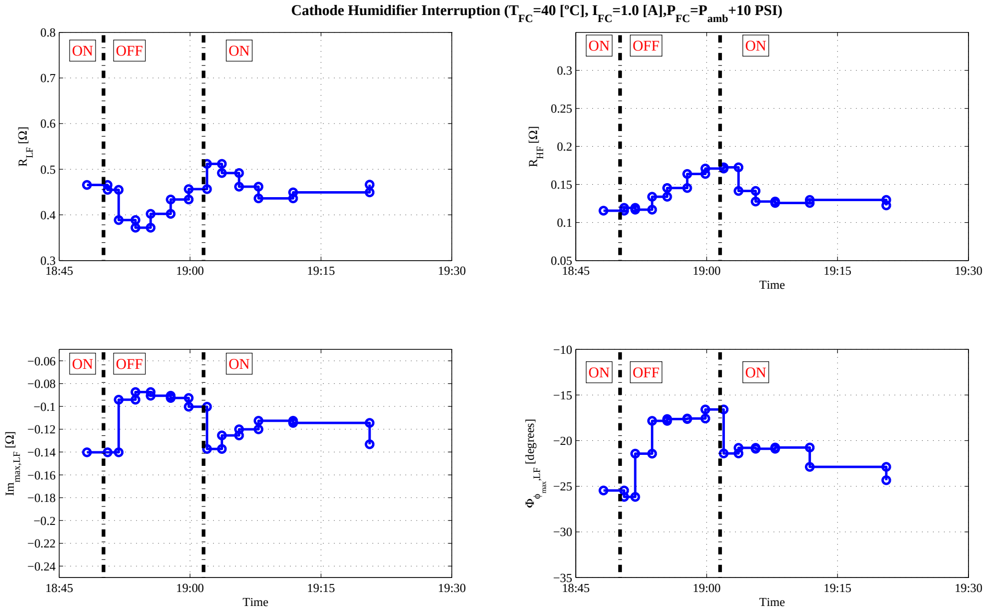

Figure C.7: Relevant characteristics, cathode humidifier, $P_{FC}{=}P_{amb}{+}10$ [PSI]

Table C.8: Relevant characteristics, cathode humidifier, $P_{FC}{=}P_amb+$ 10 [PSI]

EIS	**Hour**	V_{FC}[V]	$R_{LF}[\Omega]$	$f_{Imax,LF}$[Hz]	$Im_{Imax,LF}[\Omega]$	$\phi_{\phi max,LF}[^o]$	$f_{\phi_{max,LF}}$[Hz]	$R_{HF}[\Omega]$
113	18:41	0.45	0.466	2.00	-0.14	-25.46	3.98	0.116
114	18:50	0.46	0.455	1.74	-0.14	-26.17	2.99	0.119
115	18:51	0.49	0.389	5.14	-0.09	-21.42	5.14	0.117
116	18:53	0.48	0.372	2.99	-0.09	-17.83	5.14	0.134
117	18:54	0.45	0.402	5.14	-0.09	-17.63	8.82	0.145
118	18:57	0.42	0.434	5.14	-0.09	-17.58	8.82	0.164
119	18:59	0.40	0.457	5.14	-0.10	-16.58	8.82	0.171
120	19:01	0.38	0.512	2.99	-0.14	-21.40	5.14	0.172
121	19:03	0.42	0.492	2.99	-0.13	-20.79	2.99	0.141
122	19:05	0.44	0.462	1.74	-0.12	-20.89	5.14	0.127
123	19:07	0.45	0.436	2.99	-0.11	-20.75	2.99	0.126
124	19:11	0.45	0.449	1.74	-0.11	-22.88	5.14	0.130
125	19:13	0.45	0.466	2.00	-0.13	-24.34	3.98	0.122

C.1.4 Pressure variation: Anode humidifier interruption

In this subsection, the relevant characteristics of the anode humidifier interruption at different nominal operating pressures (P_{FC}=P_{amb} and P_{FC}=$P_{amb} + 10[PSIg] \approx 1.68$ [Bar]) are compared.

The response of the anode humidifier interruption at the operating conditions: current is $I_{FC} = 1.0$ [A], fuel cell pressure is $P_{FC} = P_{amb} + 10[PSIg] \approx 1.68$ [Bar], fuel cell temperature is $T_{FC} = 40$ [°C] and 100 [%] of relative humidity of the inlet gases (H_2/Air), is presented in the figure C.8 and in the table C.9.

Remembering that relevant characteristics of the selected responses, for P_{FC}=P_{amb}, the results are already presented in the figure C.1 and in the table C.2.

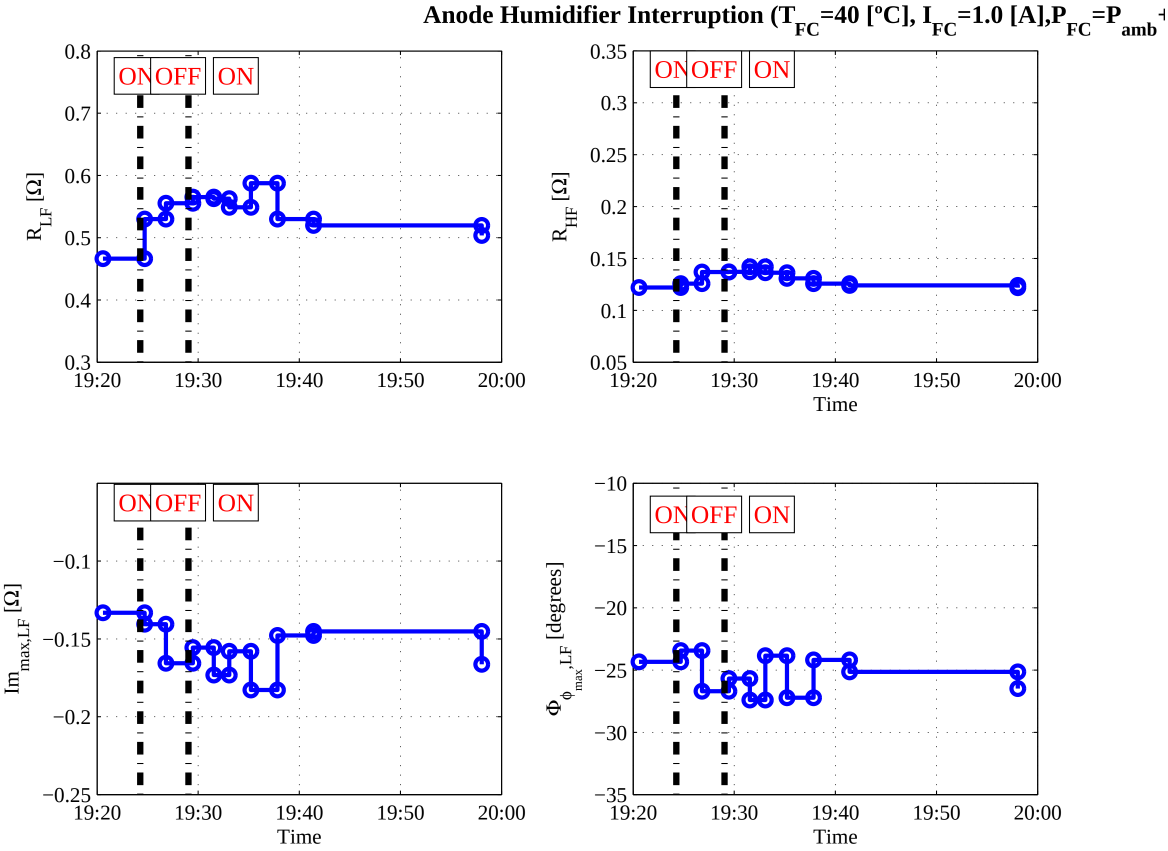

Figure C.8: Relevant characteristics, anode humidifier, P_{FC}=P_{amb}+10 [PSI]

Table C.9: Relevant characteristics, anode humidifier, P_{FC}=P_amb+ 10 [PSI]

EIS	**Hour**	V_{FC}[V]	R_{LF}[Ω]	$f_{Imax,LF}$[Hz]	$Im_{Imax,LF}$[Ω]	$\phi_{\phi max,LF}$[^{o}]	$f_{\phi_{max,LF}}$[Hz]	R_{HF}[Ω]
125	19:13	0.45	0.466	2.00	-0.13	-24.34	3.98	0.122
126	19:24	0.43	0.530	1.74	-0.14	-23.44	2.99	0.126
127	19:26	0.42	0.555	1.74	-0.17	-26.71	2.99	0.137
128	19:29	0.41	0.565	1.74	-0.16	-25.69	2.99	0.137
129	19:31	0.40	0.563	1.74	-0.17	-27.41	2.99	0.142
130	19:32	0.42	0.549	1.74	-0.16	-23.86	2.99	0.136
131	19:34	0.42	0.587	1.74	-0.18	-27.22	2.99	0.131
132	19:37	0.43	0.530	1.74	-0.15	-24.19	2.99	0.126
133	19:40	0.43	0.520	1.74	-0.15	-25.14	2.99	0.124
134	19:45	0.44	0.504	1.26	-0.17	-26.50	3.16	0.122

C.1.5 Temperature variation: cathode humidifier

In this subsection, the relevant characteristics of the cathode humidifier interruption at different nominal operating temperatures (at T_{FC}= 40 [°C], 50 [°C] and 60 [°C]) are compared. The fuel cell pressure is $P_{FC} = P_{amb}$, fuel cell current is $I_{FC} = 1.0$ [A] and 100 [%] of relative humidity of the inlet gases (H_2/Air).

Remembering that relevant characteristics of the selected responses, for T_{FC}=40 °C, the results are presented in figure C.2 and table C.3; for T_{FC}=50 °C are presented in figure C.4 and table C.5 and here only is presented the results of temperature T_{FC}=50 °C, where the figure C.9 and table C.10.

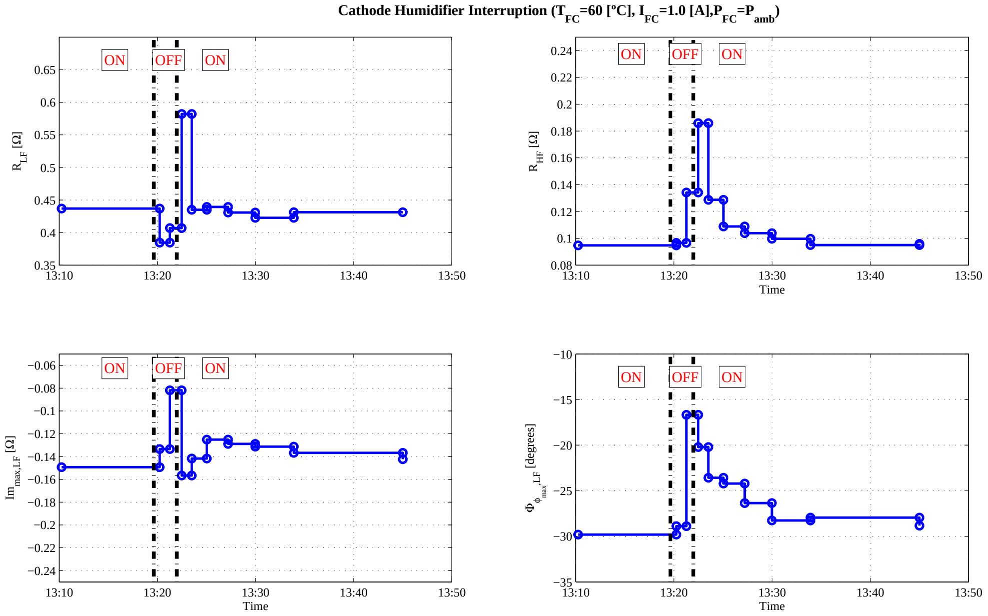

Figure C.9: Relevant characteristics, cathode humidifier, T_{FC}=60 °C

Table C.10: Relevant characteristics, cathode humidifier, T_{FC}=60 °C

EIS	**Hour**	V_{FC}[V]	R_{LF}[Ω]	$f_{Imax,LF}$[Hz]	$Im_{Imax,LF}$[Ω]	$\phi_{\phi max,LF}$ [°]	$f_{\phi_{max},LF}$[Hz]	R_{HF}[Ω]
24	13:03	0.48	0.437	1.58	-0.15	-29.81	3.98	0.095
25	13:19	0.53	0.385	1.74	-0.13	-28.89	5.14	0.097
26	13:20	0.29	0.407	8.82	-0.08	-16.68	8.82	0.134
27	13:21	0.41	0.582	2.99	-0.16	-20.21	5.14	0.186
28	13:23	0.45	0.435	2.99	-0.14	-23.57	2.99	0.129
29	13:24	0.47	0.439	2.99	-0.13	-24.21	5.14	0.109
30	13:26	0.48	0.431	1.74	-0.13	-26.35	2.99	0.104
31	13:29	0.48	0.423	1.74	-0.13	-28.26	5.14	0.100
32	13:33	0.48	0.431	1.74	-0.14	-27.95	2.99	0.095
33	13:37	0.48	0.431	2.00	-0.14	-28.82	3.16	0.096

C.1.6 Temperature variation: anode humidifier interruption

In this subsection, the relevant characteristics of temperature variations of anode humidifier responses, for the same operating conditions are compared, the response of temperatures T_{FC}= 40 [°C], 50 [°C] and 60 [°C] is analysed.

Remembering that relevant characteristics of the selected responses, for T_{FC}=40 °C, the results are presented in figure C.1 and table C.2; for T_{FC}=60 °C are presented in figure C.6 and table C.7 and here only is presented the results of temperature T_{FC}=50 °C, where the figure C.10 and table C.11.

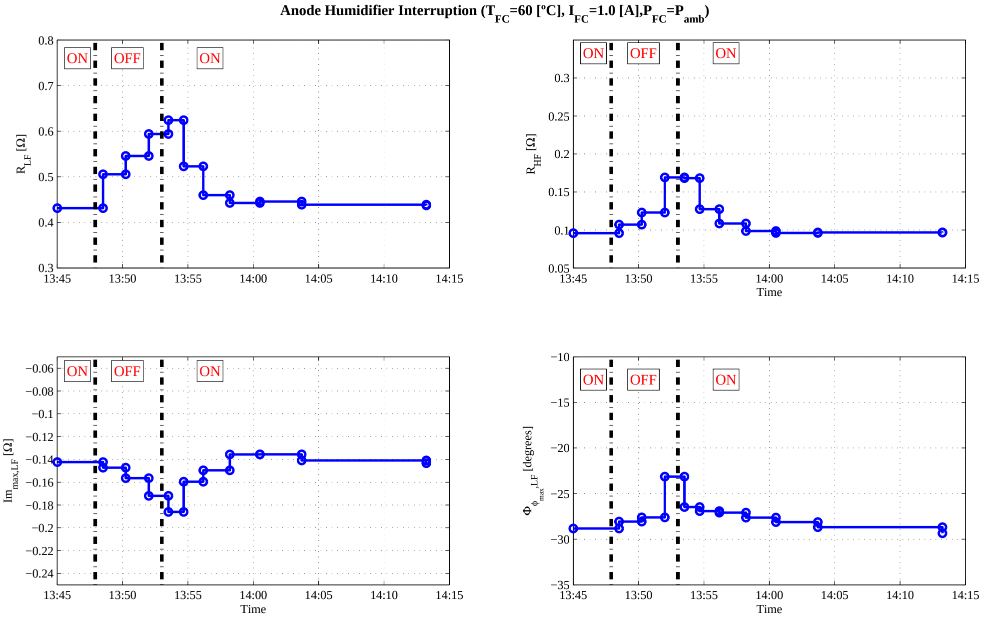

Figure C.10: Relevant characteristics, anode humidifier, T_{FC}=50 °C

Table C.11: Relevant characteristics, anode humidifier, T_{FC}=50 °C

EIS	**Hour**	V_{FC}[V]	R_{LF}[Ω]	$f_{Imax,LF}$[Hz]	$Im_{Imax,LF}$[Ω]	$\phi_{\phi max,LF}$ [^{o}]	$f_{\phi_{max,LF}}$[Hz]	R_{HF}[Ω]
25	13:32	0.44	0.51	1.58	-0.18	-30.86	3.16	0.103
26	13:44	0.48	0.48	1.74	-0.15	-27.75	2.99	0.102
27	13:45	0.50	0.38	2.99	-0.11	-23.47	5.14	0.108
28	13:46	0.46	0.36	5.14	-0.09	-19.42	8.82	0.118
29	13:48	0.36	0.46	5.14	-0.09	-16.40	15.16	0.161
30	13:49	0.28	0.55	5.14	-0.11	-15.19	15.16	0.207
31	13:51	0.37	0.58	2.99	-0.17	-22.81	5.14	0.188
32	13:52	0.42	0.50	2.99	-0.14	-24.26	5.14	0.128
33	13:54	0.44	0.46	1.74	-0.13	-25.45	5.14	0.116
34	13:58	0.44	0.47	1.74	-0.14	-26.27	2.99	0.114
35	14:04	0.44	0.50	2.00	-0.16	-28.39	3.98	0.112
36	14:17	0.43	0.54	1.74	-0.17	-28.69	2.99	0.112

Bibliography

Amphlett, J.C., Baumert, R.M., Mann, R.F., Peppley, B.A., Roberge, P.R., & Harris, T.J. 1992. Performance modelling of the Ballard Mark IV solid polymer electrolyte fuel cell. *Journal of Electrochemical Society*, **142**, 9–15.

Andreaus, B., & Scherer, G.G. 2004. Proton-conducting polymer membranes in fuel cells - humidification aspects. *Solid State Ionics - Proceedings of the Workshop on Hydrogen: Ionic, Atomic and Molecular Motion*, **168**, 311–320.

Andreaus, B., McEvoy, A.J., & Scherer, G.G. 2002. Analysis of performance losses in polymer electrolyte fuel cells at high current densities by impedance spectroscopy. *Electrochimica Acta*, **47**, 2223–2229.

Barbir, F. 2005. *PEM Fuel Cells: Theory and Practice*. Elsevier.

Barbir, F., Görgün, H., & Wang, X. 2005. Relationship between pressure drop and cell resistance as a diagnostic tool for PEM fuel cells. *Journal of Power Sources*, **141**, 96–101.

Barsoukov, E., & Macdonald, J.R. 2005. *Impedance Spectroscopy: Theory, Experiment and Applications*. 2nd. edn. John Wiley & Sons, Inc.

Bautista, M., Bultel, Y., Diard, J.-P., & Walkiewicz, S. 2002. Etude par spectroscopie d'impédance électrochimique du comportement en fonctionnement d'une pemfc. *14ème Forum sur les Impédances Electrochimiques*, 221–230.

Büchi, F.N., & Scherer, G.G. 1996. In Situ membrane resistance measurements of Nafion 117 membranes in polymer electrolyte fuel cell. *Journal of electroanalytical chemistry*, **404**, 37–43.

Büchi, F.N., Marek, A., & Scherer, G.G. 1995. In Situ Membrane Resistance measurements in Polymer Electrolyte Fuel Cell by fast auxiliary current pulses. *Journal of electrochemical society*, **142**, 1895 – 1901.

Bellows, R.J., Lin, M.Y., Arif, M., Thompson, A.K., & Jacobson, D. 1999. Neutron Image techniques for in situ measurement of water transport gradients within nafion in polymer electrolyte fuel cells. *Journal of Electrochemical Society*, **146**, 1099–1103.

Bosco, A.D., & Fronk, M.H. 2000. Fuel cell flooding detection and correction. *US Patent 6*, **103**, 1–7.

Brett, D.J.L., Atkins, S., Brandon, N.P., Vesovic, V., Vasileiadis, N., & Kusernack, A.R. 2004. Investigation of reactant transport within a polymer electrolyte fuel cell using localised CO stripping voltammetry and adsorption transients. *Journal of Power Sources*, **133**, 205–213.

Cañada Gracia, M., & Allue Fantova, M. 2009. *Diseño y construcción de una estación para el estudio de pilas de combustible.* Proyecto final de carrera. Universitat Politècnica de Catalunya.

Callaghan, P.T. 1991. *Principles of nuclear magnetic resonance microscopy.* Oxford University Press.

CFCE, Inc. 2003. Collector plate Image (c). *Clean Fuel Cell Energy.*

Ciureanu, M., & Roberge, R. 2001. Electrochemical impedance study of pem fuel cells, experimental diagnostics and modelling of air cathodes. *Journal of Physical Chemistry B*, **105**, 3531–3539.

Ciureanu, M., Mikhailenko, S. D., & Kaliaguine, S. 2003. PEM fuel cells as membrane reactors: kinetic analysis by impedance spectroscopy. *Catalysis Today - 5th International Conference on Catalysis in Membrane Reactors*, **82**, 195–206.

Cooper, K.R., Ramani, V., Fenton, J.M., & Kunz, H.R. 2005. *Experimental methods and data analyses for polymer electrolyte fuel cell.* Scribner Associates Inc.

Das, P. K., Li, X., & Liu, Z-S. 2010. Analysis of liquid water transport in cathode catalyst layer of PEM fuel cells. *International Journal of Hydrogen Energy*, **35**, 2403–2416.

Diard, J.-P., Glandut, N., Gorrec, B. Le, & Montella, C. 2005. Application des mesures d'impédance aux piles à combustibles. *17ème Forum sur les Impédances Electrochimiques*, 33–50.

Dong, Q., Kull, J., & Mench, M.M. 2005. In situ water distribution measurement in a polymer electrolyte fuel cell. *Journal of Power Sources*, **139**, 106–114.

EG&G Services, Parsons Inc. 2002. Fuel Cell Handbook. *U.S. Department of Energy, Office of Fossil energy and National Energy Technology Laboratory.*

FICT, G. 2003. Collector plate Image (b). *Fraunhofer Institute for Chemical Technology, Germany.*

Fouquet, N., Doulet, C., Noullant, C., Dauphin-Tanguy, G., & Ould-Bouamama, B. 2006. Model based PEM fuel cell state-of-health monitoring via ac impedance measurements. *Journal of Power Sources*, 905–913.

Franco, A.A. 2005. *Physical Mulstiscale Modelling of the Electrochemical Dynamics in a PEFC.* Ph.D. thesis, Université Claude Bernard Lyon 1, France.

Friede, W., Räel, S., & Davat, B. 2004. Mathematical Model and characterization of the transient behaviour of PEM fuel cell. *IEEE Transactions of power electronics*, 1234–1241.

Gebregergis, A., Pillay, P., & Rengaswamy, R. 2010. PEMFC Fault Diagnosis, Modeling and Mitigation. *IEEE Transactions on industry applications*, **46**, 295–303.

Gomez Romero, P. 2002. Pilas de combustible: energía sin humos. *Mundo Científico: Consejo Nacional para Investigaciones Científicas y Tecnologías (CONICIT)*, 66–71.

Görgün, H., Arcak, M., & Barbir, F. 2006. An algorithm for estimation of membrane water content in PEM fuel cells. *Journal of Power Sources*, **157**, 389–394.

Hakenjos, A., Muenter, H., Wittstadt, U., & Hebling, C. 2004. A PEM fuel cell for combined measurement of current and temperature distribution and flow field flooding. *Journal of Power Sources*, **131**, 213–216.

He, W., Ling, G., & Nguyen, T.V. 2003. Diagnostic tool to detect electrode flooding in proton exchange membrane fuel cells. *Journal of American Institute of Chemical Engineers (AIChe)*, **49**, 3221–3228.

Ju, H., & Wang, C.Y. 2004. Experimental validation of a PEM fuel cell model by current distribution data. *Journal of Electrochemical Society*, **151**, A1954–A1960.

Kim, J., Lee, S.M., & Srinivasan, S. 1995. High energy efficiency and high power density proton exchange membrane fuel cells-electrode kinetics and mass transport. *Journal of ElectrochemicalSociety*, **148**, 2670–2674.

Kocha, S.S., Yang, J.D., & Yi, J.S. 2006. Characterization of gas crossover and its implications in PEM fuel cells. *AIChe Journal*, **52**, 1916–1925.

Kunusch, C., Puleston, P., & Mayosky, M. 2012. *Sliding-mode control of PEM fuel cells*. Springer London.

Larminie, J., & Dicks, A. 2003. *Fuel Cell Systems Explained*. 2nd edn. Wiley and Son.

Lee, C.G., Nakano, H., Nishina, T., Uchida, I., & Kuroe, S. 1998. Characterization of a 100 cm2 class molten carbonate fuel cell with current interruption. *Journal of Electrochemical Society*, **148**, 2747–2751.

Lu, Z., Kandlikar, S.G., Rath, C., Grimm, M., Domigan, W., White, A.D., Hardbarger, M., Owejan, J.P., & Trabold, T.A. 2009. Water management studies in PEM fuel cells, Part II: Ex-situ investigation of flow maldistribution, pressure drop and two-phase flow pattern in gas channels. *Hydrogen Energy*, **34**, 3445–3456.

Lu, Z., , Daino, M.M., Rath, C., & Kandlikar, S.G. 2010. Water management studies in PEM fuel cells, Part III: Dynamic breaktrough and intermittent drainage characteristics from GDLs with and without MPLs. *Hydrogen Energy*, **35**, 4222–4233.

Ma, H.P., Zhang, H.M., Hu, J., Cai, Y.H., & Yi, B.L. 2006. Diagnostic tool to detect liquid water removal in cathode channels of proton membrane fuel cells. *Journal of Power Sources*, **162**, 469–473.

Macdonald, D.D. 2006. Reflections on the history of electrochemical impedance spectroscopy. *Electrochimica Acta*, **51**, 1376–1388.

Macdonald, J. Ross, & Barsoukov, E. 2005. *Impedance Spectroscopy, Theory, Experiment and Applications*. 2nd edn. Wiley-Interscience.

Methekar, R.N., Prasad, V., & Gudi, R.D. 20007. Dynamic analysis and linear control strategies for proton exchange membrane fuel cell using a distributed parameter model. *Journal of Power Sources*, **165**(1), 152 – 170.

Natarajan, D., & Nguyen, T.V. 2006. Effect of electrode configuration and electronic conductivity on current density distribution measurements in PEM fuel cells. *Journal of Power Sources*, **135**, 95–109.

Nikam, V. V. 2002. Collector plate Image (a). *Department of Metallurgical and Materials Engineering, University of Alabama.*

O'Hayre, R.P., Cha, S.W., Colella, W.G., & Prinz, F.B. 2009. *Fuel Cells Fundamentals.* John Wiley & Sons, Inc.

Oszcipok, M., Riemann, D., Kronenwett, U., Kreideweis, M., & Zedda, M. 2005. Statistic analysis of operational influences on the cold start behaviour of PEM fuel cells. *Journal of Power Sources*, **145**, 407–415.

Owejan, J.P., Gagliardo, J.J., Sergi, J.M., Kandlikar, S.G., & Trabold, T.A. 2009. Water management studies in PEM fuel cells, Part I: Fuel cell design and in situ water distributions. *Hydrogen Energy*, **34**, 3436–3444.

Paganin, V.A., Oliveira, C.L.F., Ticianelli, E.A., Springer, T.E., & Gonzalez, E.R. 1998. Modelistic interpretation of the impedance response of a polymer electrolyte fuel cell. *Electrochimica Acta*, **43**, 3761–3766(6).

Parthasarathy, A., Dave, B., Srinivasan, S., & Appleby, A.J. 1992. The platinum microelectrode/Nafion interface: an electrochemical impedance spectroscopic analysis of oxygen reduction kinetics and Nafion characteristics. *Journal of Electrochemical Society*, **139**, 1634–1641.

Pisani, L., Murgia, G., Valentini, M., & D'Agurnno, B. 2002. A new semi-empirical approach to performance curves of polymer electrolyte fuel cells. *Journal of Power Sources*, **108**, 192–203.

Podlubny, I. 1999. *Fractional Differential Equations.* Academic Press.

Primucci, M., Ferrer, Ll., Serra, M., & Riera, J. 2008. Characterisation of fuel cell state using Electrochemical Impedance Spectroscopy Analysis. *1st Iberian Symposium on Hydrogen, Fuel Cells and Advanced Batteries*, 1–26.

Pukrushpan, J., Peng, H., & Stefanopolou, A. 2004a. Control-Oriented Modeling and Analysis for Automotive Fuel Cell Systems. *Journal of Dynamic Systems, Measurement, and Control*, **126**, 14–25.

Pukrushpan, J.T., Stefanopoulou, A.G., & Peng, Huei. 2004b. Control of fuel cell breathing. *Control Systems, IEEE*, **24**(2), 30 – 46.

Ramani, V., Kunz, H.R., & Fenton, J.M. 2004. Investigation of Nafion/HPA composite membranes for high temperature/low relative humidity PEMFC operation. *Journal of Membrane Science*, **232**, 31–44.

Salagado, J.R.C., Antolini, E., & Gonzalez, E.R. 2004. Pt-Co/C PEMFCs electrocatalysts for oxygen reduction in H_2/O_2 synthesized by borohydride method. *Journal of Electrochemical Society*, **151**, A2143–A2149.

Satija, R., Jacobson, D.L., Arif, M., & Werner, S.A. 2004. In situ neutron technique for evaluation of water management systems in operating fuel cells. *Journal of Power Sources*, **129**, 238–245.

Schiller, C.A., Ritcher, F., Güilzow, F., & Wagner, N. 2001a. Relaxation impedance as a model for the deactivation mechanism of fuel cells due to carbon monoxide poisoning. *Physical Chemistry for Chemical Physics*, **3**, 2113–2116.

Schiller, C.A., Ritcher, F., Güilzow, F., & Wagner, N. 2001b. Validation and evaluation of electrochemical impedance spectra of systems with states that change with time. *Physical Chemistry for Chemical Physics*, **3**, 374–378.

Scribner Associates, Inc. 2004. ZPlot and ZView software for Windows (TM). *Advanced product for electrochemical research.*

Springer, T.E., Zawodzinski, T.A., Wilson, M.S., & Gottesfeld, M.S. 1996. Characterization of polymer electrolyte fuel cells using AC impedance spectroscopy. *Journal of Electrochemical Society*, **143**, 587–599.

Squadrito, G., Maggio, G., Passalacqua, E., Lufrano, E., & Patti, F. 1999. An empirical equation for polymer electrolyte fuel cell (PEFC) behaviour. *Journal of Applied Electrochemistry*, **29**, 1449–1455.

Squadrito, G., Maggio, G., Passalacqua, E., Lufrano, E., & Patti, F. 2004. Operational aspects of a large PEFC stack under practical conditions. *Journal of Power Sources*, **128**, 208–217.

Srinivasan, S., Velew, O.A., Parthasarathy, A., Manko, D.J., & Appleby, A.J. 1991. High energy efficiency and high power density proton exchange membrane fuel cells-electrode kinetics and mass transport. *Journal of Power Sources*, **36**, 299–305.

Stumper, J., Campbell, S.A., Wilkinson, D.P., Johnson, M.C., & Davids, M. 1998. In-situ methods for determination of current distributions in PEM fuel cells. *Eelctrochimica Acta*, **43**, 3773–3783.

Stumper, J., Löhr, M., & Hamada, S. 2005a. Diagnostic tools for liquid water in PEM fuel cells. *Journal of Power Sources*, **143**, 150–157.

Stumper, J., Haas, H., & Granados, A. 2005b. In-situ determination of MEA resistance and electrode diffusivity of a fuel cell. *Journal of Electrochemical Society*, **152**, A837–A844.

Teranishi, K., Tsushima, S., & S.Hirai. 2006. Analysis of water transport in PEFCs by magnetic resonance imagining measurement. *Journal of Electrochemical Society*, **153**, A664–A668.

Thomas, S., & Zalbowritz, M. 2000. *Fuel Cell - Green Power.* 1st edn. Los Alamos National Laboratory and 3M Foundation.

Ticcianelli, E.A., Derouin, C.R., & Srinivasan, S. 1988. Localization of platinum in low catalyst loading electrodes to attain high power densities in SPE fuel cells. *Journal of Electroanalytical Chemistry*, **251**, 275–295.

Toray Industries, Inc. 2003. TGP-H Carbon Fiber Paper. *Carbon Fibers and Composite Materials.*

Vega-Leal, A.P., Palomo, F.R., Barragán, F., & Covadonga-García, J. J. B. 2007. Design of control systems for portable PEM fuel cells. *Journal of Power Sources*, **169**(2), 194 – 197.

Wagner, N., Schnurnberger, W., Muller, B., & Lang, M. 1998. Electrochemical impedance spectra of solid-oxide fuel cells and polymer membrane fuel cells. *Electrochimica Acta*, **43**, 3785–3793(9).

Wang, F-C., Chen, H-T., Yang, Y-P., & Yen, J-Y. 2008. Multivariable robust control of a proton exchange membrane fuel cell system. *Journal of Power Sources*, **177**, 393–403.

Wang, X., Hsing, I., & Yue, P.L. 2001. Electrochemical characterisation of binary carbon supported electrode in polymer electrolyte fuel cells. *Journal of Power Sources*, **96**, 282–287.

Wruck, W.J., Machado, R.M., & Chapman, T.W. 1987. Current Interruption - Instrumentation and applications. *Journal of Electrochemical Society*, **134**, 539–546.

Wu, H., Li, X., & Berg, P. 2009. On the modelling of water transport in polymer electrolyte membrane fuel cells. *Electrochimica Acta*, **54**, 6913–6927.

Wu, J., Yuan, X., Wang, H., Blanco, M., J.J., Martin., & Zhang, J. 2008a. Diagnostic tools in PEM fuel cell research: Part I Electrochemical techniques. *Hydrogen Energy*, **33**, 1735–1746.

Wu, J., Yuan, X., Wang, H., Blanco, M., J.J., Martin., & Zhang, J. 2008b. Diagnostic tools in PEM fuel cell research: Part II Physical/chemical methods. *Hydrogen Energy*, **33**, 1747–1757.

Yao, K.Z., Karan, K., McAuley, K.B., Oosthuizen, P., Peppley, B., & Xie, T. 2004. A review of mathematical models for Hydrogen and direct methanol polymer electrolyte membrane fuel cells. *Fuel Cells 2004*, **4**, 3–29.

Yuan, X., Wang, H., Sun, J.C., & Zhang, J. 2007. AC Impedance technique in PEM fuel cell diagnosis - A review. *International Journal of Hydrogen Energy*, **32**, 4365–4380.